**Title**
AN EXPERIMENTAL STUDY OF THE LAMBDA-PROTON INTERACTION



**Author**
Hauptman, John Michael.

**Publication Date**
1974-08-01

LBL-3608
c.1

# AN EXPERIMENTAL STUDY OF THE LAMBDA-PROTON INTERACTION

John Michael Hauptman
(Ph. D. thesis)

August 1, 1974

Prepared for the U. S. Atomic Energy Commission
under Contract W-7405-ENG-48



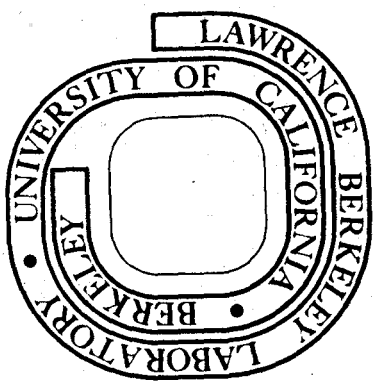


LBL-3608
c.1

## DISCLAIMER

# AN EXPERIMENTAL STUDY OF THE LAMBDA-PROTON INTERACTION

"You haven't told me yet," said Lady Nuttal, "what it is your fiancé does for a living."

"He's a statistician," replied Lamia, with an annoying sense of being on the defensive.

Lady Nuttal was obviously taken aback. It had not occurred to her that statisticians entered into normal social relationships. The species, she would have surmised, was perpetuated in some collateral manner, like mules.

"But Aunt Sara, it's a very interesting profession," said Lamia warmly.

"I don't doubt it," said her aunt, who obviously doubted it very much. "To express anything important in mere figures is so plainly impossible that there must be endless scope for well-paid advice on how to do it. But don't you think that life with a statistician would be rather, shall we say, humdrum?"

Lamia was silent. She felt reluctant to discuss the surprising depth of emotional possibility which she had discovered below Edward's numerical veneer.

"It's not the figures themselves," she said finally, "it's what you do with them that matters."

K. A. C. Manderville, The Undoing of Lamia Gurdleneck

Primary causes are unknown to us; but are subject to simple and constant laws, which may be discovered by observation, the study of them being the object of natural philosophy.

Joseph Fourier, Theory of Heat

# AN EXPERIMENTAL STUDY OF THE LAMBDA-PROTON INTERACTION

John Michael Hauptman

Lawrence Berkeley Laboratory
University of California
Berkeley, California 94720

August 1, 1974

## ABSTRACT

The results of a study of $\Lambda p$ interactions in the intermediate momentum range from 0.5 to 10.0 GeV/c $\Lambda$ laboratory momentum are presented. A total $\Lambda$ pathlength of $2.1 \times 10^6$ cm has been obtained in the 82-inch liquid hydrogen bubble chamber, corresponding to a flux of roughly 60 events/mb. Cross sections for the elastic, inelastic, and resonant production reactions are given, in addition to a measurement of the $\Lambda p$ total cross section. We have studied the channels $\Lambda p \to \Lambda p$, $\Lambda p \to \Sigma^+ p\pi^-$, $\Lambda p \to \Sigma^- p\pi^+$, $\Lambda p \to \Lambda p\pi^+\pi^-$, and $\Lambda p \to \Sigma^0 p$. We do not observe resonant or cusp-like behavior in the elastic reaction near $\Lambda p \to \Sigma^0 p$ threshold. The pion production reactions $\Lambda p \to \Sigma p\pi$ and $\Lambda p \to \Lambda p\pi\pi$ are mediated in large part by single pion exchange, and display rich resonant production of the $\frac{3}{2}^+$ baryon decuplet. Although the data are somewhat limited in statistical precision, the $\Lambda p$ interactions we have studied are approximately consistent with SU(3) symmetry.

## Introduction

Elementary particle physics continually strives to extend the boundaries of our understanding of nuclear particles and their interactions. In the very beginning of this science, the fundamental nuclear force responsible for the existence of nuclei was experimentally investigated in scattering experiments between protons.[1] As techniques became better developed, these experiments were extended in scope to include the scattering of neutrons by protons,[2] and, together with studies of the deuteron, a rather complete and harmonious description[3] of the nucleon-nucleon force was formulated.

When still higher energy protons became available at new particle accelerators, $\pi$ mesons, one of the quanta believed responsible for the nucleon-nucleon force, were produced for the first time in large numbers in the laboratory. There ensued extensive experimentation of the $\pi$-nucleon interaction, of its correlation with the nucleon-nucleon force,[4] and of the rich resonant structure in all charge states of the $\pi$-nucleon system. In 1961, the Eightfold Way[5] was proposed, in which the $\pi$ mesons were members of an irreducible representation of the mathematical symmetry group SU(3) along with five other particles, $K^+, K^0, \overline{K}^0, K^-$ and the $\eta^0$, called the pseudoscalar meson octet.

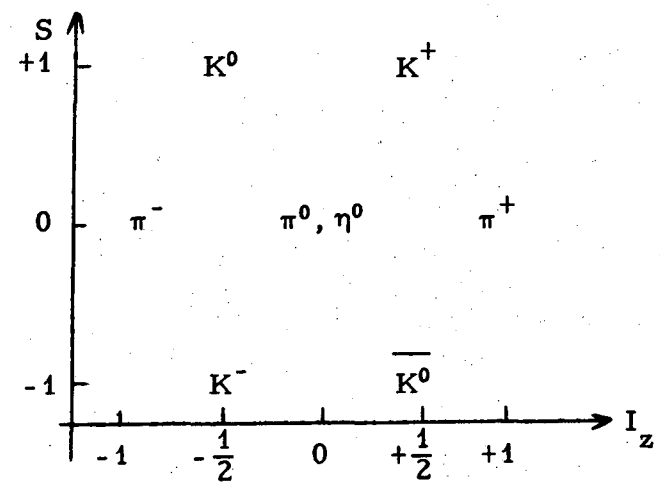


Pseudoscalar ($J^P = 0^-$)
Meson octet

The interactions of all four K mesons with nucleons were also studied in detail, augmenting the data available for study and displaying rich differentiations among these particles. The Eightfold Way also proposed that the proton and neutron were members of another representation, the baryon octet.

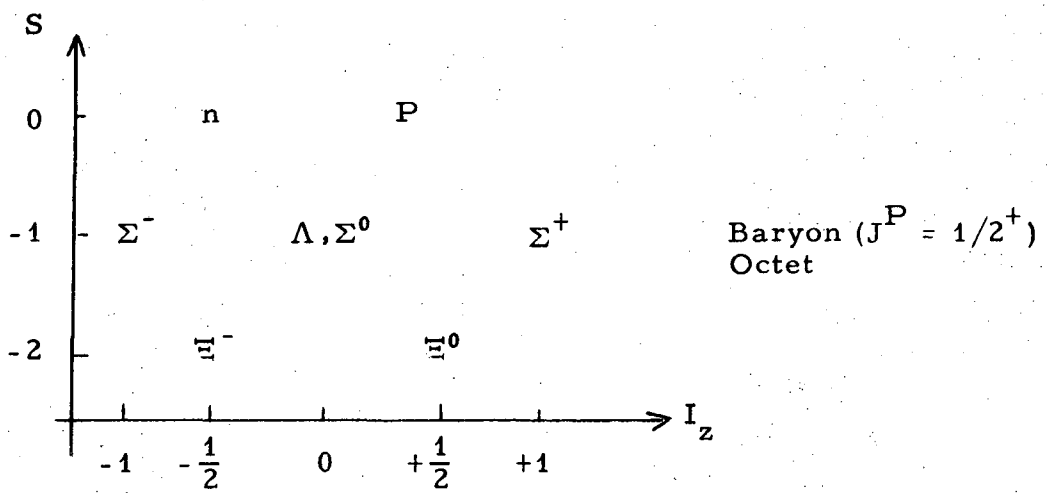


In the same sense that a complete experimental description of the meson octet was very beneficial, one attempts to assemble an experimental description of the interactions of all other members of the baryon octet, the $\Lambda, \Sigma$, and $\Xi$ hypersons with the nucleons. Possibly the easiest way to produce these particles is in high energy $K^-p$ collisions. In such interactions, the probability per collision of producing a $\Lambda$ hyperon is $\approx 0.10$, a $\Sigma$ hyperon $\approx 0.03$, and a $\Xi$ hyperon $\approx 0.007$. All the hyperons (except the $\Sigma^0$ which decays electromagnetically) have roughly the same mean lifetimes, but the $\Lambda$, besides being much more copiously produced, is more easily analyzed in an experimental apparatus than the charged $\Sigma$ hyperons for two reasons: first, it is neutral, and so

does not loose energy in a material medium, and second, it decays into two well-measurable tracks, whereas the charged $\Sigma$ hyperons are short, straight tracks which are difficult to measure accurately. The $\Xi$ hyperon, although easily analyzable, is so meagerly produced that no experiment to date has attempted a systematic study of the $\Xi$-nucleon interaction. This experiment was designed to study the $\Lambda$-nucleon interaction at momenta from 0.5 to 10.0 GeV/c.

Experimental investigation of the hyperon-nucleon interaction is severely inhibited by the short hyperon mean lifetimes of a few times $10^{-10}$ seconds. The resultant mean decay lengths for 2. GeV/c hyperons are about 14 cm for $\Lambda$, 4 cm for $\Sigma^+$, and 7 cm for $\Sigma^-$. Consequently, the bubble chamber is the only experimental technique employed to date in the study of individual $\Lambda$ interactions, primarily because the chamber liquid has served the dual purposes of $\Lambda$ production target and $\Lambda$ interaction detector. The present experiment has improved upon this technique by mounting a very dense platinum target within the chamber liquid to enhance the $\Lambda$ production rate. We have observed roughly 100,000 visible $\Lambda \rightarrow p\pi^-$ decays in the liquid hydrogen in 500,000 photographs.

Despite recent spectacular successes[6,7] in the construction of high energy hyperon beams, the intermediate energy region from 1.0 to 10. GeV has been largely unexplored. Figure 1 shows the number of individual $\Lambda p$ interactions published in the literature, reported at conferences, or reported informally, from the discovery of the $\Lambda$ hyperon in 1947 by Rochester and Butler[8] to the present time.

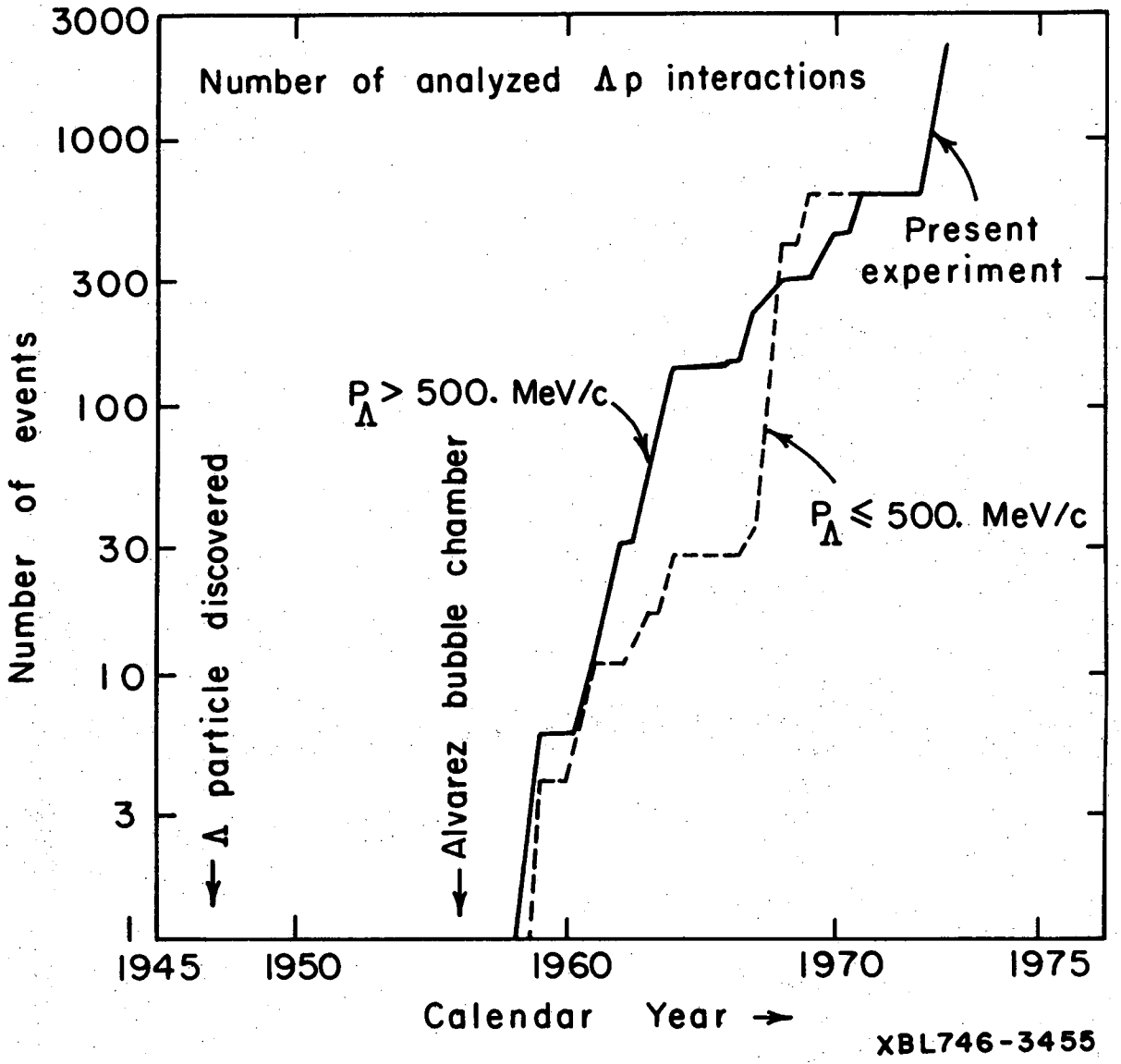


Figure 1. The number of analyzed Λp interactions, above and below 500 MeV/c, reported by investigators from the discovery of the Λ particle in 1947 to the present time.

Previous to the present experiment, direct scattering experiments[9-15] of $\Lambda$ hyperons on proton targets at momenta below 500 MeV/c, where the only channel open is the elastic, have established that the total cross section falls monotonically from about 220 mb at 100 MeV/c to about 25 mb at 500 MeV/c. Reference [13] has displayed this cross section as roughly exponentially dependent on the $\Lambda$ laboratory momentum. The scattering is found to be isotropic in the center-of-mass angle, the forward-to-backward ratio is about unity, and no $\Lambda$ polarization is observed. It may be inferred that the scattering takes place predominantly in an s-wave orbital angular momentum state. The $\Lambda$p total cross section throughout the range 200-500 MeV/c is roughly 3.5 times smaller than the np total cross section. This is not surprising since, in a meson exchange potential description, the long range $\pi$-exchange force is dominant in np scattering and disallowed in $\Lambda$p scattering due to the isospin singlet nature of the $\Lambda$. The pp and $\Lambda$p total cross sections are nearly equal in this momentum range, but the suppression of the pp cross section can be fully accounted for by coulomb repulsion effects which reduce the s-wave scattering length.

Studies of hypernuclei[16] and effective range approximation analyses[14,15] have established that the singlet and triplet s-wave scattering lengths are approximately equal and negative, $a_s \approx a_t \approx -1.6$ fermi. These imply that at very low $\Lambda$ momenta, the total cross section approaches $\sigma_T(\Lambda p) \approx \pi a_s^2 + 3\pi a_t^2 \approx 320$ mb.

At momenta above 500 MeV/c, several experiments[10,17-24] have outlined the general features of the scattering in this domain. Thus, the scattering begins to deviate from being consistent with pure s-wave

scattering,[24] and takes on a character which may be described by some admixture of p-wave scattering near $\Lambda p \rightarrow \Sigma^0 p$ threshold at $P_\Lambda$ = 642 MeV/c incident momentum. At even higher momenta, the elastic scattering becomes highly peripheral,[21] similar to the well-known nucleon-nucleon scattering, although there has been some quantitative controversy[23] on this point. The rapid decrease of the elastic cross section is arrested somewhere in the neighborhood of 20-25 mb. No experiment has observed a substantial enhancement[25a] in the elastic cross section near $\Lambda p \rightarrow \Sigma^0 p$ threshold.

The onset of inelastic channels begins with $\Lambda p \rightarrow \Sigma N$ at about 642 MeV/c, followed by single pion production in $\Lambda p \rightarrow \Lambda N \pi$ and $\Lambda p \rightarrow \Sigma N \pi$ at 900. and 1184. MeV/c, respectively, and then double pion production in $\Lambda p \rightarrow \Lambda p \pi \pi$ at 1370. MeV/c. The $\Lambda p \rightarrow \Sigma^0 p$ reaction cross section is in controversy; one experiment[23] cites 11 events for a $1.5 \pm 0.5$ mb cross section, another[21] does not analyze the reaction due to serious kinematic ambiguity problems, while a third[24] publishes 46 unambiguous events and a cross section which peaks sharply to about 10. mb just above threshold.

Since only the direction of the incident $\Lambda$ is usually known, the $\Lambda p \rightarrow \Lambda p \pi$ and $\Lambda p \rightarrow \Lambda n \pi^+$ reactions are at best constrained by four kinematic equations with four unknowns, and are very difficult to identify unambiguously. However, two experiments have published cross section measurements of the $\Lambda p \rightarrow \Lambda p \pi^0$ reaction, one[24] up to 1.5 GeV/c obtaining a linearly increasing cross section from 0 at threshold to about $5. \pm 2.0$ mb at 1.8 GeV/c. The other experiment[23] finds a momentum-averaged cross section of $4.1 \pm 0.8$ mb from 0.88 to

4.0 GeV/c.

Some data[21] suggest isovector exchange in the double pion reaction $\Lambda p \to \Lambda p\pi^+\pi^-$, and two experiments[21,23] have observed strong $\Sigma(1385)$ $\Delta(1236)$ production in this reaction, although each has only about 12 examples of the reaction.

At "asymptotic" momenta, like 5.0 GeV/c, the $\Lambda p$ elastic cross section becomes nearly constant at 8-10 mb, and rough estimations[21,23] of the total interaction cross section in these two bubble chamber experiments have given $\sigma_T \sim$ 35-40 mb with errors of order 25-40 percent. A recent counter experiment,[6] employing essentially a transmission technique, has determined that the total cross section from 6 to 20 GeV/c $\Lambda$ momentum is consistent with an average value of 34.6±0.41 mb over their entire momentum range.

The present experiment was initiated late in 1969 to strengthen the experimental understanding of the above data, and to extend the amount of data on individual $\Lambda p$ interactions above 1.0 GeV/c. We have studied the reactions

$$\Lambda p \to \Lambda p \tag{1a}$$

$$\Lambda p \to \Sigma^- p\pi^+ \tag{1b}$$

$$\Lambda p \to \Sigma^+ p\pi^- \tag{1c}$$

$$\Lambda p \to \Lambda p\pi^+\pi^- \tag{1d}$$

$$\Lambda p \to \Sigma^0 p \tag{1e}$$

$$\Lambda p \to \Lambda n\pi^+ \tag{1f}$$

$$\Lambda p \to \Lambda p\pi^0 \tag{1g}$$

in the 82-inch hydrogen bubble chamber for $\Lambda$ momenta from about 0.5 to 10.0 GeV/c.

The outline of this thesis is as follows: Section I will discuss the data gathering, with many of the details covered in Appendices I, II, and III; Section II will discuss the elastic reaction; and Section III will describe a measurement of the $\Lambda p$ total cross section employing a new technique. The inelastic reactions will be discussed in Sections IV and V, where the most difficult reactions to analyze are delegated to the latter section. Finally, a review of cross sections is given in Section VI. The appendices have been reserved for discussions of matters of little concern to the non-specialist, although Appendices I, II, and III are very important for the experiment. Appendix IV discusses Lorentz Invariant phase space calculations employed in the invariant mass fits of Section IV; Appendix V discusses $\Xi^-$ and $\Omega^-$ decays in this experiment, gives a measurement of the parity violating parameter in $\Xi^- \rightarrow \Lambda\pi^-$ decay, and presents cross sections for various final states in $\Xi^0 p$ interactions at high energies. Appendix VI details the calculation of the propagation of the $\overline{K}^0$ amplitude through the platinum plate; Appendix VII gives SU(2) and SU(3) coefficients for easy reference, quark model calculations, and U-spin amplitudes relevant to $\Lambda p$ interactions we have studied. Appendix VIII gives some details of the calculation involved in the total cross section measurement; and finally, Appendix IX gives tables of cross sections displayed in the figures. Figures and their captions appear within each section for convenience.

Section I. Description of the Experiment

A. Data Collection and Reduction.

The copious production of $\Lambda$ hyperons for a scattering experiment in the few GeV region involves the following considerations. Firstly, one may readily conclude that the bubble chamber is the only reasonable detector to use because of its $4\pi$ steradian solid angular acceptance and 100 micron spatial resolution. In addition, the $\Lambda$ mean proper lifetime, $\tau = 2.58 \cdot 10^{-10}$ seconds, and consequent mean decay length $\lambda = (p/m)c\tau$ cm, necessitates the production of $\Lambda$ hyperons within, or at least a few decay lengths from, the detector itself.

Secondly, the ratio of the $\Lambda$ hyperon production rate to the background production rate should be maximal. This is the case for $\overline{K}N$ interactions at high energy, where

$$\frac{\sigma_{\Lambda \text{ production}}}{\sigma_{\text{total}}} \cong \frac{2.2 \text{ mb}}{21.5 \text{ mb}} \cong 0.10.$$

These ratios in NN and $\pi N$ interactions are 0.023 and 0.03, respectively, and NN interactions have the further disadvantage of a large, energetic neutron background. In $\overline{K}N$ interactions, the neutron background comes primarily from the $\Lambda \rightarrow n\pi^0$ decays.

Thirdly, we have mounted a dense metal target within the bubble chamber to enhance the $\overline{K}$ interaction rate, and hence the $\Lambda$ production rate, inside the detector.[24] The highest density is desirable, since the $\overline{K}$ interaction rate per unit length is maximal, and the $\Lambda$ decay loss inside the target is minimal. Platinum was chosen for its high density and strength (only osmium is more dense, but brittle).

Finally, the choice of a $K^-$ beam was made over a $K_L^0 = \frac{1}{2}\ \bar{K}^0 + \frac{1}{2}\ K^0$ beam primarily so that the $K^-$ trajectory could be measured and projected through the platinum target, obtaining a well-defined line source for the produced $\Lambda$ particles.

The data in this thesis were obtained in a 500,000-picture exposure of the SLAC 82-inch hydrogen bubble chamber to a radiofrequency-separated 12. GeV/c negative kaon beam. Two runs were taken in September 1970 and April 1971. The beam was the C beam to the 82-inch chamber,[26] and was modified at the last quadrupole doublet to focus the dispersed beam to small dimensions in the vertical plane. The $K^-$ yield was ~ 4.5 $K^-$ mesons per pulse at the 12. GeV/c radio-frequency pass band, and at an electron intensity of about 35 ma. The $K^-$ target was a platinum plate 10.0 inches wide, 0.75 inches deep, and 3.0 inches long (or roughly one interaction length) in the beam direction. This platinum target was mounted within the liquid hydrogen of the chamber, positioned just above the beam centerline (so that other experiments might also proceed by steering their beams below the platinum), and about 4 inches downstream of the edge of the visible volume so that entering $K^-$ beam tracks are visible. Very little bubble formation was observed about sharp edges of the plate. The platinum plate was machined and bolted to mounts welded to the wall of the chamber.[27] The mounting was capable of withstanding the pulsed accelerations of the chamber body of roughly 30g per pulse, where g is the acceleration of gravity, for nearly 2 million pulses. Typical photographs of $\Lambda p$ scatters are shown on the following pages. One feature of $\Lambda$ production in high energy $K^-p$ collisions[28] is that $\Lambda$

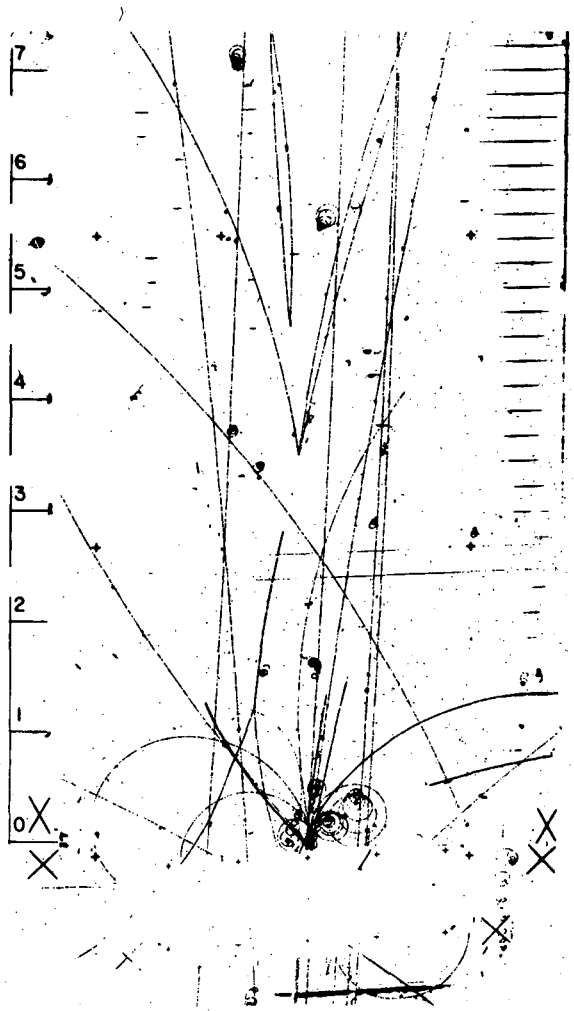

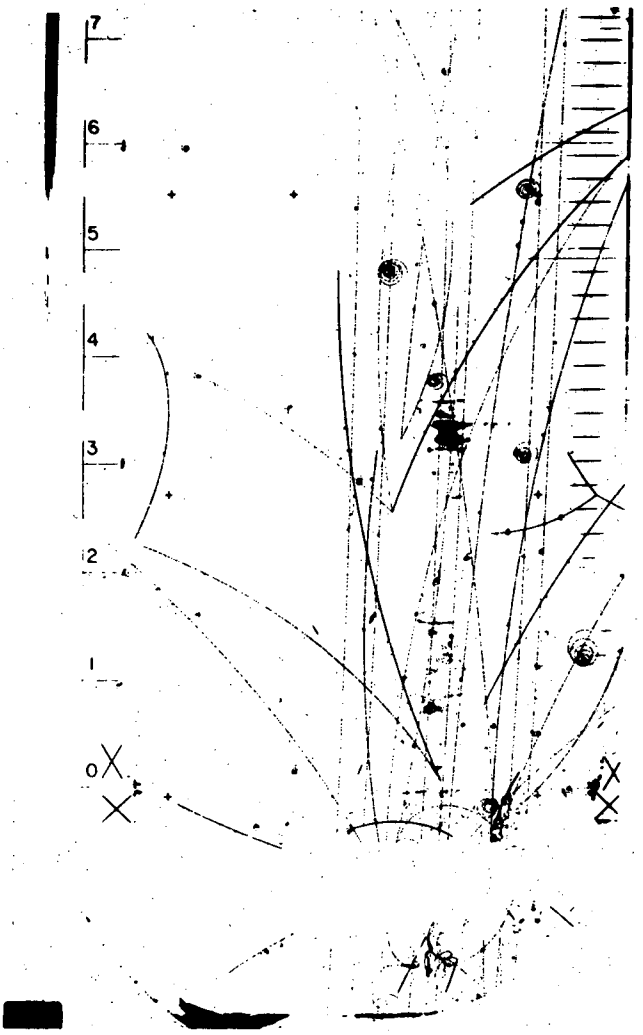
7
6
5
4
3
2
1
0

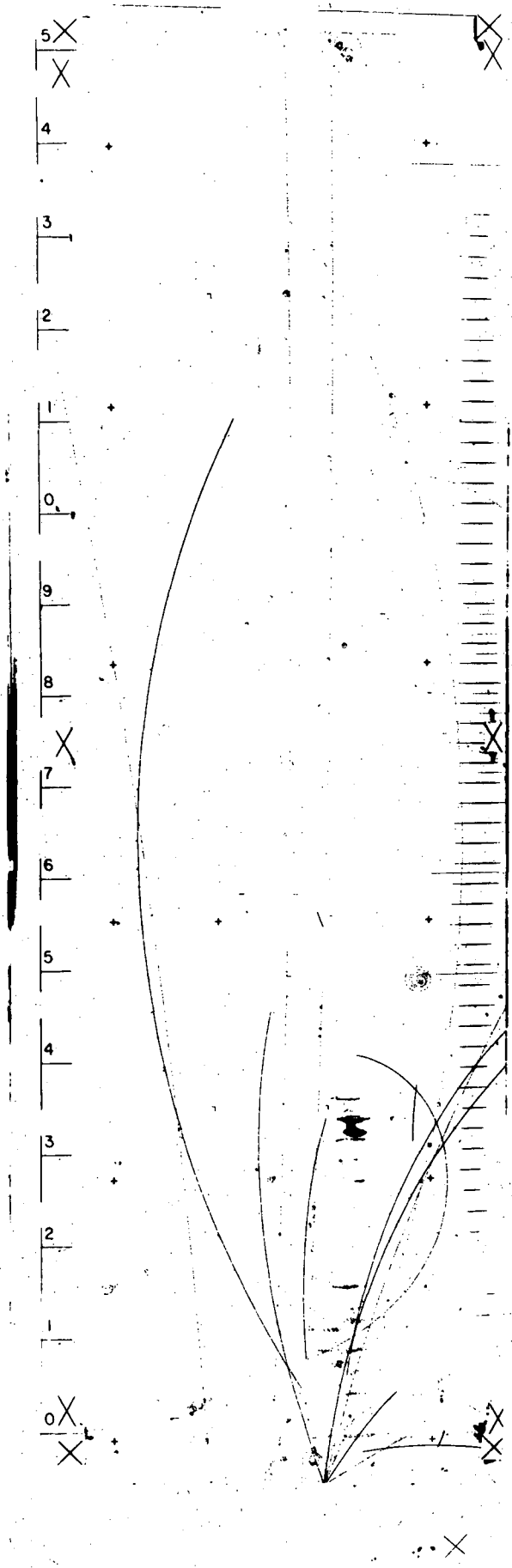
5
4
3
2
1
0
9
8
7
6
5
4
3
2
1
0

particles are not produced peripherally as in lower energy $K^-p$ collisions. In particular, for reactions yielding high pion multiplicities ($n_\pi \geq 4$), the $\Lambda$ production angular distribution in the center-of-mass is both forward and backward peaked with a mean near $\cos\theta^*_{cm} \approx 0$, and hence a mean center-of-mass longitudinal momentum near $P^*_L \approx 0.$ GeV/c. At low pion multiplicities ($n_\pi \leq 3$), the $\Lambda$ production is distinctly peripheral and forward peaked with respect to the target baryon direction. Since the $\Lambda$ production cross section at these high momenta is dominated by higher pion multiplicities, the $\Lambda$ laboratory momentum and pathlength distributions extend to rather high momenta, and are useful in this experiment up to about 10. GeV/c. These are displayed in Figs. 2a,b. The measured $\Lambda$ decays in Fig. 2b are a fraction, $f_M = 0.0667$ of the total number of $\Lambda$ decays to be found in the film on a single scan. This number is the basic cross section normalization factor for the entire experiment. The pathlength distribution in Fig. 2a has been normalized by this factor, and corrected for scanning efficiency and the visible $\Lambda$ decay branching ratio, and thus represents the actual $\Lambda$ flux in this experiment corresponding to ~60 events/mb.

The film was scanned[29] for all neutral-induced reactions, free $V^0$ decays, and charged particle induced reactions leading to a single strange particle, and charged particle decays leading to a $V^0$ decay. Those event types relevant to this analysis are sketched in Fig. 3. Prior to measurement all events found on the primary scan (except event types 6 and 7) are critically re-evaluated[33] as to their reality by a more experienced scanner who makes a sketch of the event and the interacting beam tracks in two views. This procedure was demonstrated[30] in an earlier experiment to save considerable measuring

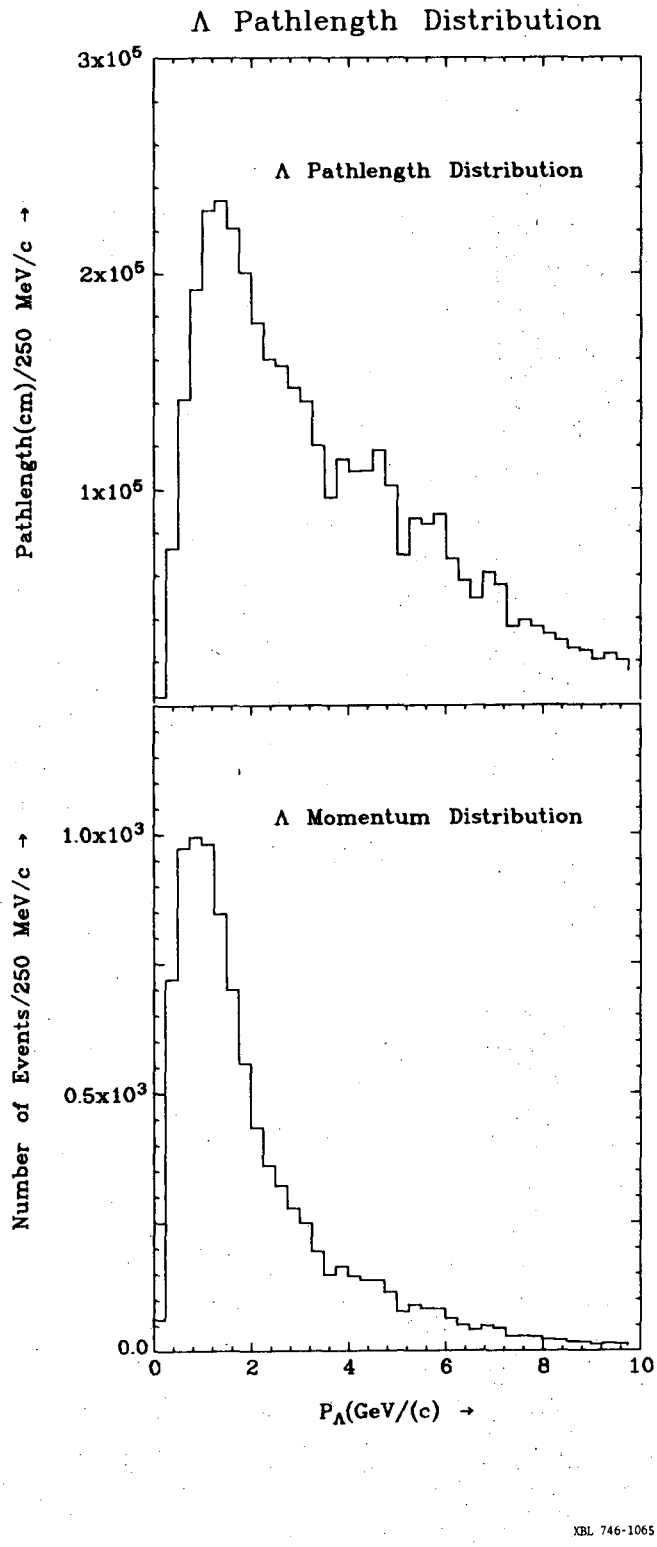


Figure 2. (a) Λ pathlength distribution for the entire experiment, corrected for scanning losses and the visible Λ decay branching fraction.
(b) Λ momentum distribution of observed Λ decaying in the liquid hydrogen.

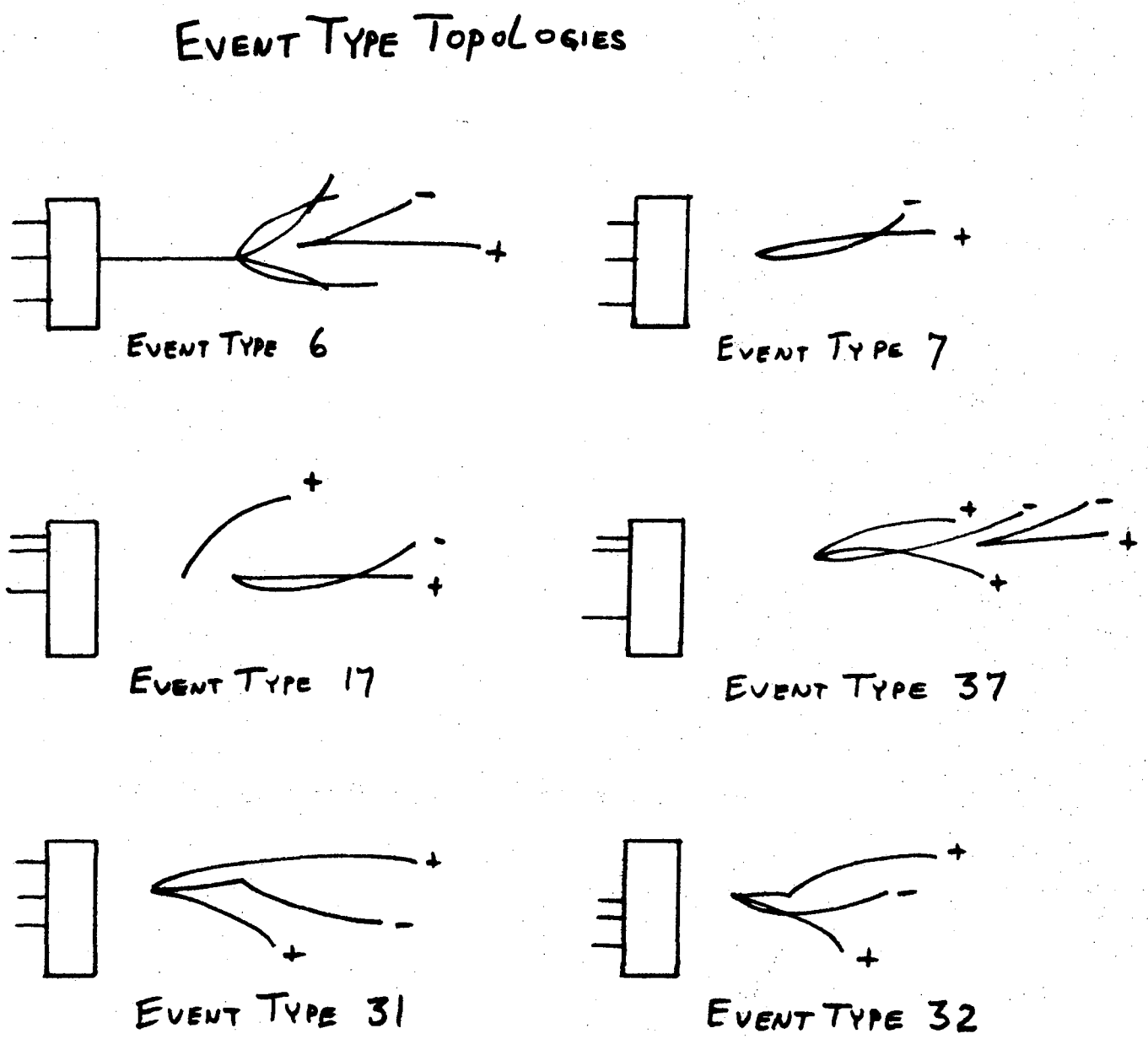


Figure 3. Event type topologies 6, 7, 17, 31, 32, and 37 relevant to the main body of this thesis. Topologies for higher charged prong multiplicities were also recorded, but not analyzed, and those with two visible strange particles are discussed in Appendix V.

time due to both the higher frequency of real interaction events in the measurement sample, and the enhanced probability of a successful measurement with the assistance of a sketch.

The events are then measured on the Franckenstein measuring machines in the LBL COBWEB system,[31] and processed through the programs MEDIT-TVGP-SQUAW. In addition to measuring the tracks participating in the interaction, measurements are also made of beam tracks which interact in either the platinum target or the liquid hydrogen for the purpose of spatially reconstructing the beam track interaction vertex. For beam tracks interacting in the platinum, all minimum ionizing tracks exiting from the platinum are also measured. These tracks are fit to a quadratic trajectory, propagated backwards through the platinum with proper multiple scattering errors and energy loss correction, and employed in a search for intersections with incoming beam tracks. A minimum chi-squared for an n-track intersection with (n-2) degrees of freedom defined the best intersection. For beam tracks interacting in the liquid hydrogen, a single point in each view is measured. All such vertices are candidates for the origin of the neutral particle which induced the reaction. We have modified EDIT (renamed MEDIT) and TVGP to accommodate the geometrical reconstruction of these beam track interactions to be used later in SQUAW in the kinematic reconstruction of reactions such as 1(e-g). Details of the origin reconstruction are given in Appendix III. Since $\Lambda p \to \Lambda p$ and $\Lambda p \to \Lambda p\pi^+\pi^-$ scatters are identifiable with or without an origin, a large sample of these scatters was used to estimate the origin reconstruction efficiency. An efficiency of $76 \pm 4$ percent was obtained.

Kinematic solutions of SQUAW consistent with energy and momentum conservation above the 0.01 confidence level are compared with bubble density ionization information at the scan table,[32] and only solutions consistent with particle identification by ionization are accepted and stored on the Data Summary Tape (DST). Whenever two or more hypotheses of possibly different constraint classes are acceptable, all are stored on the DST.[34]

Thirty percent of the data has been scanned a second time, and a very small fraction a third time, to estimate scanning efficiencies for all event types. A detailed discussion of the calculation of scanning efficiencies in this experiment is given in Appendix II of this thesis. The second scan events were subjected to the same scanning procedures as the first, and no information obtained on the first scan was employed in the second scan. We find considerable spatial variation of the scanning efficiency along the beam direction for all event types near the plate where secondary particles from the $K^-$-nucleus collisions obscure the field of view. The usual assumption that each event has an a priori probability of being found by the average scanner is not a good assumption in the few centimeters downstream of the platinum target. It was calculated that type 7 events in this region have a mean probability of being found which is about 25 percent less than in other regions of the chamber. Furthermore, the measurement failure rate was found to be higher near the platinum target than farther downstream. These efficiency variations along the beam direction have been taken into account in every aspect of the analysis of the data.

The final data sample consists of the following numbers of events (weighted for scanning efficiency and escape correction losses):

Table 1. Numbers of events.

| Reaction | Number of Events | Number of Weighted Events |
|---|---|---|
| $\Lambda p \rightarrow \Lambda p$ | 584 | 942.2 |
| $\Lambda p \rightarrow \Sigma^- p\pi^+$ | 132 | 169.4 |
| $\Lambda p \rightarrow \Sigma^+ p\pi^-$ | 60 | 107.6 |
| $\Lambda p \rightarrow \Lambda p\pi^+\pi^-$ | 181 | 221.4 |
| $\Lambda p \rightarrow \Sigma^0 p$ | 25 | 40.4 |
| $\Lambda p \rightarrow \Lambda n\pi^+$ | - | - |
| $\Lambda p \rightarrow \Lambda p\pi^0$ | - | - |

Since the latter two reactions have not been unambigiously identified, we do not attempt to quote cross sections, but do present an analysis of these reactions, together with the $\Lambda p \rightarrow \Sigma^0 p$ reaction, in Sec. V.

The elastic $\Lambda p$ scattering plus the subsequent $\Lambda$ decay [Eq.(1a)] is kinematically a 4-constraint fit: three constraints at the $\Lambda \rightarrow p\pi^-$ decay vertex and one constraint at the $\Lambda p$ interaction vertex, without knowledge of the incident $\Lambda$ direction. Knowledge of the $\Lambda$ origin coordinates contributes two additional constraints of transverse momentum balance to the kinematic fit. Chi-squared distributions for 4- and 6-constraints are shown in Figs. 4(a-b). We have found that the elastic reaction is largely unambiguous event without these two constraints on transverse momentum, and other experiments[21,23,24] have come to a similar conclusion. The elastic reaction suffers from loss of events at low momentum transfer to the recoil proton due to the inability of protons below a momentum of about 100. MeV/c to form a track long enough to be

recognized. If $t_m(\text{GeV}/c)^2$ is the minimum momentum transfer squared at which a recoil proton track is visible, and $B(\text{GeV}/c)^{-2}$ is the slope of the elastic diffraction peak, then the fraction of events lost is

$$\text{fraction lost} \approx 1 - e^{Bt_m} .$$

This is typically a correction of 0.07 to the elastic data at high momentum. The scanning efficiency for the elastic topology, event type 17 in Fig. 3, shows substantial variation through the fiducial volume, being particularly poor very near the plate. This efficiency is displayed in Fig. II.1 of Appendix II.

The reactions $\Lambda p \to \Sigma^{\pm} p \pi^{\mp}$ plus the charged $\Sigma^{\pm}$ decays are two-constraint kinematic fits without use of the incident $\Lambda$ origin coordinate; however, the charged $\Sigma^{\pm}$ hyperons have mean decay lengths of a few centimeters, and consequently their momenta are poorly determined by a sagitta measurement in a bubble chamber with a spatial resolution of roughly 100 microns in real space. Since this constraint is usually in practice not used, these events are essentially one-constraint without a $\Lambda$ origin, and three-constraint with an origin. We have taken care to remeasure topologies of the above reactions up to four times if a three-constraint fit has not been obtained. Scanning efficiencies for these topologies have been estimated from the measured scanning efficiency of the much more numerous three-prong recoils (type 30) without a decaying track, and making a subsequent correction for short $\Sigma$ decay losses and center-of-mass angular decay losses in the decays $\Sigma^{\pm} \to n\pi^{\pm}$ resulting from too small an angle between $\Sigma$ and $\pi$ to be resolved visually at the scan table. The decay $\Sigma^{+} \to p\pi^{0}$ was not used

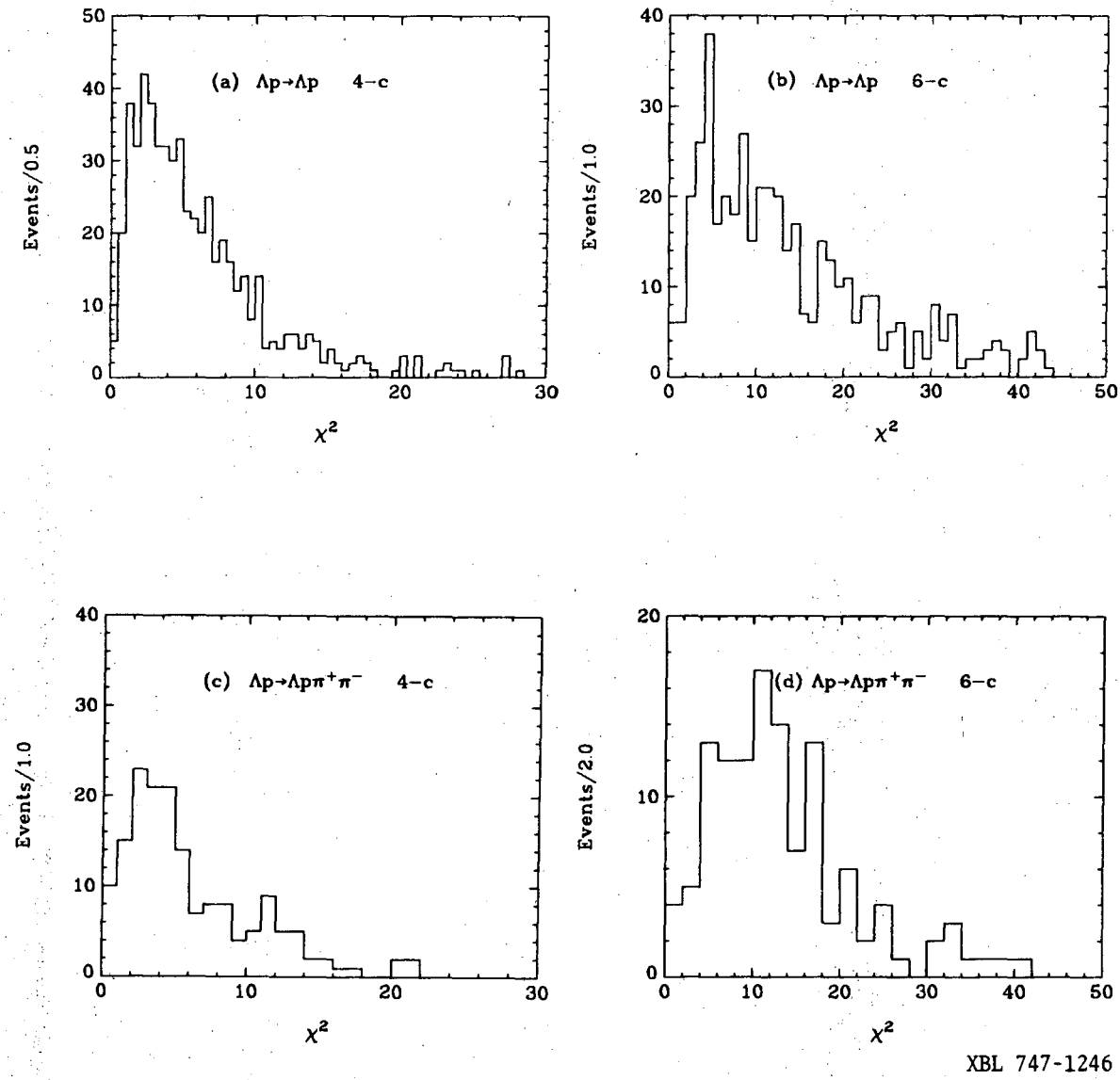


Figure 4. (a) 4-constraint (4c) chi-squared distribution for the reaction hypothesis $\Lambda p \rightarrow \Lambda p$ without use of the origin information; (b) corresponding 6-constraint (6c) chi-squared distribution using the origin information. (c) 4-constraint chi-squared for $\Lambda p \rightarrow \Lambda p \pi^+ \pi^-$ hypothesis without origin information; (d) corresponding 6-constraint with origin information.

in any cross section determination because its visual detection efficiency was only 20-30%; instead, the decay $\Sigma^+ \rightarrow n\pi^+$ was weighted by the appropriate branching ratios

$$\frac{BR(\Sigma^+ \rightarrow p\pi^0) + BR(\Sigma^+ \rightarrow n\pi^+)}{BR(\Sigma^+ \rightarrow n\pi^+)} \cong 2.03.$$

Chi-squared distributions for these fit hypotheses are shown in Figs. 5(a-d).

The $\Lambda p \rightarrow \Lambda p\pi^+\pi^-$ reaction (1d) is in the same constraint class as the elastic reaction, its scanning efficiency is very high ($\sim 0.95$), and chi-squared distributions for the four- and six-constraint hypotheses are shown in Figs. 4(c-d).

The $\Sigma^0$ production reaction $\Lambda p \rightarrow \Sigma^0 p$ (1e) requires an origin in order to be overconstrained. The overall constraints are four in number, with three constraints at the $\Lambda \rightarrow p\pi^-$ decay vertex, and one at the combined $\Lambda p \rightarrow \Sigma^0 p$ interaction vertex and the $\Sigma^0 \rightarrow \Lambda\gamma$ decay vertex. This reaction is discussed further in Sec. V.

The two reactions $\Lambda p \rightarrow \Lambda n\pi^+$ (1f) and $\Lambda p \rightarrow \Lambda p\pi^0$ (1g) are zero-constraint if the origin of the incident $\Lambda$ is known. SQUAW solutions to $\Lambda p \rightarrow \Lambda n\pi^+$ are ambiguous with at least one other solution in 90% of all cases, and $\Lambda p \rightarrow \Lambda p\pi^0$ solutions are ambiguous in 50% of all cases. Due to these severe ambiguity problems, these reactions are not as readily analyzable as the other reactions, and we defer discussion of an attempted analysis to Sec. V.

Finally, the decay $\Lambda \rightarrow p\pi^-$ is a one-constraint hypothesis without an origin, and three-constraint with an origin. The scanning efficiency

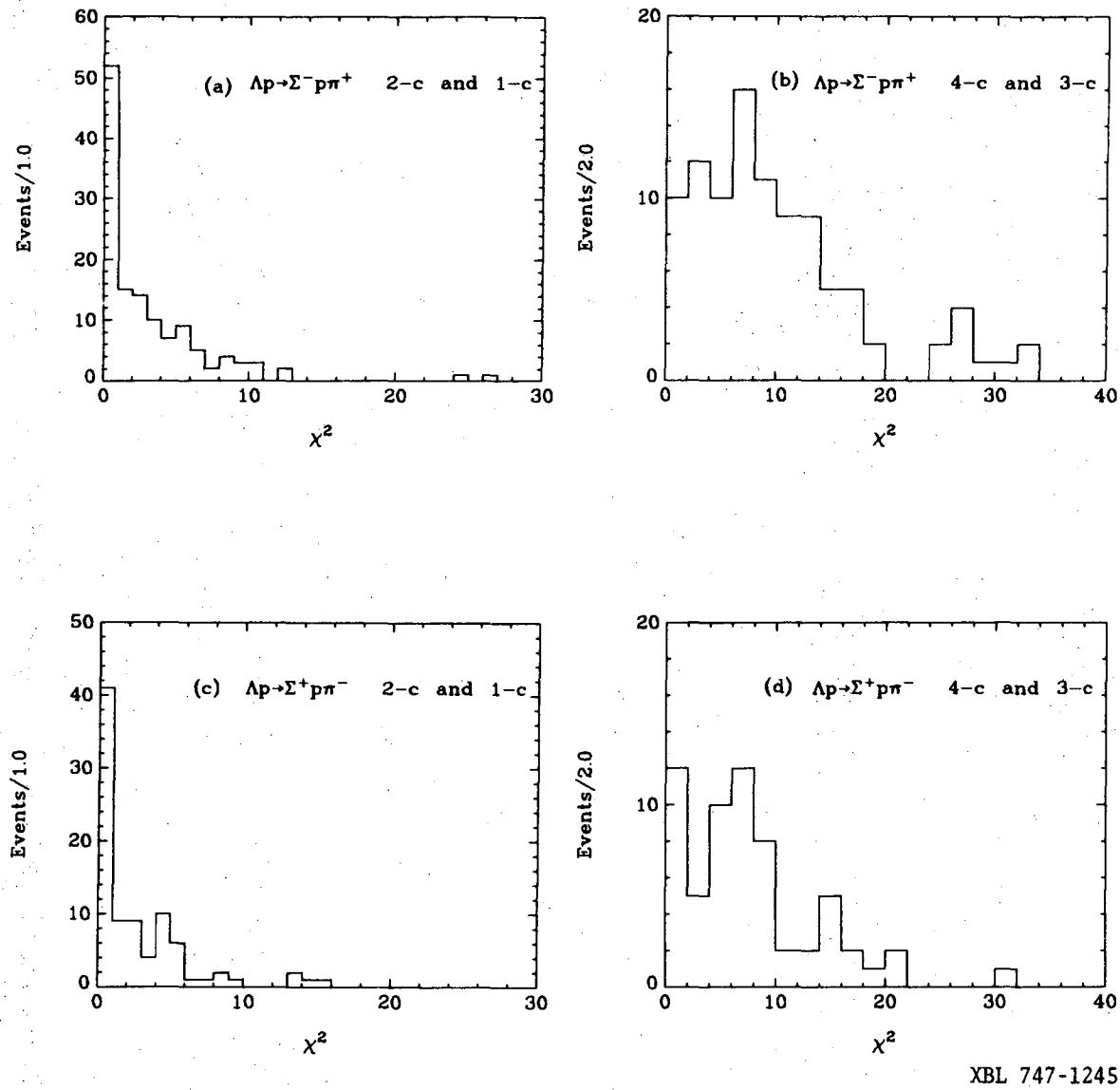


Figure 5. (a) 2-constraint chi-squared for $\Lambda p \rightarrow \Sigma^- p\pi^+$ hypothesis without origins; (b) corresponding 4-constraint with origins. (c) 2-constraint chi-squared for $\Lambda p \rightarrow \Sigma^+ p\pi^-$ hypothesis without origins; (d) corresponding 4-constraint with origins. About half of the events in these distributions have no momentum measurement of the $\Sigma$ decay track, reducing the constraint classes to 1-constraint and 3-constraint, respectively.

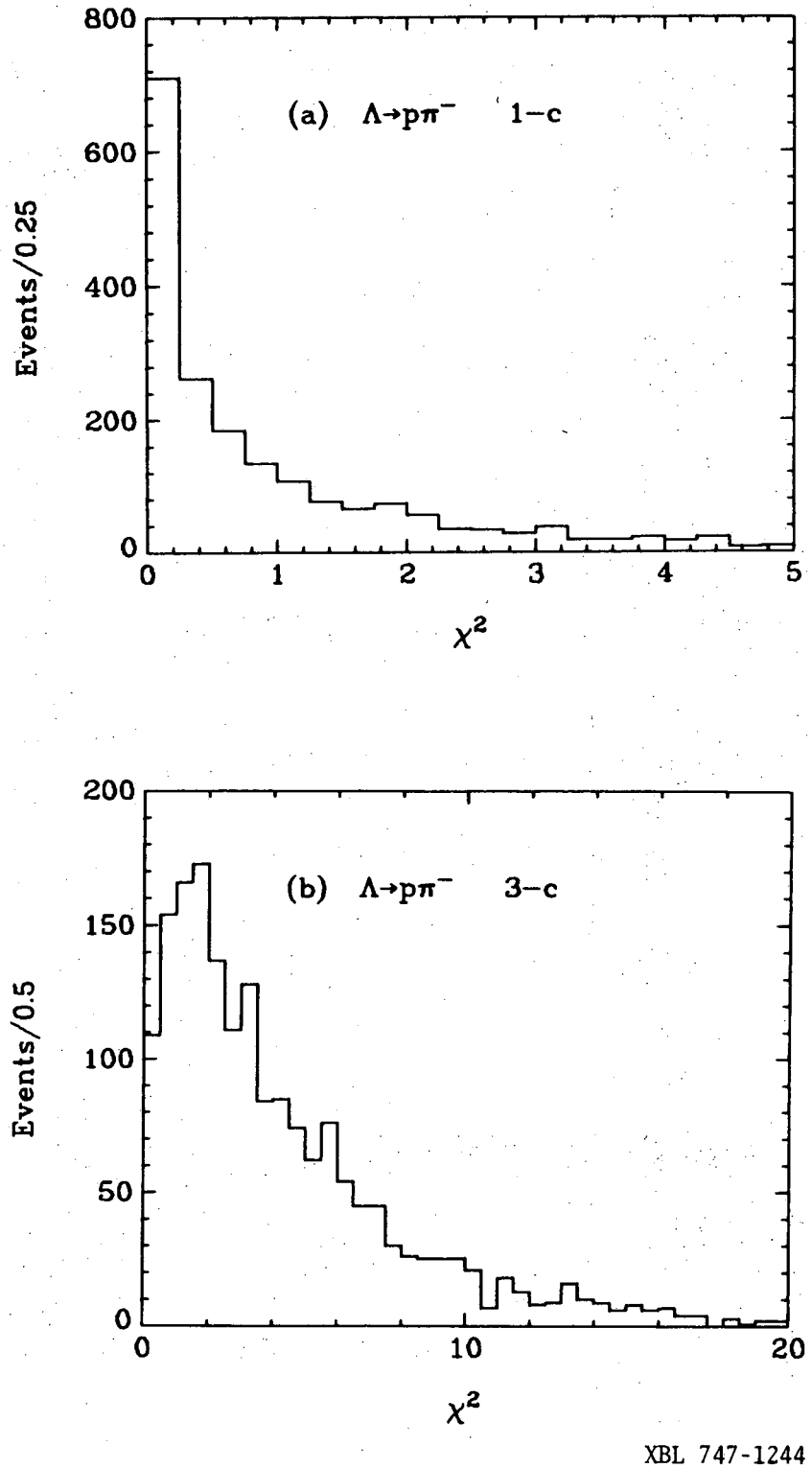


Figure 6. (a) 1-constraint chi-squared distribution of $\Lambda \rightarrow p\pi^-$ decay hypothesis; (b) 3-constraint chi-squared for the same decays using the one- or three-prong recoil vertex in event types 17 or 37 as the $\Lambda$ origin.

is relatively good in this experiment except very near the plate, where charged secondaries exiting from a beam track interaction inside the platinum can sometimes simulate the $V^0$ decay topology. The $\Lambda \rightarrow p\pi^-$ and $K_1^0 \rightarrow \pi^+\pi^-$ decays are ambiguous only in that region of $K_1^0$ decay phase space in which the $\pi^+$ decays forward in the center-of-mass. Figure 7 displays the dependence of the laboratory opening angle of the $V^0$ versus the momentum balance between positive and negative tracks. Actual $\Lambda$ and $K_1^0$ decays of the indicated momentum will fall along these curves. The $\Lambda$ and $K_1^0$ decay curves overlap near $\alpha \approx 1.0$, and since about half the $\Lambda$ phase space overlaps with a much smaller fraction of $K_1^0$ phase space, one is justified in assigning ambiguous events to the $\Lambda \rightarrow p\pi^-$ decay. After such assignment, the ambiguity rate is only 2% at a few GeV/c $V^0$ momentum.

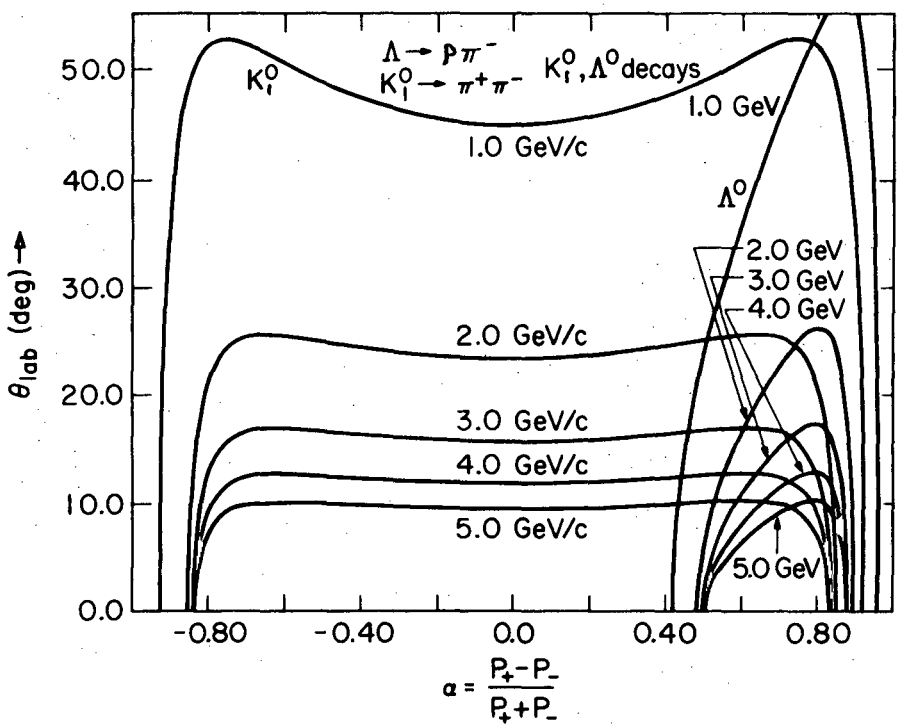


Figure 7. Plot of momentum balance between positive and negative tracks from a $V^0$ decay, $\alpha = (p_+ - p_-)/(p_+ + p_-)$, versus the laboratory opening angle of the $V^0$. $\Lambda$ and $K_1$ decays lie along the lines shown corresponding to their momenta; $\gamma \rightarrow e^+e^-$ conversions all lie along the line $\theta_{lab} = 0$.

Section II. Elastic Scattering

A. The elastic scattering cross section is shown in Fig. 8, and is very similar to the proton-proton elastic cross section represented by the solid line. The differential elastic cross sections $d\sigma/d\Omega$ and $d\sigma/dt$ are displayed in Fig. 9 as functions of the incident $\Lambda$ momentum, and one may, in particular, observe the rapid variation of the event distributions in $\cos\theta^*$ as the elastic reaction proceeds from isotropic to highly peripheral scattering. Fits of the differential cross section in t, the four-momentum transfer squared, to the form

$$\frac{d\sigma}{dt} = Ae^{Bt} \qquad 0.01 \leq -t \leq 0.41 \text{ (GeV/c)}^2 \qquad (2)$$

reveal a shrinkage of the diffraction peak very similar to that observed in pp and $K^+p$ elastic scattering, two channels believed not to be resonant in the s-channel. These fitted slopes are given in Table 2 and displayed in Fig. 10, together with pp slopes fitted by the same algorithm over the same range of t.

Table 2. Elastic slope parameter

| $P_\Lambda$(GeV/c) | Mean $P_\Lambda$(GeV/c) | B(GeV/c)$^{-2}$ |
|---|---|---|
| 0.64 - 0.90 | 0.77 | 2.39 ± 1.84 |
| 0.90 - 1.34 | 1.12 | 0.45 ± 1.26 |
| 1.34 - 2.40 | 1.87 | 3.44 ± 0.77 |
| 2.40 - 4.40 | 3.28 | 5.85 ± 0.63 |
| 4.40 - 10.0 | 5.90 | 6.55 ± 0.92 |

These data on the total and differential elastic cross sections are in accord with the published results of Kubis and Walters.[36]

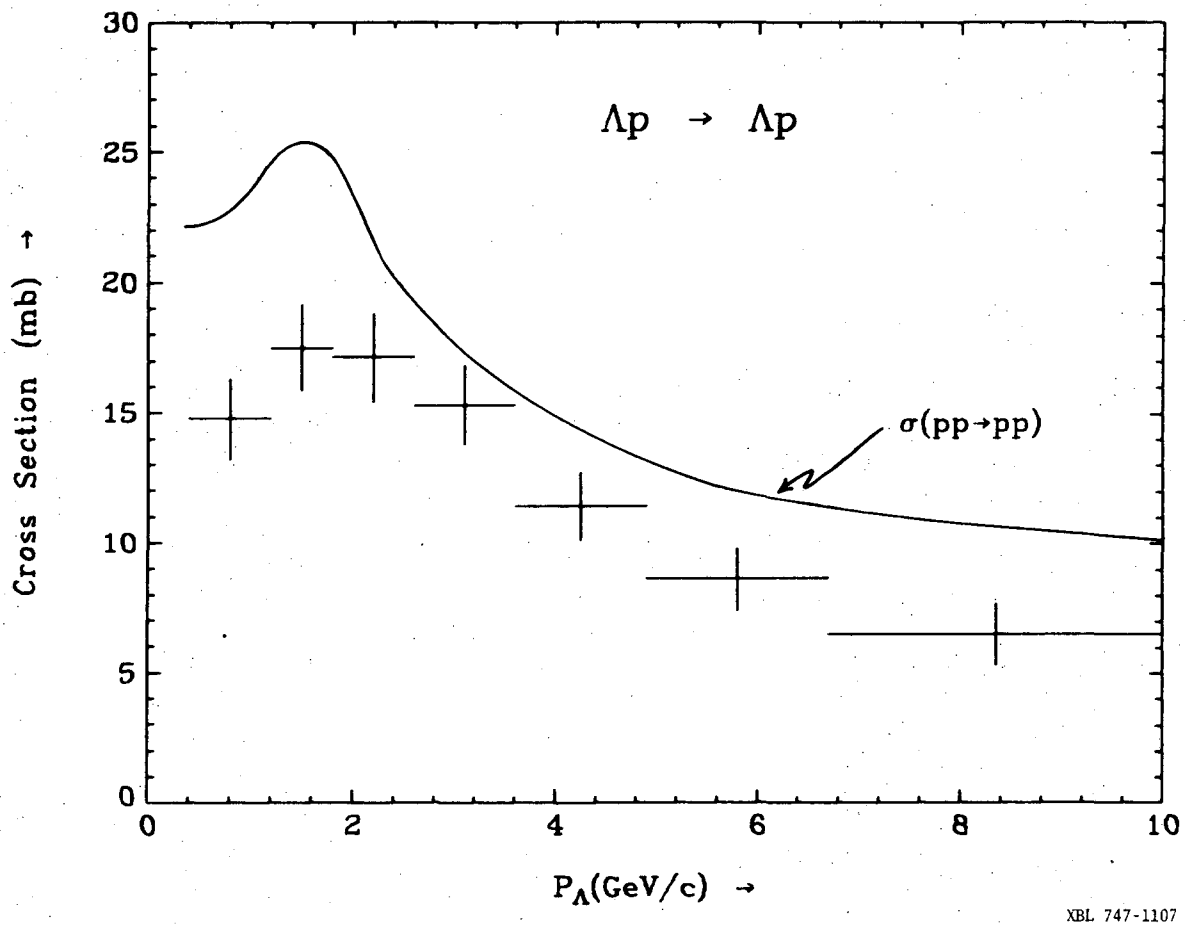


Figure 8. The elastic Λp cross section from 0.4 to 10.0 GeV/c, compared to the pp elastic cross section. Below 500 MeV/c both of these cross sections rise to very large values (see Fig. 61.)

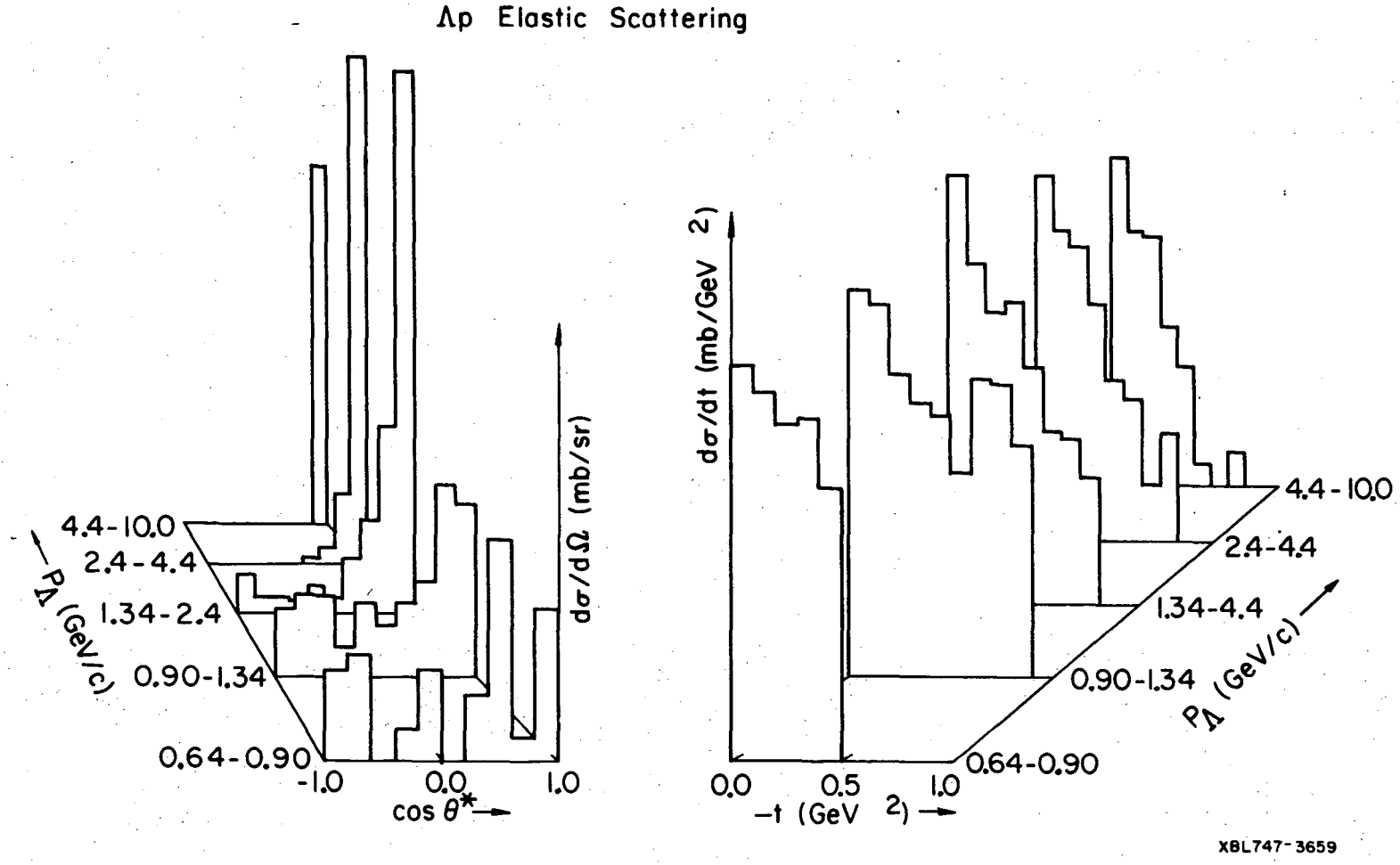


Figure 9. Differential elastic cross sections in $\cos\theta^*$ and t, versus Λ laboratory momentum. A tabulation of $[d\sigma/dt\ (MeV/GeV^2)]$ is given in Appendix IX.

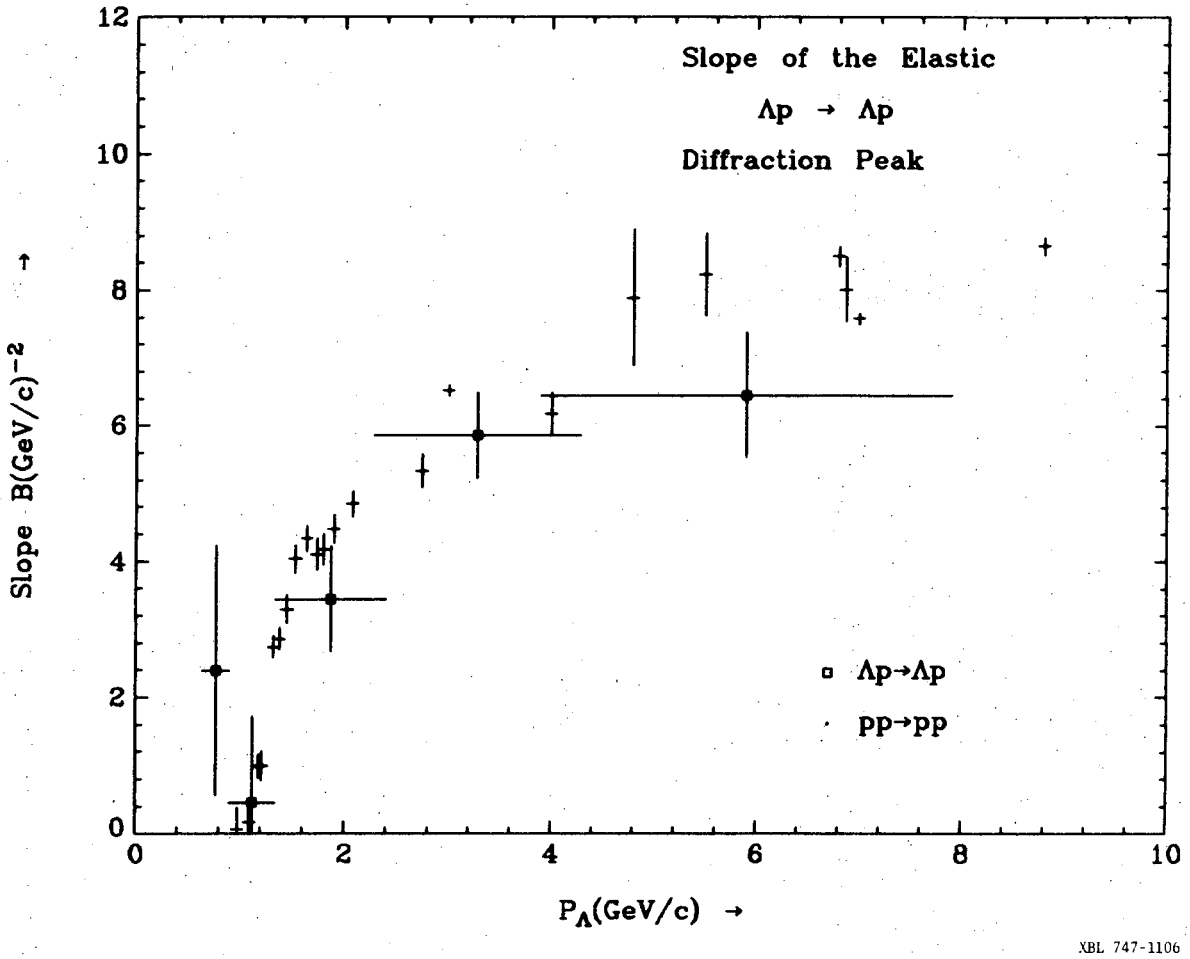


Figure 10. The elastic diffraction slope parameter fitted over the t range $0.01 \leq -t(\mathrm{GeV}/c)^2 \leq 0.41$. The data points with smaller errors are slope parameters in pp elastic scattering fitted by the same algorithm over the same range of t.

The elastic Λp and pp reactions show remarkable similarity in both the magnitude and momentum dependence of the diffraction slope parameter, and in both reactions, the optical diffraction appears to set in at the first inelastic threshold. These measurements are at some variance with a previous experiment,[23] which measured a slope parameter $B = 3.5 \pm 1.0\ (\mathrm{GeV/c})^{-2}$ averaged over the Λ momentum range 1.5 to 4.0 GeV/c.

Care has been taken in the measurement of the slope parameter to avoid a kinematic bias introduced by the averaging of data over a finite range in Λ center-of-mass momentum. The bias results from the fact that in the elastic reaction the $\cos\theta^*$ ranges for different center-of-mass momenta, q, are mapped onto different regions of t by

$$t = -2q^2(1 - \cos\theta^*), \tag{3}$$

and consequently several ensembles of elastic events at different center-of-mass momenta, all of which are isotropic in $\cos\theta^*$, will yield when combined into one ensemble a t-distribution which is not isotropic, as it must be by relation (3). We have corrected for this bias below 2.4 GeV/c Λ momentum by transforming the four-momentum transfer squared, $t_i$, for each event in a given momentum bin by the Jacobian of the transformation relating $\cos\theta^*$ to t,

$$t_i' = t_i \left(\frac{q_o}{q_i}\right)^2, \tag{4}$$

where $q_i$ is the center-of-mass momentum of that event, and $q_o$ is some appropriate average of the center-of-mass momenta of all events in the given momentum bin. This effectively averages events in $\cos\theta^*$, instead of t, by mapping each event onto the same t region. Simple

considerations indicate that the proper average, $q_o$, is just

$$q_o = \frac{1}{n} \sum_{i=1}^{n} q_i, \tag{5}$$

where n is the number of events in the bin.

B. The polarization of the outgoing $\Lambda$ in the elastic reaction has been measured over the center-of-mass angular range $0.30 \leq \cos\theta^* \leq 0.95$, and found to be small and consistent with zero. This is in accord with the results of the model of Arnold and Logan,[35] based on a Regge-pole model with SU(3) and exchange degeneracy, which states that the primary contribution to NN polarization is due to $A_2$, and not $\omega$, exchange. The isospin singlet nature of the $\Lambda$ rules out $A_2$ exchange in the elastic reaction, with a consequent reduction in the polarization. These data are given in Table 3 and Fig. 11. The polarization of the recoil nucleon in the elastic pp and np reactions, averaged over the same $\cos\theta^*$ range, is larger, ranging from 0.2 at 0.5 GeV/c, up to 0.4 at 1.4GeV/c, and then steadily falling to about 0.1 at 7.0 GeV/c.

Table 3. Polarization of $\Lambda$ in $\Lambda p \to \Lambda p$.

| $P_\Lambda$(GeV/c) | Polarization |
|---|---|
| 0.4-1.0 | 0.0 ± 0.40 |
| 1.0-2.0 | 0.07±0.20 |
| 2.0-4.0 | -0.02±0.20 |
| 4.0-10.0 | 0.17±0.30 |

The question of a cusp, or of resonant behavior, in the elastic $\Lambda p$ reaction near threshold for $\Lambda p \to \Sigma^o p$ has been of some interest since the original paper by de Swart and Dullemond.[25a]

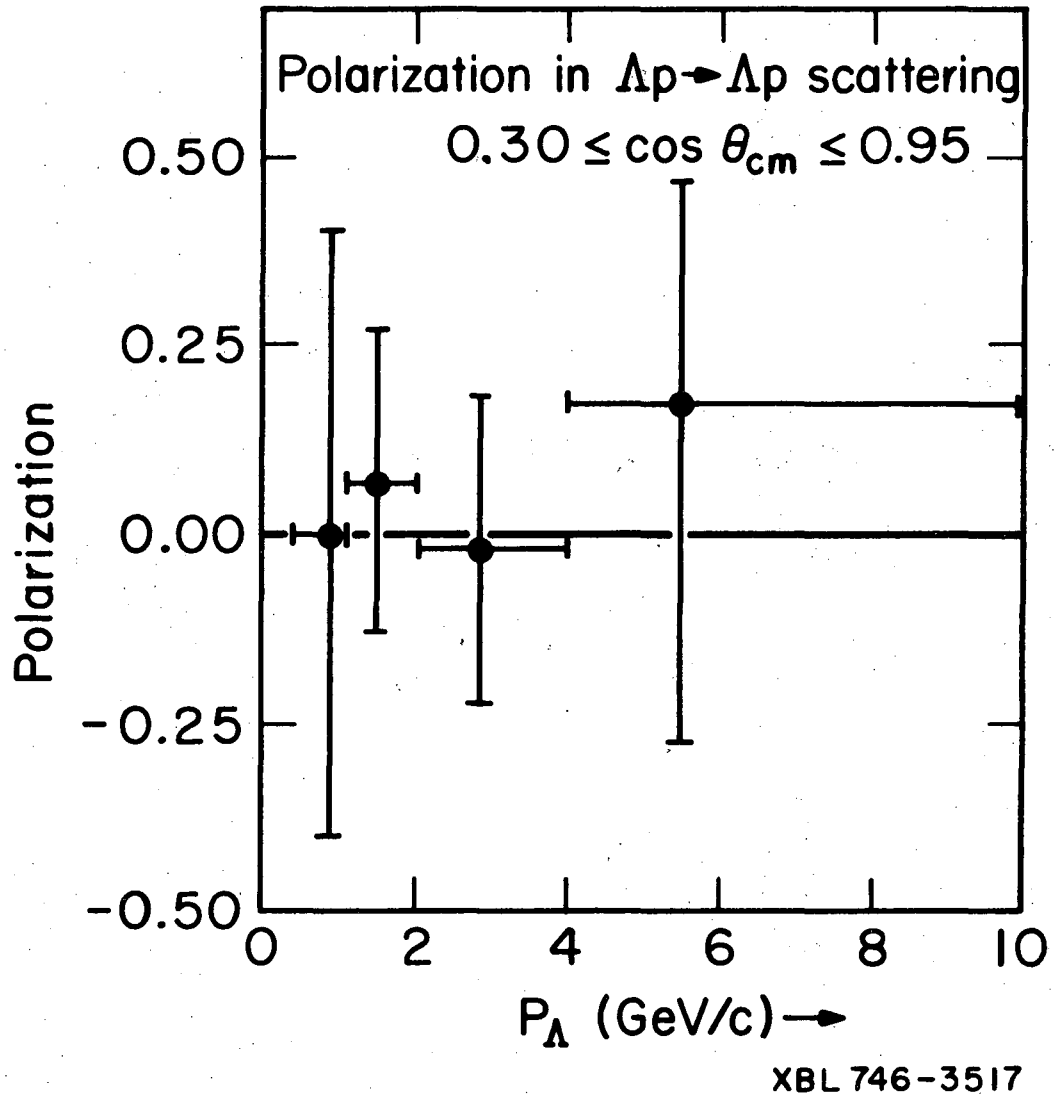


Figure 11. The polarization in $\Lambda p$ elastic scattering averaged of the center-of-mass scattering angular range $0.30 \leq \cos \theta^* \leq 0.95$.

The latest results of this continuing analysis of the lower energy hyperon-nucleon interaction have recently been published.[25b] The premise of the analysis is that baryon-baryon interactions at low energy can be described by meson theoretic potentials in a multichannel Schrödinger equation. Exchange potentials for the pseudoscalar and vector nonets, and the uncorrelated two pion exchange, were employed, and all meson-baryon couplings constants were taken from previous analyses together with SU(3) and SU(6) invariance. It was found in both their nucleon-nucleon and hyperon-nucleon descriptions that three hard core radii ($r \leq 0.4$ fm) were required as essentially a phenomenological description of the short range forces. The singlet and triplet scattering lengths and effective ranges determined by such a model were found to agree within about 10-15 percent with previous analyses of nucleon-nucleon scattering in both I = 0 and I = 1 isospin states. Their simultaneous description of all $\Lambda N$ and $\Sigma N$ scattering data in the I = 1/2 and I = 3/2 states has yielded, in particular, the $\Lambda p$ low energy parameters

$$a_s = -2.16 \pm 0.26 \text{ fm} \qquad r_s = 2.03 \pm 0.10 \text{ fm} \tag{6a}$$

$$a_t = -1.32 \pm 0.07 \text{ fm} \qquad r_t = 2.31 \pm 0.08 \text{ fm}, \tag{6b}$$

which agree well with their earlier analyses. Furthermore, their description of the $\Lambda p$ elastic cross section, shown in Fig. 61, Sec. VI of this thesis, displays a cusp in the $^3S_1$ state, where the eigenphase shift approaches $\pi/2$ near $\Lambda N \rightarrow \Sigma N$ threshold. It was noted, however, that the existence or non-existence of such cusp behavior is strongly dependent upon the triplet hard core radius taken.

We have examined our data, and find no evidence for such effects. The distributions of elastic events in both incident $\Lambda$ laboratory momentum and spatial position in the bubble chamber are displayed in Fig. 12. The downstream edge of the platinum plate is at $y \cong -86.$ cm. No apparent bias is seen in the y-distribution where one might suspect that scanning inefficiencies near the plate could possibly be responsible for a loss of events. The distribution in $P_\Lambda$ reveals no structure near $P_\Lambda = 0.642$ GeV/c, the threshold for the reaction $\Lambda p \rightarrow \Sigma^o p$. The cross section measured in this experiment from 0.30 to 1.00 GeV/c in 100-MeV/c intervals is shown in Fig. 13.

C. The ratio of the real to the imaginary part of the forward elastic scattering amplitude has been calculated from our elastic data and our measurement of the $\Lambda p$ total cross section in Sec. III of this thesis. The elastic scattering amplitude as a function of center-of-mass momentum, q, and scattering angle, $\theta^*$, is taken to be

$$f(q,\theta^*) = a(q,\theta^*) + ib(q,\theta^*); \tag{7}$$

then the differential cross section is just

$$\begin{aligned} \frac{d\sigma}{d\Omega} &= |f(q,\theta^*)|^2 \\ &= a^2(q,\theta^*) + b^2(q,\theta^*) \ . \end{aligned} \tag{8}$$

One usually parametrizes this cross section in t, where $t = -2q^2(1 - \cos\theta^*)$, as

$$\frac{d\sigma}{d\Omega} = \frac{d\sigma}{dt}\frac{dt}{d\Omega} = Ae^{Bt}\ \frac{q^2}{\pi} \ . \tag{9}$$

Evaluated at $t = 0$, this relationship is

$$a^2(q,0) + b^2(q,0) = A\ \frac{q^2}{\pi} \ .$$

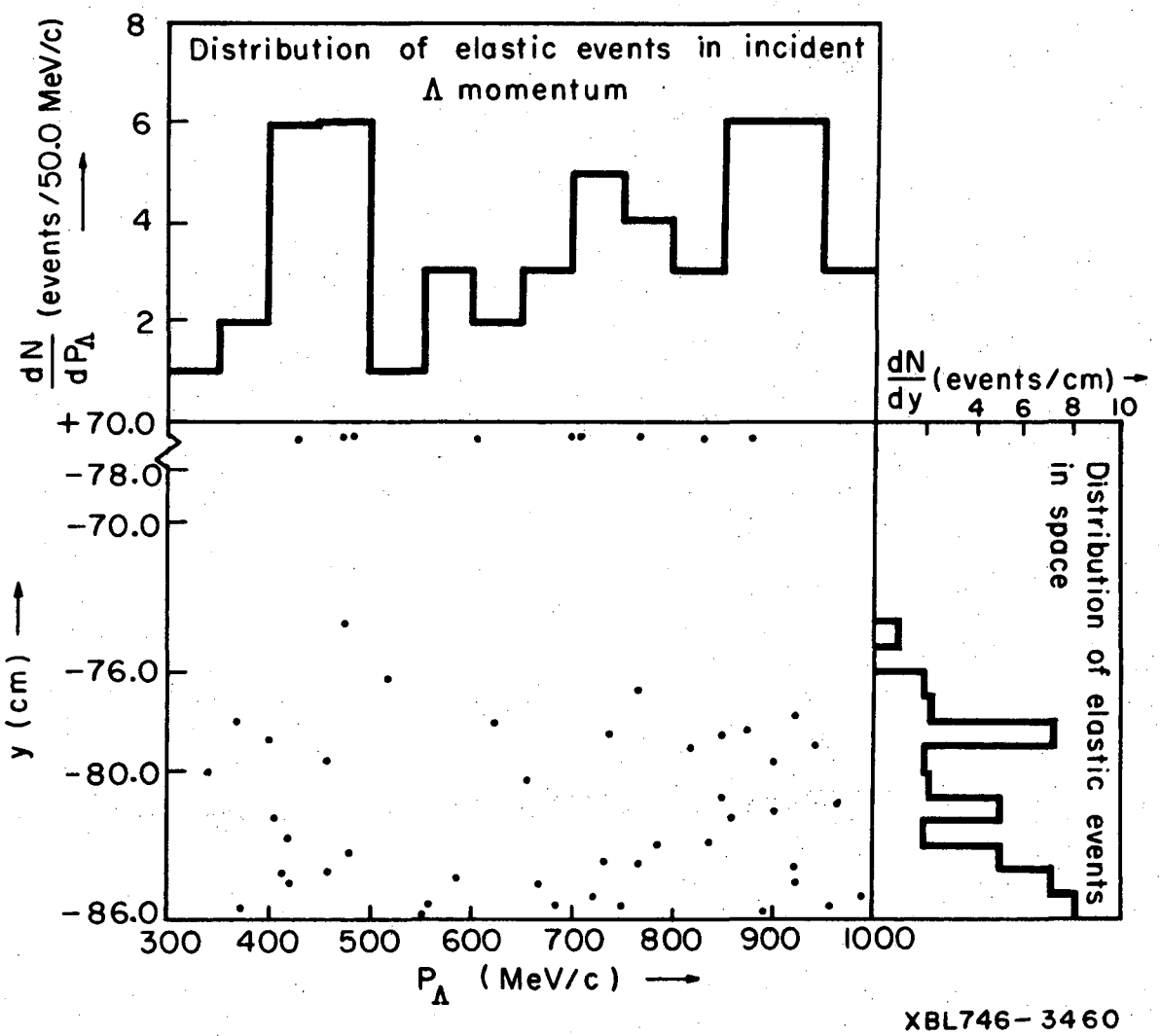


Figure 12. Distribution of Λp elastic scattering events in the plane of incident Λ momentum below 1.0 GeV/c and spatial interaction point in the chamber.

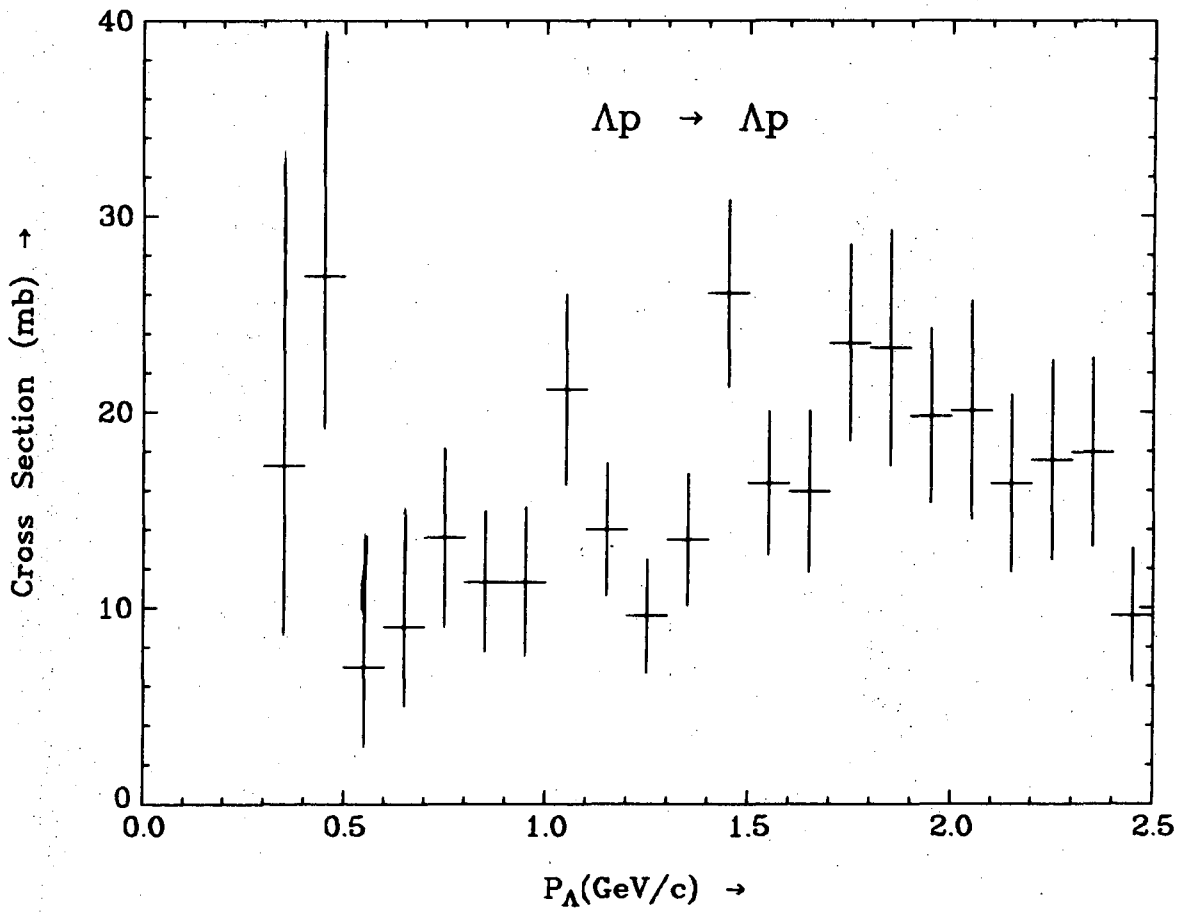


Figure 13. The elastic Λp cross section from this experiment in the low momentum region from 0.3 to 2.5 GeV/c.

The optical theorem reads

$$\sigma_T = \frac{4\pi}{q} \text{ Im } f(q,0)$$
$$= \frac{4\pi}{q} b(q,0) \ . \tag{10}$$

Solving for a(q,0) we obtain

$$|a(q,0)|^2 = q^2 \left( \frac{A(\hbar c)^2}{\pi} - \frac{\sigma_T^2}{16\pi^2} \right) \tag{11}$$

where $\hbar c = 0.624$ GeV-mb$^{1/2}$, and the units are A(mb/GeV$^2$), $\sigma_T$(mb), and q(GeV). Then the ratio of the real to the imaginary part of the forward elastic scattering amplitude is

$$|\rho(q)|^2 = \frac{|a|^2}{b^2} = \left( \frac{16\pi(\hbar c)^2 A}{\sigma_T^2} - 1 \right). \tag{12}$$

The error on $|\rho|^2$ has been obtained by varying A and $\sigma_T$ in turn by one standard deviation, and computing the variation of $|\rho|^2$. These results are shown in Fig. 14. The sign of $\rho$, usually measured by the interference of the purely real Coulomb amplitude with the real part of the nuclear amplitude, cannot be so obtained in $\Lambda p$ scattering. We might suppose that the sign will be given by the additive quark model elastic amplitude relationship (Appendix VII)

$$\text{Ampl}(\Lambda p) = \text{Ampl}(pp) + \text{Ampl}(K^- n) - \text{Ampl}(\pi^+ p). \tag{13}$$

In the range 2.0-3.0 GeV/c, the right hand side is

$$\rho(\Lambda p) \approx [-0.35]_{pp}\sigma(pp) + [0.05]_{K^- n}\sigma_T(K^- n) - [-0.20]_{\pi^+ p}\sigma_T(\pi^+ p)$$
$$\approx -0.25\, \sigma_T(\Lambda p) \ . \tag{14}$$

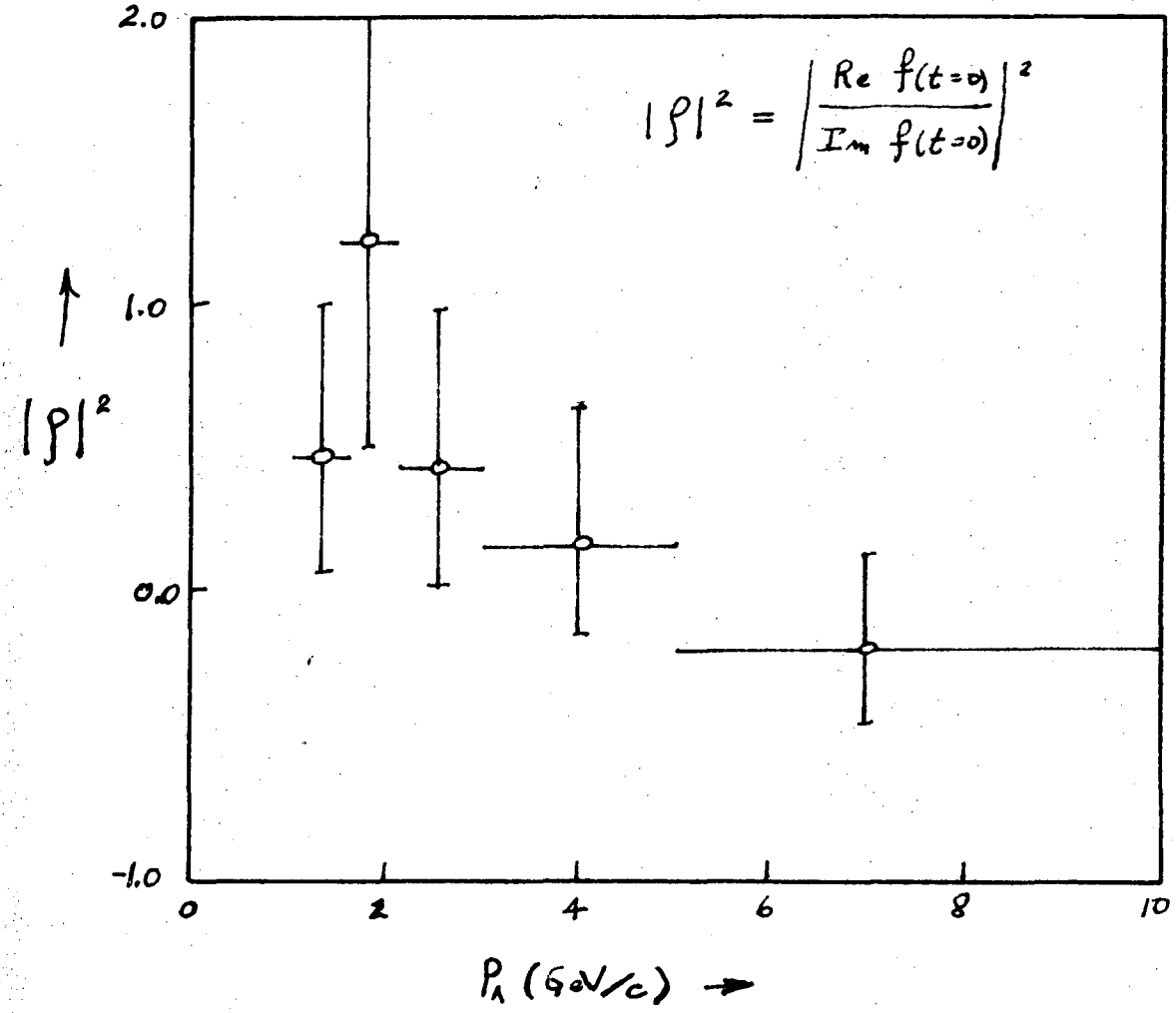


Figure 14. The square of the magnitude of the ratio of the real to the imaginary part of the forward elastic scattering amplitude.

This is speculative, since the sign of the real part of the forward $K^-n$ amplitude changes sign near 1.0 GeV/c, and furthermore, this quark model relationship for total cross sections at laboratory momenta below about 3.0 GeV/c is not satisfied.

Section III. Measurement of the $\Lambda p$ Total Cross Section

Cross sections are usually measured by counting events in known categories. In this experiment, experienced bubble chamber physicists will quickly recognize the difficulty of kinematically identifying all, or nearly all, final states in $\Lambda p$ interactions at high energies, by virtue of the fact that one missing neutral particle from the interaction reduces the number of kinematic constraints to zero, even in the most favorable case where all tracks are well-measured and the origin of the incident $\Lambda$ is known. A direct count in this experiment of neutral-induced events with a single hyperon separates out predominatly $\Lambda p$ and $\overline{K}^o p$ interaction events from the large np and small $\Xi^o p$ backgrounds, which produce either zero or two strange particles. Since the separation of the $\overline{K}^o p$ and $\Lambda p$ events cannot be done on a event-for-event basis for more than about 50 percent of the data, a subsequent separation of the $\Lambda p$ from the combined $\Lambda p$ and $\overline{K}^o p$ interaction events can be performed on a statistical basis. The crux of this statistical technique is that the spatial intensities of the $\Lambda$ and $\overline{K}^o$ flux differ within the detection region and hence, for example, hyperons produced by $\overline{K}^o$ interactions will differ considerably in their spatial distribution than those produced by $\Lambda$ interactions. Knowledge of the inclusive cross section for $\overline{K}^o p \rightarrow$ hyperon + anything, together with the assumption that $\sigma_T(\Lambda p) = \sigma(\Lambda p \rightarrow$ hyperon + anything), allows a measurement of $\sigma_T(\Lambda p)$.

A. An Idealized Calculation

Suppose that the problem is one-dimensional, and that

i) the detection region is of length L, Fig. 15;

ii) the $K^-$ target is at y = 0, and all $\Lambda$ and $\overline{K}^o$ are produced at the

target and

iii) at y = 0, the flux per unit momentum is $\Phi_\Lambda(p)$ for $\Lambda$ and $\Phi_{K_1^o}(p)$ for $K_1^o$.

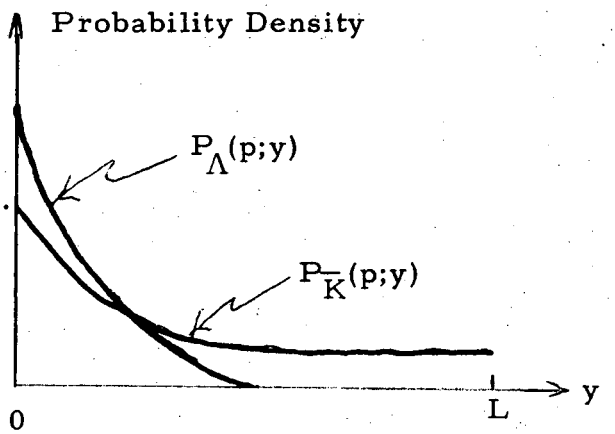


Fig. 15. The $\Lambda$ and $\bar{K}^o$ probability throughout the fiducial volume.

Then the probability of having a $\Lambda$ of momentum p at y is

$$P_\Lambda(p;y) = e^{-\left[\frac{m_\Lambda}{c\tau_\Lambda}\right] y/p} . \qquad (15)$$

Similarly, the probability of having a $\bar{K}^o$ of momentum p at y is

$$P_{\bar{K}}(p;y) = \frac{1}{4}\left[e^{-\alpha_1 y/p} + e^{-\alpha_2 y/p} + 2e^{-\gamma y/p}\cos\left\{\beta y/p\right\}\right] \qquad (16)$$

where

$$\alpha_1 = \frac{m_0}{c\tau_1} \qquad \beta = \frac{m_0 \Delta m}{c}$$

$$\alpha_2 = \frac{m_0}{c\tau_2} \qquad \gamma = \frac{\alpha_1}{2} + \frac{\alpha_2}{2} . \qquad (17)$$

Let $\sigma_\Lambda(p)$ and $\sigma_{\bar{K}}(p)$ be the inclusive hyperon production cross sections in $\Lambda p$ and $\bar{K}^o p$ collisions, respectively. Then the probability of having a hyperon produced in a region dy about y is

$$P_Y(y)dy = \frac{\rho_{LH2}\int_0^\infty \Phi_\Lambda(p)P_\Lambda(p;y)\sigma_\Lambda(p)dp + \rho_{LH2}\int_0^\infty 2\,\Phi_{K_1^o}(p)P_{\bar{K}}(p;y)\sigma_{\bar{K}}(p)dp}{\int_0^L dy' \left\{\text{numerator}\right\}} dy \tag{18}$$

This probability essentially separates the $\Lambda$ component from the $\bar{K}$ component in hyperon production by virtue of the fact that the $\bar{K}$ amplitude survives throughout the detection region, whilst the $\Lambda$ dies exponentially in the forward 1/3 of the detection region.

In addition, the Poisson probability of finding N hyperons where $\bar{n}$ are expected on the basis of the production cross reactions $\sigma_\Lambda(p)$ and $\sigma_{\bar{K}}(p)$ is

$$P[N \mid \bar{n}] = \frac{\bar{n}^N e^{-\bar{n}}}{N!}, \tag{19}$$

where

$$\bar{n} = \rho_{LH_2}\int_0^L dy \int_0^\infty dp \left[\bar{\Phi}_\Lambda(p)\sigma_\Lambda(p)\;\; P_\Lambda(p;y) + 2\;\phi_{K_1^o}(p)\sigma_{\bar{K}}(p)\; P_{\bar{K}}(p;y)\right]. \tag{20}$$

Then the likelihood function is the product of this Poisson probability and the product of the N probabilities of finding the hyperons at the $y_i$:

$$\mathcal{L} = P[N \mid \bar{n}] \prod_{i=1}^{N} P_Y(y_i)\,. \tag{21}$$

For computational convenience, one usually forms the function

$$\begin{aligned} f &= -\ell n\,\mathcal{L} \\ &= -\ell n\, P[N|\bar{n}] - \sum_{i=1}^{N} \ell n\, P_Y(y_i) \\ &\cong -N\ell n\,\bar{n} + \bar{n} + \ell n\, N! - \sum_{i=1}^{N} \ell n\, P_Y(y_i)\,. \end{aligned}$$

The minimum of this function determines the best estimate of the total cross section, $\sigma_T(p)$.

An alternative method, and in fact the one employed in this Section, is to calculate the spatial distribution of all hyperons according to (18), and compare this with the observed experimental distribution in the chi-squared sense. The best estimate of the total cross section is then obtained by adjusting $\sigma_T(\Lambda p)$ as a function of momentum so as to minimize the chi-squared, taking care, of course, that the contributions to this chi-squared are roughly uniform throughout the chamber.

B. The Actual Calculation

A proper treatment involves essentially three generalizations of the ideal calculation: the propagation of the $\Lambda$ and $\bar{K}^o$ amplitudes through the chamber in three dimensions, corrections due to visual inefficiencies, and the production of $\Lambda$ and $\bar{K}^o$ in the liquid hydrogen ($LH_2$).

1). $\Lambda$ and $K_1^o$ Decay Distribution Calculations

A measurement technique relying upon an experimental spatial distribution function must have a good understanding of spatial biases and efficiencies.[39] A necessary test of these is provided by $\Lambda \rightarrow p\pi^-$ and $K_1^o \rightarrow \pi^+\pi^-$ spatial decay distributions which are theoretically understood to be

$$\frac{dN}{dy} = \frac{e^{-y/\lambda\tau}}{\lambda_\tau} \text{ (decays/cm)}, \qquad (22)$$

where $\lambda_\tau$ is the $\Lambda$ or $K_1^o$ mean decay length, $\lambda_\tau = Pc\tau/m$, $\tau$ being the proper mean lifetime of the $\Lambda$ or $K_1^o$ state. An ensemble of event type 7 $V^o$ decays[38] in a 20-cm fiducial volume near the plate[40] is used to calculate the decay distribution throughout the chamber in

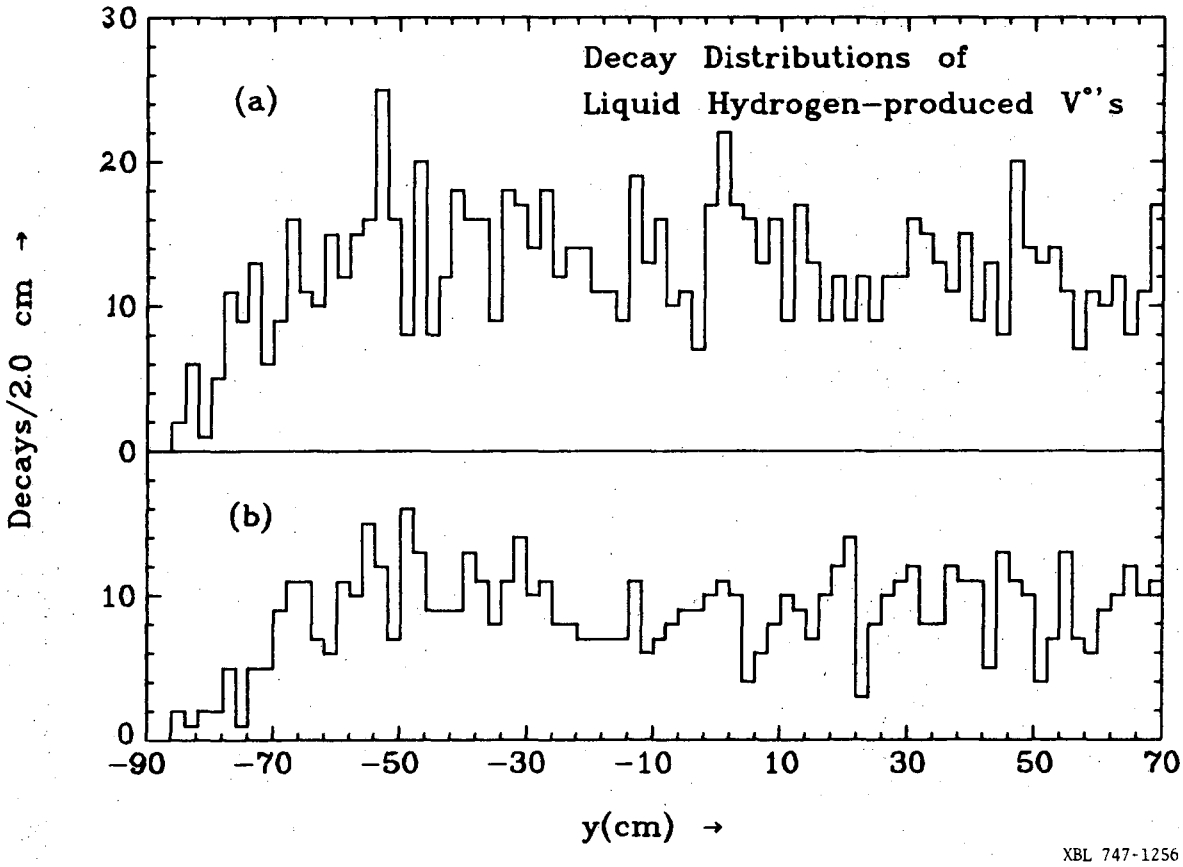


Figure 16. (a) Spatial decay distribution of $K_1^o \rightarrow \pi^+\pi^-$ decays observed produced from beam track interactions in the liquid hydrogen ($LH_2$). (b) Same for $\Lambda \rightarrow p\pi^-$ decays.

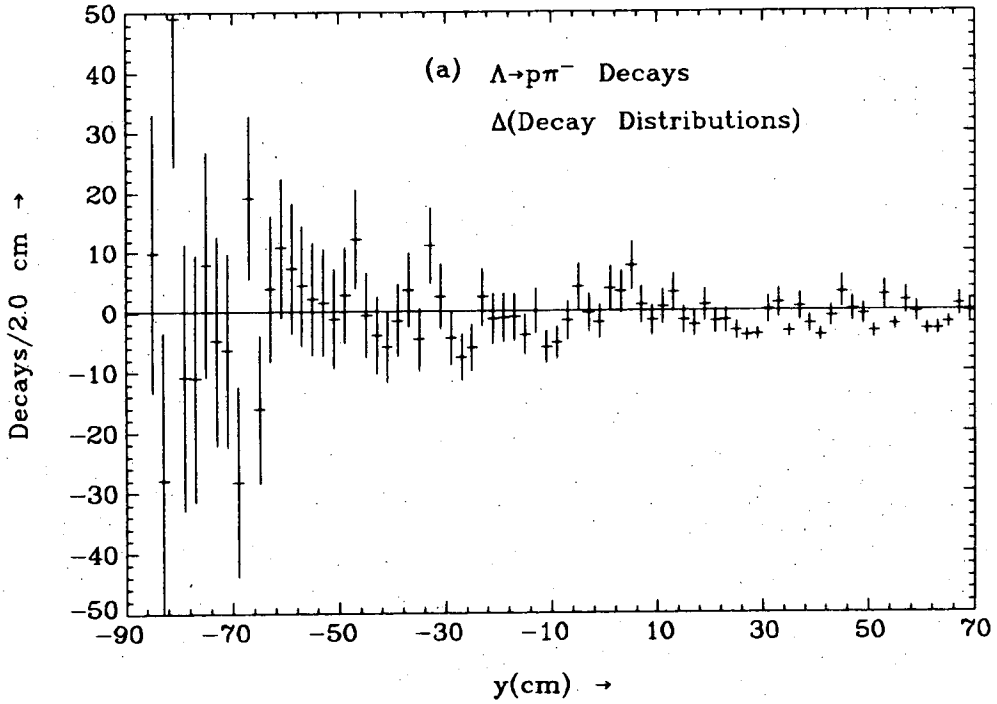


Figure 17. $\Lambda \rightarrow p\pi^-$ decays.

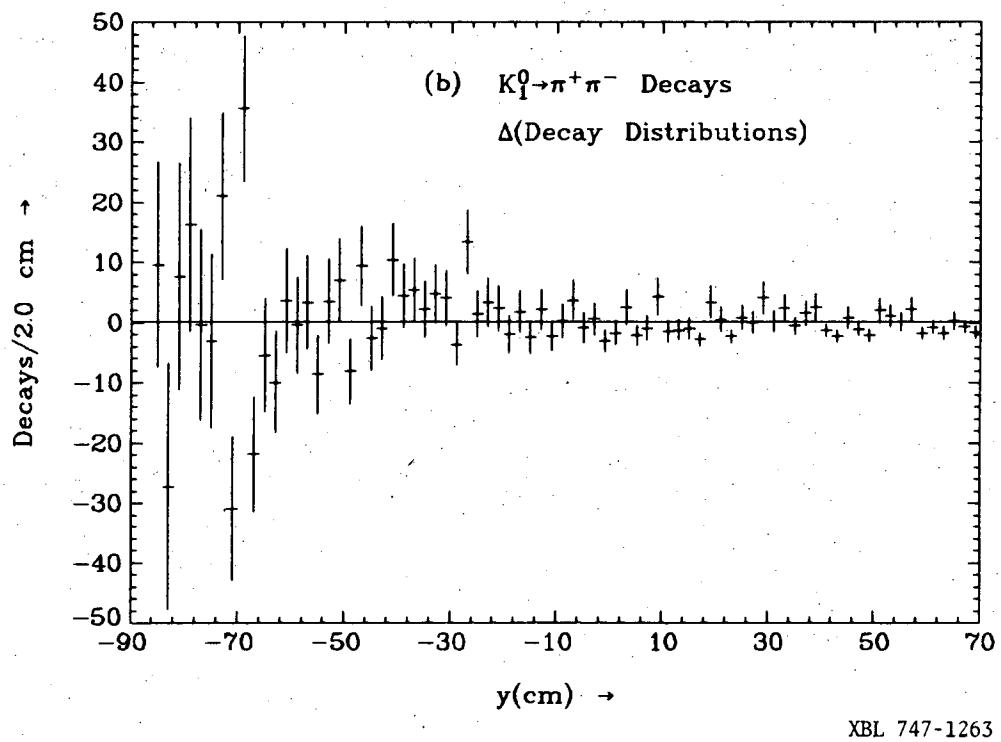


Figure 18. The difference of the $K_1^o \rightarrow \pi^+\pi^-$ experimental and calculated decay distributions. The $\Delta$ in this figure, and all subsequent figures in this Section, denotes the subtraction of the calculated spatial distribution of a given quantity from the experimentally observed distribution of that quantity.

accordance with Eq. (22). Details of this calculation are given in Appendix VIII.

2) Flux Calculations

The Lambda Flux:

For a given visible $\Lambda \rightarrow p\pi^-$ decay in a fiducial volume slab of depth dy centered at y in the chamber, the total number of such decays in the film represented by this event is

$$dn_i = \frac{1}{BR \cdot f_M \cdot \eta_7(y_i)} \, dy,$$

where $y_i$ is the $\Lambda$ decay position, $\eta_7(y_i)$ the scanning efficiency, and BR = .642 (visible decay branching ratio). The fraction of film measured for pathlength is $f_M = 0.0667$. Then the $\Lambda$ pathlength through the section dy at y is

$$\frac{dL(y)}{dy} = \frac{1}{dy} \sum_i dn_i \, \frac{P_i}{m_\Lambda} \, c\tau_\Lambda$$

$$= \frac{1}{dy \, BR \cdot f_M} \sum_i \frac{1}{\eta_7(y_i)} \left[ \frac{P_i}{m_\Lambda} \, c\tau_\Lambda \right] \qquad (23)$$

where the sum is over all $\Lambda$ decaying in dy, the $i^{th}$ decay having momentum, $p_i$, and position, $y_i$.

Assuming a $\Lambda p$ total cross section, $\sigma_T(\Lambda p)$, of 35 mb and the density of the liquid hydrogen, $P_{LH_2} = 0.060$ gm/cm$^3$, the resultant distribution of hyperons is calculated as

$$\frac{dN_y}{dy}(y) = \frac{dL}{dy}(y) \, \sigma_T(\Lambda p) \left( \frac{\rho_{LH_2}}{m_p} \right) \quad \text{hyperons/cm}$$

and displayed in Fig. 20.

To calculate the $\bar{K}^o$ flux, we separate the calculation into two parts: (i) the $\bar{K}^o$ amplitude deriving from $\bar{K}^o$ produced in the platinum plate; and the (ii) $\bar{K}^o$ amplitude produced in the liquid hydrogen. The scanning instructions required the scanner to distinguish between $V^o$ produced at vertices in the hydrogen (ET6) and those with no production origin other than the platinum plate (ET7). Examination of the spatial distributions of ET6 and ET7 indicate that this requirement was satisfied well by the scanners, that is, the spatial distributions resemble very well the expected ones,

$$\frac{dN}{dy}(ET6) \sim 1 - e^{-y/\lambda}$$

$$\frac{dN}{dy}(ET7) \sim e^{-y/\lambda} ,$$

where $\lambda$ is a typical mean decay length for the sample. We employ these identifications in the following calculation of the $\bar{K}^o$ amplitude.

(i) $\bar{K}^o$ amplitude from the platinum plate. For each ET7 $\bar{K}^o_1 \to \pi^+\pi^-$ decay in a restricted 10 cm long fiducial volume near the plate,

FID2. $-20. \leq x(cm) \leq +20.$

$-84. \leq y(cm) \leq -74.$

$+3. \leq z(cm) \leq +34.$

the decay is

a) weighted by the probability, $W_K$, that the $K^o_1$ was a $\bar{K}^o$, not a $K^o$, upon exiting from the plate. We have calculated this probability using the solutions of K. Case[41] and M. L. Good,[42] and find

$$W_{\bar{K}} \cong 0.97.$$

In addition, the decay is

b) weighted by the inverse of the probability of having decayed in FID2,

$$\text{weight} = \frac{1}{1 - e^{-d_2/\lambda_1}}$$

where

$d_2$(cm) = the three-dimensional potential flight distance inside FID2,

$\lambda_1$(cm) = mean $K_1^o$ decay length ( = $\frac{P}{m_K} c\tau_1$)

c) weighted by the inverse of the visible branching ratio $BR(K_1^o \to \pi^+\pi^-)$,

$$\text{weight} = BR^{-1} = (.687)^{-1};$$

d) weighted by the inverse of the fraction of film measured for $V^o$ decays, weight = $f_M^{-1}$;

e) weighted by the inverse of the scanning efficiency at the decay point $y_i$, weight = $\eta_7(y_i)^{-1}$; and

f) weighted by 2 for the $K^o$ decay probability into $K_1^o$. Altogether, each $K_1^o \to \pi^+\pi^-$ decay in FID2 represents a total number of $\bar{K}^o$ particles exiting from the plate equal to

$$N_K = \frac{2 W_{\bar{K}}}{(1 - e^{-d_2/\lambda_1}) \, BR(K_1^o \to \pi^+\pi^-) \, f_M \eta_7(y_i)},$$

where $\lambda_1$ is its mean decay length and $y_i$ its decay position. To calculate the $\bar{K}^o$ at y in the chamber, we define in Fig. 19 the trajectory of the $K^o$ in FID1

A - point of $K^o$ entry into fiducial volume FID1,

B - point of exit from FID1,

y - coordinate along beam direction (very nearly same as 82" chamber TVGP y-coord.)

u - coordinate along $K^o$ line-of-flight.

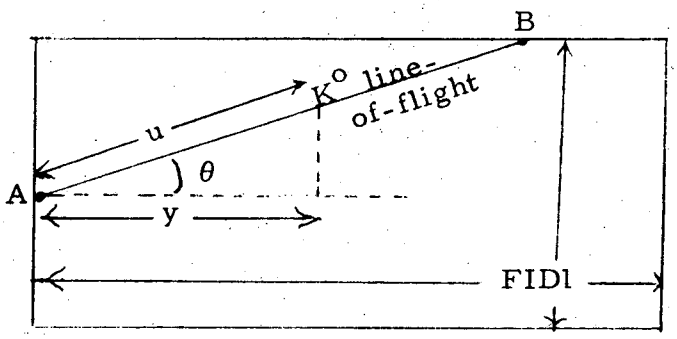


Fig. 19 $K^o$ trajectory.

Then the probability, $P^{\overline{K}_{plate}}$, of having a $K^o$ state of momentum P at u is, using (16),

$$P^{\overline{K}_{plate}} = P_{\overline{K}}(P, \frac{y}{\cos\theta}) \qquad (24)$$

where $y = u \cos\theta$. Each $K_1^o$ decay is so propagated through the chamber in y until its potential path exists from the fiducial volume, after which point $P^{\overline{K}_{plate}} = 0$.

ii) The $\overline{K}^o$ amplitude produced in the liquid hydrogen. There are two assumptions we make to simplify the calculation: firstly, we assume that the $\overline{K}^o$ production angular and momentum distributions are the same in $K^-$Pt and $K^-p$ collisions; and secondly, that the $K_1^o$ decay distribution is the same as the $\overline{K}^o$ production distribution.

We are then able to utilize the calculated $P_{Y(y)}^{\overline{K}_{plate}}$ distribution in (i) above, and numerically integrate its contribution at a point y by summing over the "source function" of ET6 $K_1^o \to \pi^+\pi^-$ decays upstream of y in the chamber. Specifically,

$$P_{Y(y)}^{\overline{K}_{LH_2}} = \int_0^y \frac{\rho_6(y')}{\int \rho_7(y'')dy''} \frac{P_{Y(y-y')}^{\overline{K}_{plate}}}{W_{\overline{K}}} dy' \qquad (25)$$

where $\rho_6(y)$ and $\rho_7(y)$ are the $K_1^o$ decay distributions, corrected for scanning losses, of hydrogen produced $\bar{K}^o$ and plate produced $\bar{K}^o$, respectively. Note that we have taken care of the $\bar{K}^o$ loss due to $K^o$ regeneration in the platinum by renormalizing $P_Y^{K_{plate}}(y)$ by $W_{\bar{K}}^{-1}$. Neglecting the y-dependence of $\rho_6(y)$ and $\rho_7(y)$, and noting that $P_Y^{\bar{K}_{plate}}(y) \sim \frac{1}{4} + \frac{3}{4} e^{-y/\lambda}$, the behavior of $P_Y^{\bar{K}_{LH_2}}$ in y is roughly

$$P_{Y(y)}^{\bar{K}_{LH_2}} \sim \frac{1}{4} y + \frac{3}{4} \lambda .$$

Finally, the total spatially dependent hyperon contribution from $\bar{K}^o$ flux is proportional to the sum of Eq. (24) and Eq. (25)

$$P_{Y\ (y)}^{\bar{K}_{plate}} + P_{Y\ (y)}^{\bar{K}_{LH_2}} ,$$

weighted, of course, by the $\bar{K}^o p$ hyperon production cross section and the density of liquid hydrogen, and integrated over the $\bar{K}^o$ momentum. That is, the number of hyperons in a region dy at y produced by $\bar{K}^o p$ collisions is

$$\frac{dN_Y^{\bar{K}}}{dy}(y)\, dy = dy \int_0^\infty dP_K \left\{ P_{Y\ (y)}^{\bar{K}_{plate}} + P_{Y\ (y)}^{\bar{K}_{LH_2}} \right\} N_K \sigma_{\bar{K}}(P_K) \left( \frac{\rho_{LH_2}}{m_p} \right)$$

hyperons/cm. (26)

This quantity is shown plotted in Fig. 21.

As a check on the validity of the above calculation of the spatial distribution of hyperons arising from $\bar{K}^o p$ interactions, we have performed the same calculations for the $\Lambda p$ interactions using an assumed cross section. This result is displayed in Fig. 22. The difference between this calculation, which separates the plate contribution and the

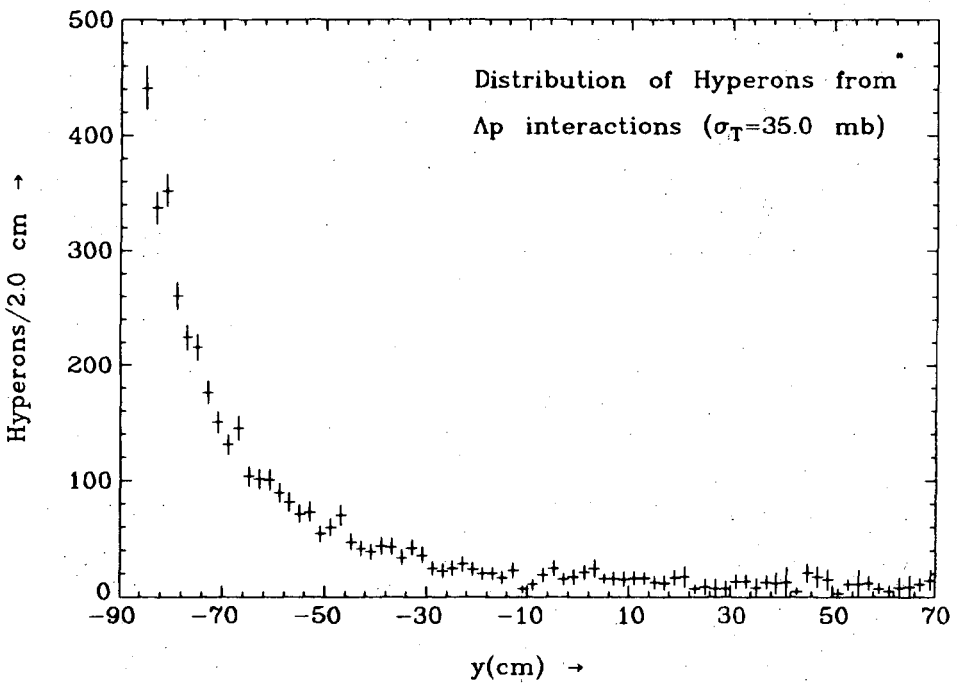


Figure 20. Calculated spatial distributions of hyperons produced in Λp interactions assuming that $\sigma_T(\Lambda p)$ = 35.0 mb at all momenta. This calculation computes the Λ flux through each slab of $LH_2$, dy, perpendicular to the beam direction, as the sum of the mean decay lengths of all Λ decaying in that slab dy.

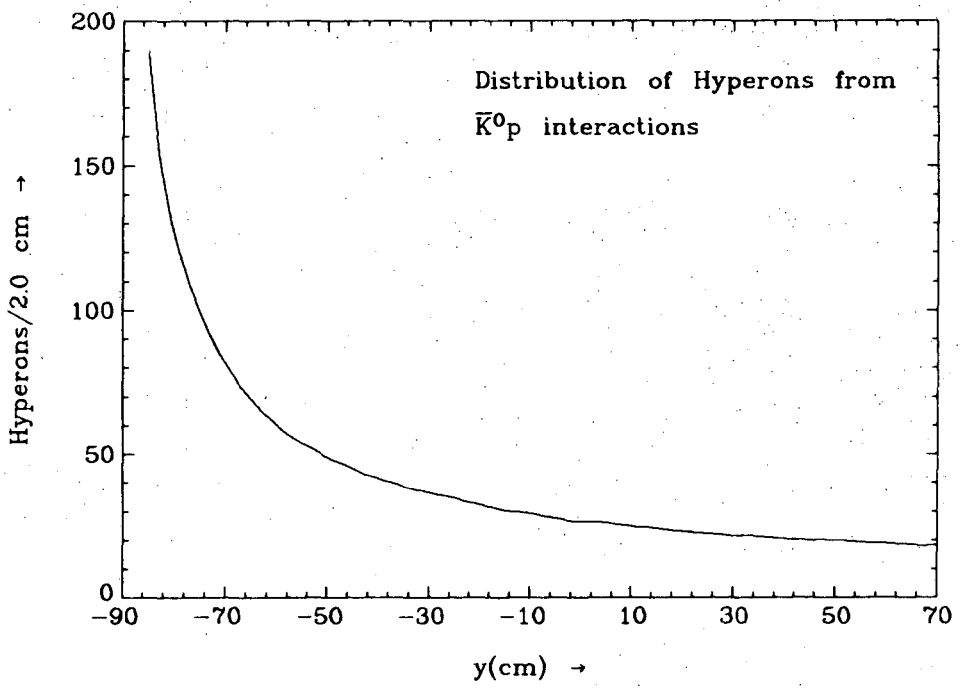


XBL 747-1262

Figure 21. Calculated spatial distribution of hyperons produced in $K^0$p interactions using the inclusive hyperon production cross section given in this Section.

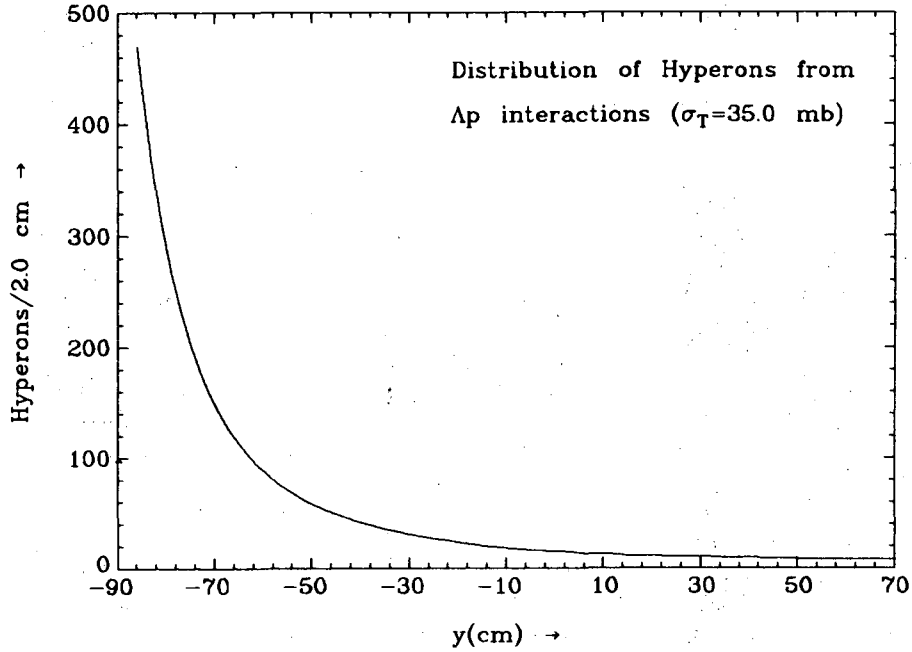


Figure 22. Calculated spatial distributions of hyperons produced in Λp interactions assuming that $\sigma_T(\Lambda p)$ = 35.0 mb at all momenta. This calculation has separated the contribution from plate-produced and $LH_2$-produced Λ hyperons.

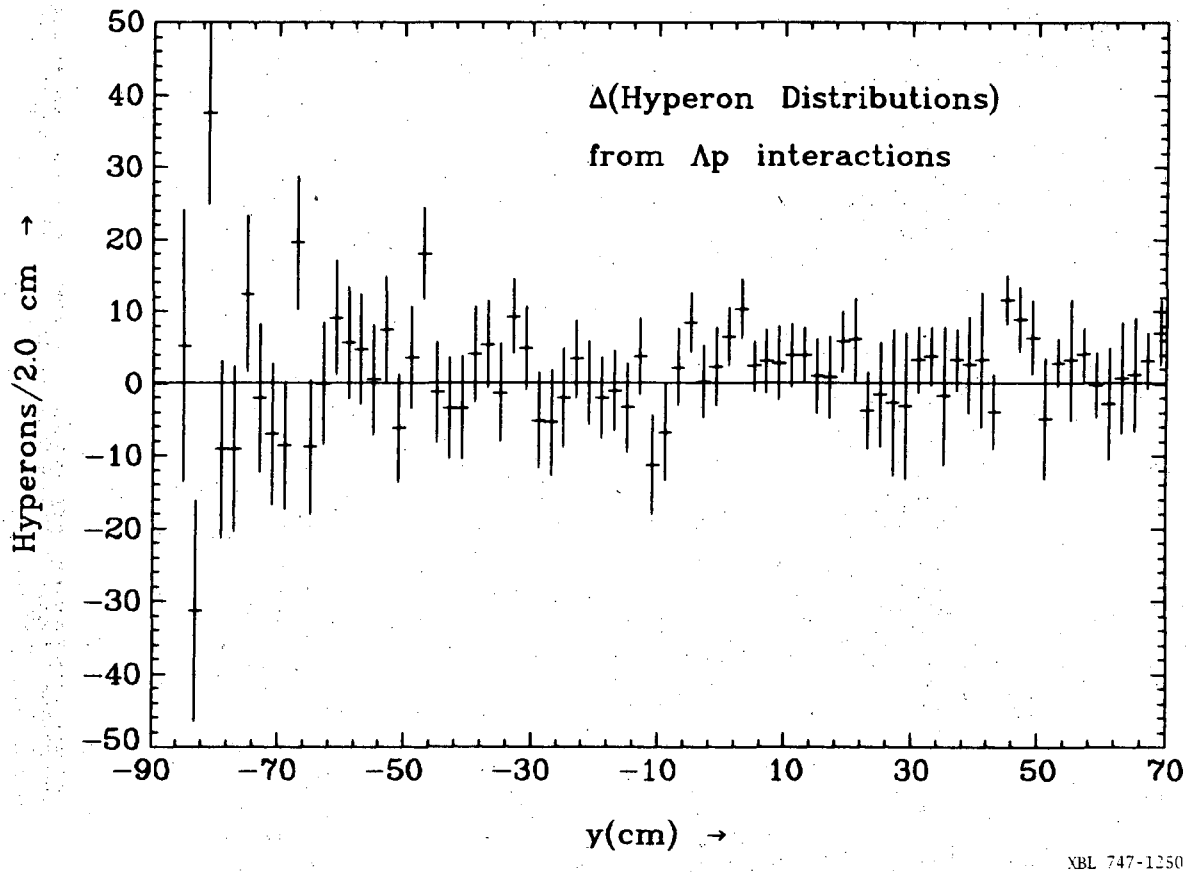


Figure 23. Bin-for-bin subtraction of the calculated hyperon distribution in Figure 22 from that distribution in Figure 19.

liquid hydrogen contribution, and the calculation performed above in Eq. 23, is shown as a function of y in Fig. 23. For 78 degrees-of-freedom, the chi-squared for the consistency of these calculations is 78.64. We conclude that the determination of the $\bar{K}^o$ amplitude is adequate.

The second method of calculating the hyperon distribution arising from $\Lambda p$ interactions can be readily employed to examine the incident $\Lambda$ momentum dependence of the resultant hyperon distributions. Accordingly, we have chosen five bins in $\Lambda$ laboratory momentum,

(a) $1.0 \leq P_\Lambda$ (GeV/c) $< 1.5$

(b) $1.5 \leq P_\Lambda$ (GeV/c) $< 2.0$

(c) $2.0 \leq P_\Lambda$ (GeV/c) $< 3.0$

(d) $3.0 \leq P_\Lambda$ (GeV/c) $< 5.0$

(e) $5.0 \leq P_\Lambda$ (GeV/c) $< 10.0$

and performed the calculation for each separately. These results are shown in Fig. 24(a-e). In addition, the hyperon distribution arising from $\Lambda$ produced by changed particle interactions in the liquid hydrogen (predominantly $K^-$ beam track) is shown as (f) in Fig. 24. The above distributions are very useful in extracting the momentum dependence of the $\Lambda p$ total cross section.

3. Hyperon Event Count Calculations

All $\Lambda \rightarrow p\pi^-$ and $\Sigma^\pm \rightarrow n\pi^\pm$ decays from event types 17, 31, 32, and 37 are counted as hyperons. Further details of the hyperon counting procedure are given in Appendix VIII. The resultant experimental distribution of hyperons in the 82-inch hydrogen bubble chamber is shown in

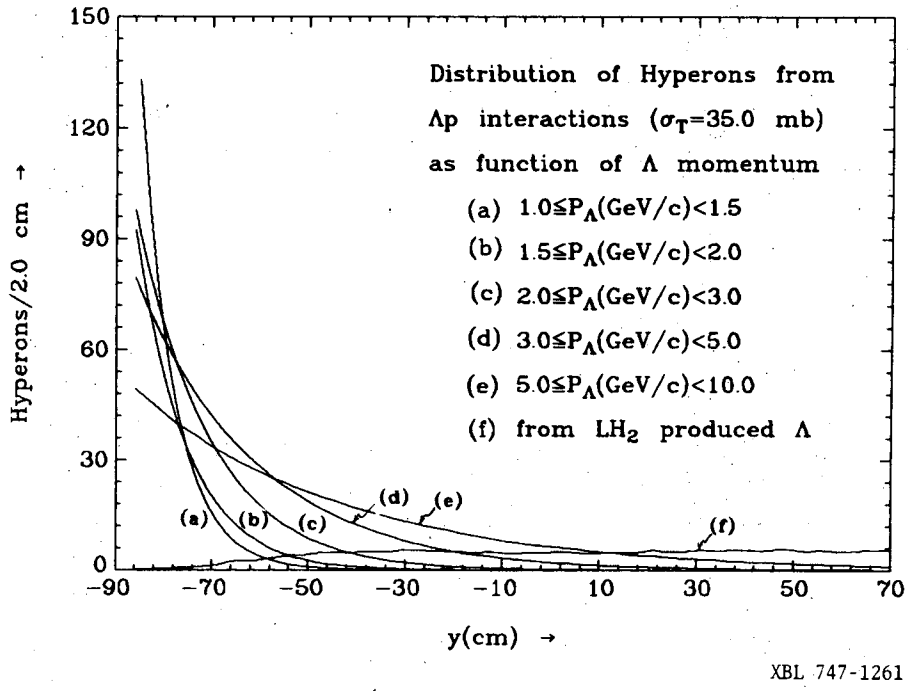


Figure 24. Calculated hyperon distributions as a function of incident Λ momentum, curves (a) through (e), for Λ produced in the platinum plate, and assuming $\sigma_T(\Lambda p)$ = 35.0 mb. Curve (f) is the hyperon distribution for Λ produced in the $LH_2$, and is averaged over all Λ momenta.

Fig. 25. The total calculated hyperon distribution is in Fig. 26.

4. The Inclusive Hyperon Production Cross-Section in $\overline{K}^o p$ Collisions

A rough approximation to the inclusive hyperon production cross section, $\sigma_{\overline{K}}$, is afforded by the difference

$$\sigma_K = \sigma_T(K^- p) - \sigma_T(K^+ p) - \sigma_{cex}(K\ p)$$

which subtracts out all those channels in $K^- p$ not leading to hyperons, including the charge exchange reaction not allowed in $K^+ p$.
The above difference is very well measured, and is shown as curve A in Fig. 27.

We may also estimate the cross section by adding up all available channels in the charge symmetric reaction $K^- n$ from the compilation of Morrison,[43] yielding curve B in Fig. 27.

A third alternative is that, below single pion threshold in the $\overline{K}N$ system, we may take

$$\sigma_{\overline{K}} = \sigma_T(K^- p) - \sigma_{el}(K^- p) - \sigma_{cex}(K^- p),$$

while above threshold we take the difference

$$\sigma_{\overline{K}} = \sigma_T(K^- p) - \sigma_T(K^+ p) - \sigma_{cex}(K^- p)\ .$$

We have used this third estimation in the present calculation of the total cross section. It is the same as the first except at lower momenta where our $\overline{K}^o$ flux is small; the second estimation evidently suffers from a failure to add up all the relevant reactions, some of which are not easily available over such a broad spectrum in $\overline{K}$ momentum.

C. Estimate of the Total Cross Section From a Chi-squared Fit

The above specified calculations have been performed on the entire experimental data from this experiment. Examination of the

experimental distribution of hyperons found in the chamber, Fig. 25, reveals the expected exponential fall-off in the forward part of the chamber, and the nearly flat distribution in the downstream half of the chamber. For comparison, the sum of the calculated hyperon distributions from $\Lambda p$ and $\bar{K}^o p$ interactions is displayed in Fig. 26. A bin-for-bin subtraction of this calculated hyperon distribution from the experimental, assuming

$$\sigma_T(\Lambda p) = 35.0 \text{ mb} \quad 1.0\text{-}10.0 \text{ GeV/c}, \text{ [1st approximation]}$$

yields the discrepancy distribution of Fig. 28. We infer a total cross section smaller than the first approximation value above by virtue of the deficiency of experimental events in the forward region of the chamber. The rather narrow structure of this deficiency in y indicates, upon inspection of Fig. 24(a-e), that the total cross section is smaller at lower momenta.

A more quantitative estimation is obtained by the following calculation. Let $\Delta(y)$ be the discrepancy distribution of hyperons (Fig. 28),

$$\Delta(y) = \left[\frac{dN_Y}{dy}(y)\right]_{\text{expt'l}} - \left[\frac{dN_Y}{dy}(y)\right]_{\text{calc.}} ;$$

let

N = number of bins in y

$\sigma(y)$ = error on calculated hyperon distribution

and

$f_k(y)$ = calculated distribution of hyperons for some $\Lambda$ momentum bin, k.

That is, the functions $f_k(y)$ are just those plotted in Fig. 24 for k = a,b,c,d, or e. We define a chi-squared for a given assumption of

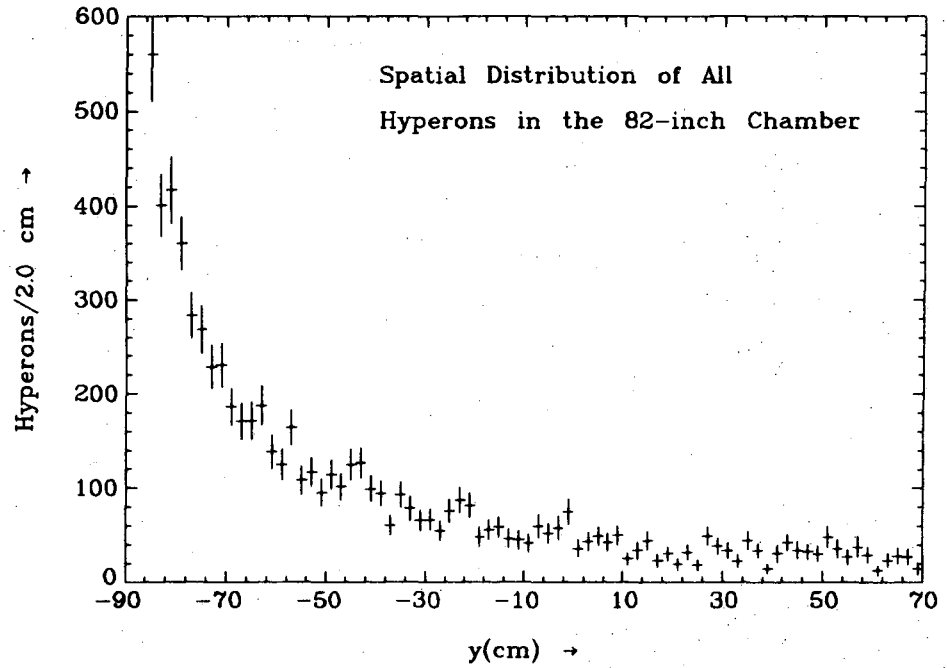


Figure 25. Experimental spatial distribution of all hyperons observed in the 82-inch hydrogen chamber, corrected for all experimental efficiencies and SU(2) branching fractions to undetectable hyperon decay final states.

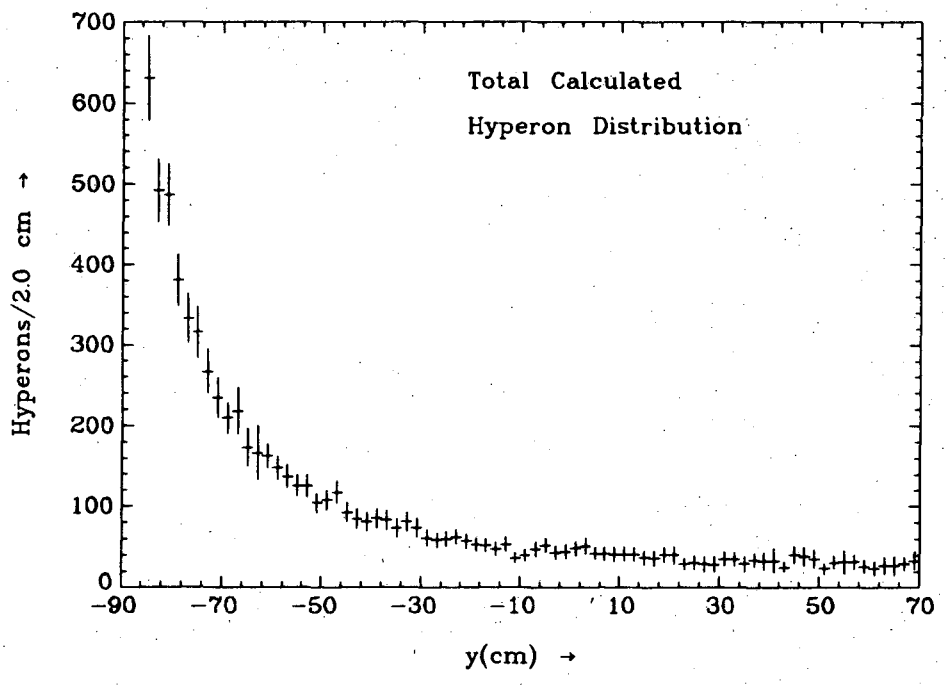


Figure 26. Total calculated spatial distribution of hyperons from $\Lambda p$ and $\bar{K}^{o}p$ interactions, sum of the distributions in Figures 19 and 21.

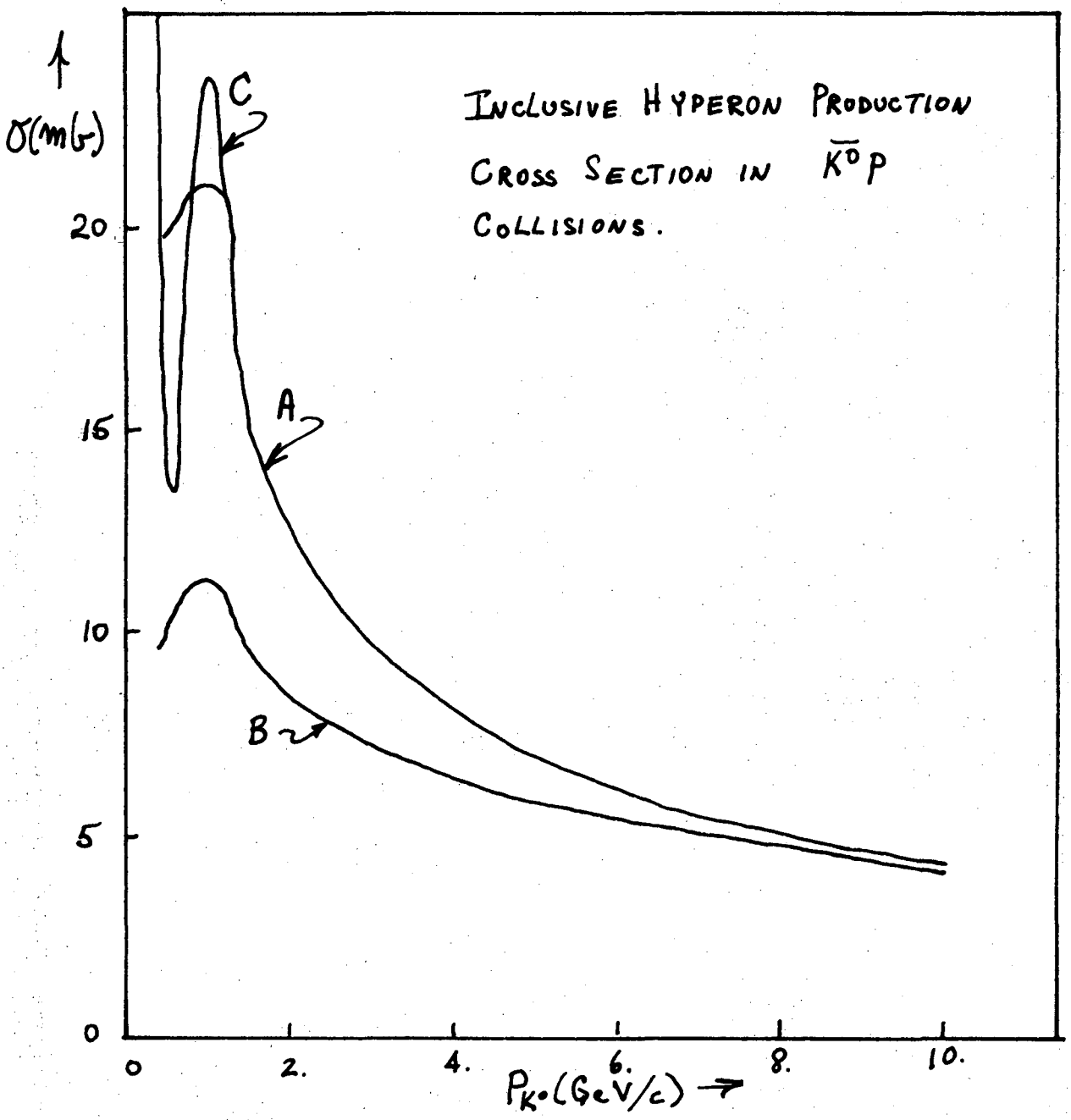


Figure 27. Inclusive hyperon production cross section in $\bar{K}^0 p$ interactions over the momentum spectrum of the $K_1^0$ decays in this experiment. The curves A, B, and C are estimations described in the text.

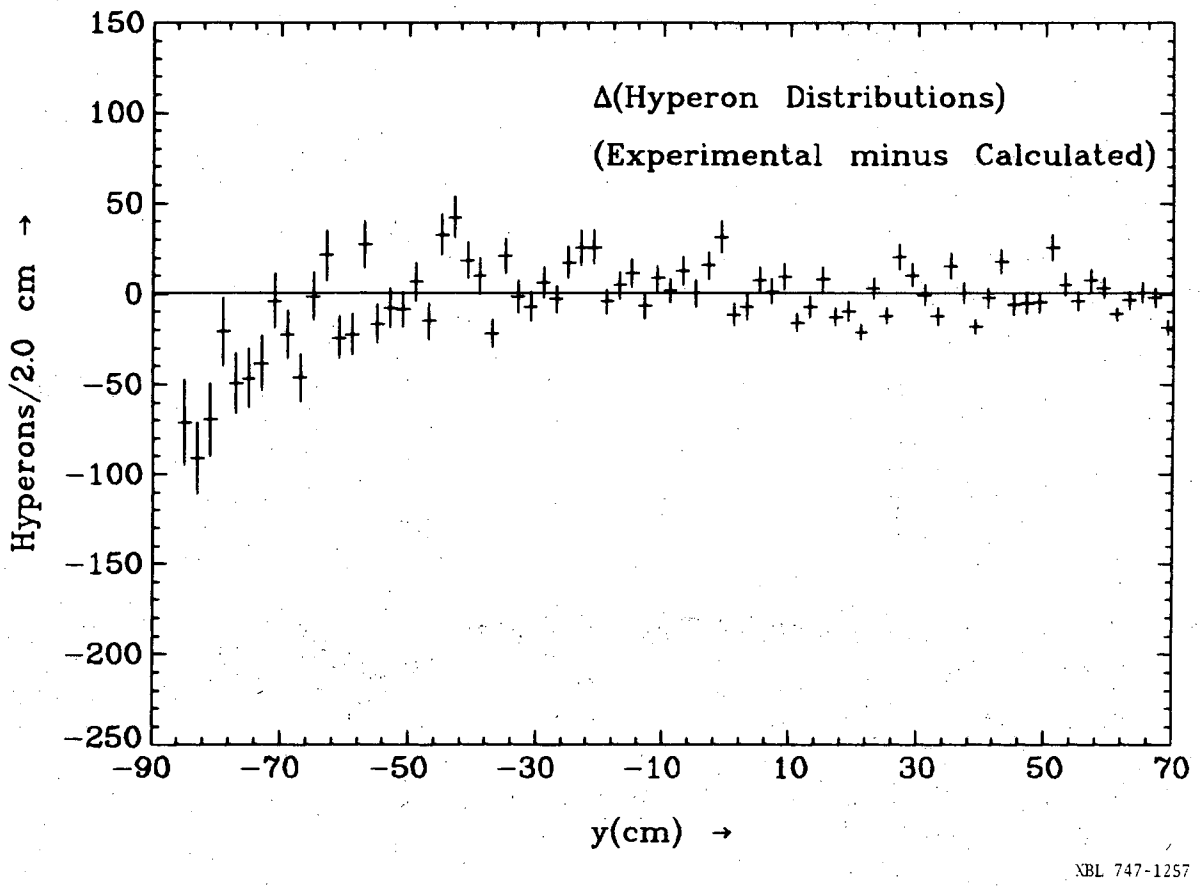


Figure 28. The experimental minus the calculated hyperon distributions for the assumption $\sigma_T(\Lambda p) = 35.0$ mb at all momenta.

$\sigma_T(\Lambda p)$ to be

$$\chi^2 = \sum_{i=1}^{N} \left[ \frac{\Delta(y_i) - \sum_k a_k f_k(y)}{\sigma(y_i)} \right]^2 ,$$

where the $a_k$ are coefficients to be adjusted as corrections to the assumed $\sigma_T(\Lambda p)$.

The error $\sigma(y_i)$ on the discrepancy distribution

$$\Delta(y_i) = \frac{dN^{exp}}{dy}(y_i) - \frac{dN^{calc}}{dy}(y_i) \equiv E_i - C_i$$

is just given by

$$\sigma(y_i)^2 = \delta E_i^2 + \delta C_i^2 ,$$

since the experimental and calculated hyperon distributions are independent. Both $\delta E_i$ and $\delta C_i$ have statistical contributions from the hyperons and the $V^o$ decays observed, respectively, and systematic errors from the scanning efficiency determination. A derivation of $\delta E_i$ and $\delta C_i$ is given in Appendix VIII. For a good guess at $\sigma_T(\Lambda P)$, the $\chi^2$ will be near minimum, and

$$a_k \cong 0, \quad \text{for all } k.$$

We will iterate the estimation of $\sigma_T(\Lambda p)$ by adjusting the $a_k$ such as to minimize the $\chi^2$.

In the least squares sense, the minimum in $\chi^2$ is given for those $a_k$ such that

$$\frac{\partial \chi^2}{\partial a_k} = 0, \quad \text{for all } k.$$

These k equations are

$$\sum_{i=1}^{N} \frac{[\Delta(y_i) - \sum_k a_k f_k(y_i)]\, f_k(y_i)}{\sigma^2(y_i)} = 0, \quad \text{for each } k.$$

Direct inversion of this $k \times k$ matrix to obtain the $k$ coefficients $a_k$ is not desirable since the error on the theoretical distribution, $\sigma(y)$, is dependent upon the $a_k$. Approximately solving for each $a_k$, we obtain

$$a_k = \frac{\sum_{i=1}^{N} \left\{ \frac{f_k(y_i)}{\sigma^2(y_i)} \left[ \Delta(y_i) - \sum_{j \neq k} a_j f_j(y_i) \right] \right\}}{\sum_{i=1}^{N} \left[ \frac{f_k(y_i)}{\sigma(y_i)} \right]^2} .$$

Such a form is suitable to an iterative solution.

Since the $a_j$ on the right-hand-side are not known, these equations can be iterated from some initial values, such as $a_j = 0$, all $j$. These coefficients $a_k$ are strongly correlated, as is evident from Fig. 24. Consequently, we have found it prudent to iterate these equations many times (50 is sufficient) in order to obtain stable solutions.

An iteration such as the above to nullify the discrepancy deviations of Fig. 28 leads one to the estimate that

$$\begin{aligned}
\sigma_T &= 23.94 \text{ mb} \quad 1.0 \leq P_\Lambda (\text{GeV}/c) < 1.5 \\
&= 24.28 \text{ mb} \quad 1.5 \leq P_\Lambda (\text{GeV}/c) < 2.0 \\
&= 26.62 \text{ mb} \quad 2.0 \leq P_\Lambda (\text{GeV}/c) < 3.0 \\
&= 32.11 \text{ mb} \quad 3.0 \leq P_\Lambda (\text{GeV}/c) < 5.0 \\
&= 37.72 \text{ mb} \quad 5.0 \leq P_\Lambda (\text{GeV}/c) < 10.0
\end{aligned} \qquad [2^{\text{nd}} \text{ Approximation}]$$

The behavior of the coefficients $a_k$ is shown in Fig. 29, and the resultant discrepancy distribution is shown in Fig. 30. Since the $LH_2$ contribution to the hyperons from $\Lambda p$ interactions (curve (f) of Fig. 24) has been averaged over all $\Lambda$ momenta, this procedure must be repeated to obtain a 3$^{rd}$ approximation using the 2$^{nd}$ approximation values of (45) as input. In practice, we stop here with

$$\sigma_T = 23.61 \pm 6.8 \text{ mb} \quad 1.0 - 1.5 \text{ GeV/c}$$
$$= 24.46 \pm 6.8 \text{ mb} \quad 1.5 - 2.0 \text{ GeV/c}$$
$$= 29.24 \pm 6.6 \text{ mb} \quad 2.0 - 3.0 \text{ GeV/c}$$
$$= 32.12 \pm 8.0 \text{ mb} \quad 3.0 - 5.0 \text{ GeV/c}$$
$$= 36.09 \pm 8.0 \text{ mb} \quad 5.0 - 10.0 \text{ GeV/c} \cdot$$

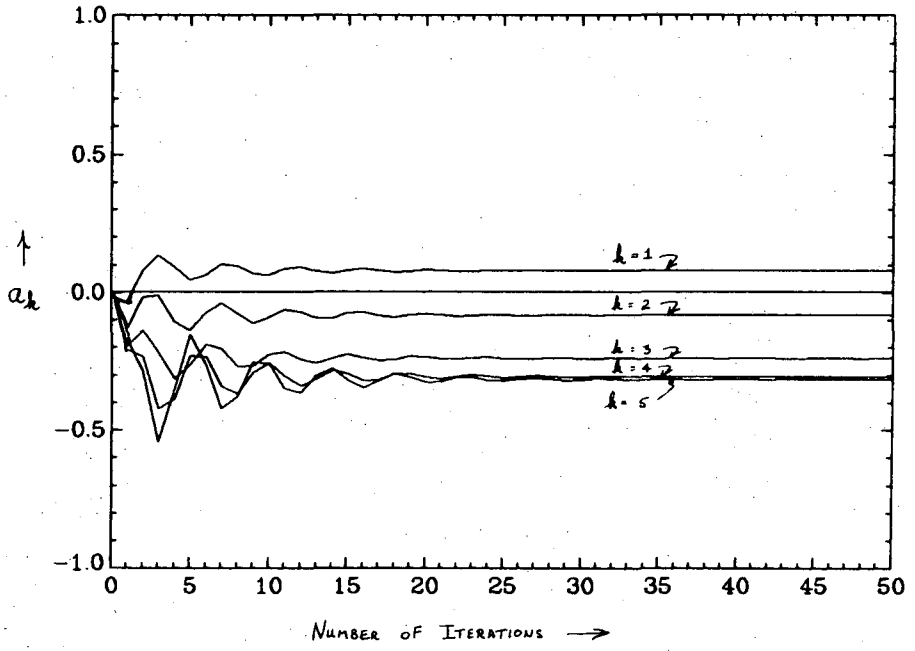


XBL 747-1259

Figure 29. Iterated coefficients $a_k$, $\chi^2$ fitted fractional corrections to the assumed total cross section.

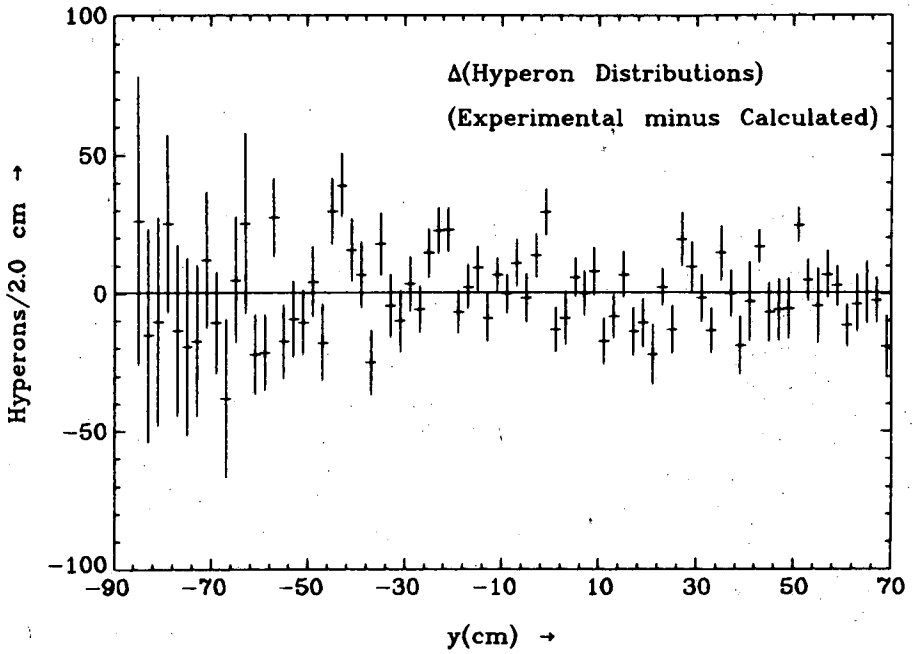


Figure 30. The experimental minus the calculated hyperon distributions for the fitted Λp total cross section.

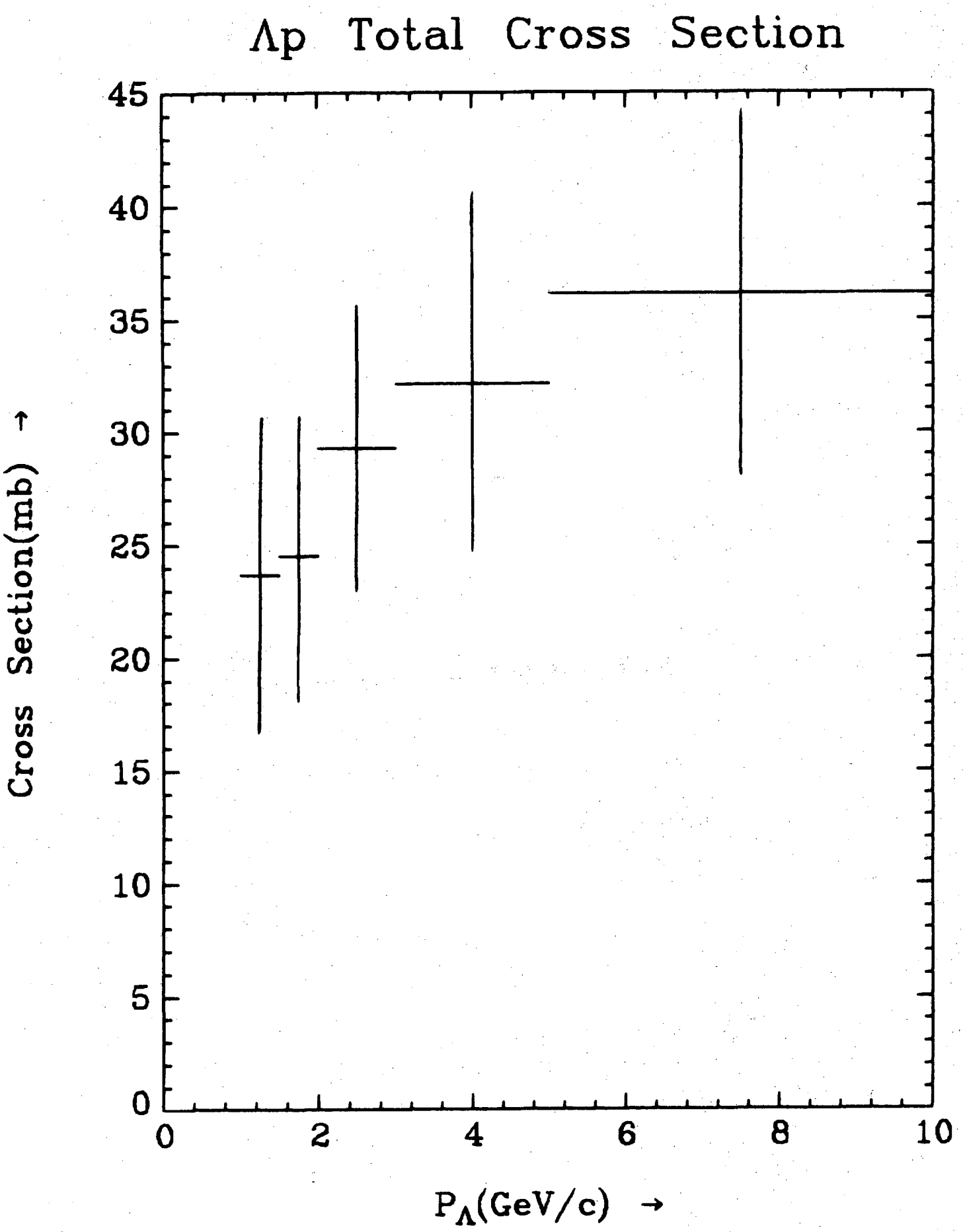


Figure 31. The Λp total cross section as measured in this experiment.

Section IV. Inelastic Scattering

A. Single Pion Production: The Reaction $\Lambda p \to \Sigma p \pi$.

The cross sections for the single pion production reactions

$$\Lambda p \to \Sigma^- p \pi^+ \tag{27a}$$

$$\Lambda p \to \Sigma^+ p \pi^- \tag{27b}$$

are given in Figs. 32a,b. Superposed on each cross section is a relatively well-measured nucleon-nucleon cross section at the same center-of-mass momentum for comparison. We observe that to a fair approximation the $\Lambda p \to \Sigma^- p \pi^+$ cross section is a constant multiple, $r = 0.18$, of the $pp \to np\pi^+$ cross section from threshold to 10.0 GeV/c. Similarly, the $\Lambda p \to \Sigma^+ p \pi^-$ cross section is equal to roughly 70 to 80 percent of the $np \to pp\pi^-$ cross section throughout our full momentum spectrum.

We have estimated cross sections for the quasi-two-body processes

$$\Lambda p \to \Sigma^- \Delta^{++} \tag{28a}$$

$$\Lambda p \to \Sigma^+ \Delta^o. \tag{28b}$$

The $(p\pi)$ invariant mass distribution in the reaction $\Lambda p \to \Sigma^- p \pi^+$ indicates strong $\Delta^{++}$ production; indeed, roughly half of the events proceed through the quasi-two-body process [Eq. (28a)]. There is little evidence of $\Delta^o$ production in $\Lambda p \to \Sigma^+ p \pi^-$. Detailed fits to these mass distributions were performed employing a simple combination of Lorentz invariant phase space for the process $\Lambda p \to \Sigma p \pi$ and a p-wave Breit-Wigner for the $\Delta_{1236}$. Invariant phase space was calculated according to Hagedorn,[44] and properly summed over our momentum distribution of incident $\Lambda$. Hence, if there are N events of a particular reaction and $P(s,M)dM$ is the phase space available to an invariant mass between M and M+dM in that reaction of total center-of-mass energy $\sqrt{s}$, then the

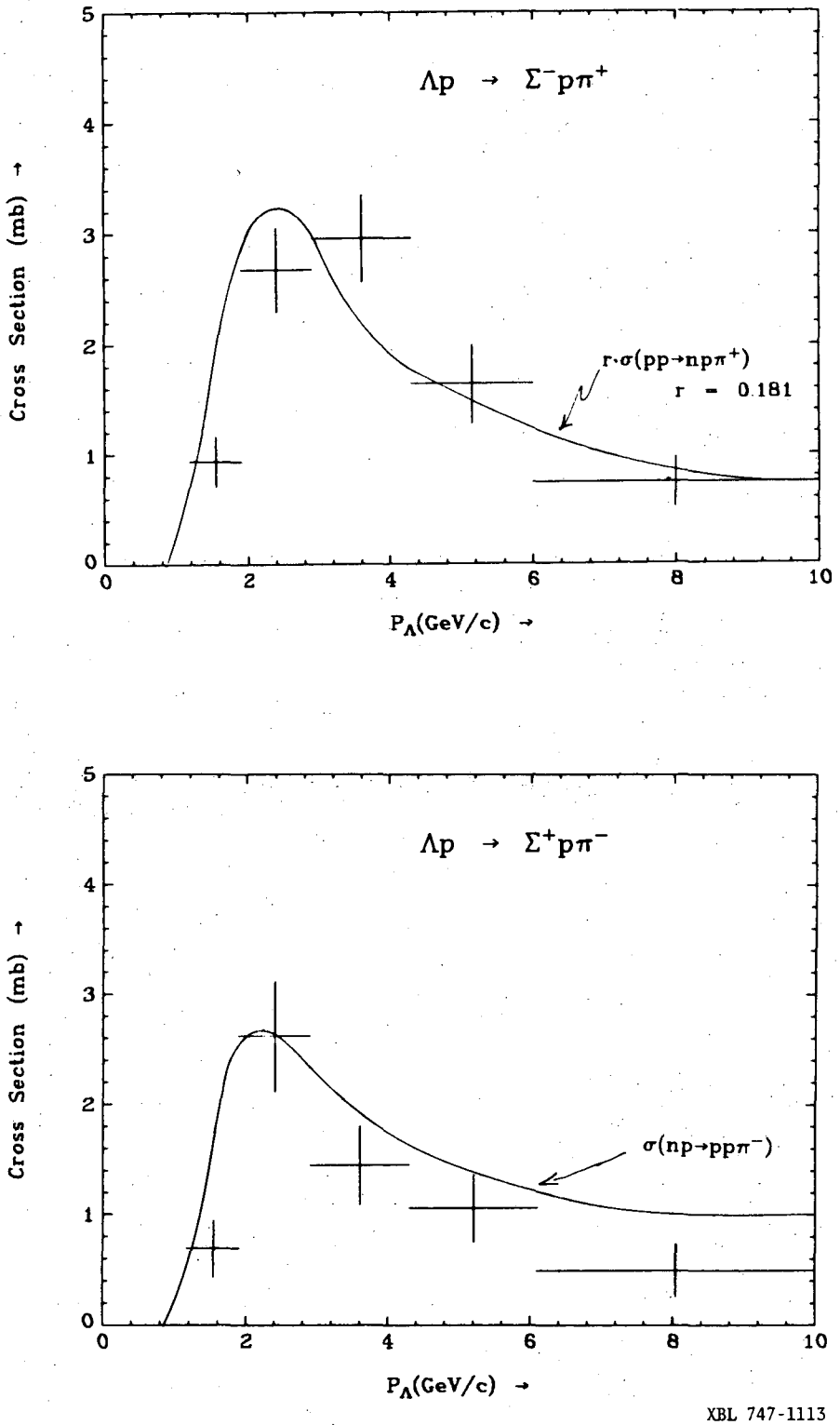


Figure 32. (a) Cross section for the process $\Lambda p \rightarrow \Sigma^- p\pi^+$; superposed is a constant times the cross section for $pp \rightarrow np\pi$. (b) Cross section for $\Lambda p \rightarrow \Sigma^+ p\pi^-$; superposed is the cross section for $np \rightarrow pp\pi^-$ referred to the same center-of-mass momentum.

total phase space in these fits is taken to be

$$P(M)dM = \sum_{i=1}^{N} P(s_i, M)dM. \qquad (29)$$

The Breit-Wigner form taken for a p-wave decay of a resonant state of mass $M_R$ and width $\Gamma_R$ is

$$BW(M) = \frac{1}{\pi} \frac{\Gamma/2}{(M_R - M)^2 + (\Gamma/2)^2}, \qquad (30)$$

where the width is taken to be

$$\Gamma = \Gamma_R \frac{p}{p_R} \frac{p^2/(p^2 + m_\pi^2)}{p_R^2/(p_R^2 + m_\pi^2)}, \qquad (31)$$

with $p_R$ the center-of-mass momentum in the resonant decay of mass $M_R$, and p the center-of-mass momentum of the decay particle in the rest frame of M. The masses and widths used were 1385,34 MeV for $\Sigma_{1385}$ and 1236,110 for $\Delta_{1236}$. The results of these fits are the solid lines of Figs. 33a,b. The lower line is the invariant phase space alone; the upper line is the fitted sum of phase space and the Breit-Wigner. In Table 6 the fraction of the total number of events in that channel attributable to either phase space ($f_{PS}$) or resonant production ($f_{BW}$) is given.

Table 6. Results of the mass fits to a sum of Lorentz invariant phase space and a p-wave Breit-Wigner

| | | Threshold$\leq P_\Lambda$(GeV/c)$\leq$10 | | 3 $\leq P_\Lambda$(GeV/c)$\leq$5 | |
|---|---|---|---|---|---|
| Reaction | Resonant Breit-Wigner | $f_{BW}$ | $f_{PS}$ | $f_{BW}$ | $f_{PS}$ |
| $\Lambda p \to \Sigma^- p\pi^+$ | $\Delta^{++} \to p\pi^+$ | 0.55 ± 0.13 | 0.45 ± 0.13 | 0.52 ± 0.12 | 0.48 ± 0.12 |
| $\Lambda p \to \Sigma^+ p\pi^-$ | $\Delta^0 \to p\pi^-$ | 0.08 ± 0.16 | 0.92 ± 0.16 | 0.0 ± 0.15 | 1.0 ± 0.15 |

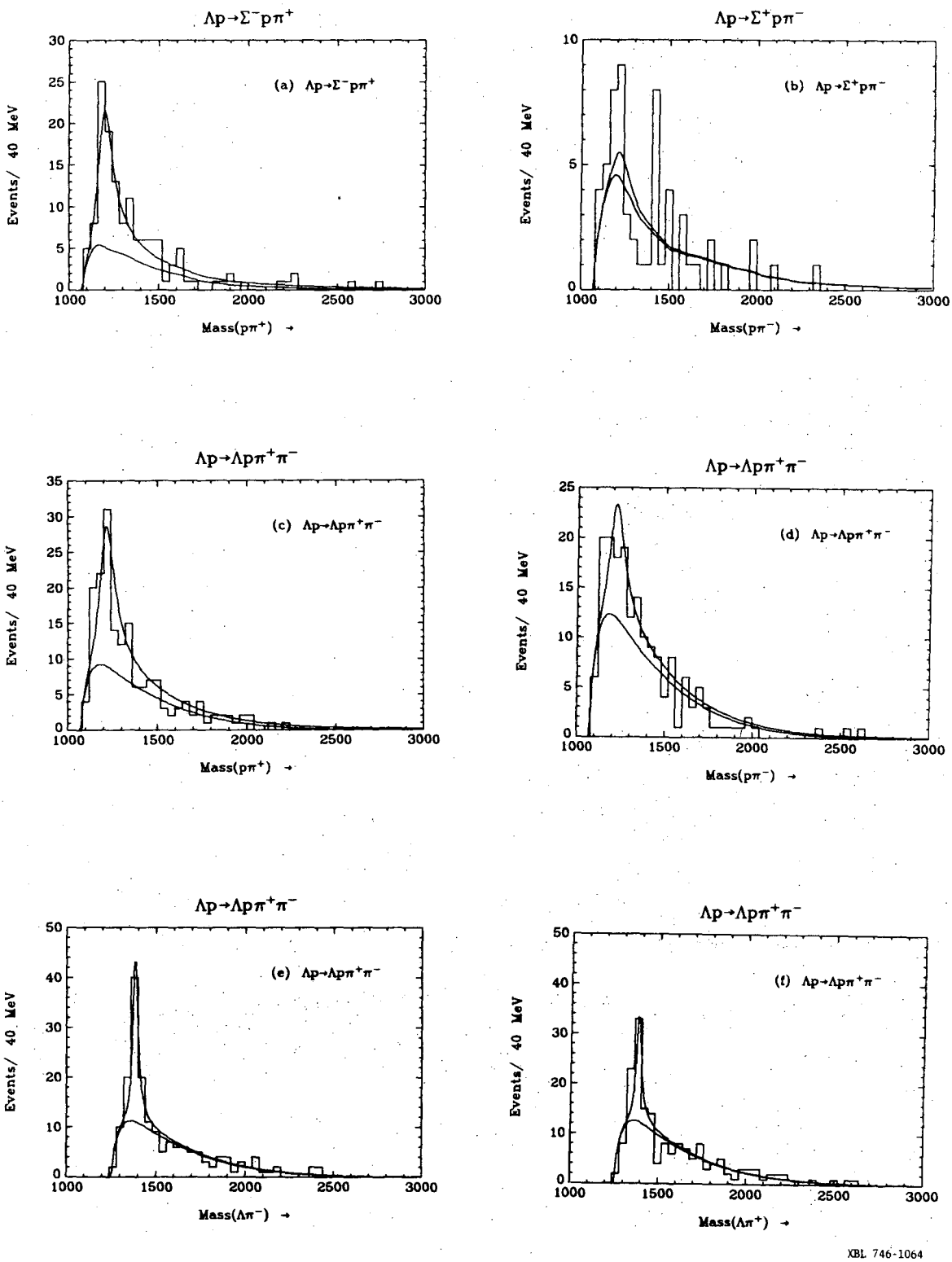


Figure 33. Invariant mass distributions in single and double pion final states. (a) The $(p\pi^+)$ mass distribution in the reaction $\Lambda p \to \Sigma^- p\pi^+$; (b) the $(p\pi^-)$ mass distribution in the reaction $\Lambda p \to \Sigma^+ p\pi$; (c) the $(p\pi)$, (d) the $(p\pi^-)$, (e) the $(\Lambda\pi^-)$, and (f) the $(\Lambda\pi^+)$ mass distributions in the reaction $\Lambda p \to \Lambda p\pi^+\pi^-$.

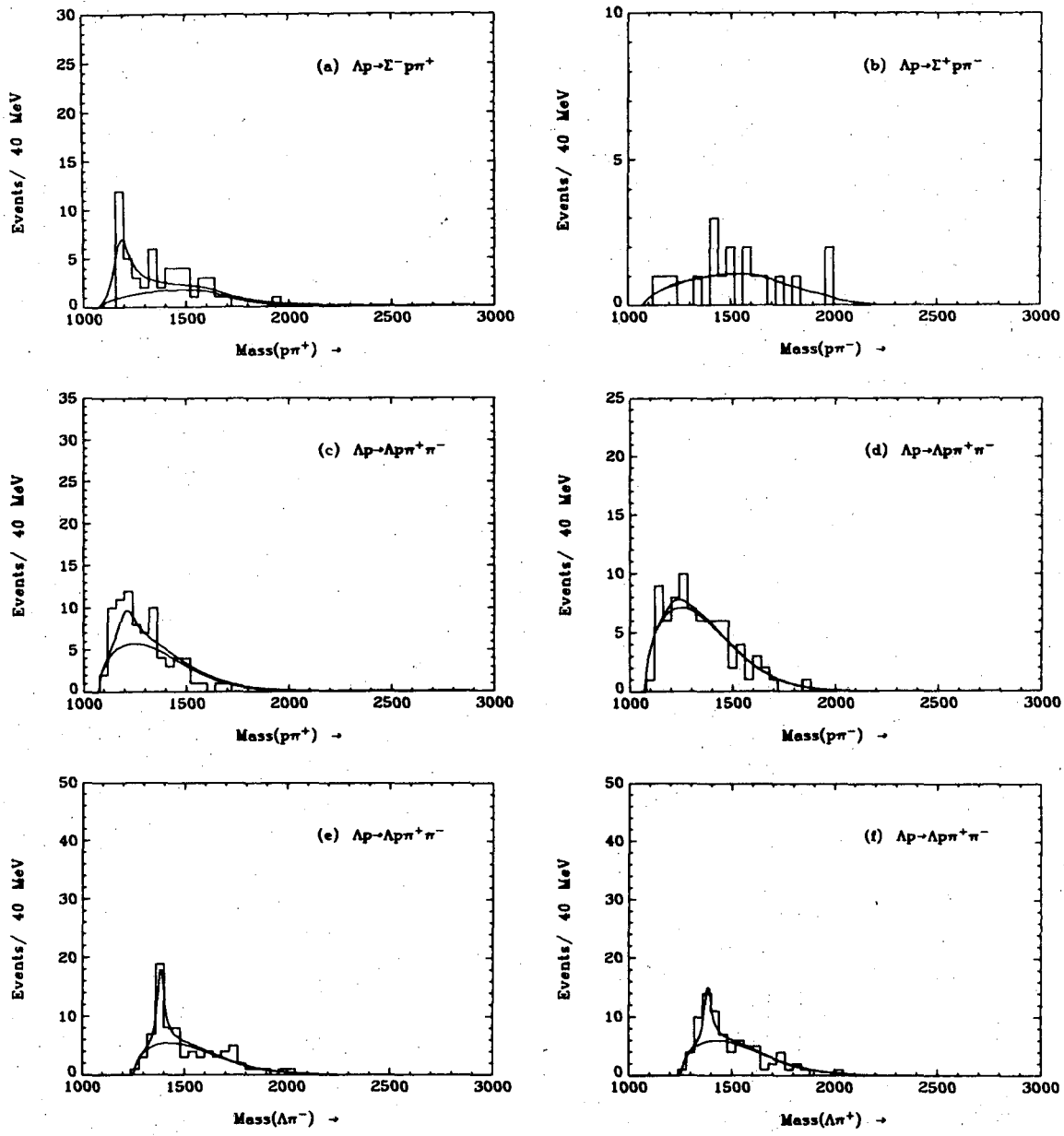


Figure 33B. The same mass distribution fits as in Figure 33 above, except that only $\Lambda p \rightarrow \Lambda p\pi^+\pi^-$ events induced by $\Lambda$ between 3 and 5 GeV/c have been used in the fits.

The production cross sections for $\Lambda p \rightarrow \Sigma p\pi$ are given below, averaged over two regions of $\Lambda$ momentum; from threshold to 10 GeV/c, and from 3 to 5 GeV/c. The corresponding momentum-averaged resonant production cross sections for $\Lambda p \rightarrow \Sigma\Delta$ are also given.

| | $\text{Threshold} \leq P_\Lambda\,(\text{GeV/c}) \leq 10$ | $3 \leq P_\Lambda\,(\text{GeV/c}) \leq 5$ |
|---|---|---|
| $\langle\sigma(\Lambda p \rightarrow \Sigma^- p\pi^+)\rangle$ | $1.50 \pm 0.12$ mb | $2.40 \pm 0.9$ mb |
| $\sigma(\Lambda p \rightarrow \Sigma^- \Delta^{++})$ | $0.82 \pm 0.20$ mb | $1.25 \pm 0.32$ mb |
| $\langle\sigma(\Lambda p \rightarrow \Sigma^+ p\pi^-)\rangle$ | $1.00 \pm 0.15$ mb | $1.40 \pm 0.80$ mb |
| $\sigma(\Lambda p \rightarrow \Sigma^+ \Delta^0)$ | $0.08 \pm 0.16$ mb | $0.0 \pm 0.23$ mb |

Dalitz plots for the reactions Eq. 47a,b are given in Figs. 34a,b. The kinematic boundaries of these Dalitz plots are, of course, not well-defined in this experiment for any ensemble of events since the incident beam is a spectrum in momentum. Any analysis of the Dalitz plot would require a careful normalization of the density in each mass cell $dm_1\, dm_2$ according to the incident $\Lambda$ momentum spectrum.

A single pion exchange analysis in the Jackson frame at the $p\pi\Delta$ vertex indicates that the pion exchange features of the reaction $\Lambda p \rightarrow \Sigma^- \Delta^{++}$ are similar to those of $pp \rightarrow n\Delta^{++}$ at similar momenta. Although neither reaction satisfies well the expectations of $0^-$, $\frac{1}{2}^+$ p-wave scattering at the $p\pi\Delta$ vertex, where the angular dependence is

$$|\psi(\alpha, \phi)|^2 = \text{constant}\,(1 + 3\cos^2\alpha), \qquad (32)$$

both reactions display very similar behavior in their Gottfried-Jackson ($\alpha$) and Treiman-Yang ($\phi$) angular dependences, Figs. 35b,c and Figs. 36a,b. The t - distribution for these events displays the distinctive forward peaking expected from one pion exchange, Fig. 35a.

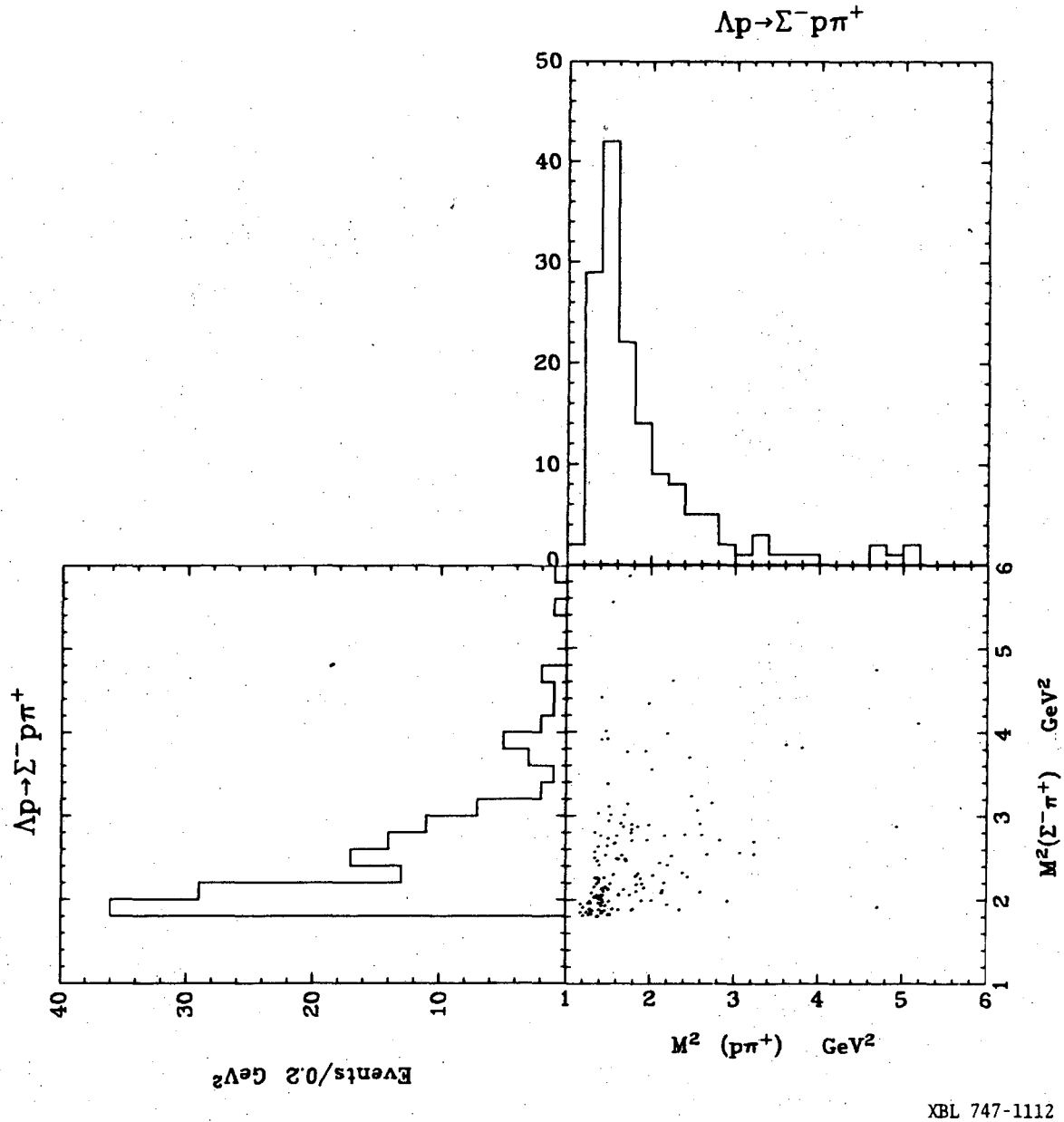


Figure 34. (a) Dalitz plot for the reaction $\Lambda p \rightarrow \Sigma^- p\pi^+$.

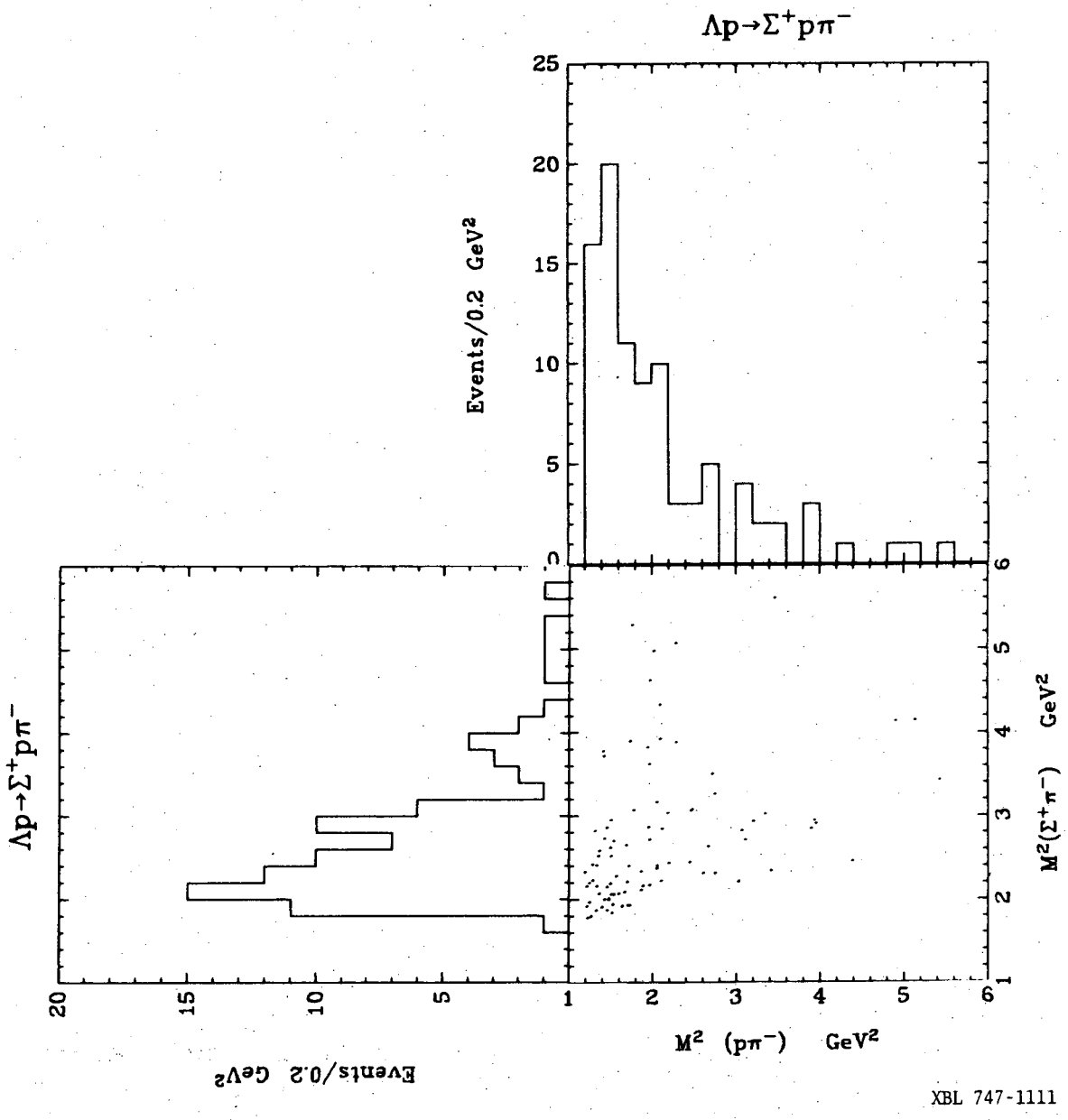


Figure 34b. Dalitz plot for the reaction $\Lambda p \rightarrow \Sigma^+ p\pi^-$.

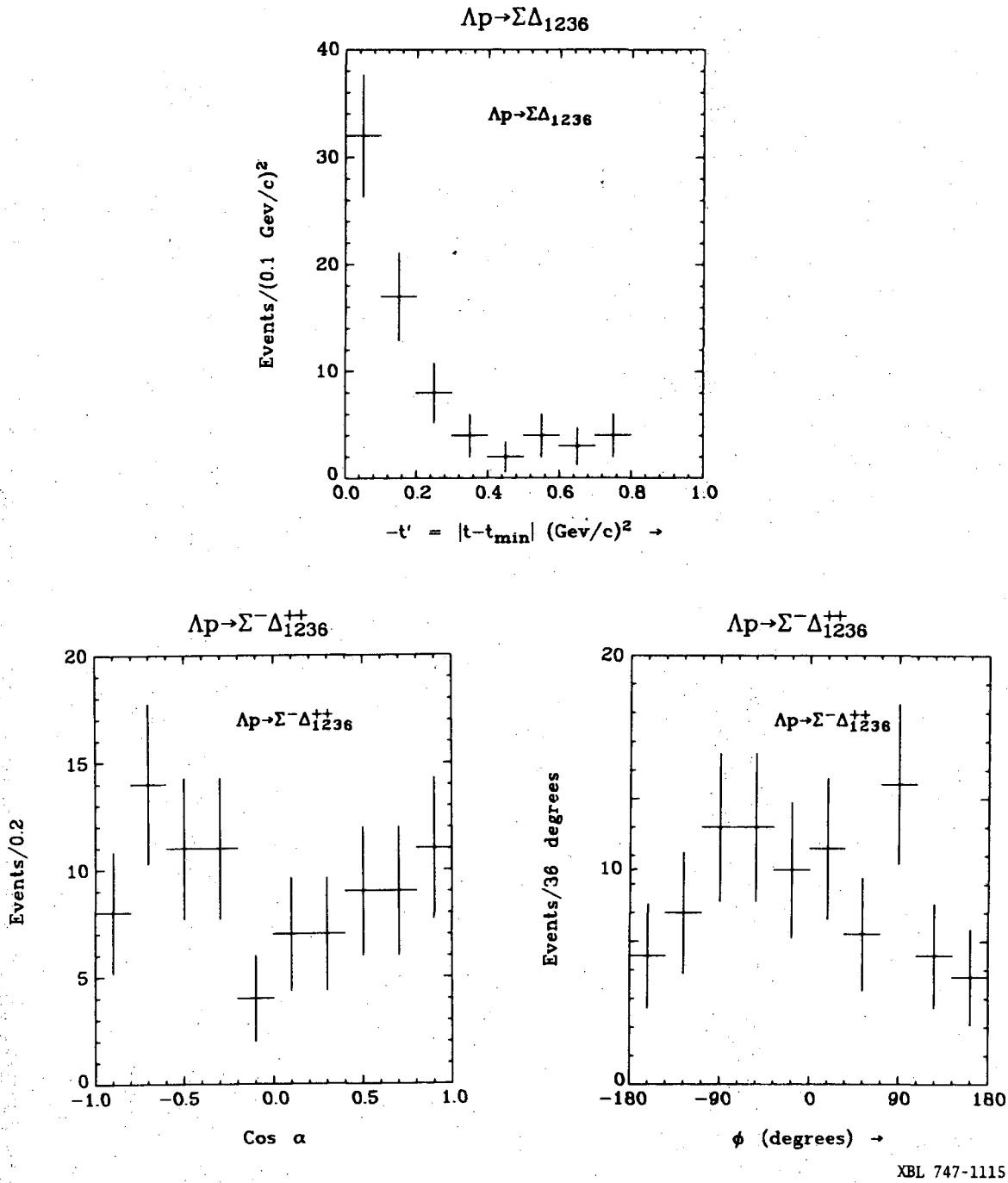


Figure 35. (a) Momentum transfer squared distribution of $\Lambda$ to $\Sigma$ in the reaction $\Lambda p \rightarrow \Sigma\Delta_{1236}$. (b) Jackson angle in the Jackson frame at the $p\pi\Delta$ vertex; (c) the Treiman-Yang angle at the $p\pi\Delta$ vertex.

Assuming that the reaction (28a) proceeds entirely by single pion exchange, and noting that the SU(3) $\Lambda\Sigma\pi$ coupling is purely symmetric whereas the $NN\pi$ coupling is a linear combination of symmetric and anti-symmetric SU(3) couplings, an examination of the relative reaction rates for the processes in Fig. 37a,b yields a measure of the ratio of symmetric to anti-symmetric coupling at the $NN\pi$ vertex. The relative rates are given by

$$\frac{\sigma(\Lambda p \rightarrow \Sigma^- \Delta^{++})_{\pi \text{ exch}}}{\sigma(pp \rightarrow n\ \Delta^{++})_{\pi \text{ exch}}} = \frac{2}{3}(1 - f)^2 \qquad (33)$$

where f is the ratio of anti-symmetric to symmetric plus anti-symmetric coupling. A fit to the cross section ratio of relation (33) yields the value, Fig. 32a,

$$r = 0.18 \pm 0.05 = \frac{2}{3}(1-f)^2, \qquad (34)$$

whence

$$f = \frac{F}{F+D} = 0.48 \pm 0.07\ . \qquad (35)$$

This value is consistent with other determinations of this quantity.[49-51] See Fig. 38.

The baryon-pion mass distributions in the reactions of relation (33) are very similar. The $(n\pi^+)$ and $(p\pi^+)$ mass distributions from an experiment studying the reaction $pp \rightarrow np\pi^+$ at 4.0 GeV/c[46] are displayed in Fig. 39. The dash-dotted line on the $(p\pi^+)$ mass distribution is the sum of 50 percent $\Delta_{1236}$ Breit-Wigner and 50 percent phase space. Their measurement of the fraction of Breit-Wigner is $0.50 \pm 0.02$, in good agreement with our fraction of $0.55 \pm 0.03$. One reviewer, S. Nilsson,[47] has stated that the production of $\Delta^{++}$ in about 50 percent

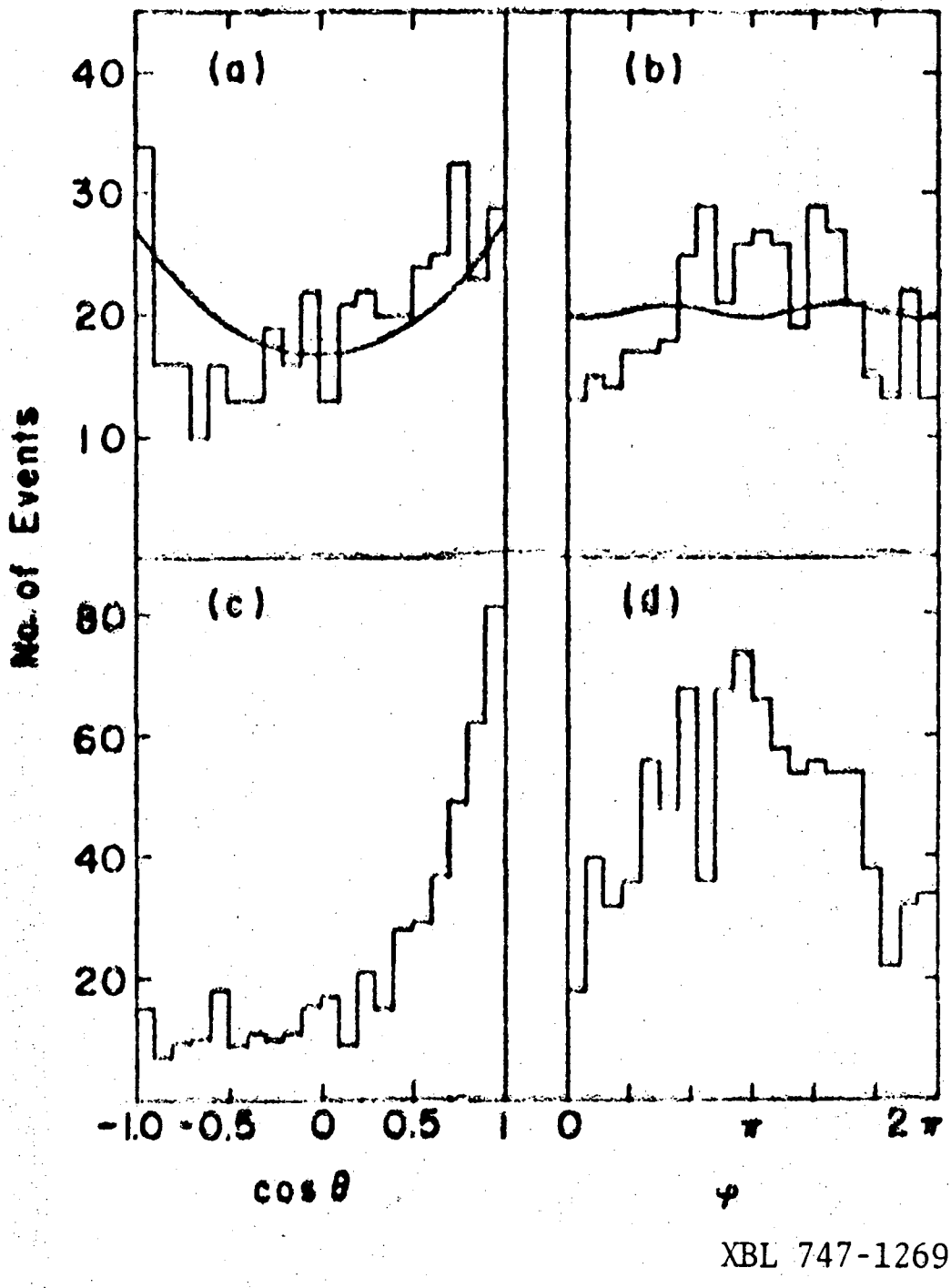


XBL 747-1269

Figure 36. (a) Cosine of the Gottfried-Jackson angle in the reaction $pp \rightarrow n\Delta^{++}$ at the $p\pi\Delta$ vertex; (b) the Treiman-Yang angle at the $p\pi\Delta$ vertex. (c) and (d) are the backgrounds under the distributions of (a) and (b) above, obtained by selecting $(p\pi^+)$ masses near to, but outside of, the $\Delta_{1236}$ band. (These data are from Ref. 48).

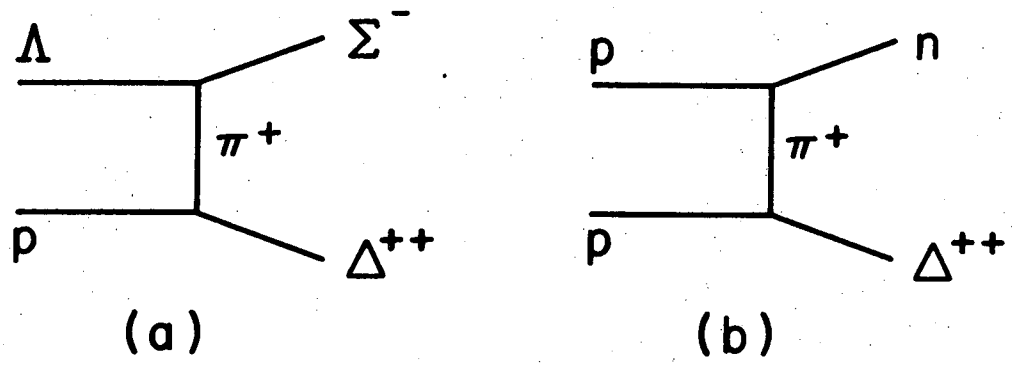


Figure 37. Single pion exchange diagrams presumed to mediate the reactions (a) $\Lambda p \rightarrow \Sigma^- \Delta^{++}$, and (b) $pp \rightarrow n\Delta^{++}$.

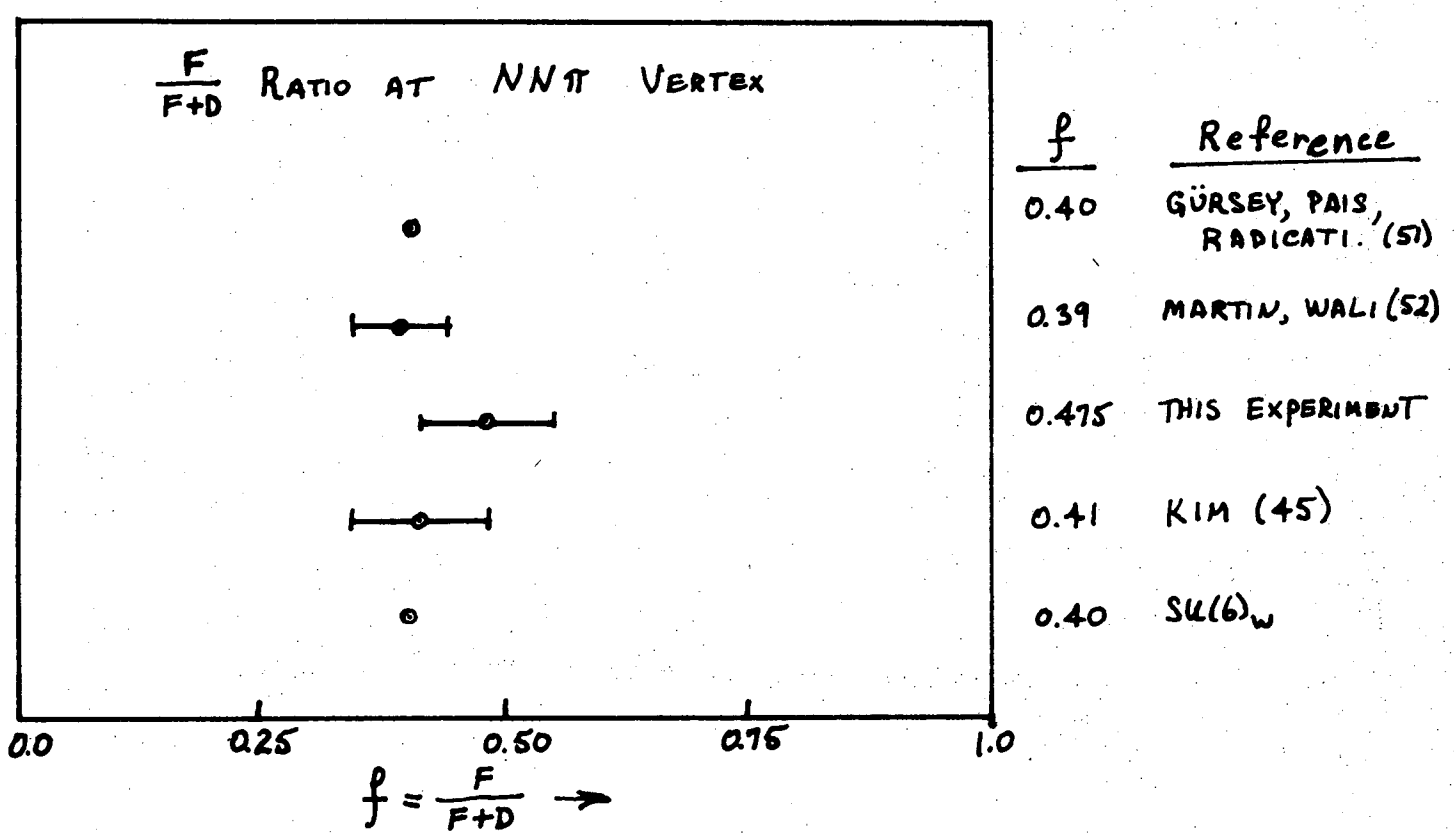


Figure 38. Measurements of the F/(F+D) ratio at the NNπ vertex.

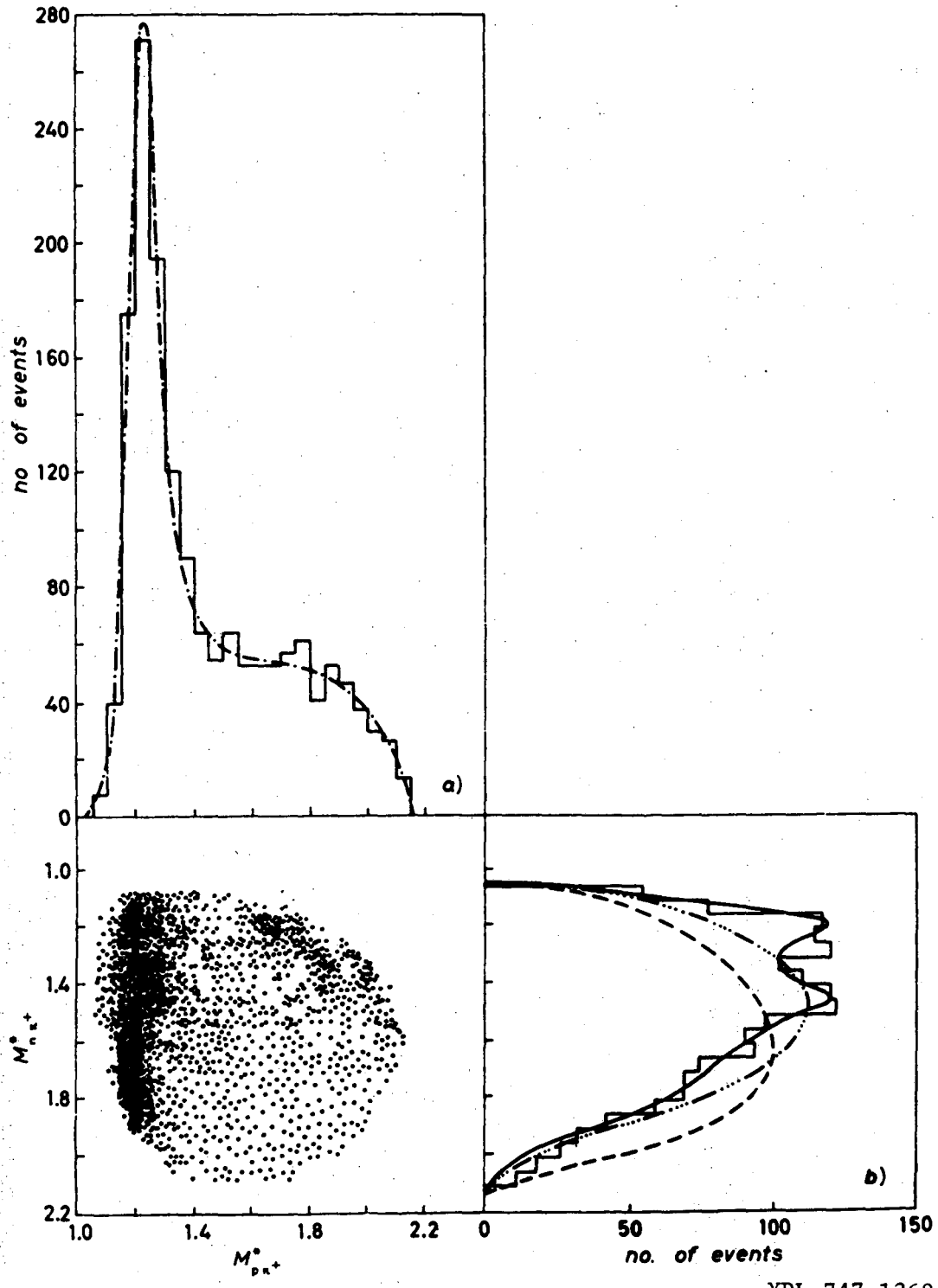


Figure 39. Scatter plot for the reaction $pp \rightarrow np\pi^+$ obtained from Ref. 46.

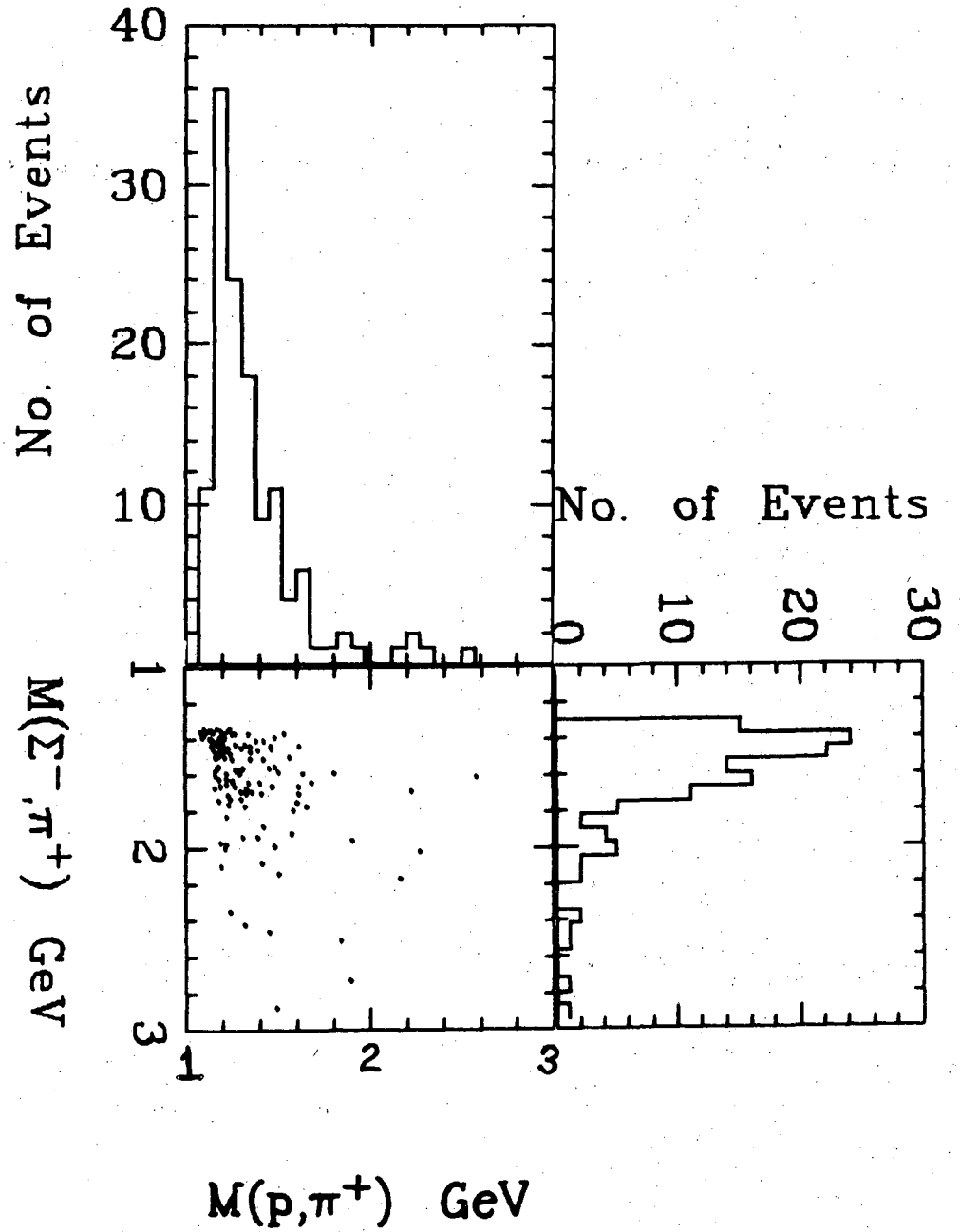


Figure 40. Scatter plot for the reaction $\Lambda p \rightarrow \Sigma^- p \pi^+$ from this experiment.

of the events is a general feature of inelastic pp interactions. For direct comparison, our $(\Sigma^-\pi^+)$ and $(p\pi^+)$ mass distributions are shown in Fig. 40.

The same comparison can be performed with our measurement of the $\Lambda p \to \Sigma^+\Delta^o$ cross section and data for the $np \to p\Delta^o$ reaction. However, the low SU(2) production probability for $\Delta^o$ provides for only a weak comparison due to both large statistical fluctuations and uncertainties in the fitting of the mass distributions, as is already evident from Fig. 33b.

B. Double Pion Production: The Reaction $\Lambda p \to \Lambda p\pi^+\pi^-$

The cross section for the two pion production reaction

$$\Lambda p \to \Lambda p\pi^+\pi^- \tag{36}$$

is displayed in Fig. 41, in which the solid curve superposed is a representation of the $np \to np\pi^+\pi^-$ cross section obtained from the literature.[50,49,53] We observe that the $\Lambda p$ cross section is consistent with equality to the np cross section at all momenta from threshold to 10.0 GeV/c.

This reaction proceeds strongly through the quasi-two-body process

$$\Lambda p \to \Sigma_{1385}\Delta_{1236} \tag{37}$$

in both measured charge states of the $\Sigma_{1385}$ and $\Delta_{1236}$ decuplet baryons. This is evidenced by inspection of the $(\Lambda\pi)$ and $(p\pi)$ invariant mass distributions in Figs. 33c,e for the $(\Lambda\pi^-)$ $(p\pi^+)$ combination and in Figs. 33d,f for the $(\Lambda\pi^+)$ $(p\pi^-)$ combination. Triangle plots for both combinations are displayed in Figs. 42a,b. Fits of these mass distributions to a sum of Lorentz invariant phase space and a p-wave

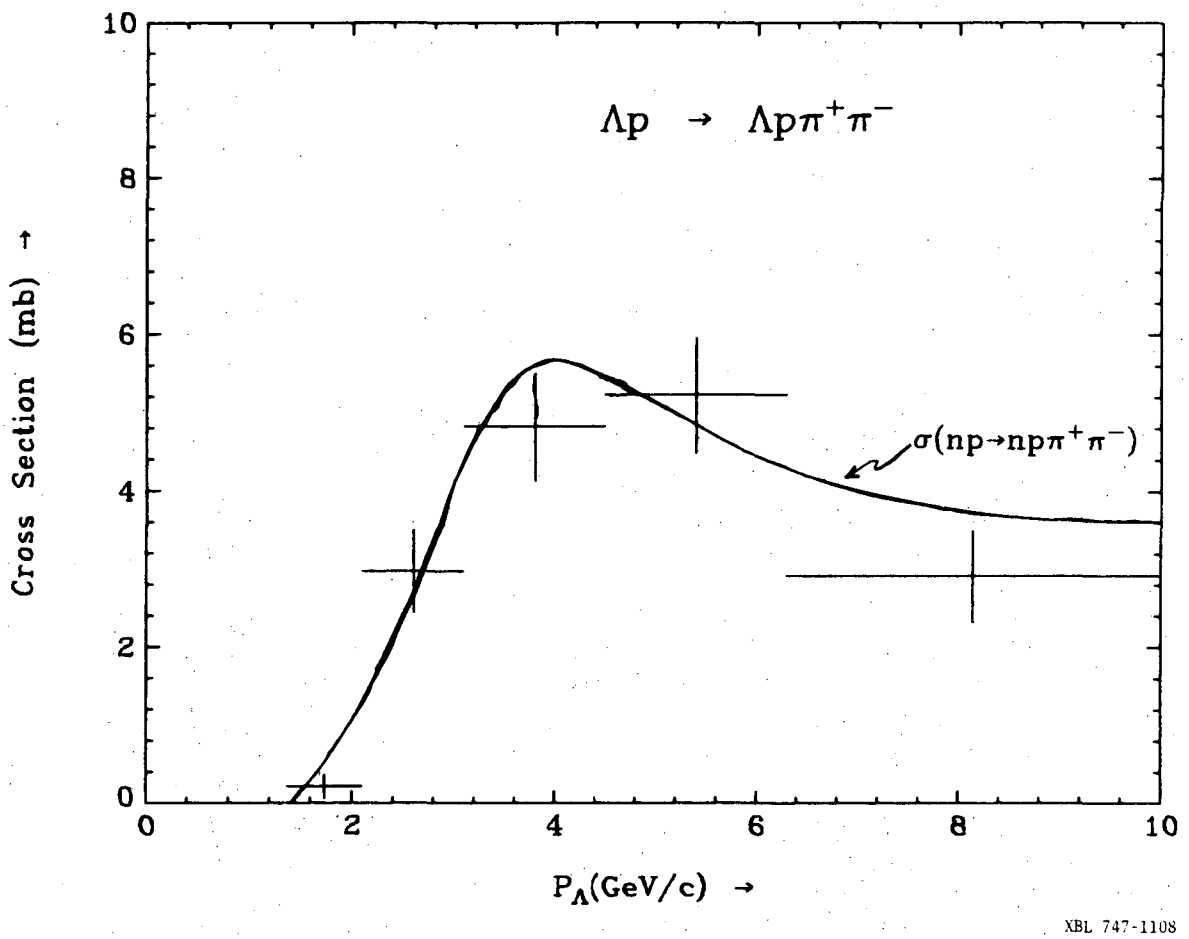


Figure 41. Cross section for $\Lambda p \rightarrow \Lambda p\pi^+\pi^-$ from threshold to 10.0 GeV/c. Superposed is the cross section for two pion production in np scattering, $np \rightarrow np\pi^+\pi^-$.

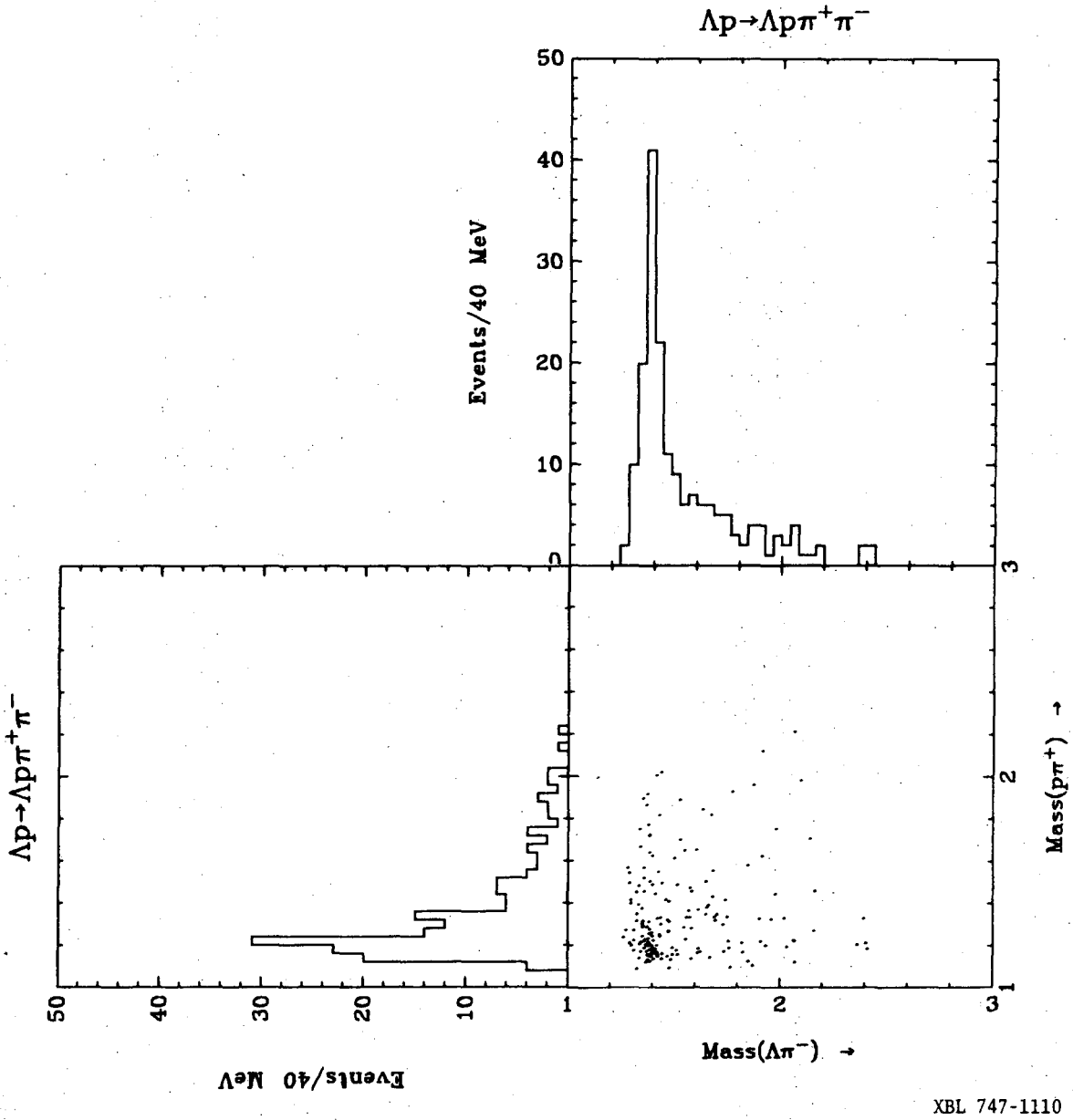


Figure 42. (a) $\Lambda p \rightarrow \Lambda p\pi^+\pi^-$ triangle plot of the masses $(\Lambda\pi^-)$ vs. $(p\pi^+)$.

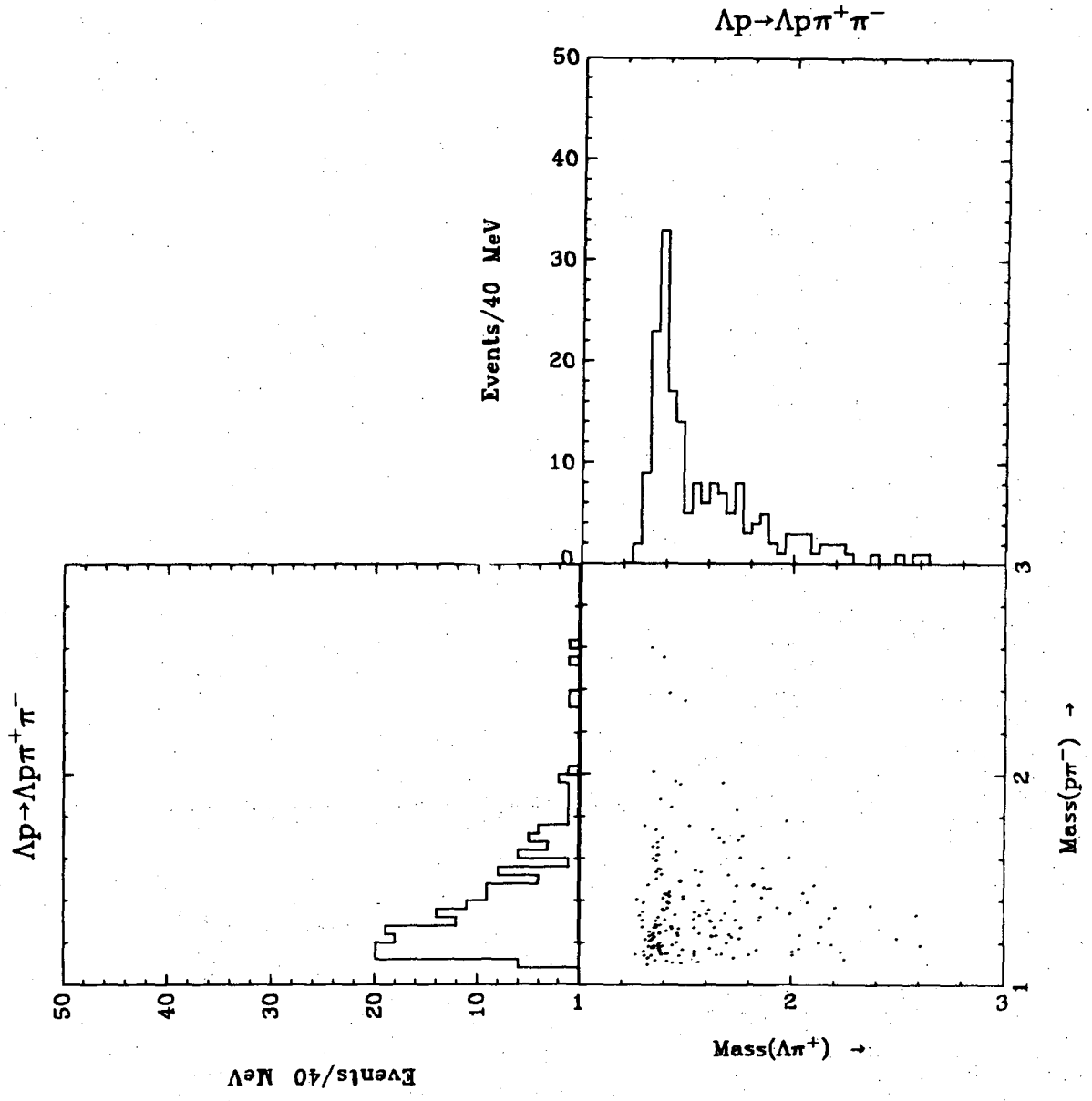


Figure 42(b). $\Lambda p \to \Lambda p\pi^+\pi^-$ triangle plot for the other mass combination, $(\Lambda\pi^+)$ vs. $(p\pi^-)$.

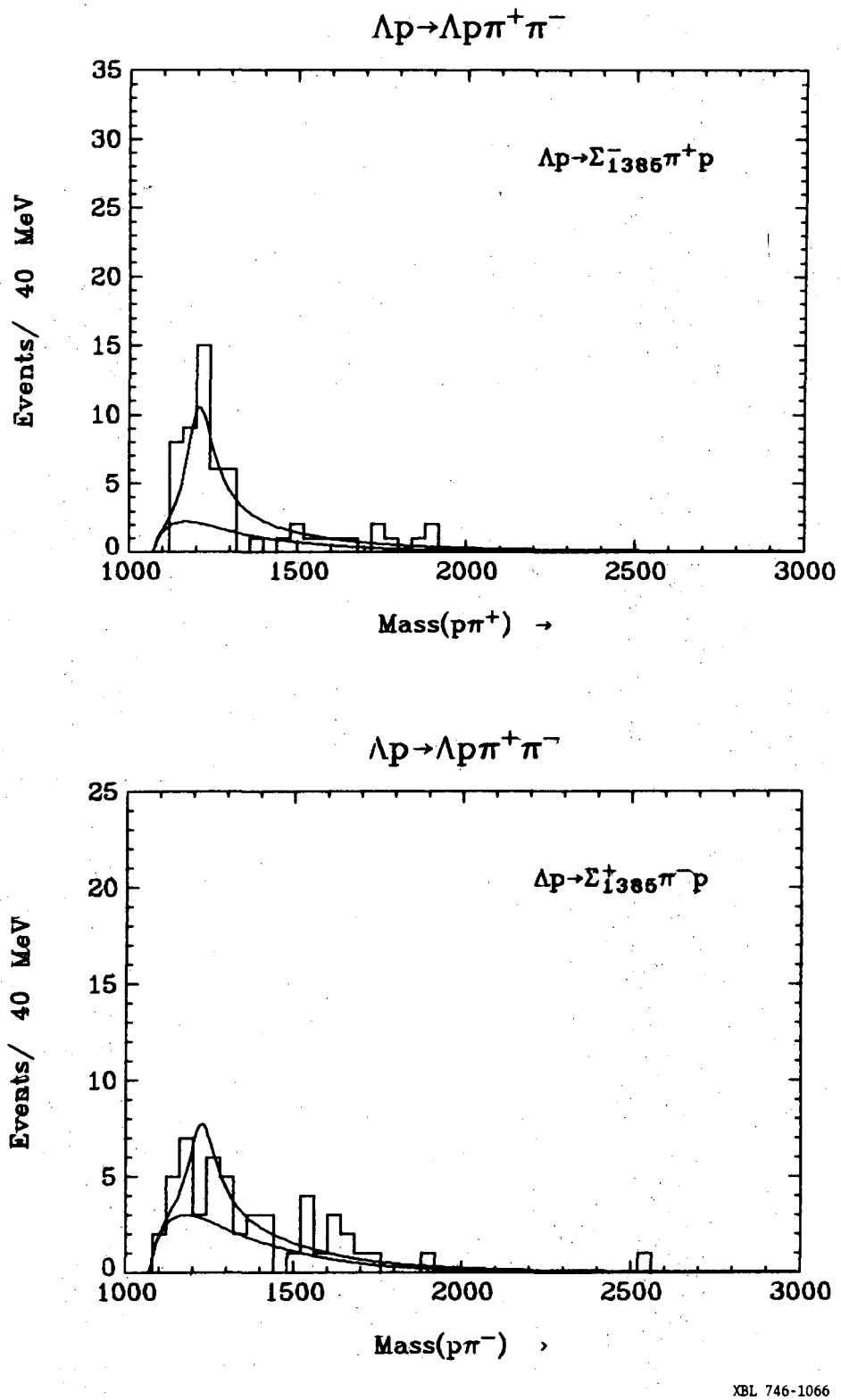


Figure 43. $p\pi$ mass distributions for the reactions (a) $\Lambda p \to \Sigma^-_{1385} p\pi^+$ and (b) $\Lambda p \to \Sigma^+_{1385} p\pi^-$. Curves shown are results of fits of these data to a sum of phase space and $\Delta_{1236}$ production (upper curves). The lower curves represent phase space alone.

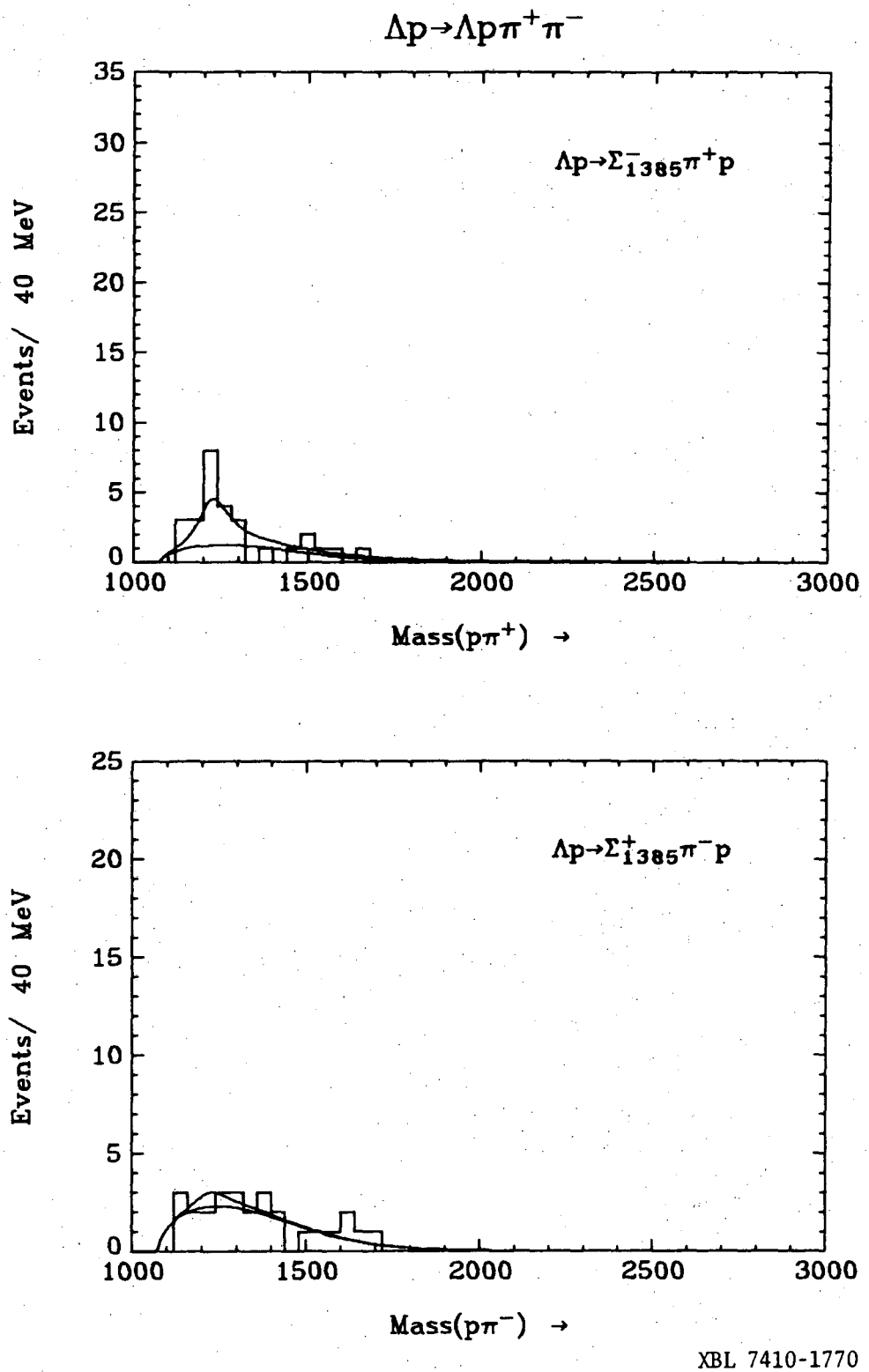


Figure 43B. Same as Figure 43, except only incident Λ between 3 and 5 GeV/c used in the fits.

Breit-Wigner for the $\Sigma_{1385}$ and $\Delta_{1236}$ resonant states have been performed to extract an estimate of the resonant production cross sections. The solid lines of Figs. 33c-f are the results of these fits, where the lower curve on each plot is the contribution of phase space alone, and the upper curve is the sum of phase space and the fitted Breit-Wigner. Numerical results are given in Table 7.

Table 7. Results of the mass distribution fits to phase space plus a p-wave Breit-Wigner

| Reaction | Resonant Breit-Wigner | Threshold $\leq P_\Lambda$(GeV/c)$\leq$10 | | 3$\leq P_\Lambda$(GeV/c)$\leq$5 | |
|---|---|---|---|---|---|
| | | $f_{BW}$ | $f_{PS}$ | $f_{BW}$ | $f_{PS}$ |
| $\Lambda p \rightarrow \Lambda p\pi^+\pi^-$ | $\Delta^{++} \rightarrow p\pi^+$ | 0.44 ± 0.10 | 0.56 ± 0.10 | 0.23 ± 0.17 | 0.77 ± 0.17 |
| | $\Sigma^-_{1385} \rightarrow \Lambda\pi^-$ | 0.31 ± 0.07 | 0.69 ± 0.07 | 0.27 ± 0.09 | 0.73 ± 0.09 |
| $\Lambda p \rightarrow \Lambda p\pi^+\pi^-$ | $\Delta^{o} \rightarrow p\pi^-$ | 0.18 ± 0.12 | 0.82 ± 0.12 | 0.04 ± 0.17 | 0.96 ± 0.17 |
| | $\Sigma^+_{1385} \rightarrow \Lambda\pi^+$ | 0.21 ± 0.06 | 0.79 ± 0.06 | 0.20 ± 0.08 | 0.80 ± 0.08 |

A cut was made on the narrow and well-defined $\Sigma_{1385}$ resonance in the above events, and the resulting sample was fit for the fraction of $\Delta$ resonance present. The results of these fits are given in Table 8 and Figs. 43a,b.

Table 8. Results of the fits to $\Delta$ Breit-Wigner and phase space in the reactions $\Lambda p \rightarrow \Sigma_{1385} p\pi$.

| Reaction | Resonant Breit-Wigner | Threshold $\leq P_\Lambda$(GeV/c)$\leq$10 | | 3 $\leq P_\Lambda$(GeV/c)$\leq$5 | |
|---|---|---|---|---|---|
| $\Lambda p \rightarrow \Sigma^-_{1385} p\pi^+$ | $\Delta^{++} \rightarrow p\pi^+$ | 0.66 ± 0.18 | 0.34 ± 0.18 | 0.55 ± 0.20 | 0.45 ± 0.20 |
| $\Lambda p \rightarrow \Sigma^+_{1385} p\pi^-$ | $\Delta^{o} \rightarrow p\pi^-$ | 0.01 ± 0.25 | 0.99 ± 0.25 | 0.12 ± 0.28 | 0.88 ± 0.28 |

The momentum-averaged $\Lambda p \rightarrow \Lambda p\pi^+\pi^-$ cross section in Fig. 41 is 3.48 ± 0.28 mb averaged from threshold to 10 GeV/c, and 5.09 ± 1.0 mb averaged from 3 to 5 GeV/c. The above mass fits allow an estimate of

the resonant production cross sections given in Table 9.

Table 9. Momentum-averaged resonant production cross sections.

| | Threshold $\leq P_\Lambda$ (GeV/c) $\leq 10$ | $3 \leq P_\Lambda$ (GeV/c) $\leq 5$ |
|---|---|---|
| $\langle\sigma(\Lambda p \rightarrow \Lambda p\pi^+\pi^-)\rangle$ | 3.48 ± 0.28 mb | 5.09 ± 1.0 mb |
| $\sigma(\Lambda p \rightarrow \Lambda\pi^-\Delta^{++})$ | 1.54 ± 0.40 mb | 1.20 ± 0.70 mb |
| $\sigma(\Lambda p \rightarrow \Lambda\pi^+\Delta^{o})$ | 0.62 ± 0.40 mb | 0.20 ± 1.0 mb |
| $\sigma(\Lambda p \rightarrow \Sigma^-_{1385}p\pi^+)$ | 1.10 ± 0.30 mb | 1.40 ± 0.50 mb |
| $\sigma(\Lambda p \rightarrow \Sigma^+_{1385}p\pi^-)$ | 0.72 ± 0.25 mb | 1.0 ± 0.4 mb |
| $\sigma(\Lambda p \rightarrow \Sigma^-_{1385}\Delta^{++})$ | 0.7 ± 0.3 mb | 0.76 ± 0.35 mb |
| $(\Lambda p \rightarrow \Sigma^+_{1385}\Delta^{o})$ | 0.0 ± 0.7 mb | 0.12 ± 0.35 mb |

The $(\Lambda\pi\pi)$ and $(p\pi\pi)$ mass distributions, Figs. 44a and 45a, contain some structure at low mass. The solid curves represent the invariant phase space available to the $(\Lambda\pi\pi)$ and $(p\pi\pi)$ systems. The strong production of $\Sigma_{1385}$ and $\Delta_{1236}$ resonant states determined above may suggest, however, that this structure is due in part to kinematic reflections, that is, one high baryon-pion mass combination necessarily constrains the other baryon-pion combination to lower masses by energy conservation. These reflections are not completely understood even in high statistics nucleon-nucleon interactions. In addition to this kinematic effect, there is another due to the circumstance that the $\Lambda$ beam is not monoenergetic. In a multi-body interaction induced by a particle just above the kinematic threshold, all mass combinations are near their minimum mass. We have removed events induced by low momentum $\Lambda$, accepting $\Lambda p \rightarrow \Lambda p\pi^+\pi^-$ events only for incident $\Lambda$ above 3.0 GeV/c. The same distributions of baryon-pion mass, Figs. 46a and 47a, reveal considerably less structure.

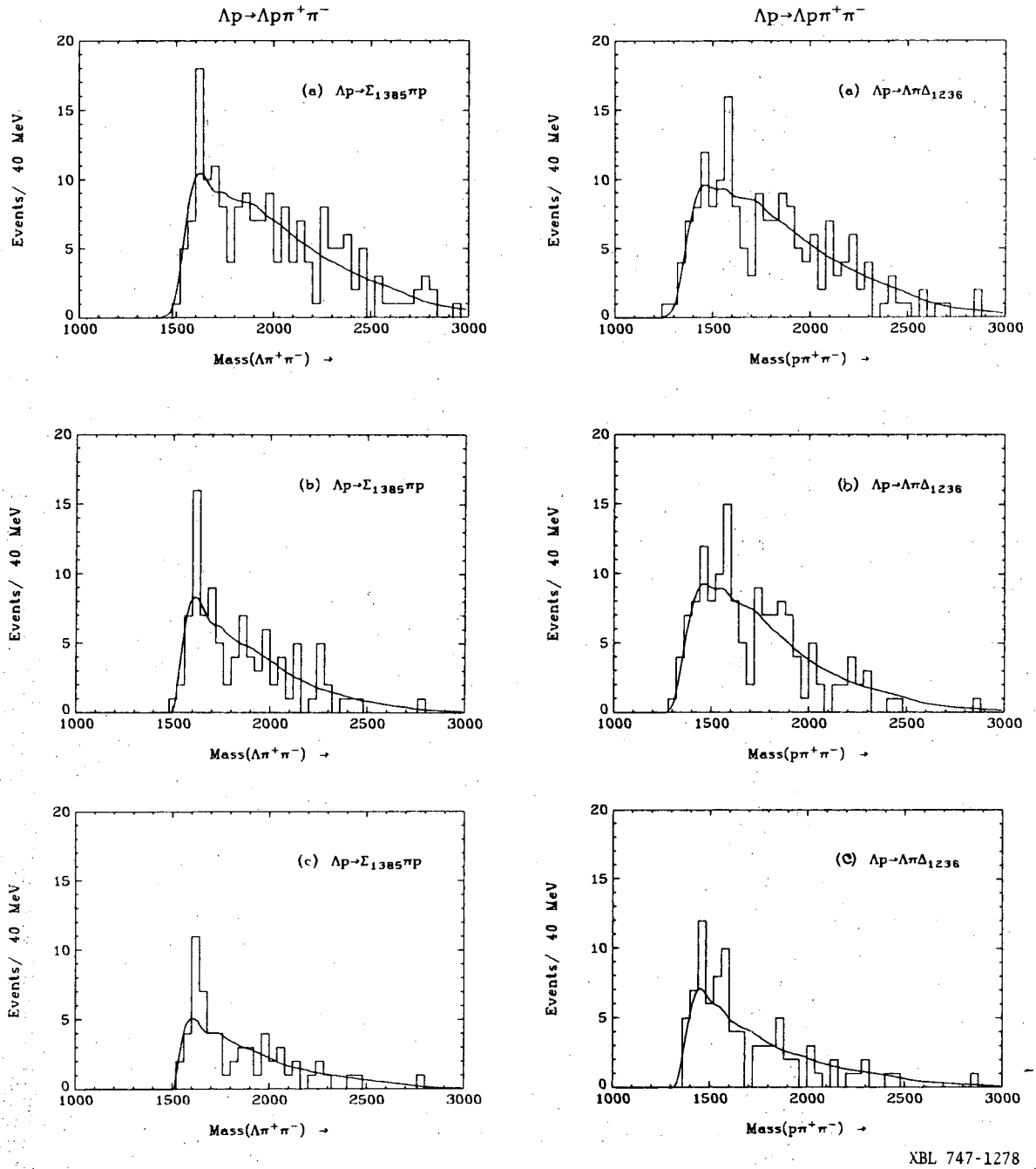


Figure 44. The $(\Lambda\pi\pi)$ mass distribution for (a) all events for the reaction $\Lambda p \rightarrow \Lambda p\pi^+\pi^-$; (b) after a cut on the $(\Lambda\pi)$ mass at $\pm\,\Gamma$ ( = 34 MeV); (c) cut at $\pm\,\Gamma/2$.




Figure 45. The $(p\pi\pi)$ mass distribution in the reaction $\Lambda p \rightarrow \Lambda p\pi^+\pi^-$ for (a) all events; (b) cut on $(p\pi)$ mass at $\pm\,\Gamma$ ( = 110 MeV); (c) cut at $\pm\,\Gamma/2$.

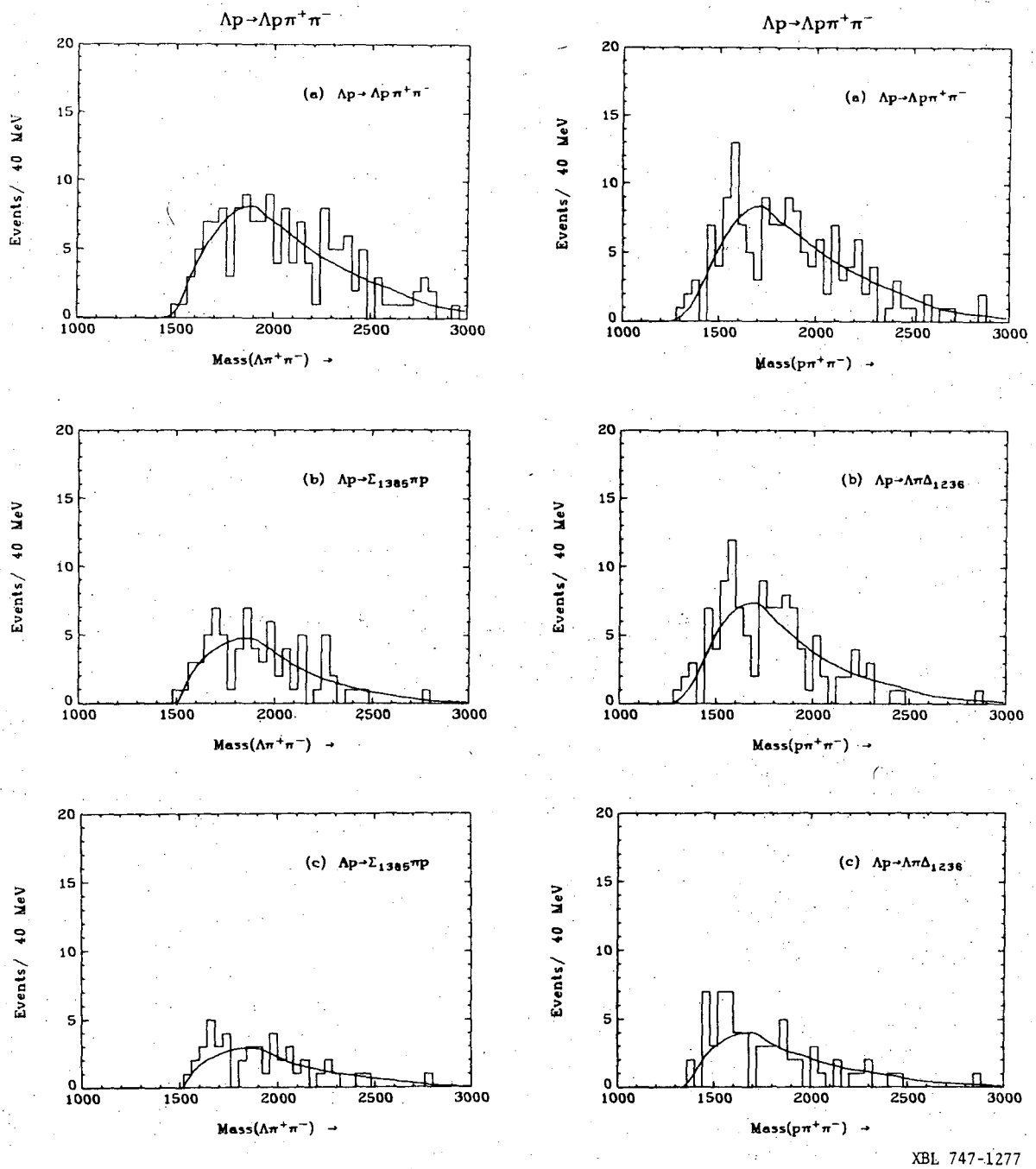


Figure 46. The ($\Lambda\pi\pi$) mass distribution in the reaction $\Lambda p \rightarrow \Lambda p\pi^+\pi^-$ for $\Lambda$ momenta above 3.0 GeV/c. (a) through (c) have the same meaning as in Figure 44.

Figure 47. The ($p\pi\pi$) mass distribution in the reaction $\Lambda p \rightarrow \Lambda p\pi^+\pi^-$ for $\Lambda$ momenta above 3.0 GeV/c. (a) through (c) have the same meaning as in Figure 45.

These distributions have been examined for $\Lambda\pi\pi$ and $p\pi\pi$ states which decay to $\Sigma_{1385}\pi$ and $\Delta_{1236}\pi$, respectively. The motivation for such a search is to ascertain if a strange analogue to the Roper resonance, observed in $N\pi$ and $N\pi\pi$ systems, exists. If it does, the requirement that it be diffractively produced with the same quantum numbers as the $\Lambda$, $I(J^P) = 0(\frac{1}{2}^+)$, demands that this strange Roper be produced with a nearly constant cross section, and hence exist in the data at higher $\Lambda$ momenta, and that it decay to at least a $(\Lambda\pi\pi)$ system, since a $(\Lambda\pi)$ system cannot be isospin 0. Two different selections on the $(\Lambda\pi)$ and $(p\pi)$ mass spectra have been made: the first accepts baryon-pion mass combinations within one resonance width of the $\Sigma_{1385}$ or $\Delta_{1236}$, Figs. 46b and 47b, and the second accepts combinations within one-half width, Figs. 46c and 47c. These latter mass distributions show little evidence for any structure. There is meager evidence for a state at $M(\Lambda\pi\pi) \approx 1660$ MeV, but it is by no means compelling. We do not observe the Roper in its decay to $\Delta\pi$ (branching ratio = 0.16) at a mass $M(p\pi\pi) \approx 1400$-1470 MeV.

In addition to the mass distribution analyses of the preceding paragraphs, we have examined the hypothesis that the reaction

$$\Lambda p \rightarrow \Sigma_{1385}\Delta_{1236} \qquad (38)$$

proceeds by single pion exchange, Fig. 48a. The Gottfried-Jackson and Trieman-Yang angular dependences at the $p\pi\Delta$ vertex, Figs. 49b, c, agree reasonably well with this hypothesis. Indeed, with the exception of the datum at $\cos\alpha \approx -1.0$, we observe that the experimental distributions follow closely the expected ones

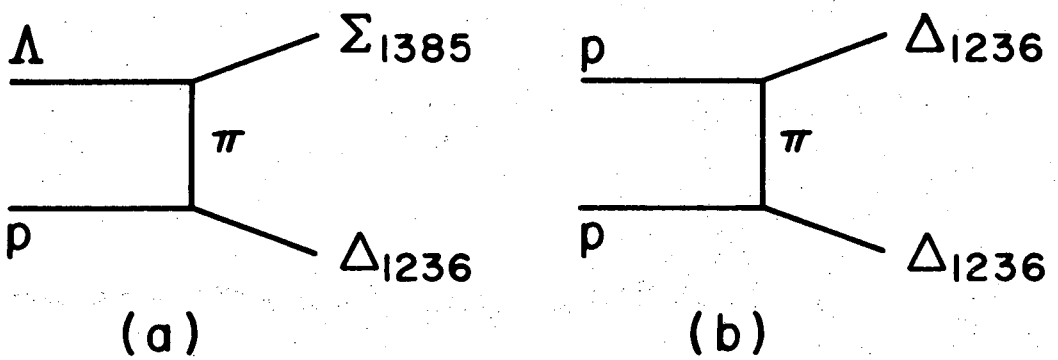


Figure 48. Single pion exchange diagrams in the reactions $\Delta p \rightarrow \Sigma_{1385}\Delta_{1236}$ and $pp \rightarrow \Delta_{1236}\Delta_{1236}$.

$$|\psi(\cos\alpha)|^2 \propto 1 + 3\cos^2\alpha \tag{39}$$

and

$$|\psi(\phi)|^2 \propto \text{constant}. \tag{40}$$

The Jackson and Trieman-Yang angles at the $\Lambda\pi\Sigma_{1385}$ vertex are displayed in Figs. 49 d, e, and are expected to have the same dependences as (30) and (40). Furthermore, the distribution of the momentum transfer squared (less the kinematic minimum), $t' = t - t_{min}$, is peaked near $t' = 0$ as expected. This pion exchange reaction is kinematically farther from the pion pole than reactions 48 a, b. Since the pion propagator depends on t as

$$\text{pion propagator} \approx \frac{1}{t - m_\pi^2}, \tag{41}$$

and $m_\pi^2 \approx 0.02\ \text{GeV}^2$ is quite small, the differential cross section for this pion exchange process is large near the minimum t. In elastic scattering of, say, nucleons the minimum momentum transfer, $t_{min}$, is 0, whereas in np charge exchange[53] $t_{min}$ is non-zero but very small. In $\Lambda p \to \Sigma^0 p$, $t_{min}$ is also quite small, in $\Lambda p \to \Sigma^- \Delta^{++}$ $t_{min}$ is large, and in $\Lambda p \to \Sigma_{1385}\Delta_{1236}$, $t_{min}$ is still larger.

For the process $\Lambda p \to \Sigma_{1385}\Delta_{1236}$ we display on Figs. 50 a, b the $\cos\theta^*$ and t' angular distributions as a function of incident $\Lambda$ momentum.

In this section, we have found similarity between the momentum dependence of the single pion production reactions in $\Lambda$-nucleon and nucleon-nucleon interactions,

$$\Lambda p \to \Sigma p \pi$$
$$N p \to N p \pi .$$

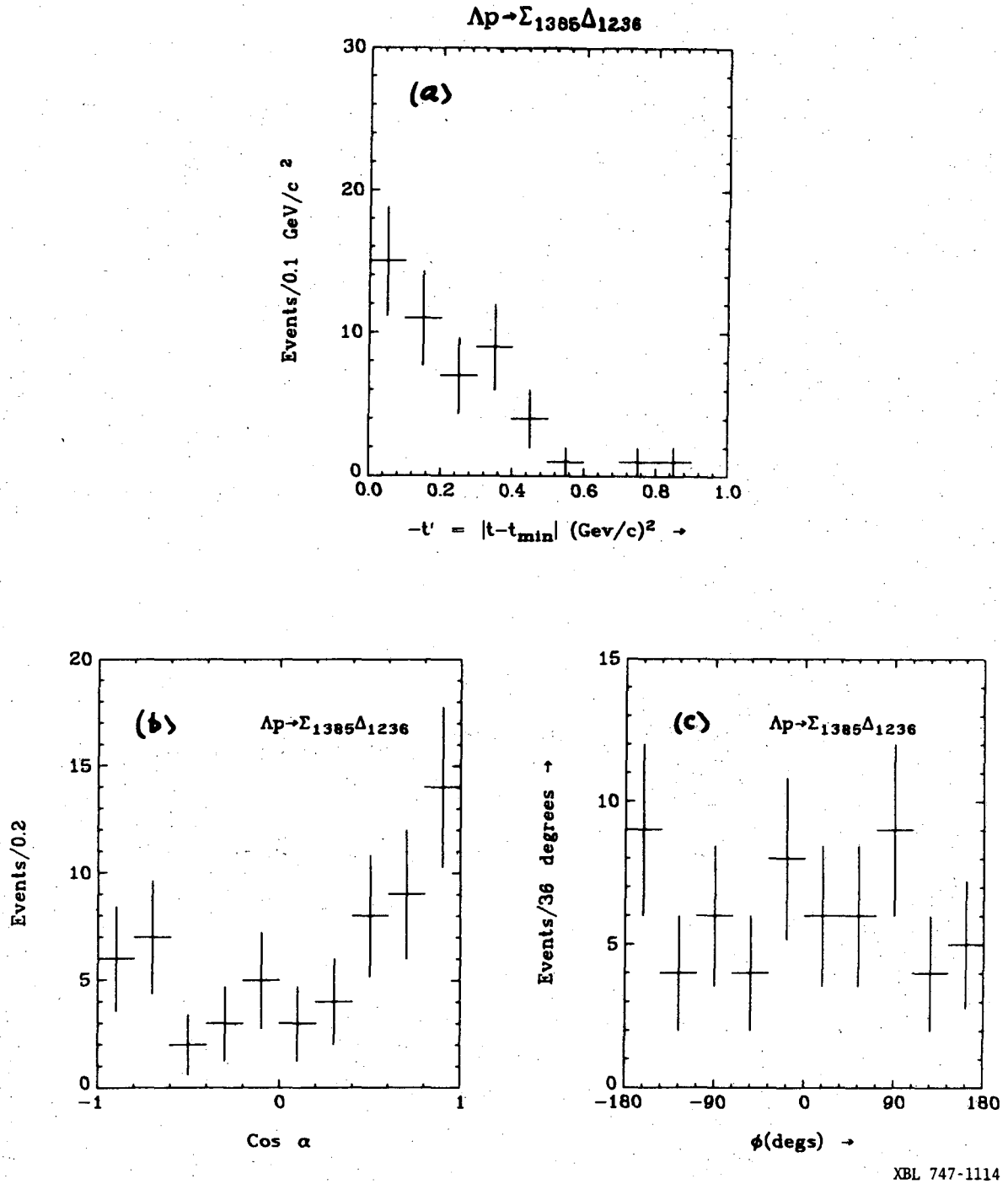


Figure 49. Single pion exchange features of the reaction $\Lambda p \rightarrow \Sigma_{1385}\Delta_{1236}$: (a) the t' distribution; (b) the Gottfried-Jackson angle; (c) the Treiman-Yang angle.

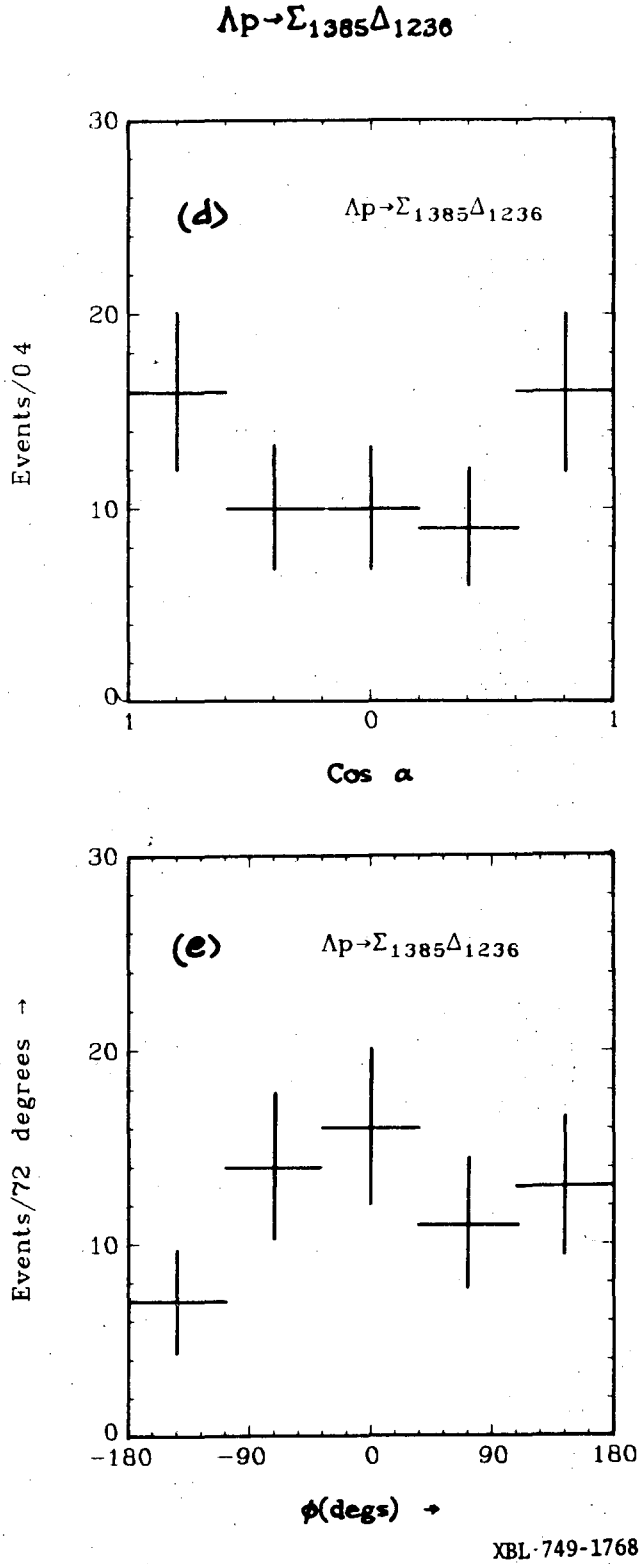


Figure 49. (d) The Jackson angular distribution at the $\Lambda\pi\Sigma_{1385}$ Vertex; (e) the Treiman-Yang angular distribution at $\Lambda\pi\Sigma_{1385}$ vertex.

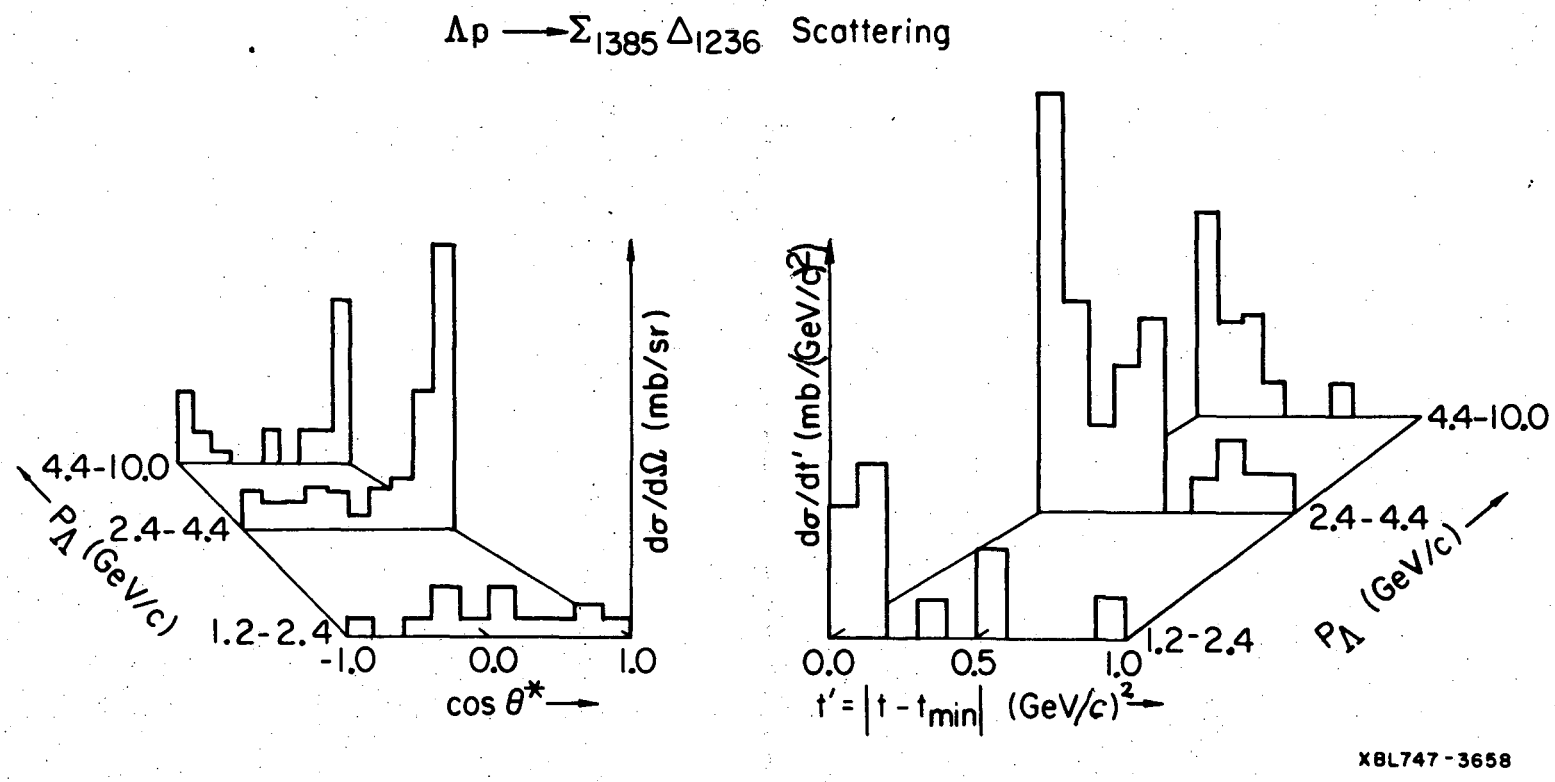


Figure 50. Cosine $\theta^*$ and t' distributions in the reaction $\Lambda p \rightarrow \Sigma_{1385}\Delta_{1236}$ as a function of $\Lambda$ momentum.

The double pion production reactions

$$\Lambda p \rightarrow \Lambda p\pi\pi$$

$$Np \rightarrow Np\pi\pi$$

also have similar behaviors from kinematic threshold to 10.0 GeV/c. The $\Lambda p$ reactions appear to be dominated by single pion exchange, and production of $\Sigma_{1385}$ and $\Delta_{1236}$ states.

Section V. Poorly Constrained Reactions

A. Introduction to the Problem

This section analyzes ensembles of events in zero- and one-constraint multivertex fits from SQUAW.[55] Our attention to this problem arises from the desire to measure the 1-constraint/2-vertex[56] production reaction

$$\Lambda p \rightarrow \Sigma^{o} p, \tag{42a}$$

and correctly separate this ensemble of events from others, e.g.,

$$\Lambda p \rightarrow \Lambda p \pi^{o} \ (0C/1V) \tag{42b}$$

$$\Lambda p \rightarrow \Lambda n \pi^{+} (0C/1V) \tag{42c}$$

and even

$$\Lambda p \rightarrow \Lambda p \ (1C/1V) \ . \tag{42d}$$

We commence by reviewing what SQUAW does in a zero-constraint situation such as reaction (42b).

For a given set of (well-) measured physical quantities, $m_j$, from TVGP, SQUAW first finds some first approximation starting values, $X_j$, for all particles at a vertex, using energy-momentum conservation and the $m_j$. Given a kinematic hypothesis, the conditions of energy-momentum conservation yield the best fitted values, $\overline{X}_j$, subject to the errors on the $m_j$. Because the conservation equations are non-linear, the equations are iterated in the sense that the output values ($X_j$) from one interaction are the input values ($\overline{X}_j$) to the next iteration.

A kinematic solution is found if

$$\text{FSUM} = \sum_i |f_i| < \epsilon_1 \qquad (\epsilon_1 = 0.1 \text{ MeV})$$

and

$$|\chi^2 - \overline{\chi}^2| < \epsilon_2, \qquad (\epsilon_2 = 0.075) \tag{43}$$

where $f_i$ are the constraints, and $\overline{\chi}^2$ is the chi-squared between the fitted $x_j$ and the measured $m_j$ on the previous iteration.

On each iteration in a fit, XVSET is called to check if all fitted values are in the physical region. If not, the step size in the iteration is reduced by some factor $\epsilon$, i.e., the approximate value $\overline{X}$ from the previous iteration (assumed to be physical) is stepped to the new value $X'$,

$$X' = \overline{X} + \epsilon(X - \overline{X}),$$

instead of the value X, which had been found to be unphysical. The factor $\epsilon$ is initialized at a value $\sim \frac{1}{2}$, and successively reduced by $\frac{1}{2}$ each cut. A maximum of ~ 20 cuts are allowed before IFAIL = 20, 21 (too many total, or successive, cut steps).

On the first approximation at a zero-constraint vertex, if the values $X_j$ are not all in the physical region, i.e. the discriminant of the quadratic equation governing the solution is negative, then the discriminant is forced to be zero, with a corresponding re-evaluation of the first approximation momentum of the incoming neutral particle (in the case of $\Lambda p \rightarrow \Lambda p \pi^o$).[55]

Such a measure will obviously not improve a non-physical situation, unless other over-constrained vertices in the fit can have their first approximation values pulled to such an extent as to bring the zero-constraint vertex into the physical region. In the case of the 0C/1V $\Lambda p \rightarrow \Lambda p \pi^o$, the other vertex is the 3C $\Lambda \rightarrow p\pi^-$ vertex, which in general is well known, and consequently the above measure has a limited chance of success.

For a real $\Lambda p \rightarrow \Lambda p \pi^o$ reaction measured in the film, the fitted quantities $X_j$ are presumably in, or very close to, the physical region, and only lie outside due to non-zero measurement errors. In such a

case where some one of the $X_j$ is not physical, it is possible that

$$|\chi^2 - \bar{\chi}^2| < \epsilon_2$$

and

$$\text{FSUM} < \epsilon_1,$$

but no physical solution is allowed, and the final status of the event is

$$\begin{aligned} &\chi^2 \text{ good}, \\ &\text{FSUM good}, \\ &\text{IFAIL} = 20 \text{ or } 21, \end{aligned} \tag{44}$$

and the hypothesis is rejected.

We have considered such a possibility in connection with a class of events which are, from the point of view of SQUAW, kinematically unambiguous examples of the reaction (42a)

$$\Lambda p \rightarrow \Sigma^o p.$$

The method of analysis is essentially the same as that technique employed in $K^o$ 3-body decay analysis in which one examines the discriminant of the quadratic equation governing energy-momentum conservation in the reaction.

B. Related Problems

$\Sigma$ decay.

The reader will remember a similar situation encountered in the early days when charged $\Sigma$ were reconstructed in bubble chambers. On occasion a charged decay, identified as a $\Sigma$ by bubble density, failed to fit the $\Sigma$ decay hypothesis, and only satisfied momentum-energy conservation for a charged K decay. The reason is straightforward. A 200 MeV/c $\Sigma^+$ has a mean decay length of ~ 200 (2.4cm)/1190 ~ 0.4 cm. The momentum of so short a track cannot be deduced from a curvature

measurement, and so the $\Sigma$ decay vertex has four unknown quantities: the incident $\Sigma$ momentum and the three-momentum of the missing neutral from the decay. Furthermore, the direction of such a track is poorly measured, and the transverse momentum depends on this direction, $\hat{a}$, and the changed secondary momentum, $\vec{p}_s$, as

$$p_T = |\vec{p}_s| \sin\theta \tag{45}$$

where $\cos\theta = \hat{a}\cdot\hat{p}_s$ .

This quantity cannot exceed the center-of-mass momentum, $p_0^*$, determined rather precisely by the masses of the particles involved in the decay. The condition that

$$p_T \leq p_0^* \tag{46}$$

is equivalent to the condition that the discriminant of the quadratic equation governing the decay be positive.

In this situation, however, the remedy is simple enough: the culprit is clearly the short charged track, and its direction $\hat{a}$ is to be changed in the plane of the decay so that $p_T = p_0^*$ .

Neutral Three-Body K Decay

One usually separates the $K_{\pi 3}$ decay mode from both $K_{\ell 3}$ modes on the basis of the variable

$$(P_0')^2 \equiv \frac{m_K^2}{P_T^2 + m^2}\,(P_{\pi^o}^{*2} - P_T^2), \tag{47}$$

where $m$ is the effective mass of both charged particles assuming that the decay is $K^o \rightarrow \pi^+\pi^-\pi^o$. In this $K_{\pi 3}$ decay, the missing transverse momentum, $P_T$, and the momentum of the $\pi^o$ in the $K^o$ rest frame, $P_{\pi^o}^*$, are such that $P_T \leq P_{\pi^o}^*$, hence $(P_0')^2 \geq 0$ for $K_{\pi 3}$, but predominantly

negative for $K_{\ell 3}$ (since $P_T$ is larger). A typical distribution of $(P'_0)^2$ is shown in Fig. 51.

The physical separation is made on the basis of monte carlo simulation of the $(P'_0)^2$ distribution for given experimental errors on the measured particles.

In such experiments one usually has a $K_2^o$ beam produced a large distance from the detector, spark chambers, or a bubble chamber, and so the angular resolution of the $K_2^o$ direction is good compared to the charged decay prong measurements. The resolution near $(P'_0)^2 = 0$ is $\sim 0.002$ GeV$^2$, by visual inspection of Fig. 51,

$$\Delta\sqrt{(P'_0)^2} = 45.0 \text{ MeV/c}. \tag{48}$$

Figure 51 is from a bubble chamber experiment, for which this is a typical momentum error on a charged track.

C. Reconstruction of Zero-Constraint Solutions

Suppose in a reaction

$$a + b \rightarrow c + d + e \tag{49}$$

where a, e are neutral particles, and $P_\mu^k = (E^k, p_1^k, p_2^K, p_3^K)$ is the four-vector of particle k, we define the difference four-vector

$$D_\mu \equiv P_\mu^a - P_\mu^e = P_\mu^c + P_\mu^d - P_\mu^b, \tag{50}$$

where the equality on the right derives from energy-momentum conservation. The right-hand side is measured, and the left-hand side contains the four unknown quantities, the three-momentum of the neutral particle e, and the magnitude of the momentum of the incident neutral a

$$P_1^e,\ P_2^e,\ P_3^e, \text{ and } \left[(P_1^a)^2 + (P_2^a)^2 + (P_3^a)^2\right]^{1/2}, \tag{51}$$

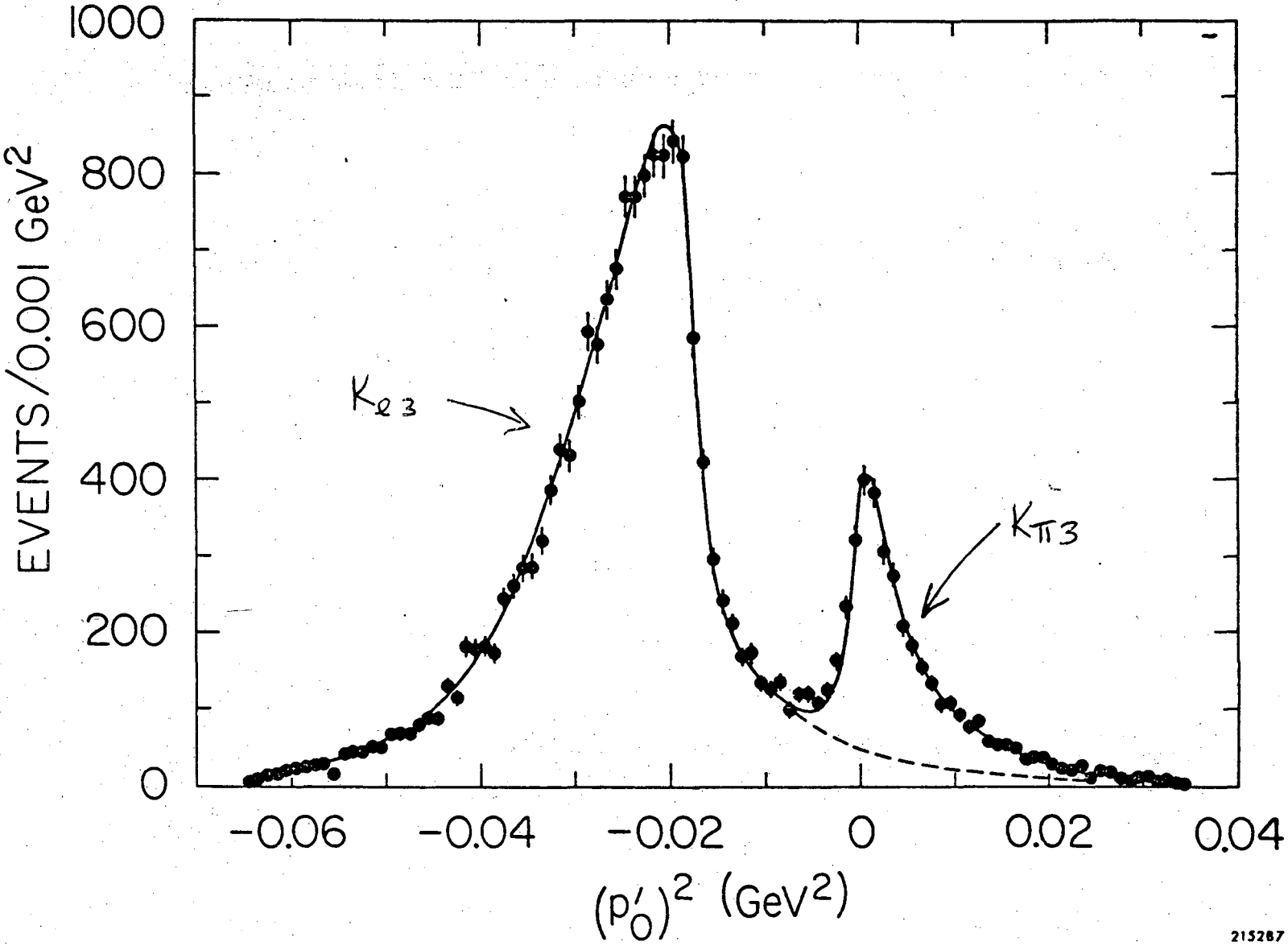


Figure 51. A typical $(p'_0)^2$ distribution in $K^o$ three-body decay. This data is from a bubble chamber experiment, and is typical of the momentum resolution obtainable.

with

$$D_\mu D^\mu = \text{invariant.} \tag{52}$$

Given a direction for the incoming neutral particle a, $\hat{a} = (a_1, a_2, a_3)$, the two neutral particle four-vectors must satisfy

$$P^a_\mu - P^e_\mu = D_\mu . \tag{53}$$

In detail, these equations are

$$\sqrt{m_a^2 + P_a^2} - D_0 = \sqrt{m_e^2 + P_e^2} , \tag{54a}$$

$$P_a a_1 - D_1 = P_e e_1 , \tag{54b}$$

$$P_a a_2 - D_2 = P_e e_2 , \tag{54c}$$

$$P_a a_3 - D_3 = P_e e_3 , \tag{54d}$$

where $e = (e_1, e_2, e_3)$ is the direction of neutral particle e,

$$1 = \sum_{i=1}^{3} a_i^2 = \sum_{i=1}^{3} e_i^2 , \tag{55}$$

and $P_a$, $P_e$ are the magnitudes of the three-momenta of a, e. Substituting the momentum equations into the energy equation yields

$$(m_a^2 - m_e^2) + (D_0^2 - \sum_i D_i^2) + 2P_a \Sigma a_i D_i = 2D_0 \sqrt{m_a^2 + P_a^2} \tag{56}$$

The second term on the left-hand side is $D_\mu D^\mu$, and we define

$$\alpha \equiv (m_a^2 - m_e^2) + D_\mu D^\mu \tag{57}$$

(some effective mass difference squared between initial and final states). Then (56) is

$$\alpha + 2P_a \sum_i a_i D_i = 2D_0 \sqrt{m_a^2 + P_a^2}$$

or

$$P_a^2 \left\{ 4 \left[ \sum_i a_i D_i \right]^2 - 4D_0^2 \right\} + P_a \left\{ 4\alpha \sum_i a_i D_i \right\} + \left\{ \alpha^2 - 4D_0^2 m_a^2 \right\} = 0, \tag{58}$$

whence the discriminant is

$$D = 16D_0^2 \left\{ \alpha^2 - 4m_a^2 (D_0^2 - [\Sigma a_i D_i]^2) \right\}, \tag{59}$$

with units of $[\text{Energy}]^6$.

The uncertainty in D due to measurement errors is approximately calculated by altering the components of $D_\mu$ by one standard deviation in measured p, $\phi$, $\lambda$, and computing the variation of the discriminant with respect to these quantities,

$$\frac{\partial D}{\partial p}, \frac{\partial D}{\partial \phi}, \frac{\partial D}{\partial \lambda}.$$

Then the standard deviation error on D is taken to be

$$\delta D = \sqrt{\left(\frac{\partial D}{\partial P} \Delta p\right)^2 + \left(\frac{\partial D}{\partial \phi} \Delta \phi\right)^2 + \left(\frac{\partial D}{\partial \lambda} \Delta \lambda\right)^2}. \tag{60}$$

where $\Delta p$, $\Delta \phi$, $\Delta \lambda$ are the one standard deviation errors.

With respect to the incident neutral direction, the discriminant has a maximum value when the quantity

$$\Sigma a_i D_i$$

is maximal, that is, when the incident neutral direction is the same as the sum of all measured final momenta. In this circumstance,

$$\Sigma a_i D_i \sqrt{D_1^2 + D_2^2 + D_3^2}$$

and

$$D_{max} = 16D_0^2 \left\{ \alpha^2 - 4m_a^2 D_\mu D^\mu \right\}. \tag{61}$$

In $K^o$ three-body decay, if one defines $D_\mu$ to be the four-vector sum of the two measured final particles, then (58) and (59) describe the kinematics of that decay.

The quantity analogous to $(P_0')^2$ in $K^o$ three-body decay is

$$Z \equiv [\Sigma a_i D_i]^2 - \left\{ D_0^2 - (\frac{\alpha}{2m_a})^2 \right\} [E]^2 . \qquad (62a)$$

The condition for the existence of a solution is

$$Z \geq 0 ,$$

or that

$$\Sigma a_i D_i \geq \sqrt{(D_0 - \frac{\alpha}{2m_a})(D_0 + \frac{\alpha}{2m_a})} . \qquad (62b)$$

D. Examination of the discriminant distribution for all $\Lambda p \rightarrow \Lambda p\pi^o$ fits on the DST, Fig. 52, reveals that $D_{\Lambda p\pi^o}$ is strongly peaked near $D_{\Lambda p\pi^o} = 0$, with a long tail extending beyond $D_{\Lambda p\pi^o} \approx 3000.0$ GeV$^6$. A finer examination near $D_{\Lambda p\pi^o} \approx 0$, inserts in Fig. 52, shows that the peaking persists down to resolutions in $D_{\Lambda p\pi^o}$ of 1.0 GeV$^6$. For orientation, a rather special class of events was generated in the monte carlo sense[57] to simulate the process

$$\Lambda p \rightarrow \Sigma^o_{1385} p \rightarrow \Lambda p\pi^o . \qquad (63)$$

It must be emphasized that this ensemble of events does not represent the true ensemble of $\Lambda p \rightarrow \Lambda p\pi^o$ events in this experiment. An unbiased ensemble of $\Lambda p \rightarrow \Lambda p\pi^o$ events has not, in fact, been obtained, and furthermore the intermediate process in relation (63) does not represent all possible processes, nor does the incident $\Lambda$ momentum of 2.5 GeV/c represent the actual spectrum of incident $\Lambda$. Consequently, we may

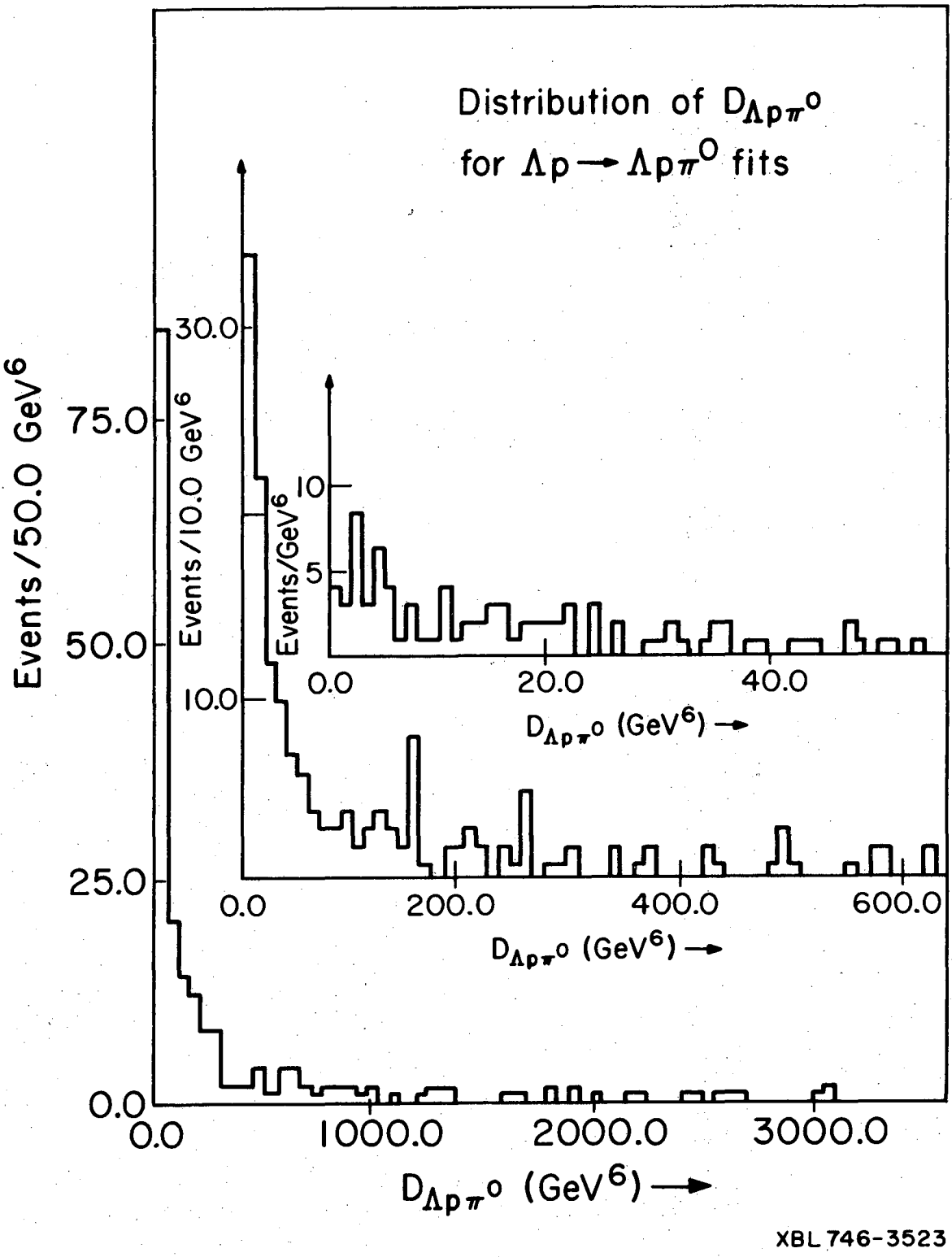


Figure 52. Distribution of the discriminant of the quadratic equation for all successful SQUAW fits to the reaction $\Lambda p \rightarrow \Lambda p\pi^0$. Inserts show finer resolution near 0.

draw only qualitative conclusions from these events. The discriminant distribution for these events is shown in Fig. 53a, and displays the preference for a zero discriminant value. Further light is shed on this distribution by smearing the z-coordinate of the monte carlo $\Lambda$ origin as a Gaussian of width $\sigma_z = 0.5$ cm, a rough estimate derived from the results of Appendix III. The resultant discriminant distribution in Fig. 53b reveals a significant spill-over of events to negative values, events which are unidentifiable with TVGP-SQUAW.

We have investigated the hypothesis that $\Lambda p \rightarrow \Lambda p\pi^o$ events with negative discriminant values have been incorrectly identified as $\Lambda p \rightarrow \Sigma^o p$ events. This hypothesis is a good one, since the events are generally low momentum interactions, they usually contain both a 3-c $\Lambda \rightarrow p\pi^-$ decay fit and a proton by ionization, and there is some kinematic overlapping of these two reactions at momenta from 1-2 GeV/c as revealed by a PHONY program[58] analysis.

We have calculated the $\Lambda p \rightarrow \Lambda p\pi^o$ discriminant, $D_{\Lambda p\pi^o}$, for SQUAW fits to $\Lambda p \rightarrow \Lambda p\pi^o$ and $\Lambda p \rightarrow \Sigma^o p$ hypotheses. Figure 54a gives $D_{\Lambda p\pi^o}$ for $\Lambda p \rightarrow \Lambda p\pi^o$ events near 0, which is positive as required; (b) gives $D_{\Lambda p\pi^o}$ for 45 unambiguous SQUAW fits to $\Lambda p \rightarrow \Sigma^o p$, in which is seen that, except for 10 events, $D_{\Lambda p\pi^o}$ tends near, but less than, 0. However, an estimation of the errors on the $D_{\Lambda p\pi^o}$ reveals in (c) that only five events are within 1 standard deviation of 0, and in (d) that only 13 events are within 3 standard deviations of 0. We are justified in assigning some of these 45 $\Lambda p \rightarrow \Sigma^o p$ fits to the reaction $\Lambda p \rightarrow \Lambda p\pi^o$ (on the basis of Fig. 54b).

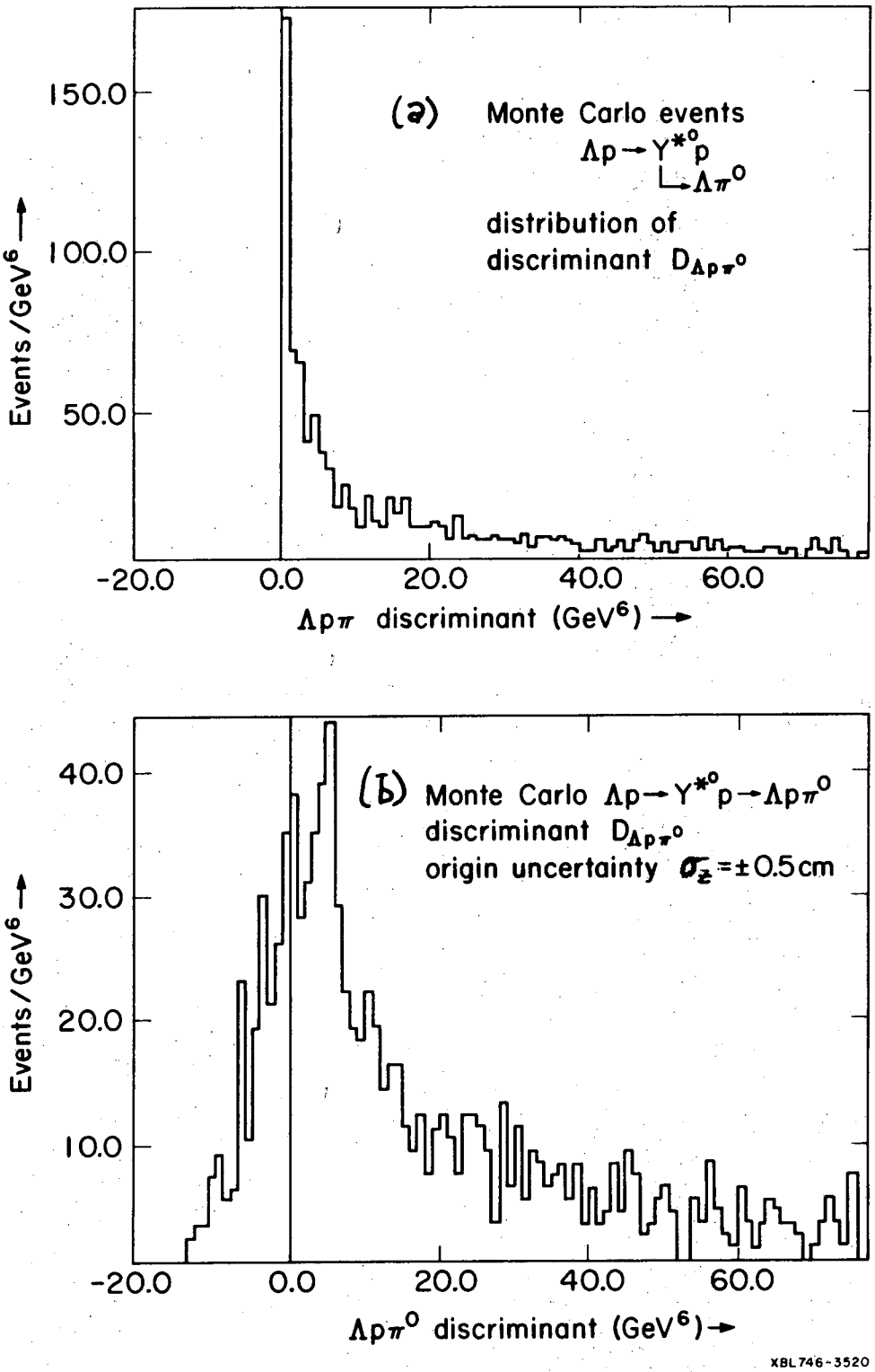


Figure 53. Monte carlo calculation of the discriminant distribution for the process $\Lambda p \rightarrow \Sigma^{o}_{1385} p \rightarrow \Lambda\pi^{o} p$ for (a) no errors, and (b) a mean Gaussian error on the z-coordinate of the $\Lambda$ origin of 0.5 cm.

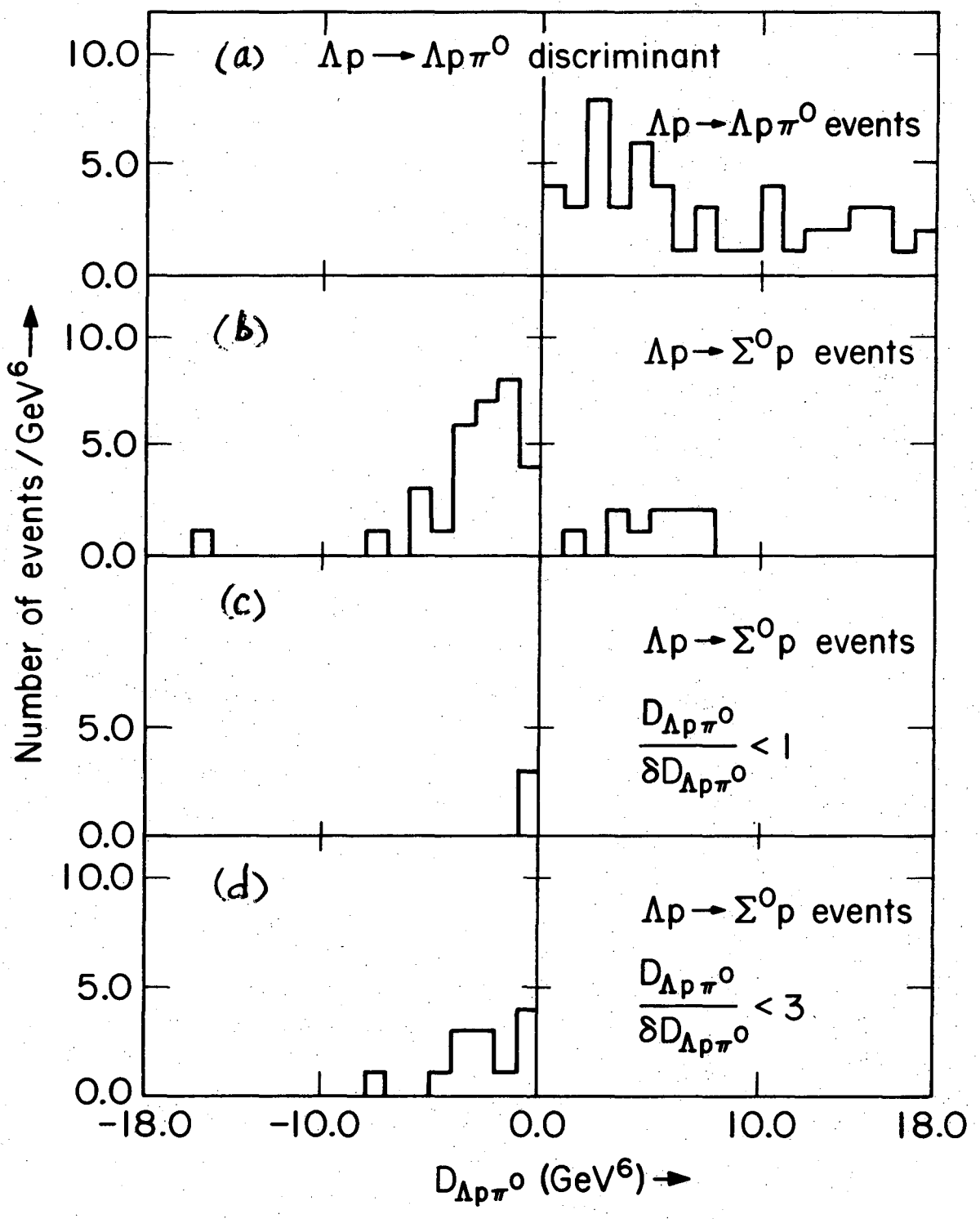


XBL 746-3524

Figure 54. Distribution for the discriminant for the reaction $\Lambda p \rightarrow \Lambda p \pi^0$ for (a) SQUAW identified $\Lambda p \rightarrow \Lambda p \pi^0$; (b) SQUAW unambiguous $\Lambda p \rightarrow \Sigma^0 p$; (c) SQUAW unambiguous $\Lambda p \rightarrow \Sigma^0 p$ within 1 standard deviation of zero discriminant; and (d) same as (c), but within 3 standard deviations.

However, precise assignment is sensitive to the cut on the number of standard deviations,

$$\left( \frac{D_{\Lambda p\pi^o}}{\delta D_{\Lambda p\pi^o}} \right) ,$$

in which the errors could not be accurately calculated from the information stored on the DST.

Monte Carlo examples of $\Lambda p \to \Sigma^o p$ indicate that the $\Lambda p \to \Lambda p\pi^o$ discriminant is large and negative (Fig. 55) $D_{\Lambda p\pi^o} \approx -20\ \text{GeV}^6$; that is, examples of $\Lambda p \to \Sigma^o p$ seem unlikely to fit the $\Lambda p \to \Lambda p\pi^o$ hypothesis.

The maximum value of the $\Lambda p \to \Lambda p\pi^o$ discriminant, irrespective of the origin, Fig. 56, indicates that only 20 out of 45 $\Lambda p \to \Sigma^o p$ events have a maximum $D_{\Lambda p\pi^o}$ which is positive (4 events are off scale). Aside from the small errors on the 3-c $\Lambda$ decay fit and the TVGP reconstruction errors on the recoil proton track, those events in Fig. 56 with $\max \left\{ D_{\Lambda p\pi^o} \right\} < 0$ cannot possibly satisfy the $\Lambda p \to \Lambda p\pi^o$ hypothesis. The one-constraint chi-squared distribution for these unambiguous $\Lambda p \to \Sigma^o p$ events in Fig. 57a is not normal. A remeasurement of these 45 events gave the following results:

(a) 12 percent do not fit the $\Lambda p \to \Sigma^o p$ hypothesis upon remeasurement;

(b) 18 percent have a one-constraint chi-squared exceeding 5.0 on both measurements:

(c) 11 percent have a $\Lambda p\pi^o$ discriminant within 1 standard deviation of $D_{\Lambda p\pi^o} = 0$;

(d) 11 percent fit a 4c or 6c $\Lambda p \to \Lambda p$ hypothesis; and

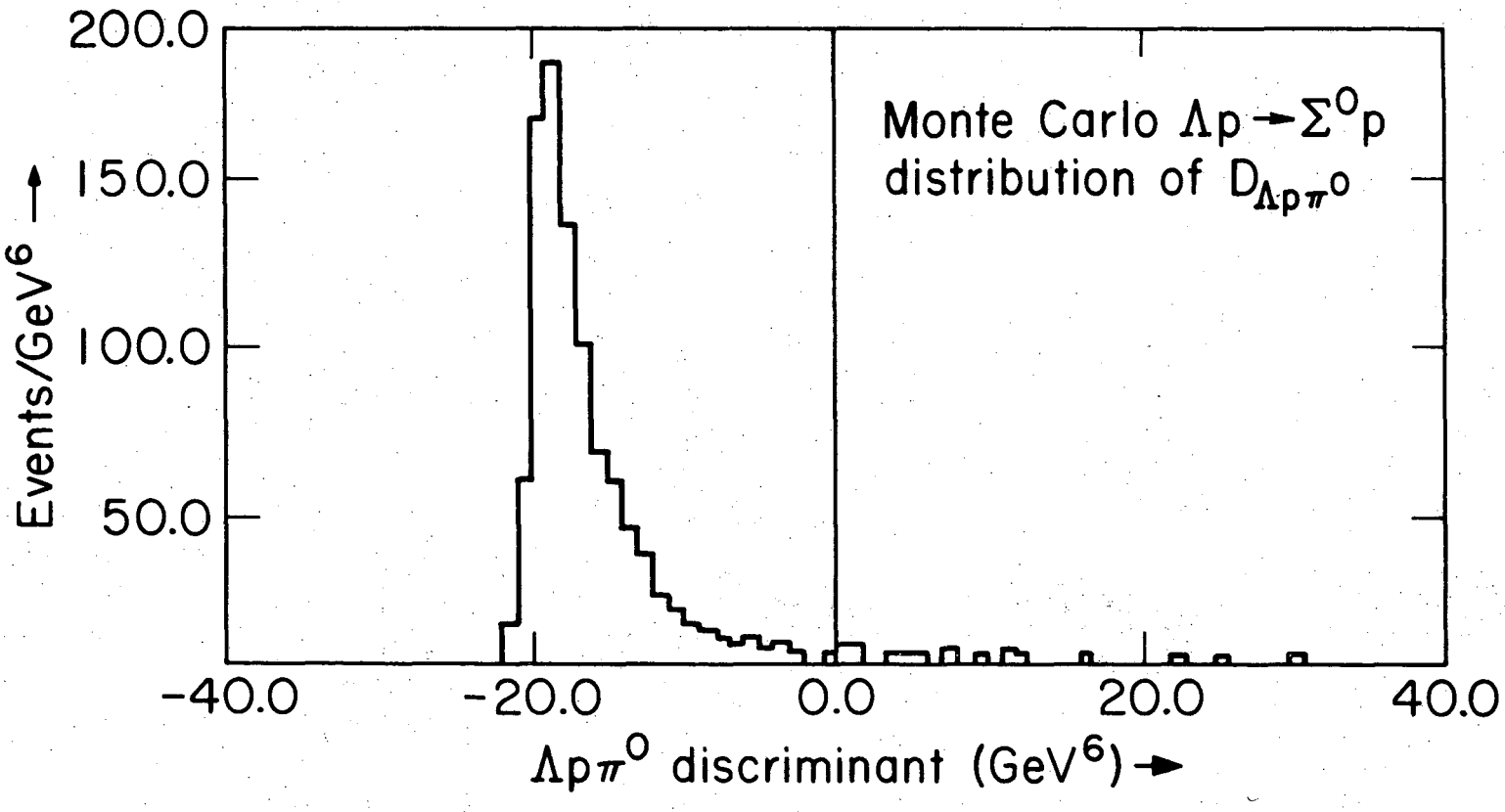


Figure 55. Distribution of the discriminant for monte carlo $\Lambda p \rightarrow \Sigma^0 p$ events.

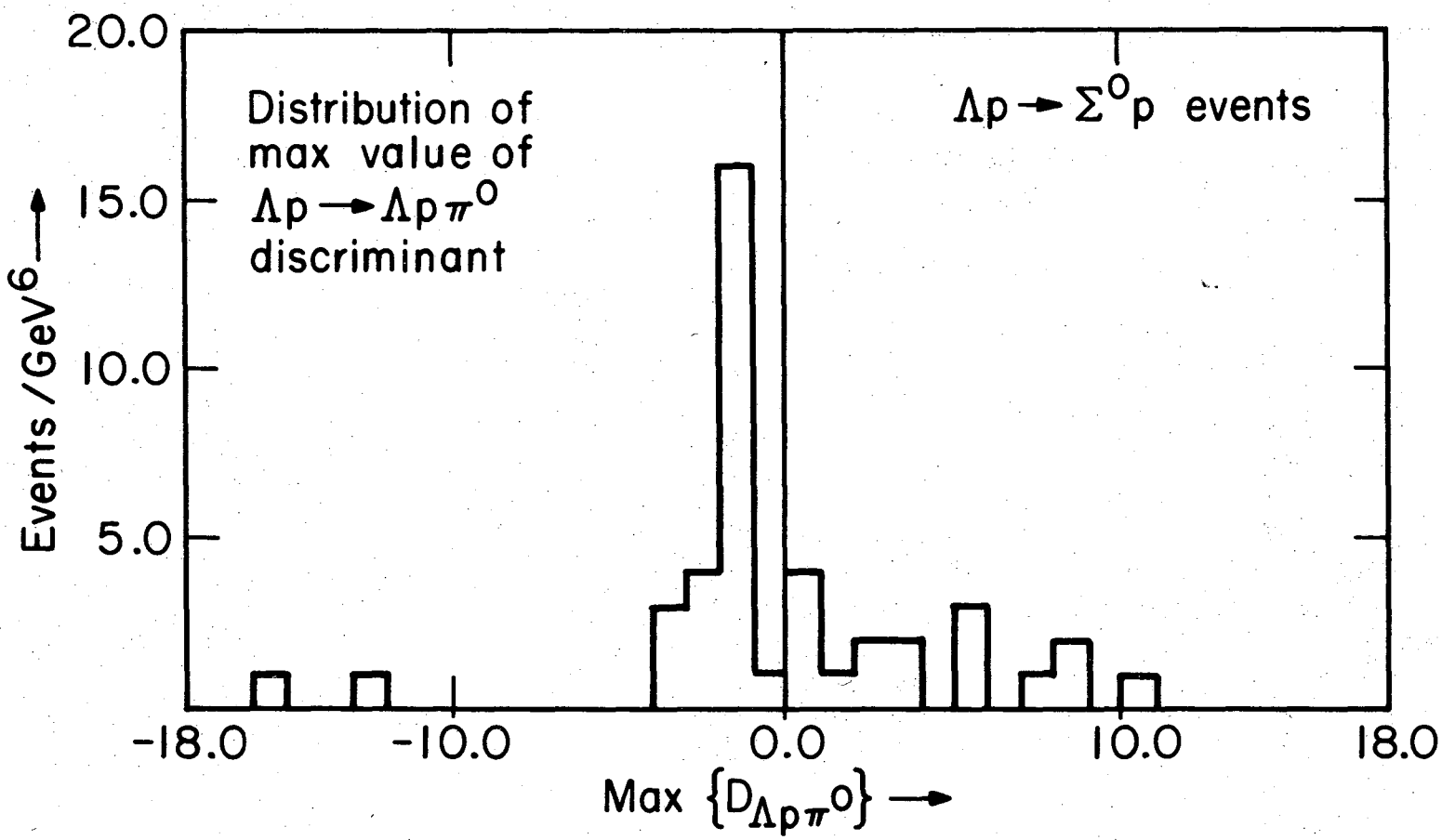


Figure 56. Maximum possible value of the $\Lambda p \rightarrow \Lambda p \pi^o$ discriminant for SQUAW unambiguous $\Lambda p \rightarrow \Sigma^o p$ events.

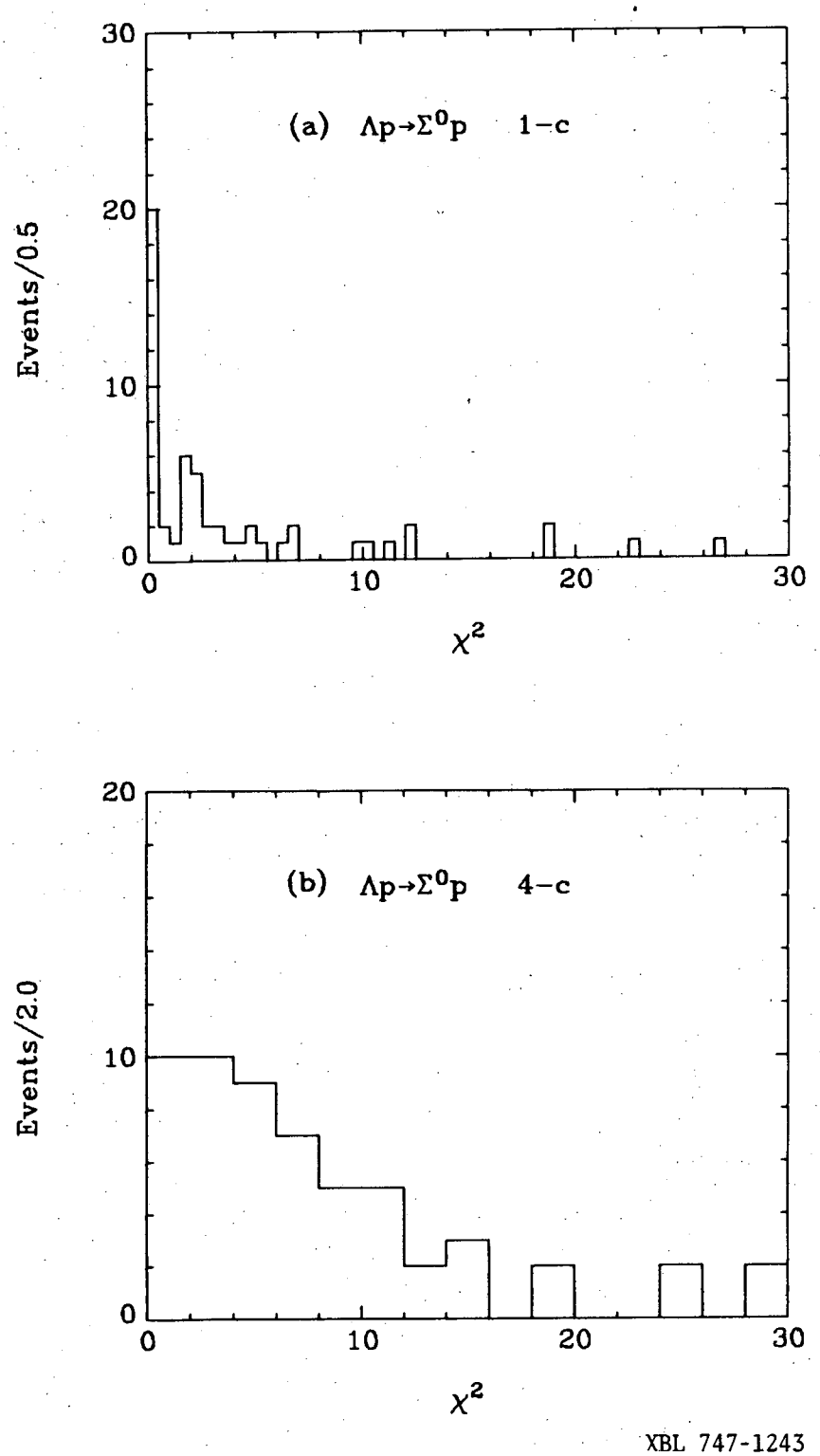


Figure 57. (a) the 1c/2v chi-squared distribution for the reaction hypothesis $\Lambda p \rightarrow \Sigma^0 p$; (b) the 4c/3v chi-squared.

(e) 56 percent are reproducible as unambiguous $\Lambda p \to \Sigma^o p$ events. (a) through (d) add up to more than 51 percent because some events fell into more than one category. By rejecting events in (b)-(d) and accepting events in (a) and (e), we are led to the cross section for $\Lambda p \to \Sigma^o p$ in Fig. 58. The t' distribution for this process in given in Fig. 59. Also plotted is the cross section expected from $\Sigma^- p \to \Lambda n$ data using SU(2) and detailed balance. The analysis of these events is still uncertain.

The present kinematic fitting program SQUAW used mass, inverse momentum, azimuth, and dip angles in the constraint equations. It may be that another set, such as energy and three cartesian components of momentum, are more appropriate[54] in a kinematic fit to the reaction $\Lambda p \to \Sigma^o p$. The low momentum photon in the $\Sigma^o \to \Lambda\gamma$ decay may strongly distort chi-squared space if inverse momentum appears as one of the constraint equations.

The discriminant distribution for all SQUAW fits to $\Lambda p \to \Lambda n\pi^+$ in Fig. 60 displays a preference for $D_{\Lambda n\pi^+} \approx 0$. A possible approach to the resolution of the cross sections for reactions 62b,c might proceed along the following lines:

(a) the discriminant probability distribution may be calculated in the monte carlo sense with realistic measurement errors;

(b) the y-position of the interaction in the bubble chamber gives, from the results of Sec. III, the relative probability that this event was induced by a $\Lambda$ or $\overline{K}^o$;

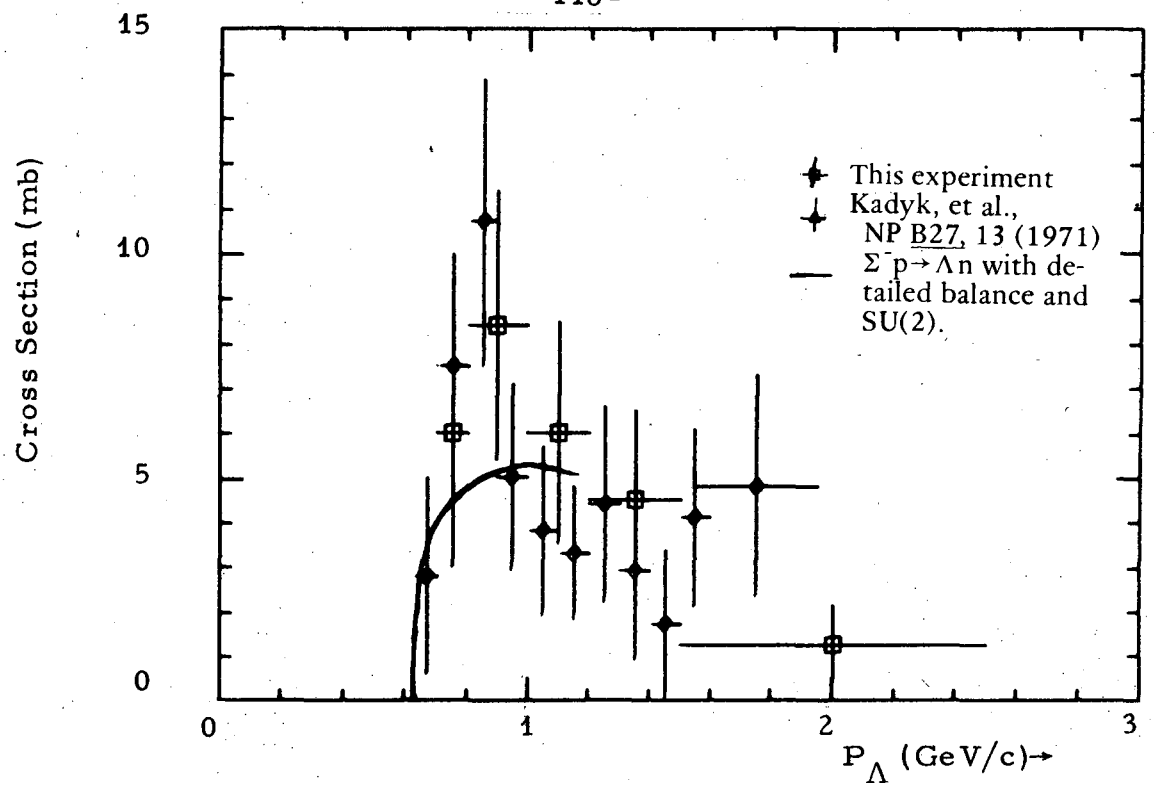


Figure 58. The cross section for the reaction $\Lambda p \to \Sigma^o p$.

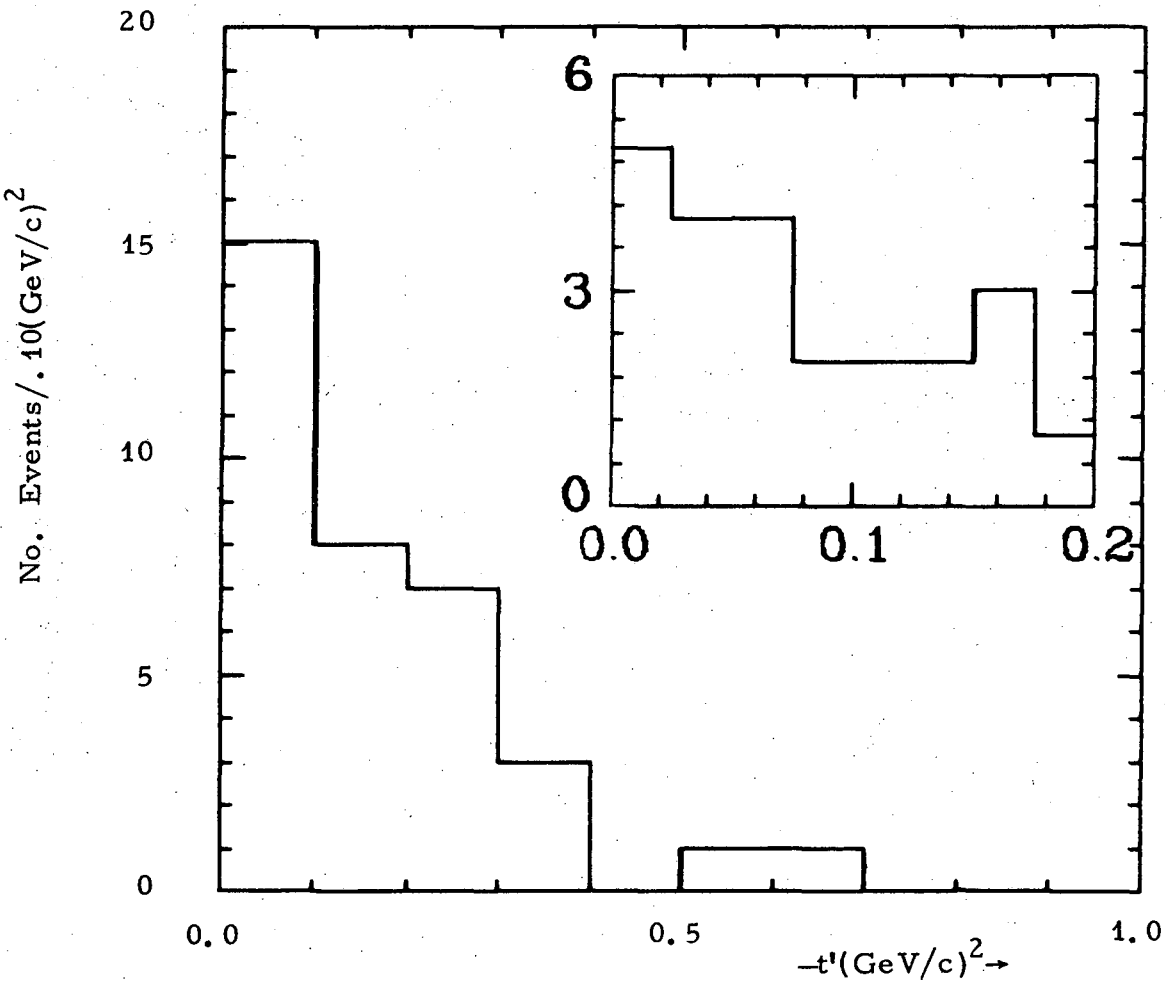


Figure 59. The momentum transfer squared distribution for the reaction $\Lambda p \to \Sigma^o p$.

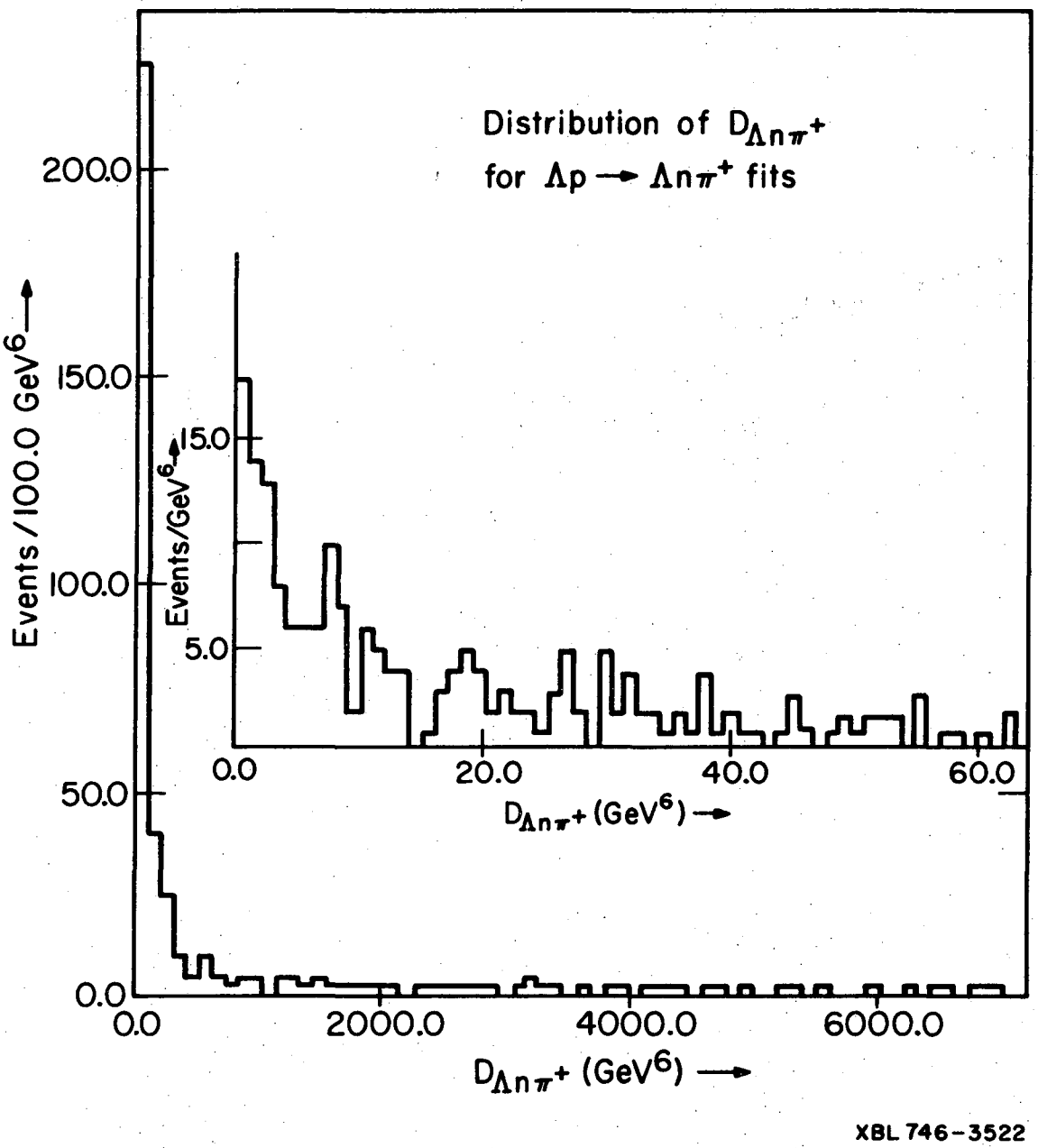


Figure 60. Discriminant distribution for SQUAW fits to the reaction $\Lambda p \rightarrow \Lambda n\pi^+$.

(c) a parameter $\rho$ may be defined as

$$\rho = \frac{t}{t_{max}} , \quad 0 \leq \rho \leq 1 , \tag{64}$$

where for a given reaction hypothesis $t$ is the momentum transfer squared between the incoming and outgoing strange particle, and $t_{max}$ is the maximum allowed

$$t_{max} = \sum_i m_i^2 - s . \tag{65}$$

Then $\rho$ might separate events like $\bar{K}^o \to \Lambda$ ($\rho \approx 1$) from $\Lambda \to \Lambda$ and $\bar{K}^o \to \bar{K}^o$ ($\rho \approx 0$).

(d) the SU(2) constraint that (Appendix VII)

$$| \langle \Lambda n \pi^+ | \Lambda p \rangle |^2 = 2 \quad | \langle \Lambda p \pi^o | \Lambda p \rangle |^2$$

holds also for the differential cross section, and is, for example, a relatively strong handle on the $\pi$ momentum spectrum from these reactions. Since the backgrounds for these reactions differ essentially due to partial ionization identification of the recoil positive track, this constraint may be helpful in estimating the background level.

In the above four points, (a) and (c) require dynamical assumptions for their use. One may, however, allow the constraints on these to be so loose that the assumptions are valid and at the same time useful. Thus, one might say in (a) that the probability of a reaction hypothesis is unity if

$$\text{Discriminant} \leq 100.0 \text{ GeV}^6$$

and small $\approx 0.1$ if

$$\text{Discriminant} > 100.0 \text{ GeV}^6 .$$

In (b), one might assign probability unity if the reaction is peripheral, and a small probability $\approx 0.1$ if non-peripheral.

Point (b) is straightforward, and a precise probability may be assigned. In (d), a probability may be assigned in a fit to $\Lambda p \rightarrow \Lambda p \pi^o$ on the basis of the $\pi^o$ momentum in relation to the $\pi^+$ spectrum of unambiguous $\Lambda p \rightarrow \Lambda n \pi^+$ fits. Conversely, the neutron in $\Lambda p \rightarrow \Lambda n \pi^+$ must have the same spectrum as the proton in $\Lambda p \rightarrow \Lambda p \pi^o$, which is directly measured in the chamber. When an improved sample of these reactions has been obtained, the probability distributions of (a) and (c) may be recalculated, and the whole process iterated. This analysis has not been completed.

## Section VI. Review of Lambda-Proton and Nucleon-Nucleon Cross Sections

Compilations of hyperon-nucleon cross sections have been published by two groups; Alexander et al.[59] in 1969, and by the Particle Data Group at Lawrence Berkeley Laboratory[60] in 1970. We present in this section Λp, np, and pp cross sections from 0.1 to 20 GeV/c, excluding primarily those data points with very large errors, and consequently little information content.

Below 500 MeV/c the Λp, pp, and np reactions are elastic; Fig. 61 displays these three total cross sections from 100 to 700 MeV/c. The pp total cross section is strongly suppressed by Coulomb repulsion, and at zero momentum, the total pp and np cross sections approach 4.0 b and 20.3 b, respectively. The Λp cross section approaches roughly that value given by the singlet and triplet s-wave scattering lengths determined from scattering data in the 100-300 MeV/c range, $\sigma_T = \pi a_s^2 + 3\pi a_t^2 = 320$ mb.

The total and elastic cross sections as measured in the present experiment are shown in Fig. 62, while the total cross-section measurement of Ref. 6 is displayed in Fig. 63. All of the above data is displayed in Fig. 64, in which it is apparent that the high momentum Λp interaction is quite similar to the np interaction, while the low momentum behavior is considerably different in magnitude, if not momentum dependence. The same plot as above, but with our data averaged over $0.4 \leq P_\Lambda \leq 1.2$, is displayed in Fig. 65.

The very high momentum Λp cross section is of particular comparative interest to the pp cross section from the point of view of a simple additive quark model. If all the quark-quark amplitudes are additive[61],

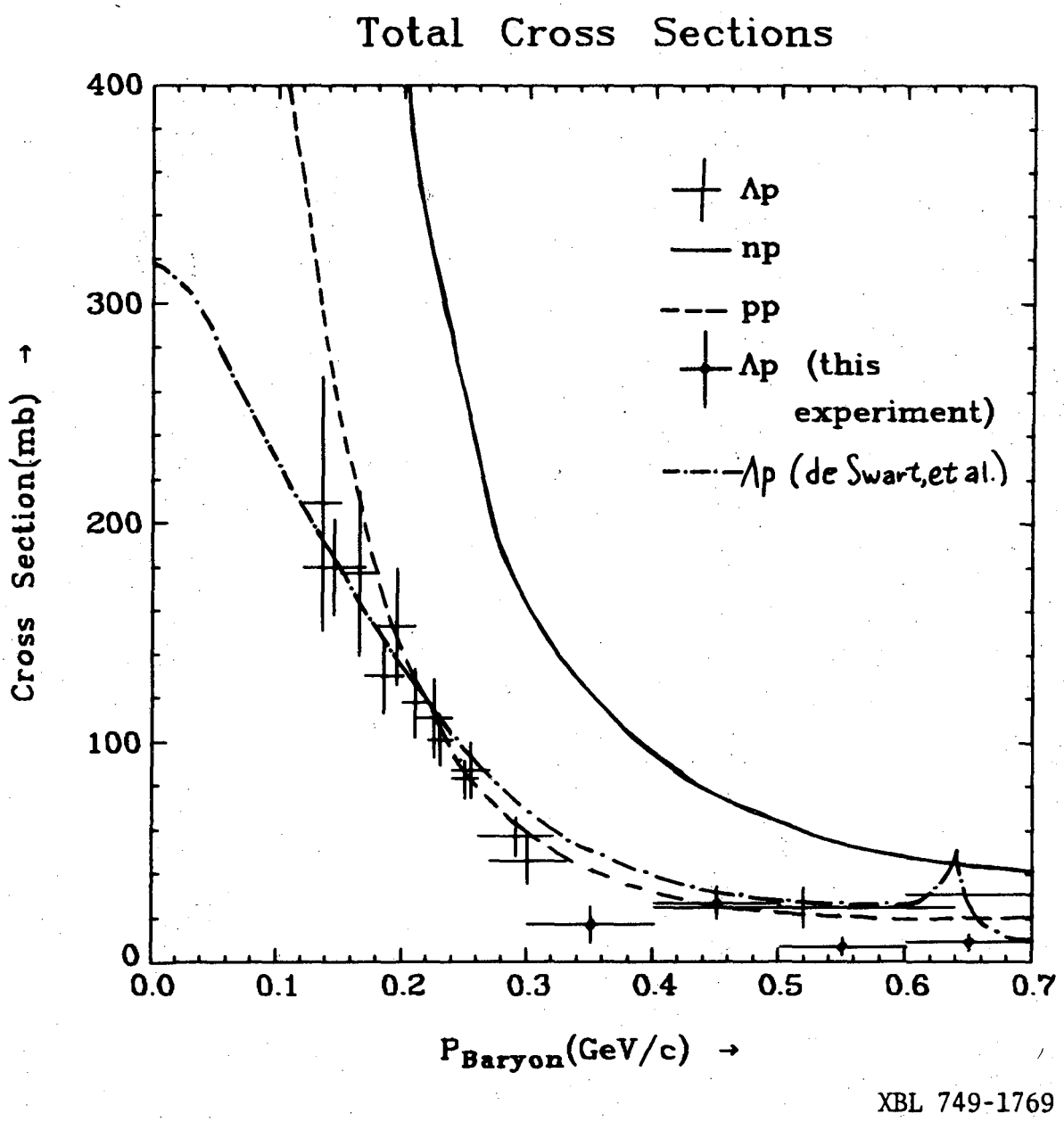


Figure 61. Baryon-baryon total cross sections from 0.0 to 0.7 GeV/c.

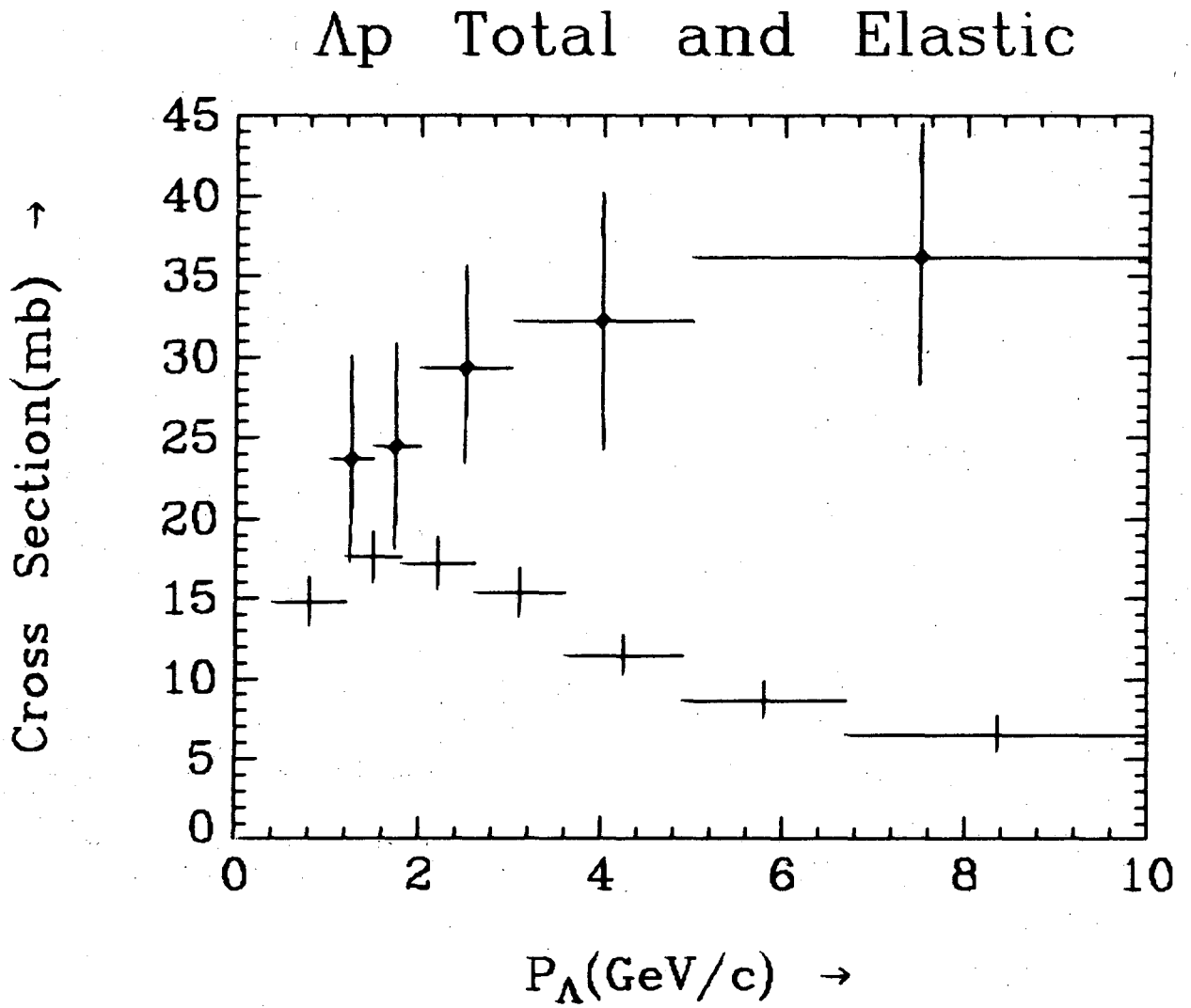


Figure 62. The total and elastic Λp cross sections as measured in this experiment.

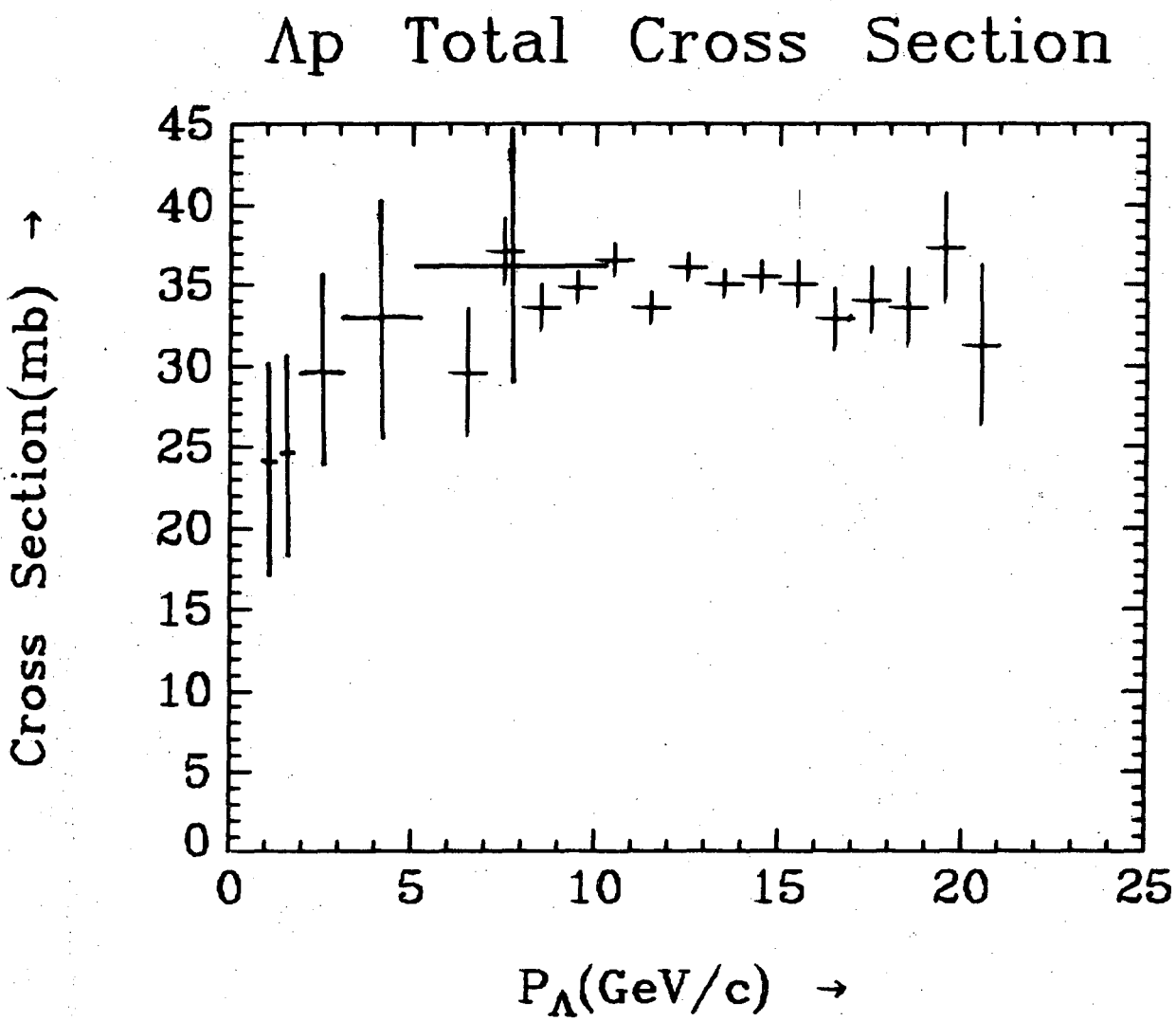


Figure 63. The total cross section measurement of Ref. 6.

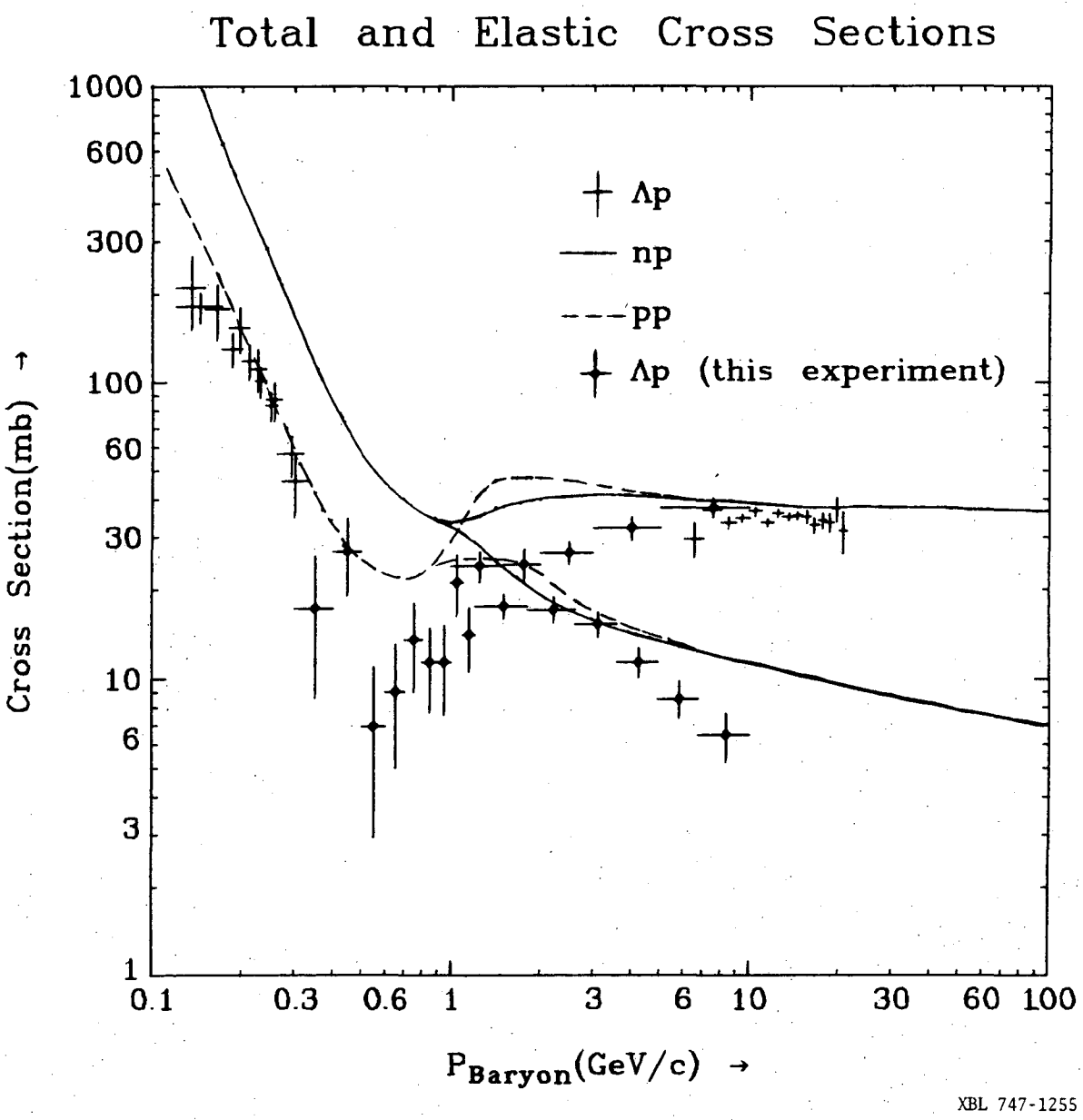


Figure 64. Baryon-baryon total and elastic cross sections. Only the data from this experiment is shown in the intermediate momentum range from 0.4 to 10 GeV/c.

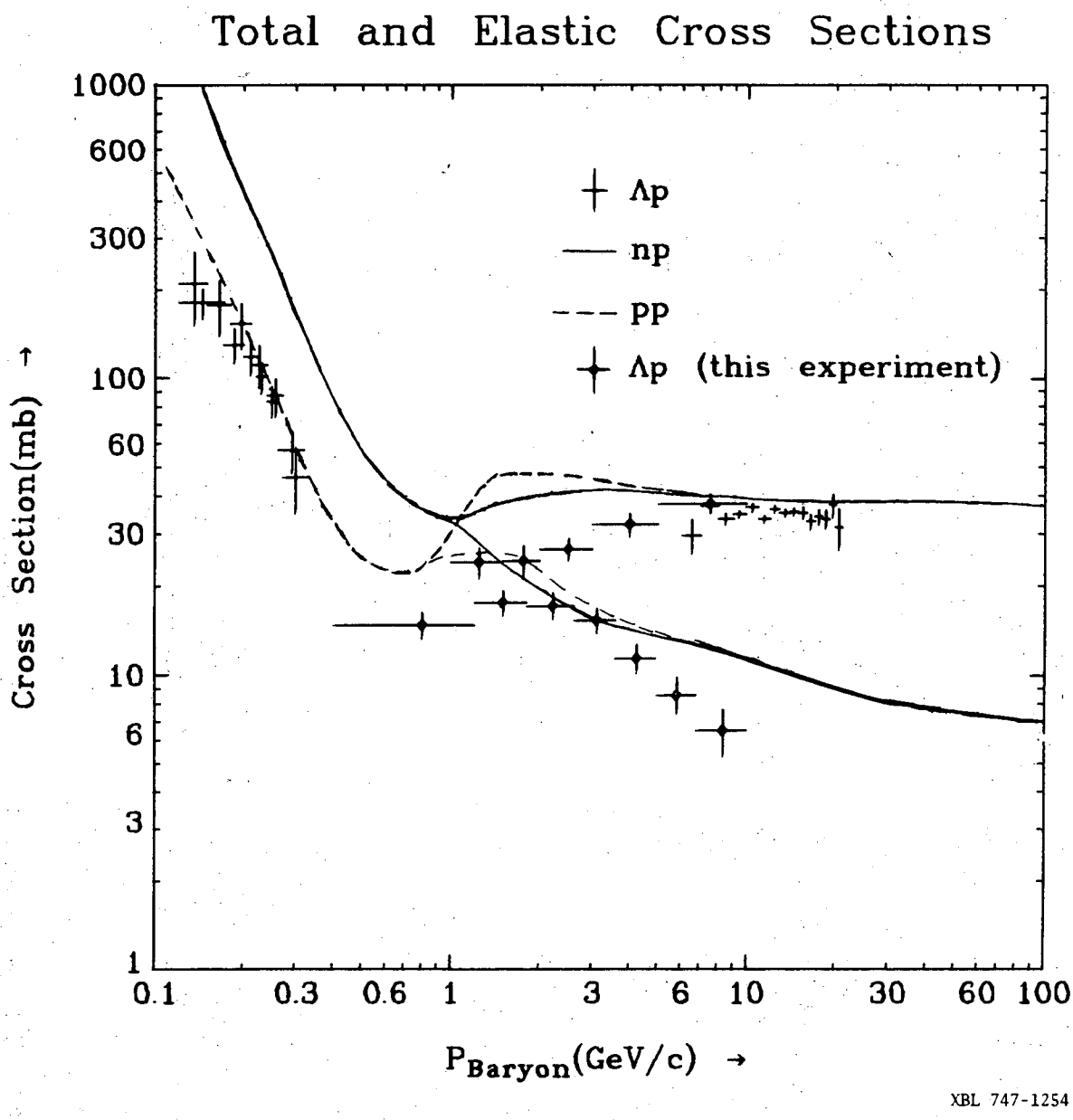


Figure 65. Same as Figure 64, except that the data from 0.4 to 1.2 GeV/c has been averaged.

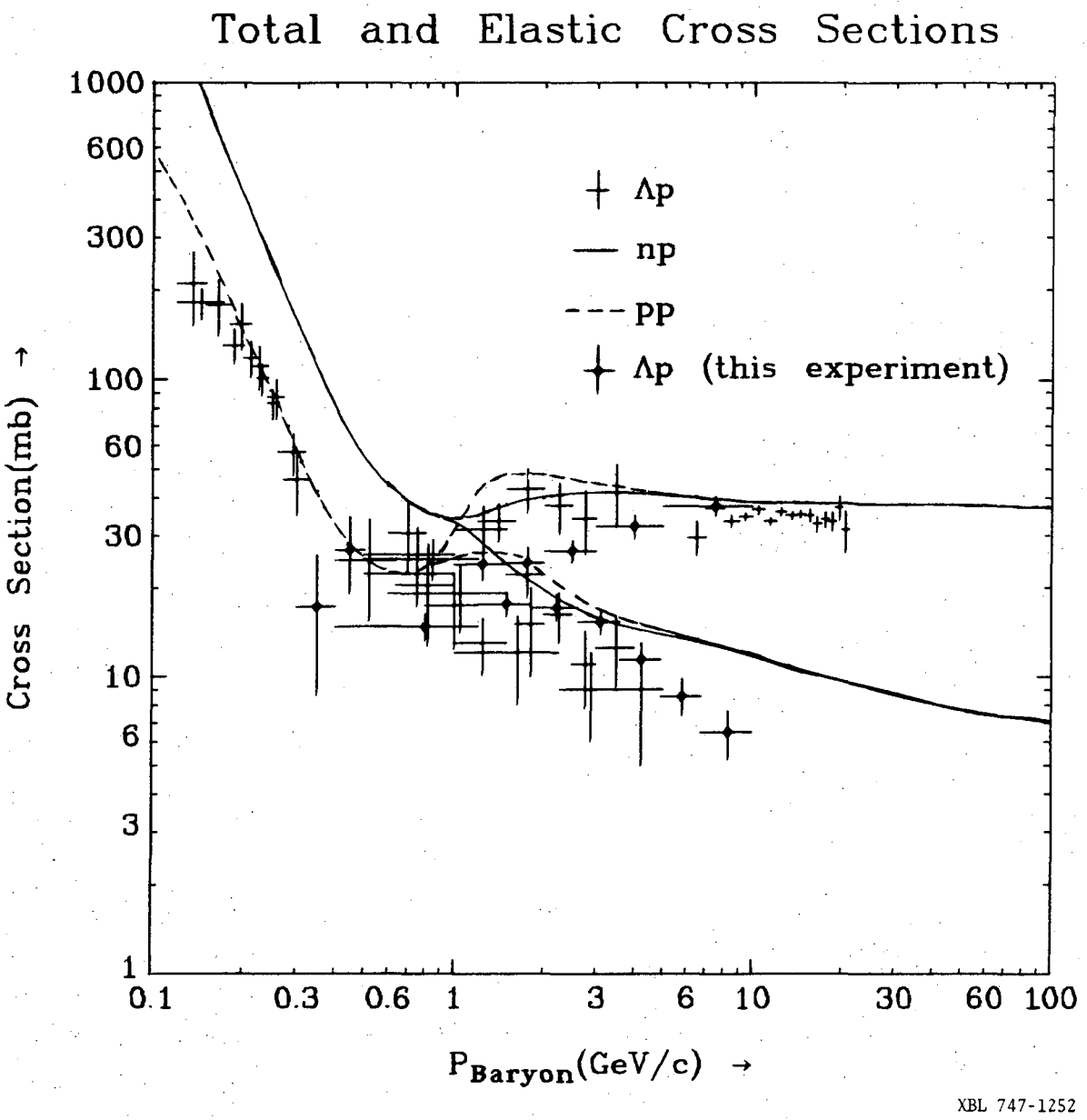


Figure 66. All the available Λp data from this experiment, Ref. 6, and Ref. 60.

then one may state that (Appendix VII)

$$\sigma_T(\Lambda p) = \sigma_T(pp) + \sigma_T(K^- n) - \sigma_T(\pi^+ p) \ , \tag{66}$$

that is, the difference between the $\Lambda p$ and pp total cross sections is just that difference due to the single strange quark, which is exhibited in the difference between $K^- n$ and $\pi^+ p$ total cross sections. This relationship is satisfied very well by the data of Gjesdal et al., whose total cross section is consistent with a constant value of

$$\sigma_T = 34.6 \pm 0.41 \text{ mb} \tag{67}$$

over their entire momentum range from 6.0 to 20.0 GeV/c. The quark result is

$$\sigma_T = 35.2 \pm 0.6 \text{ mb}, \tag{68}$$

and is also nearly independent of momentum in this range. This relation is difficult to test at lower momenta, essentially because there is no prescription to account for mass difference effects among the reactions.

Kaiser[62] has developed many group theoretical relationships among hyperon-nucleon and nucleon-nucleon scattering cross sections. All of his relationships involving incident $\Lambda$ hyperons are the following:

$$2\left\{ |\langle \Lambda p|\Lambda p\rangle|^2 + |\langle \Sigma^o p|\Lambda p\rangle|^2 + |\langle \Sigma^+ n|\Lambda p\rangle|^2 \right\} \geq |\langle np|np\rangle|^2 \tag{69a}$$

$$2\left\{ |\langle \Sigma^o_{1385} p|\Lambda p\rangle|^2 + |\langle \Sigma^+ \Delta^o\rangle|^2 \right\} \geq |\langle \Delta^o p|np\rangle|^2 = |\langle \Delta^+ p|pp\rangle|^2 \tag{69b}$$

$$2\left\{ |\langle \Sigma^o_{1385} \Delta^+|\Lambda p\rangle|^2 + |\langle \Sigma^+_{1385} \Delta^o|\Lambda p\rangle|^2 \right\} \geq |\langle \Delta^o \Delta^+|np\rangle|^2 \tag{69c}$$

$$2\left\{ |\langle \Sigma^- p\pi^+|\Lambda p\rangle|^2 + |\langle \Sigma^- \Sigma^+ K^+|\Lambda p\rangle|^2 + |\langle \Xi^- p K^+|\Lambda p\rangle|^2 \right\} \geq |\langle \Sigma^- p K^+|np\rangle|^2$$

In addition, there are two SU(2) relationships:

$$|\langle \Sigma^+_{1385} n|\Lambda p\rangle|^2 = 2\,|\langle \Sigma^o_{1385} p\ \Lambda p\rangle|^2 \tag{70a}$$

$$2\,|\langle \Sigma^o p|\Lambda p\rangle|^2 = |\langle \Sigma^+ n|\Lambda p\rangle|^2 \tag{70b}$$

Thus relation (69a) can be simplified using (70b).

These relationships are, in fact, not very useful, as Kaiser has noted. Relations (69) assume the form of inequalities fundamentally because the physical $\Lambda^o$ state is not a pure U-spin state, as are the neutron and proton states. Furthermore, the cross sections in relations (69) are very difficult, or impossible, to measure; for example, (69a) contains the reaction $\Lambda p \to \Sigma^o p$ discussed above in Sec. V, and whose cross section is in doubt; relation (69b) contains the reactions $\Lambda p \to \Lambda p \pi^o$ and $\Lambda p \to \Lambda n \pi^+$, both of which are zero-constraint and highly ambiguous with other reaction hypotheses (Sec. V); and relation (69c) contains the reaction $\Lambda p \to \Lambda p \pi^o \pi^o$, which is unfittable in this experiment. Only relation (69d) is straightforwardly satisfied, since

$$2\sigma(\Lambda p \to \Sigma^- p \pi^+) \approx 6.0 \pm 1.0 \text{ mb}$$

at 3.0 GeV/c, which is greater than

$$\sigma(np \to \Sigma^- p K^+) \cong 0.025 \pm 0.005 \text{ mb}$$

also at 3.0 GeV/c, without reference to the reactions $\Lambda p \to \Sigma^- \Sigma^+ K^+$ and $\Lambda p \to \Xi^- p K^+$.

We will attempt to present measurements of amplitudes in U-spin space based upon neutron-proton and lambda-proton cross section measurements. With reference to Appendix VII, the elastic $\Lambda p$ scattering amplitude can be written

$$A(\Lambda p) = \frac{\langle \Lambda p | \Lambda p \rangle \hbar c}{4\pi \sqrt{s}} \qquad (70a)$$

$$= \frac{\hbar c}{4\pi\sqrt{s}} \left[ \frac{1}{2} a_{3/2} + a_{1/2} \right]$$

where $a_{3/2}$ and $a_{1/2}$ are the matrix elements for scattering in total

U-spin states U = 3/2 and U = 1/2, respectively. Similarly, the np amplitude is

$$A(np) = \frac{\hbar c}{4\pi\sqrt{s}} [a_{3/2}] \ . \qquad (70b)$$

Employing the optical theorem,

$$\sigma_T(s) = \frac{4\pi}{k} \hbar c \ \mathrm{Im}\ f(s,0)$$

we have

$$\mathrm{Im}\ a_{1/2}\Big|_{t=0} = \frac{k\sqrt{s}}{2(\hbar c)^2} [2\sigma_T(\Lambda p) - \sigma_T(np)] \ . \qquad (71a)$$

Trivially, from 70b, we also have

$$\mathrm{Im}\ a_{3/2}\Big|_{t=0} = \frac{k\sqrt{s}}{2(\hbar c)^2} [\sigma_T(np)] \ . \qquad (71b)$$

These quantities are shown in Fig. 67.

This thesis concludes at this point, probably leaving behind many unfinished analyses of this data, however imprecise it may be by comparison to the data of other particle interactions. Although only a few quantitative tests of SU(3) symmetry have been made, and the elastic polarization and real part of the forward elastic amplitude are too poorly determined for precise comparison, we are gratified that these lambda-proton reactions we have studied are approximately consistent with SU(3). This of course does not rule out consistency with other descriptions. In particular, the Regge-pole model of Kubis and Walters[36] has calculated lambda-proton cross sections based upon the nucleon-nucleon Regge parameters determined by Rarita, et al.,[64] and SU(3) symmetric coupling constants. Our data is in accord with their published differential elastic

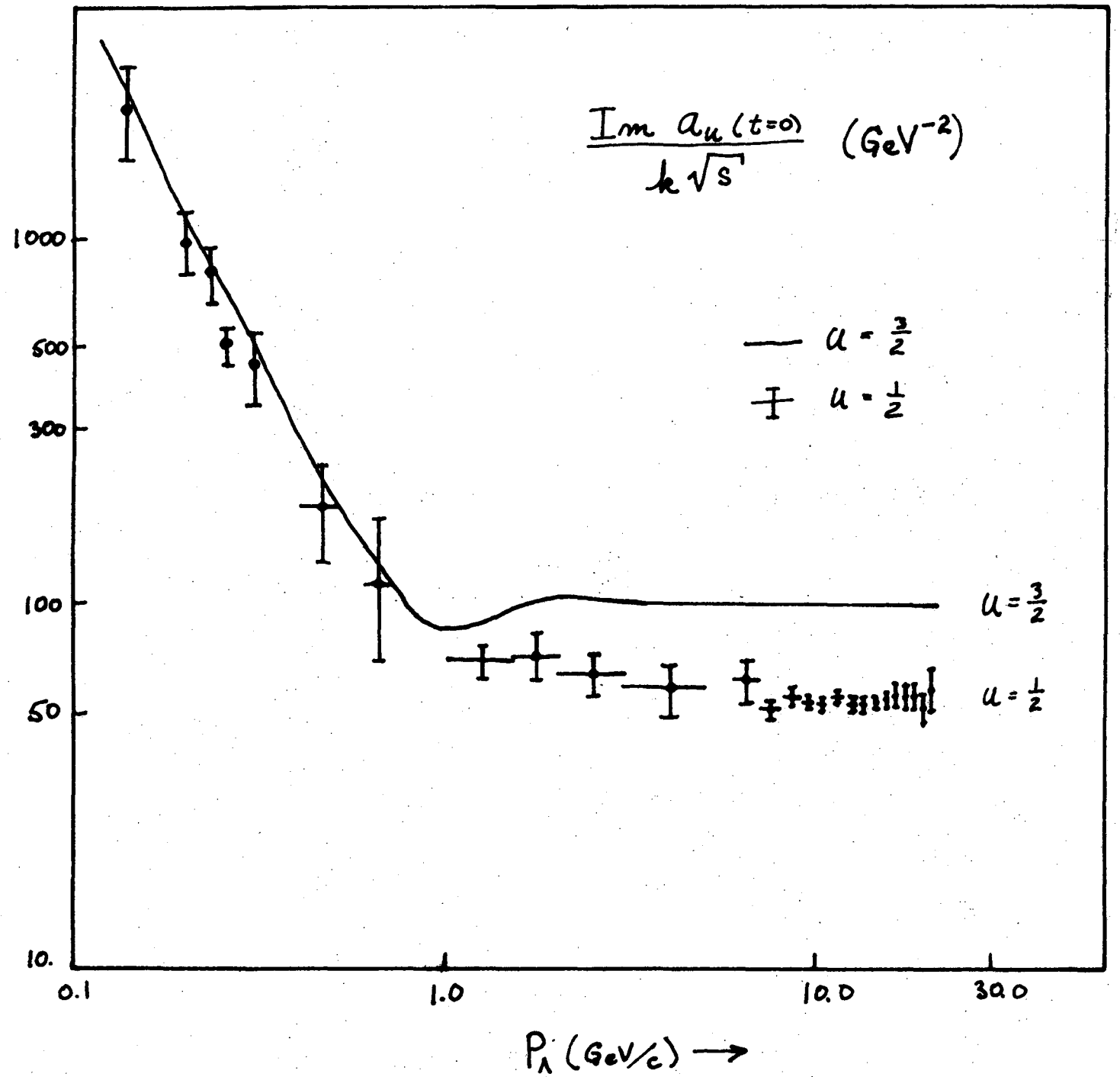


Figure 67. The imaginary part of the forward U-spin amplitudes in $\Lambda p$ and np scattering, U = 3/2 and U = 1/2.

cross section at $P_\Lambda$ = 7.0 GeV/c, and their integrated elastic cross section from 3.0 to 10.0 GeV/c. Our data does not agree with their total cross section in the 3.0 to 5.0 GeV/c region, however.

Further study of the $\Lambda p$ interaction is warranted, we feel, not so much in the very high momentum regime, but in the transition region from below the first inelastic threshold up to about 4 GeV/c where most of the inelastic channels have already set in. A precise comparison of the $\Lambda p$ and np reactions in this region may reveal features of particle exchanges not obtainable in other reactions, since the $\Lambda$ is an isospin singlet particle, the only singlet (aside from the $\Omega^-$) available for direct scattering experiments.

INTRODUCTION

1. Wells, and Tuve, et al. Phys. Rev. 50, 806 (1936).

2. Amaldi, Fermi, Phys. Rev. 50, 899 (1936).

3. Richard Wilson, The Nucleon-Nucleon Interaction; Experimental and Phenomenological Aspects, Wiley (1962).
Review of Modern Physics, 39, 1967. Eds. A.E.S. Green, M. H. MacGregor and R. Wilson.

4. See, for example, Hamilton, High Energy Physics, Vol. I, Academic Press (1967).

5. M. Gell-Mann, California Institute of Technology Synchroton Laboratory Report CSTL-20 (unpublished).
M. Gell-Mann and Y. Ne'eman, The Eightfold Way, New York, Benjamin, 1964.
M. Gell-Mann, Nucl. Phys. Rev. 125, 1067 (1962).
Y. Ne'eman, Nucl. Phys. 26, 222 (1961).

6. Gjesdal, et al., Phys. Lett. 40B, 152 (1972).

7. Badier, et al., Phys. Lett. 41B, 387 (1972).

8. Rochester and Butler, Nature. 160, 855 (1947).

9. Alexander, et al. Phys. Rev. Lett. 7, 348 (1961).

10. Groves, Phys. Rev. 129, 1372 (1963).

11. Piekenbrock, Oppenheimer, Phys. Rev. Lett. 12, 625 (1964).

12. Sechi-Zorn, et al. Phys. Rev. Lett. 13, 282 (1964).

13. Alexander, et al. Phys. Rev. Lett. 13, 484 (1964).

14. Alexander, et al. Phys. Rev. 173, 1452 (1968); see also the review paper Nucl. Phys. B10, 554 (1969).

15. Sechi-Zorn, et al. Phys. Rev. 175, 1735 (1968).

16. See, for example, Proceedings of the International Conference on Hypernuclear Physics, Vols. I and II, Argonne National Laboratory, May 5-7, 1969.

17. Crawford, et al., Phys. Rev. Lett. 2, 174 (1959).

18. Arbuzov, et al., Journ. Exper. Theor. Phys. 15, 676 (1962).

19. Beilliere, et al., Phys. Lett. 12, 350 (1964).

20. Vishnevskii, et al., Soviet Jour. Nucl. Physics 3, 511 (1966).

21. Bassano, et al., Phys. Rev. 160, 1239 (1967).

22. Cline, et al., Phys. Lett. 25B, 446 (1967).

23. Charlton, et al., Phys. Lett. 32B, 720 (1970).

24. Kadyk, et al., Nucl. Phys. B27, 13 (1971).

25a. de Swart and Dullemond, Ann. Phys. 16, 263 (1961).

25b. Nagels, Rijken, and de Swart, Ann. Phys. 79, 338 (1973).

SECTION I

26. Designed by J. J. Murray and S. Flatté.

27. W. Pope and J. Carrieri, Lawrence Berkeley Laboratory, Mechanical Engineering, Drawing No. 14D9853.

28. See, for example, Aderholz et al., Nuclear Physics B5, 606 (1968); Sisterson et al., Nuclear Physics B6, 205 (1968).

29. Experiment 30 Scanning Instructions, Trilling-Goldhaber Internal Note, TN-167 (1970).

30. J. A. Kadyk et al., Nuclear Physics B27, 13 (1971). Scanning instructions are Trilling-Goldhaber Internal Notes TN-150, 153, and 163.

31. Experiment 30 Measuring Instructions, Trilling-Goldhaber Internal Note TN-171.

32. Experiment 30 Post-scan Instructions, Trilling-Goldhaber Internal Note TN-177.

33. Pre-scan Instructions for Experiment 30, Trilling-Goldhaber Internal Notes TN-169.

34. In fact, all solutions found by SQUAW are stored on the DST, but those not accepted at the scan table are given a negative mark (or reaction) number, and are not used in the analysis. Such a complete DST allows a more thorough analysis of kinematic ambiguities between reactions.

SECTION II

35. Arnold and Logan, Phys. Rev. 177, 2318 (1969).

36. Kubis and Walters, Nucl. Phys. B17, 547 (1970).

37. Orear, Notes on Statistics for Physicists, UCRL-8417, Aug. 13, 1958.

SECTION III

38. Event type 7 is a $V^o$ decay topology with no visible origin in the liquid hydrogen, that is, apparently produced in the platinum plate. (Experiment 30 Scanning Instructions, Trilling/Goldhaber Internal Technical Note, N-167).

39. A detailed discussion of scanning efficiencies in this experiment is given in Appendix II.

40. We have taken the fiducial volume, FID3, to be defined by

$$\begin{aligned} -20. &\leq x(cm) \leq +20. \\ -76. &\leq y(cm) \leq -66. \\ +3. &\leq z(cm) \leq +34. \end{aligned}$$

41. Ken M. Case, Phys. Rev. 103, 1449 (1956).

42. M. L. Good, Phys. Rev. 106, 591 (1957).

43. Flaminio, et al., CERN/HERA 70-6, October 1970.

SECTION IV

44. Hagedorn, Relativistic Kinematics, pp. 80-97, Benjamin, 1963. A short description of this calculation is given in Appendix IV of this thesis.

45. J. K. Kim, Phys. Rev. Lett. 19, 1079 (1967).

46. S. Coletti, et al., Nuovo Cimento 49, 479 (1967).

47. S. Nilsson, The Nucleon-Nucleon Interaction at High Energies, in Methods in Subnuclear Physics, Vol. IV, Part 1 (Strong Interactions), Gordon and Breach Science Publishers, 1970.

48. G. Alexander, et al., Phys. Rev. 154, 1284 (1967).

49. A. P. Gasparyan, et al., Soviet Journal of Nuclear Physics 14, 429 (1972).

50. Quoted cross sections by different authors at the lower end of this momentum spectrum do not agree. We have taken some average of these cross sections as the particular representation given here.

51. Gursey, Pais, Radicati, Phys. Rev. Lett. 13, 299 (1964).

52. Martin, Wali, Nuovo Cimento 31, 1324 (1964).

53. O. Benary, et al., ibid, pg. 153.

SECTION V

54. Orin Dahl, private communication.

55. Alvarez Programming Note P-126, Dahl, Day, Solmitz, Gould, pg. 46 (1968).

56. We consider the 3-c $\Lambda \rightarrow p\pi^-$ vertex fit to constitute the measurement of an outgoing track from the interaction vertex. We suppress reference to these three constraints and do not count the $\Lambda$ decay vertex. Hence, $\Lambda p \rightarrow \Sigma^o p$ we call 1c/2v, not 4c/3v.

57. The incident $\Lambda$ momentum was 2.5 GeV/c, and the center of mass t-distribution was taken to be $e^{3t}$.

58. Program PHONY, Trilling-Goldhaber Technical Note TN-143, E. R. Burns, et al., April 1968.

SECTION VI

59. Alexander et al., Nucl. Phys. B10, 554 (1969).

60. Benary et al., A Compilation of Hyperon-Nucleon Reactions, Particle Data Group, Lawrence Berkeley Laboratory, UCRL-20000 YN (1970).

61. H. J. Lipkin, F. Scheck, Phys. Rev. Lett. 16, 71 (1966); and E. M. Levin, L. L. Frankfurt JETP Lett. 2, 65 (1965).

62. G. D. Kaiser, Nuovo Cimento 52, 458 (1967).

Acknowledgements

I am especially grateful to my family, my grandmother Mrs. Leila Peck, who typed much of this thesis, mother Ila and father Carl, sisters Pam and Monica, and brother Joseph, for their generous understanding of these years in graduate school. Friends through these years, especially Roy, Ruth, Mary, John, and Elaine, added to the already dual pleasures of physics and Berkeley.

The Stanford Linear Accelerator Center and the 82-inch bubble chamber crew are acknowledged for their stable operation during the data taking.

I acknowledge the excellent scanning of the bubble chamber film at all levels by Irene Witowski, and the scanning supervision of Belinda Worthen. Harriet Rice has carefully logged the production computer runs and the several hundred data tapes for this experiment.

This experiment was easy, largely due to the timely advice of then fellow graduate students Dr. James MacNaughton and Dr. Jonathan Chan, who made me aware of the difficulties and problems of massive data reduction before the experiment began.

I thank Dr. John A. Kadyk, who originally proposed the use of a platinum target to enhance $\Lambda$ production in an earlier experiment at the Bevatron, for his assistance in this experiment, and for his careful reading of the manuscript.

Finally, I thank Prof. George H. Trilling for many things, but mainly for his guidance, inspiration, and enthusiasm for and appreciation of physics, which is contageous to all those around him.

This work was supported by the United States Atomic Energy Commission.

APPENDIX I. Data Reduction

Introduction

This note details how, in the lambda-proton experiment, we have dealt with the problem[1] of getting information from the film, through at least three encounters with the scan table, to the selected summary tape with high reliability. We have attempted, first, to reduce the number of separate computer jobs to be submitted, since personnel effort and error is proportional to the number of separate steps requiring personnel interaction; and second never to discard any information about an event, no matter how trivial or even outdated it may be. An event is updated by a new entry, both events are deactivated by a code for the type of update, and a third event image, with all accumulated information, remains active in the master list. In the end, for each event, one can trace the time-history complete with all remarks made, all updates and changes made, and the terminal status of that event.

1. Standard Event Image Format

Each event is described by 50 variables, given below, which are packed into a 16-word event image,[2] the first 8 words, or 80 columns, of which compose a card image completely compatible with COBWEB input. Events are stored on magnetic tape in binary mode, 32 events

---

[1] At the time this experiment began, August 1970, there did not exist a data reduction system in the T-G group employing the teletypes and adequate to cope with the complexity in this type of experiment. See Trilling/Goldhaber Internal Notes TN-160, TN-166.

[2] In the future, we may choose to pack more efficiently in order to store more events on a 2400-foot physical tape. Present limit is about 110,000 events.

per record.

| | | |
|---|---|---|
| 1. | IACTIVE | activation - deactivation flag |
| 2. | IROLL | roll number |
| 3. | IFRAME | frame number |
| 4. | IKN | K number |
| 5. | IBMTKS | beam tracks interacting in plate |
| 6. | IBM2 | beam tracks, cont. |
| 7. | IORIG | origin flag |
| 8. | IET | event type |
| 9. | IGRID(1) | first grid |
| 10. | IGRID(2) | second grid |
| 11. | IML(1) | master list X coordinate (for first grid) |
| 12. | IML(2) | master list Y coordinate (for first grid) |
| 13. | IPNLID | Panal tape number |
| 14. | IEXP | experiment |
| 15. | IOP | scanner, operator |
| 16. | ITIME | date |
| 17. | ITIME | time |
| 18. | IREJ | reject flag |
| 19. | IRNG(1) | range 1 |
| 20. | IRNG(2) | range 2 |
| 21. | ITYPSCN | type scan (1 or 2) |
| 22. | ICODE | indicative data change code |
| 23. | ICHNG | new data to replace old |
| 24. | IC2 | scan 1, 2 discrepancy flag |

| | | |
|---|---|---|
| 25. | ICH2 | punch flag |
| 26. | ICRR | alphanumeric indicative data and new data |
| 27. | IDTMS | date measured |
| 28. | ISUST | Sioux status |
| 29. | IRMNO | remeasurement number |
| 30. | IMP | measuring machine |
| 31. | IORD | ordinate number on panal tape |
| 32. | IVERS | Sioux version |
| 33. | IPHYSRS | physics resolution flag |
| | IFEX(14) | fourteen unused storage locations |
| 48. | ILOGWRD | update commands for this event (packed) |
| 49. | IMRKS | accepted marks for this event (packed) |
| 50. | ICOMWRD | physicist comments (packed) |

Figure I-1 specifies the locations of each of the above variables in the 16-word event image, together with the format in binary mode. Commas are the delimiters between separate pieces of information. On this Mechanics Paper, each horizontal grid spacing is two (2) characters, or 12 octal bits.

2. Scanning and Measuring

We have chosen a route[3] in which a scanner searches for all event types and records only identification information - roll, frame, grids, event type, and type of scan.[4] This is scan 1.

Each event of potential physics importance is looked at by a more experienced scanner and critically judged as to its reality. If the event is considered real, it is prepared for measurement in the COBWEB

Event Image

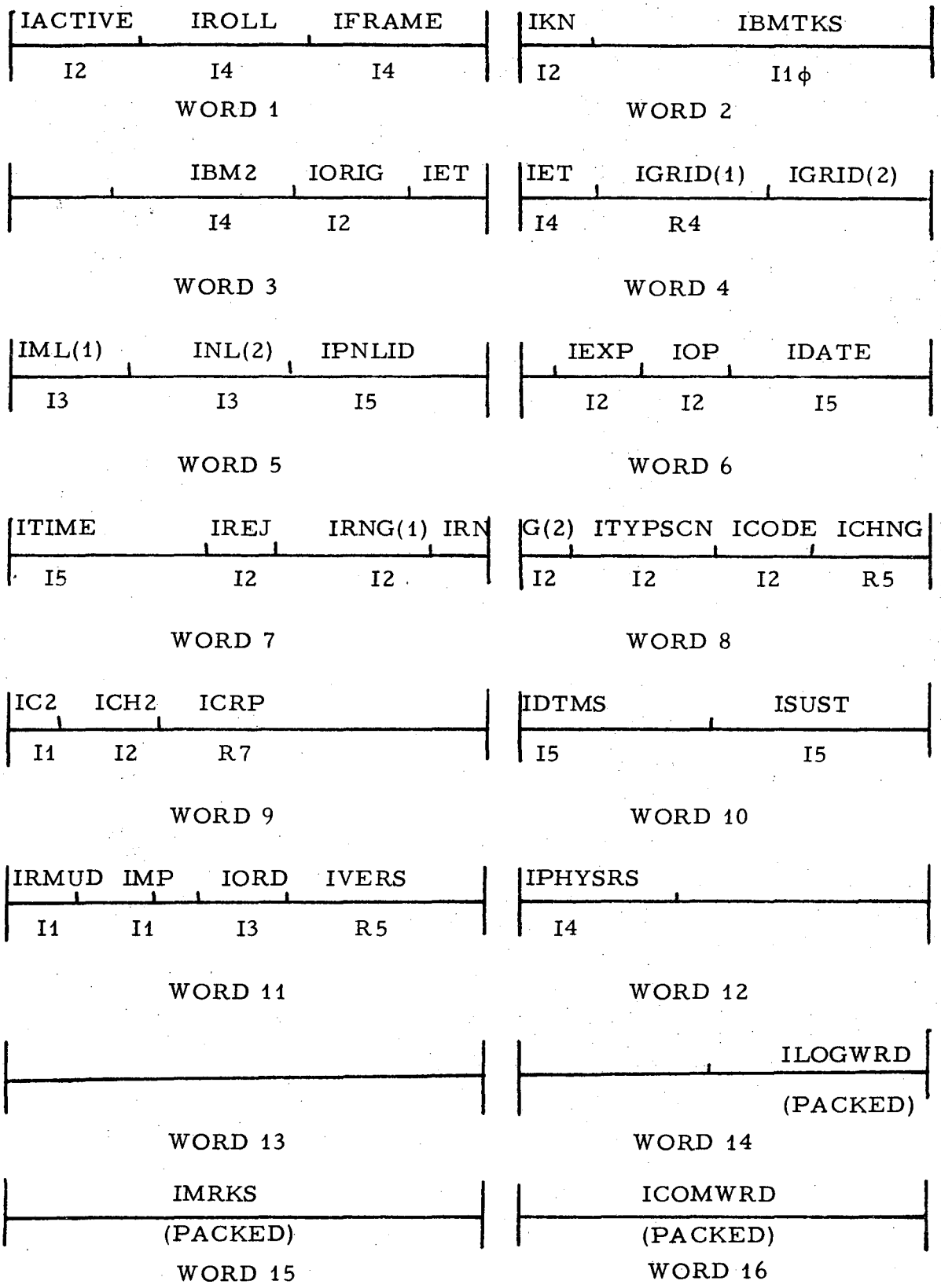


Figure I.1 Packing format of event variables in the event image.

system by correcting any frame, grid, or event type errors, adding ranges, and making a sketch of both the event and beam tracks which interact in the platinum plate.[5] This is scan 3.

Similarly for re-scan events, the same procedures are followed, except that the types of scan are numbered 2 and 5, respectively.

These scan data are entered on the COBWEB system teletypes[6] in the following formats:

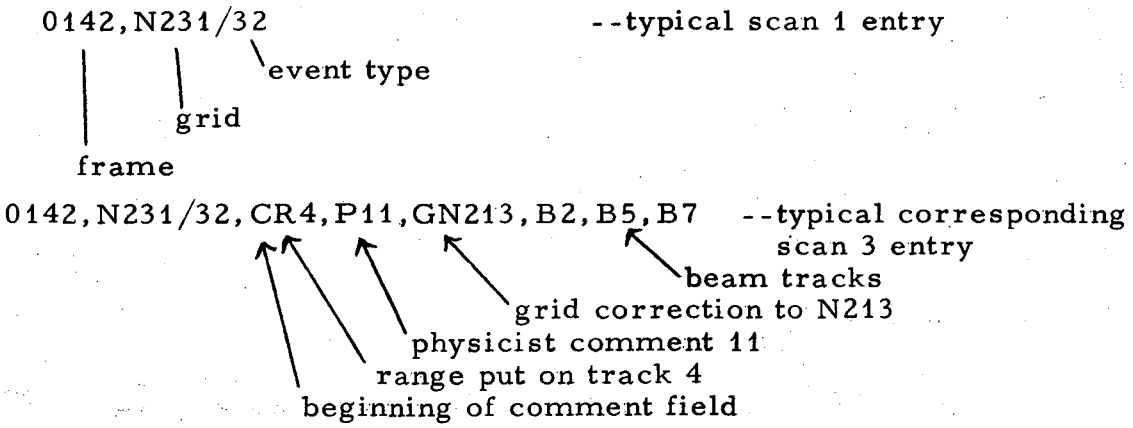


Scan reports such as these, from all scan tables, are deposited on the M44 tape, the daily output of the COBWEB system. Program LEO (see Section 4) is a trimmed down version of EREDIT (written by B. Albrecht for the LBL COBWEB system), which decodes this information and constructs the master list event image of Fig. I.1.

---

[3]Derived from that employed on a previous experiment, Exp. 76; see scanning instructions, TN-150, TN-153.

[4]Scanning instructions for Exp. 30, TN-167

[5]Pre-scan instructions for Exp. 30, TN-169.

[6]General COBWEB teletype Scan Instructions, TN-152

Particular event types (presently 3, 5, 9, 17, 31, 32, 37, 77) declared real on Scan 3 are punched out of the master list during the routine weekly LEO-SORT-LIBRA run (Section 4), and the events are flagged (ICH2 = 77) to prevent duplicate punching at any later time. The master list format is compatible with COBWEB, and the cards are read directly into the system and measured.[7] Measured events on the COBWEB M44 output tape are processed through the programs MEDIT-SORT-TVGP-SQUAW.

The program MEDIT is a modified version of the standard EREDIT program and performs the additional task of filling up a track bank with beam and outgoing track digitizations on the film plane, calling the SCORPIO program to reconstruct origins with errors in each view,[8] and storing these origins on the PANAL output tape. TGVP has been modified to accommodate these special origins in subroutines LSVERT and VTXCAL and to treat the large error ellipse properly.

3. Selection of Final Data Sample

Simultaneous with punching the COBWEB card, a post scan card is punched for later use at the scan table where, with SIOUX print-out and ionization information, a selective decision[9] is made on the measured event. Five decisions are possible:

---

[7]Measuring Instructions, TN-171

[8]Neutral Origin Reconstruction in Exp. 30, Appendix III

[9]Post-scan Instructions for Exp. 30, TN-177

| | Physics Resolution flag (PR) |
|---|---|
| 1. accept as an identified reaction, or reactions. | $1000 \leq PR \leq 9900$ |
| 2. accept as a free $\Lambda^o$ or $K^o$ decay; $e^+e^-$ pair or $K_2^o$ decay | $700 \leq PR \leq 709$ |
| 3. remeasure | $401 \leq PR \leq 409$ |
| 4. reject | PR = 400 or $421 \leq PR \leq 429$ |
| 5. defer | PR = 440 |

This decision is mark-sensed out the post scan card, along with other remarks and/or corrections to the event. These mark-sensed cards are gang-punched with PANAL tape numbers, interpreted, and read into the master list during the routine weekly LEO-SORT-LIBRA run. The master list is then matched with the various SIOUX tapes in the program ARIES to select the events and write them on the DST, which is immediately merged with the old DST to produce a new DST. All events exisint on the SIOUX tape are written onto the DST; all SQUAW fits accommodated by the DST are stored on the event record.

Those CPM's fitted by SQUAW and selected by the post-scanner have a positive CPM number in the starting location for that fit; all other CPM's have a negative CPM number.

All events on the DST have a physics resolution flag which identifies the data reduction status of that event record and which is crucial for the selection of a complete data sample while data reduction is still in progress.

4. Data Flow of All Scanning and Measuring Information

The flow of all scan information is in Fig. I.2. Solid lines and enclosures denote actual scan information; dashed lines denote the interface between scan information and measurement information.

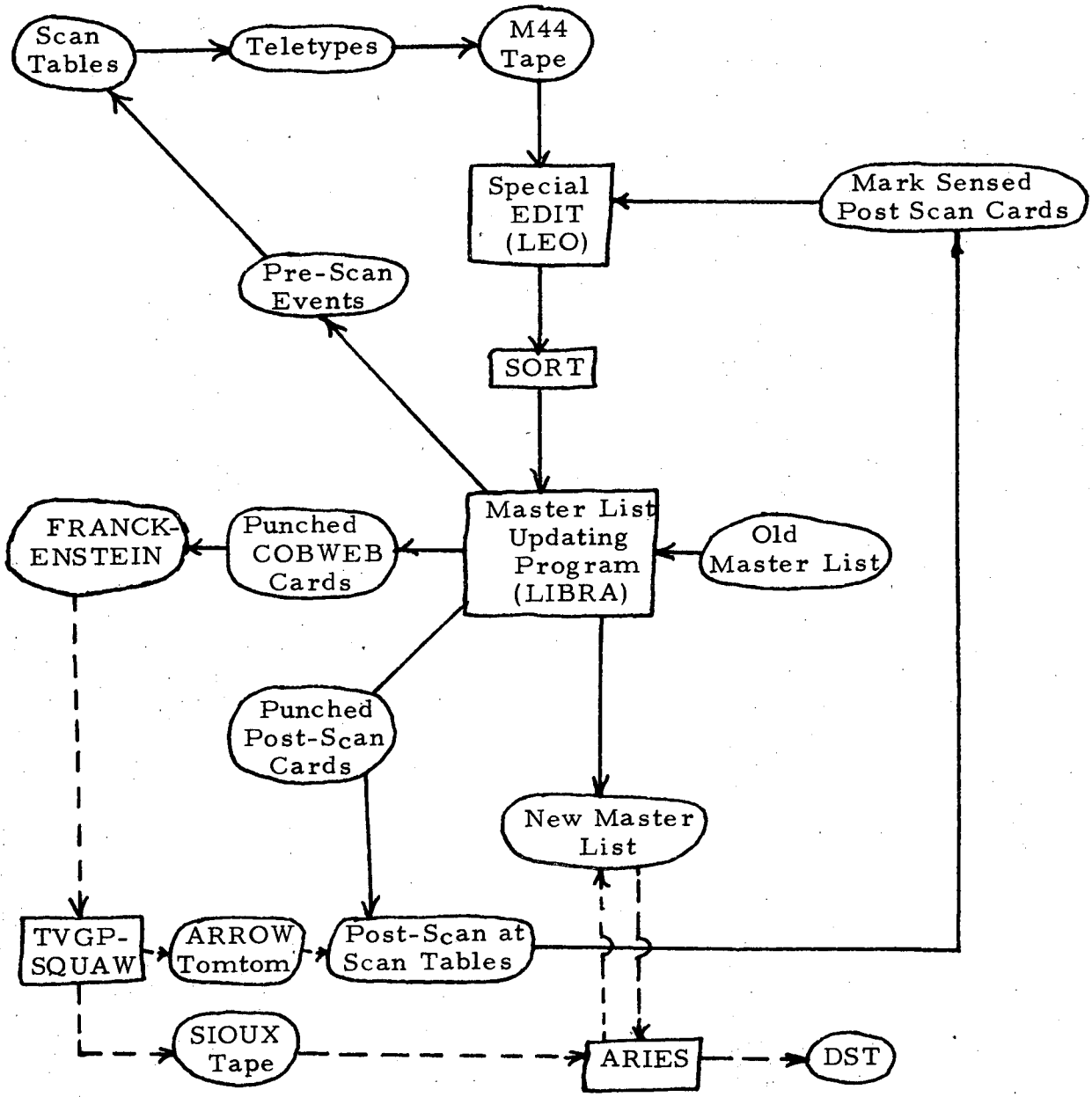


Figure I.2 Data Flow of Scan Information in this Experiment.

The triple execution LEO - SORT - LIBRA performs the following reductions of data:

LEO: a) EDITs the M44 tape, decodes the teletype input data, and constructs event images:

b) reads in mark-sensed post scan cards, decodes mark numbers and update commands for selection of SIOUX TAPE.

SORT: a) sorts event images by roll-frame.

LIBRA: a) updates old master list with new events from LEO.

b) punches out events called real at pre-scan for COBWEB measurement.

c) punches out post-scan cards for later use at scan table.

d) provision for ad hoc corrections to any event at either input or output to LIBRA, e.g., to correct wrong roll numbers, types of scan, etc.

e) checks all incoming events for errors, such as inconsistencies in input information and allowed ranges of variables.

The updating procedures are very complicated but essentially they perform all the operations demanded by the pre-scanners or post scanners, such as setting the physics resolution flag, accumulating all the update, comments, ranges, etc., for deposition onto the up dated event image.

LEO-SORT-LIBRA is typically run once a week, and, for an old master list tape of 60,000 events and 2300 new events from the teletypes, uses approximately 400 CP seconds, or about 700. accounting

units (AU) of computer time on the 6600. These numbers are from the update to ML.48, Log Book I, page 69.

The data flow of measurement information follows the conventional reduction route, with the exception of a sorting of the PANAL tape after the MEDIT execution:

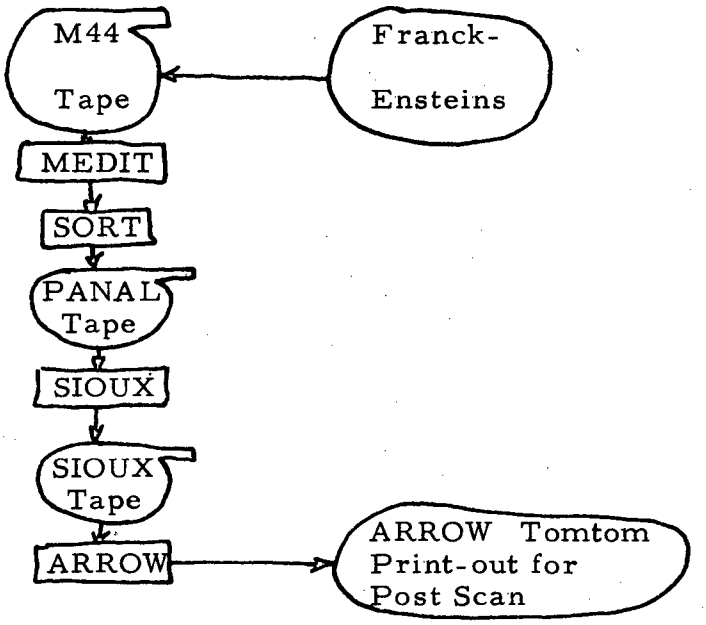


FIGURE I.3 Data Flow of Measurement Information.

The DST selection process, the interaction of the master list with the SIOUX tapes, is done in the program ARIES and can be done on each week's PANAL, or less frequently on multiple SIOUX tapes. In practice, we select 10 weeks of measurement in one computer run.

The program ARIES reads a SIOUX tape and a master list tape, performs the following exchange of information, and writes out a selected data summary tape and an updated master list. The following transfers of information are made:

| | SIOUX | ML | DST Location |
|---|---|---|---|
| (event type) | | IET → | D (5) |
| (PANAL type) | JPNLID → | IPNLID → | D (21) |
| (measure type) | JDTMS → | IDTMS | |
| (SIOUX status) | JSUST → | ISUST → | D (15) |
| (remeasure numbers) | | IRNNO → | D (4) |
| (PANAL ordinate) | JORD → | IORD → | D (20) |
| (SIOUX version) | JVERS → | IVERS | |
| (physics resolution flag) | | IPHYSRS → | D (14) |
| (accepted CPM's) | | IMRKS → | D (16)-D(19) |
| (all fitted CPM's) | All fitted marks → | IFEX (14) | |

The flow diagram is:

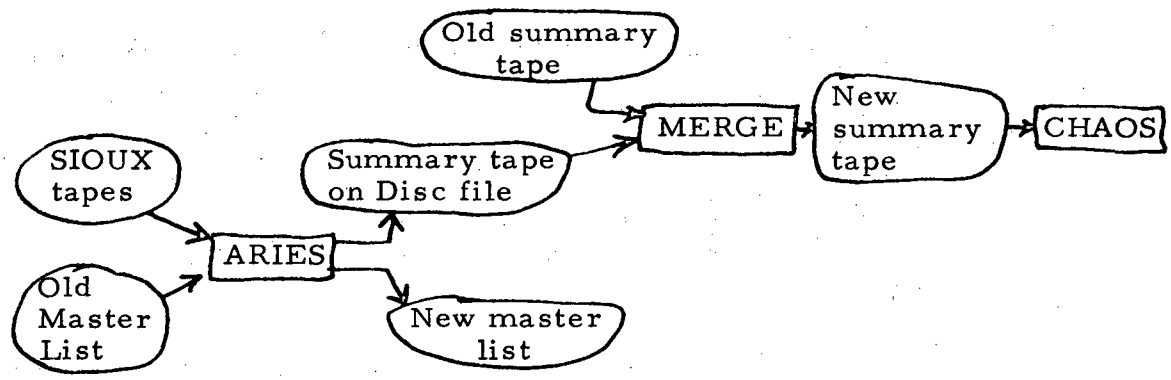


FIGURE I.4 Flow diagram

The data flow diagram indicates that there is a cumulative, updated summary tape each time ARIES is run. The CHAOS program is merely to check that the newly made DST is complete.

In summary, the primary functions are inter-related as in Fig. I.5.

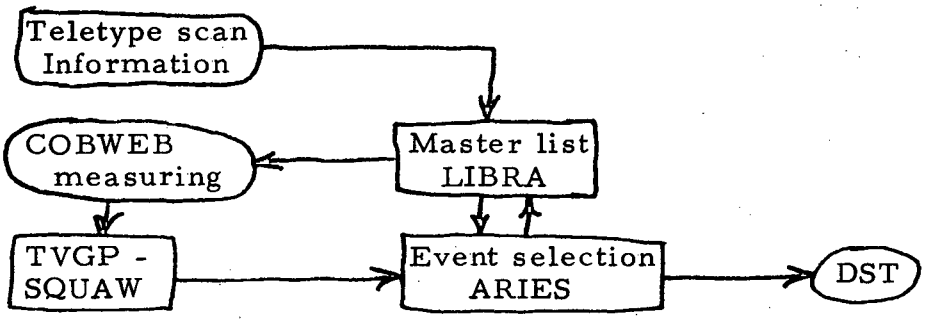


FIGURE I.5 Interrelationship of scanning and measuring information.

The master list is the main depository of information and also controls the disposition of measurement information. Such a centralized system has strong merits: a single person is capable of monitoring the progress of all aspects of the data reduction by just looking through the LIBRA output each week; any (obvious) errors are detected within a week or two of their origin; because all information which leaves the master list must at some time return, there is a continuous redundancy checking on "leaky buckets" of information in the system.

The remeasurement stages of a bubble chamber experiment can be most troublesome if one does not have an understanding of the present status of all events. In particular, the calculation of cross sections while the experiment is in the midst of remeasurement can be most difficult and tedious. For this reason primarily the physics resolution flag has been employed most thoroughly during these repeated interactions of the master list with the SIOUX tapes.

The logic in these numbers is fairly simple if one bears in mind that the physics resolution flag for a particular event is always monotonically increasing as that event progresses through the data reduction

chain. Thus, scanned events are initialized at ten times the origin number, pre-scanned events are numbered in the 300's, post-scanned events are numbered in the 400's if they are not to progress further, the 700's if terminal free $V^o$ decays, and in the 1000's if accepted. The units digit always counts the remeasurement number. For accepted events, the tens digit counts the number of accepted marks for that event.

Finally, events on the SIOUX tapes not selected by a post-scanner (e.g. another measurement is preferentially accepted, post scan card lost enroute to post-scanner, etc,) are given the following physics resolution flag on the summary tape record.

1. EOF on master list tape before EOF on SIOUX tape.
   This cannot be.
2. Master list event has already selected a SIOUX event.
3. No match on master list for this SIOUX EVENT.
4. Attempted scan card number match failed.
5. Master list roll-frame number exceed SIOUX roll-frame.
   SIOUX tape must be unsorted.
6. No match on PANAL tape number.
7. Marks sensed on card are not on the SIOUX record.

These codes are further elucidated in the appendix following this note.

As an example of the strength of this scheme, Fig. I.6 displays the disposition of events during remeasurement. RN stands for remeasurement number, and PR for physics resolution.

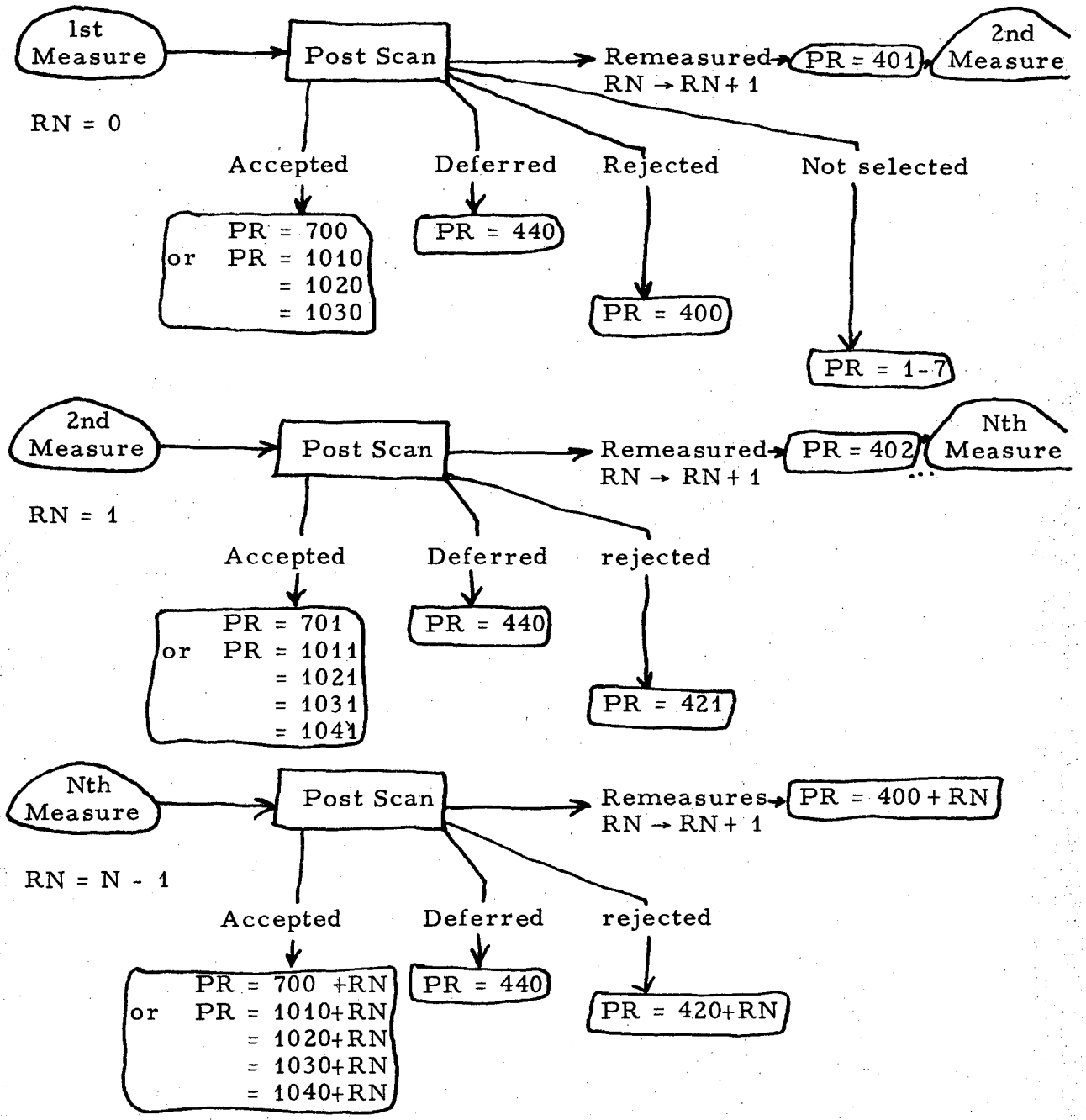


FIGURE I.6 Disposition of events during remeasurement.

After a sample of ~ 1000 2nd measure events had been processed through the Post Scan, the fractions to pass along each channel were

| | |
|---|---|
| Accepted | ~ 2/3 |
| Rejected/deferred | ~ 0 |
| Remeasured | ~ 1/3 |

The convergence in RN is fairly rapid.

5. Recycling

This experiment intends to measure cross sections, and to that end all loopholes for cost events must be found.

Scans 1, 2. It was found that some events entered on the teletypes never found their way to the master list. Since the event frequency per frame is about 0.35 (for rolls 101-301) as special program SPY[10] was written which examines the master list for "frame gaps", "unfinished rolls", and "missing rolls." That is, we specify frame gap lengths, N,M (say, = 20 frames), and if in N frames we find no event, or if the last event on a roll is not within M frames of 667 (the nominal roll length), we print out the rolls, frames, operators, and dates involved.

We trace down each computer-found gap by comparison with the original teletype sheets. In the past, the vast majority have been found to be real and due to several causes: M44 tape was bad or blank on one day; M44 tape for that day never read into the master list; roll, or parts of it, never scanned at all, etc. A careful list of these gaps is made to be scanned or re-entered as appropriate. Beginning in May 1971, we ceased scanning for the most frequent event types, 6 and 7. This greatly reduces the usefulness of the above SPY program. Nevertheless, a very efficient search for lost events can be made by a program intended for another purpose.[11] The program is a "conflict" program which compares one scan against another to determine which events were found in common and which were not. The program may be modified to check for when N or more events in a sequence have been found one scan but not the other (for N = 4, say). In this way, the conflict program can function as a lost event finder for re-scanned rolls

[10] Available as a utility routine, Section 6.

[11] Scanning Efficiencies in Appendix II.

only, about 30% of the experiment.

Scans 3, 5. If a pre-scan event does not match and update a first scan event, it is de-activated (IACTIVE = 39) and left in the master list. The first scan event remains active in the master list. Events to be pre-scanned may have been entered with incorrect ID information, or may have been overlooked and never pre-scanned at all. No matter what the mechanism of loss is for a pre-scan event, a list of first scan entries not yet updated can always be made from the master list, and the pre-scan events can be re-cycled through the teletypes to try either again or for the first time. There can be no loss of pre-scan events. This is called clean-up pre-scan.

Scans 4, 6. If an event pre-scanned as real on scan 3 or 5 does not show up on a SIOUX tape it can be punched out again from the master list for another try at measurement. This process can be repeated until all events intended for measurement are actually measured.

In summary, let us note here one important fact: the data reduction efficiency depends almost entirely on the efficiency of getting first scan events from the teletypes, off the M 44 tapes, to the master list. Subsequent to this step, the data reduction is independent of loopholes for event loss of human error (other than my own software errors in the system). One can randomly skip pre-scan events, loose COBWEB cards intended for measurement, loose mark-sensed post scan cards, or whatever, but in any case the first scan event image is on the master list and will not be lost, and the event cannot escape being reduced.

6. Usage of the Master List - Utility Routines

The master list was designed to be very accessible to analysis by

those not familiar with every detail of its construct. We have written compact "user routines" to be used with any master list tape, as CHAOS is used with a summary tape. The data cards for filters and tallies, lists, or plots are very simple, although only one set of filters can be imposed at one execution.

The possible operators are:

LIST or READ (decipher code numbers into English)

FILTER

SELECT

ANTI-SELECT

TALLY

COINCIDENCE TALLY (double coincidence only)

PLOT

PUNCH

SPY

with one operation per data card; the objects of these operators are all 50 elements of the event image; the ranges or values of the objects follow. A blank card stops the set of filters and operations.

A list of words recognized by the coding is in Appendix A.8 in this note.

These samples will illustrate the above.

LIST,ACTIVE,REJECT,PHYSICS,MARKS,PCOMS

The list operation prints out each event (subject to the filters), and below the event the code number, and in English the meaning

of the code. This particular example will interpret the "active", "reject", and "physicist comment" codes, and print out the physics resolution flag and the accepted marks for the event.

```
FILTER,ROLL,101,200
```

Accepts only roll numbers R, $101 \leq R \leq 200$.

```
SELECT,ACTIVE,0,50
SELECT,ET,17,31,32,37
S,ORIG,3,5
```

Accepts only event types 17, 31, 32, 37, and origins 3 and 5, for active events from first scan (ACTIVE = $\phi$) and re-scan (ACTIVE = 5 $\phi$)

```
ANTI-SEL,PHYSRS, 330,400
AS,ET,30
```

Does not accept ("anti-selects") any event with physics resolution flag equal to 330 or 400; does not accept event type 30,

```
TALLY,ET,17,31,32,37
T,ORIGIN,3,5
```

Counts the number of each event type 17, 31,32, 37, and also the number of events originating on scans 3 and 5.

```
COINCID,ET,17,ORIGIN,3
C,ET,17,ORIG,5
```

Counts the number of event type 17 originating on scans 3 and 5. Up to 100 tallies and coincidence tallies can be made.

PLOT,DATE,ROLL,ORIGIN,3

Do a plot of the date (abscissa) versus the roll number (ordinate), labelling the points by the origin flag, and make three (3) copies of the plot. The point labels and the number of copies are optional parameters.

SPY,50,70

Check the master list for missing events by finding frame gaps of 50 frames or more with no events, and unfinished rolls with no event in the last 70 frames of the nominal roll length (667 frames). The frame gaps 50 and 70 are optional. Default values are 30 and 30

PUNCH,ET,3,9

Punch out (for COBWEB) all event types 3 and 9. (Presumably subject to other filters on roll number, remeasure number, punch flat (ICH=2),etc.)

Two additional routines are intended for somewhat more specialized access to the master list:

USE 3Ø: The program USE30 is to Exp. 3Ø master list as KIOWA is to SIOUX tapes, in the sense that each event image is unpacked into the readable IDBLK common block array. The user then does whatever FORTRAN logic he wishes on one pass through the master list tape. USE3Ø

employs all the operations of SUPER as data card input to facilitate subset selection.

ADHOC: This program is intended to make ad hoc alterations of a master list tape (e.g. to correct roll number, type of scan errors, etc., or to throw a subset of events off the master list). The output tape is sorted by Roll-Frame and a new master list tape is written.

## APPENDIX IA. CODES

Index of codes given below:

1. Origin flag
2. Type-of-scan flag
3. Physics Resolution flag
4. Activation - deactivation flag
5. Update flag
6. Reject codes
7. Operator numbers
8. SUPER code words

(For the sake of brevity, the codes 4 through 8 are not included in this appendix, but appear in TN-186, Trilling/Goldhaber Internal Technical Note.)

1. The origin flag (JORIG) on an event image status where the image originated and can have the values:

   1 - first (primary) scan

   2 - second (re-scan) scan

3 - pre-scan of events found on first scan

4 - post-scan of events found on first scan

5 - pre-scan of events found on second scan

6 - post-scan of events found on second scan

7 - Irene Witkowski 07 scan near plate

8 - unused

9 - training scan

2. The type of scan (ITYPSCN) can be 1 or 2 for active events, but set equal to the origin flag for those images which update an existing image on the master list but are then de-activated immediately.

3. The physics resolution flag (IPHYSRS) is intended to be to the master list data stream what the SIOUX status word is to the measurement-SIOUX data stream. The physics resolution flag is on both the master list and the DST. As an event filters through the data reduction process, the physics resolution flag is graduated monotonically. At any point in the process, events of a particular category can be isolated for any purpose, e.g. to measure, to list, to re-examine events in a particular reject category, etc.

| | PR flag | |
|---|---|---|
| SCAN | 10 | event scanned at table; initialization is 10 origin of event image. |
| | 90 | |
| PRE-SCAN | 300 | event pre-scanned, not real. |
| | 301 | event rejected at pre-scan: PR = 300 plus physicist comment block number (1-14) which gives reason for rejection |
| | 314 | |
| | 330 | event declared real at the pre-scan |
| POST-SCAN | 400 | event rejected at post-scan (RF = 4 on card). |
| | 401 | event remeasured at post-scan (RF = 3 on card); PR = 400 + remeasure number |
| | 409 | |
| | 421 | event rejected after remeasurement (RF =4 on card); PR = 420 + remeasure number. |
| | 429 | |
| | 440 | event deferred at post-scan (RF = 5 on card). |
| | 700 | event accepted as ET 6,7 (RF = 2 on card). |
| | 1010 | event accepted (RF = 1 on card; PR = 1000 + 10 · (number of accepted marks) + (remeasure number) |
| | 1049 | |
| | 1 | EOF on master list tape before EOF on SIOUX tape. This cannot be. |
| | 2 | Master list event has already selected a SIOUX tape event. |
| | 3 | No match on master list for this SIOUX event. |
| | 4 | Attempted scan card numbers match failed. |


5 Master list roll-frame number exceeds SIOUX roll-frame.

SIOUX tape must be unsorted.

6 No match on PANAL tape number.

7 Marks sensed on card are not on the SIOUX record.

## APPENDIX II. Scanning Efficiencies

In principle, the calibration of cross sections depends on every detail of the data reduction system. In this experiment, such a system exists,[1] and is designed to be a total experiment reduction system monitoring every event from initial detection to final summary tape selection. Furthermore, the Master List tape contains both present information and all past history for every event.

Therefore, it is natural to calculate scanning efficiency information, at any point in the reduction process, directly from the Master List tape.

A program was written to conflict Scan 1 events against Scan 2 events at any level in the reduction process, i.e., at first scan, prescan, or post-scan, and to count up, for each event type, the number found on Scan 1 only, on Scan 2 only, and in common.

From these numbers scanning efficiencies are readily calculated. Following the analysis of Fett[2] we choose variables

$m_i \equiv$ no. of events found on scan i

$m_{ij} \equiv$ no. of events found in common on scans i,j

$m_j \equiv$ no. of events found on scan j.

Making the usual assumptions that each event has an a priori probability of being found, that this probability is constant for all events, scanners, times of day, etc., and that each scan is independent, we have an estimate for the efficiency, $\eta_j$, of the jth scan

$$\hat{\eta}_j = \frac{m_{ij}}{m_i} \quad . \tag{II.1}$$

The distribution of this estimate can be derived from an assumed binomial distribution of $m_{ij}$ (for fixed $m_i$)

$$P(m_{ij}|m_i) = \frac{m_i!}{m_{ij}!(m_i - m_{ij})!}\, \eta_j^{m_{ij}}(1 - \eta_j)^{m_i - m_{ij}} \tag{II.2}$$

which has mean

$$\left\langle m_{ij} \right\rangle = \eta_j m_i$$

and standard deviation

$$\sigma(m_{ij}) = \sqrt{m_i \eta_j (1 - \eta_j)} \quad .$$

Then the standard deviation in the estimate $\hat{\eta}_j$, for $m_i$ constant, is

$$\sigma(\hat{\eta}_j) = \frac{\sigma(m_{ij})}{m_i} = \sqrt{\frac{\eta_j(1 - \eta_j)}{m_i}} \tag{II.3}$$

in terms of the measured number $m_i$ and the <u>a priori</u> efficiency, $\eta_j$, which we do not know. However, if the deviation of the estimate $\hat{\eta}_j$ from the true efficiency $\eta_j$ is $\alpha$, then

$$\eta_j - \hat{\eta}_j = \pm\, \alpha \tag{II.4a}$$

where

$$\alpha = \pm \sqrt{\frac{\eta_j(1 - \eta_j)}{m_i}} \tag{II.4b}$$

or, substituting $(\hat{\eta}_j \pm \alpha)$ for $\eta_j$,

$$\alpha = \pm \sqrt{\frac{(\hat{\eta}_j \pm \alpha)(1 - \hat{\eta}_j \mp \alpha)}{m_i}} \quad . \tag{II.4c}$$

Then we get

$$\alpha = \frac{(+\ 1 - 2\hat{\eta}_j) \pm \sqrt{(1 - 2\hat{\eta}_j)^2 - 4(m_i + 1)(\hat{\eta}_j - 1)\hat{\eta}_j}}{2(m_i + 1)} \quad , \tag{II.4d}$$

so the true efficiency is

$$\eta_j = \hat{\eta}_j \pm \left\{ \frac{(1 - 2\hat{\eta}_j)}{2(m_i + 1)} \pm \frac{\sqrt{4m_i\hat{\eta}_j(1 - \hat{\eta}_j) + 1}}{2(m_i + 1)} \right\} \quad , \tag{II.5}$$

entirely in terms of measured quantities, and where for large $m_i$ we obtain the efficiency

$$\eta_j = \hat{\eta}_j \pm \sqrt{\frac{\hat{\eta}_j(1 - \hat{\eta}_j)}{m_i}} \quad . \tag{II.6}$$

An estimate of the true number of events is

$$\hat{N} = \frac{m_j}{\eta_j} = \frac{m_i m_j}{m_{ij}} \tag{II.7}$$

which has an approximate distribution, from a complicated calculation by Fett, with standard deviation

$$\sigma(\hat{N}) = \sqrt{\hat{N}\,\frac{(1-\hat{\eta}_i)(1-\hat{\eta}_j)}{\hat{\eta}_i\hat{\eta}_j}} \qquad \text{(II.8)}$$

if $m_i$ and $m_j$ are large.

We have employed the above program to treat the grid coordinate as the independent variable, and have so obtained measures of spatially-dependent scanning efficiencies for the event types 7, 17, and 30 as a function of the 82-inch chamber y-coordinate (very nearly the beam direction). These are displayed in Fig. II.1.

The need for such calculations naturally arose in our measurement of the total $\Lambda p$ interaction cross section, described in Sec. III, in which the spatial distributions of events are critical to that measurement. Inconsistencies between the experimental and calculated $\Lambda \to p\pi^-$ and $K_1^0 \to \pi^+\pi^-$ decay distributions led us, after many other estimations performed and rejected, to seriously question the possible spatial variation of a topological scan efficiency. We then calculated these efficiencies from the master list scan data. The data bases used in the displays in Fig. II.1 are the following[3]:

ET 7 Scan 1 vs. scan 2 data; every tenth roll from 101 to 301.

ET 17 Scan 4 vs. scan 5 and 6 data; all rolls from 101 to 301, and 2250 to 2637.

ET 30 Scan 3 vs. scan 5 data; all rolls from 101 to 301, and 2250 to 2637.

Furthermore, the following corrections were performed on the data:

(a) ET 7 events with the scanner comment S11 (possible $e^+e^-$ pair) were removed from the sample so as not to underestimate the scan efficiency due to possible misidentification of $e^+e^-$ pairs by different scanners. This is measured to be a 10-15% effect near the end of the chamber; and,

(b) ET 17 events with the comments P91 to P97, or P194 (flare, obscuration problems) were removed from the sample to avoid mismatches between Ø4 measurement failures near the plate or the flare and pre-scanned Ø5 data.

In the case of kinematically identified states, such as $\Lambda^0 \to p\pi^-$ $K_1^0 \to \pi^+\pi^-$, the well-known lifetimes allow a precise calculation of the spatial distributions of these events from any sub-ensemble. Specifically, we have chosen an ensemble of $\Lambda \to p\pi^-$ decays in the fiducial volume

$$\begin{aligned} \text{FID 3:} \quad -20 \leq x(\text{cm}) &\leq 20 \\ -76 \leq y(\text{cm}) &\leq -66 \\ 3 \leq z(\text{cm}) &\leq 34, \end{aligned} \tag{II.9}$$

weighted each decay by the inverse of the probability to decay in FID 3, and calculated the decay distribution throughout the chamber. The ratio of the actual experimental distribution to this calculated distribution, $\eta^{DST}$, is shown in Fig. 2a. It was found to be insensitive to variations in FID 3, and also to variations in a lower momentum cutoff imposed between 0.25 and 1.0 GeV/c $\Lambda$ momentum.

Qualitatively, Figs. 1a and 2a are similar, but differ in magnitude near the plate, the master list efficiency being the larger. This difference can be accounted for by two effects: (a) large numbers of events

missed by both scanners, and (b) a measuring inefficiency near the plate. The measuring inefficiency, or failure probability, was measured for ET 7 events by taking the ratio of failed events ($9000 \leq$ STATUS $\leq 20000$) to all events as a function of the master list grid coordinate. That distribution is shown in Fig. 3a, and peaks near the plate, presumably do to obscuration by overlapping tracks.

We have performed two estimations of the magnitude of effect (a).

(1) A simple calculation is the following: let

$P_o$ = probability of finding an event on scan 1 and scan 2

$P_1$ = probability of finding an event on scan 1 or scan 2, not both

$P_2$ = probability of finding an event on neither scan

$P_3$ = probability of event failing measurement, (II.10)

and

$N_1$ = number of events found on one scan only

$N_{12}$ = number of events found in common on scan 1 and scan 2

$N_T$ = true number of events in film,

and where we have the constraint that

$$P_0 + P_1 + P_2 + P_3 = 1 \ . \tag{II.11}$$

By these definitions, we have

$$N = (P_0 + \frac{P_1}{2}) N_T \tag{II.12}$$

$$N_{12} = P_0 N_T \ ,$$

and by the assumptions above on the first page of this note, the master list efficiency is

$$\eta^{ML} = \frac{N_{12}}{N_1} = \frac{P_0}{P_0 + \frac{P_1}{2}} \tag{II.13}$$

This efficiency is displayed in Figs. 1a-c, d-f for event types 7, 17, and 30. Further, for states such as $\Lambda \to p\pi^-$ and $\Lambda p \to \Lambda p$, one can calculate the spatial distribution of events from an assumed unbiased ensemble, compare this with the entire distribution, and determine the efficiency variation, or bias. For ET 7, $\Lambda \to p\pi^-$ decays inside FID 3, this DST efficiency described above is

$$\eta^{DST} = \frac{P_0 + (P_1/2)}{(P_0+P_1+P_2)_{FID\ 3}} \qquad (II.14a)$$

where the denominator is determined within FID 3, and the numerator has $P_1/2$ since events from only one scan were measured. Now, FID 3 was chosen so that $P_2 \cong 0$; then

$$\eta^{DST} = \frac{P_0 + (P_1/2)}{(1-P_3)_{FID\ 3}} \qquad (II.14b)$$

where

$$(1-P_3)_{FID\ 3} \cong 0.97 \qquad (II.15)$$

by inspection of Fig. 3a. Using (11), (13), and (14)

$$P_2 = 1 - \left[\eta^{DST}\eta^{ML}(1-P_3)_{FID\ 3}\left(\frac{2}{\eta^{ML}} - 1\right)\right] - P_3 \ . \qquad (II.16)$$

Substituting bin-for-bin the values of $\eta^{DST}$, $\eta^{ML}$, and $P_3$ from Figs. 1-3 for ET 7 yields the probability distribution of $P_2$ displayed in Fig. 3b. (2) a special third scan was made of roll nos. 220, 250 near the plate where this effect is anticipated to be large. An expert scanner was asked to look very carefully, and so we do not claim these three scans are equivalent. The results are that, of at least 94 events in the first subgrid bin, 14 new events we found on this third scan, where on the basis of the scan efficiency of Fig. 1a, a third scan should have found

only 6 new events. However, the nature of this special third scan was such that this random miss rate was very small; assuming it is negligible,

$$\frac{8}{94} \simeq 8.5\%$$

of the events were missed by both first and second scanners beyond the usual random miss rate. This is a lower limit, since the third scanner may also have missed some additional events.

We conclude by noting that, in the first subgrid bin near the plate, the probability that an event type 7 event will be missed by both scanners is as least 0.085±0.030, and very likely as large as 0.235±0.040 (Fig. 3b). This effect is surely due to visual obscuration of $V^0$ decay topologies by outgoing tracks from $K^-$ $Pt^{195}$ interactions. This effect is present in bins farther downstream to a lesser extent, as seen in Fig. 3b, and appears to be negligible near $y \simeq -80$ cm.

## REFERENCES

1. Data reduction in Exp. 30, TN-186.

2. E. Fett, Methods in Subnuclear Physics, Vol. I, p. 36.

3. The types of scan are numbered as follows:

   1 and 2 Primary and re-scan (TN-167)

   3 and 5 Pre-scan of 1 and 2, respectively (TN-169)

   4 and 6 Post-scan of 3 and 5, respectively (TN-177)

APPENDIX IIA. Tabulation of Scanning Efficiencies, Event Types 7, 17, 30.

small y; near plate.

| y(bin)* | ET 7 | | | ET 17 | | | ET 30 | | |
|---|---|---|---|---|---|---|---|---|---|
| | $\eta$ | $+\Delta\eta$ | $-\Delta y$ | $\eta$ | $+\Delta\eta$ | $-\Delta\eta$ | $\eta$ | $+\Delta\eta$ | $-\Delta\eta$ |
| 1 | .749 | +.016 | -.017 | .290 | .057 | -.051 | .640 | .089 | -.100 |
| 2 | .870 | .014 | -.015 | .692 | .060 | -.067 | .857 | .049 | -.069 |
| 3 | .851 | .017 | -.019 | .647 | .064 | -.069 | .909 | .035 | -.053 |
| 4 | .866 | .015 | -.017 | .542 | .070 | -.070 | .718 | .066 | -.077 |
| 5 | .907 | .015 | -.017 | .714 | .060 | -.068 | .919 | .035 | -.057 |
| 6 | .906 | .016 | -.019 | .821 | .060 | -.083 | .960 | .025 | -.060 |
| 7 | .895 | .018 | -.021 | .757 | .063 | -.077 | .807 | .047 | -.057 |
| 8 | .905 | .021 | -.026 | .609 | .095 | -1.04 | .816 | .049 | -.061 |
| 9 | .895 | .023 | -.028 | .833 | .057 | -.079 | .857 | .049 | -.069 |
| 10 | .898 | .022 | -.028 | .742 | .070 | -.085 | .818 | .051 | -.065 |
| 11 | .871 | .027 | -.033 | .783 | .073 | -.097 | .963 | .018 | -.035 |
| 12 | .891 | .025 | -.031 | .810 | .071 | -.099 | .931 | .034 | -.063 |
| 13 | .888 | .027 | -.034 | .857 | .060 | -.093 | .909 | .039 | -.063 |
| 14 | .853 | .032 | -.038 | .765 | .086 | -.116 | .891 | .038 | -.054 |
| 15 | .882 | .031 | -.039 | .700 | .091 | -.110 | .778 | .061 | -.076 |

* Transformation from bin indices to SIOUX y-coordinates is, approximately,

$$y(\text{cm}) \simeq -84.786 + 1.428\,[\,y(\text{bin})-1.\,]\ ,$$

i.e., the bin size is 1.428 cm.

APPENDIX IIA (continued)

small y;
near plate

| y(cm) | $\eta_{DST}$ ($\Lambda \to p\pi^-$) $\eta$ | $\Delta\eta$ | $\eta_{DST}$ ($\Lambda p \to \Lambda p$) $\eta$ | $+\Delta\eta$ | $-\Delta\eta$ |
|---|---|---|---|---|---|
| -85. | .469 | .025 | .469 | .10 | -.10 |
| -83. | .684 | .035 | .870 | .13 | -.15 |
| -81. | .758 | .038 | .590 | .13 | -.13 |
| -79. | .823 | .045 | .841 | .16 | -.17 |
| -77. | .863 | .055 | .990 | .20 | -.20 |
| -75. | .827 | .058 | .870 | .12 | -.20 |
| -73. | .880 | .060 | .990 | .20 | -.25 |
| -71. | .897 | .060 | .655 | .25 | -.25 |
| -69. | .950 | .050 | .682 | .25 | -.25 |
| -67. | .930 | .070 | .910 | .09 | -.23 |
| -65. | .808 | .080 | .945 | .06 | -.28 |
| -63. | .949 | .100 | .750 | .20 | -.25 |

| y(cm) | ET 7 $P_2$ | $\Delta P_2$ | ET 7 $P_3$ | $\Delta P_3$ |
|---|---|---|---|---|
| -85. | .235 | .040 | .141 | .020 |
| -83. | .102 | .040 | .069 | .010 |
| -81. | .020 | .045 | .057 | .010 |
| -79. | -.004 | .045 | .048 | .010 |
| -77. | -.065 | .055 | .059 | .012 |
| -75. | -.013 | .060 | .039 | .012 |
| -73. | -.055 | .060 | .022 | .010 |
| -71. | -.085 | .060 | .019 | .010 |
| -69. | -.100 | .050 | .036 | .010 |
| -67. | -.120 | .070 | .024 | .012 |
| -65. | .005 | .080 | .037 | .020 |
| -63. | | | .034 | .020 |

Referring to equations (10) and (16) in the text.

APPENDIX IIA (continued)

large y;
whole chamber

| | ET 7 | | | ET 17 | | | ET 30 | | |
|---|---|---|---|---|---|---|---|---|---|
| y(cm) | $\eta$ | $+\Delta\eta$ | $-\Delta\eta$ | $\eta$ | $+\Delta\eta$ | $-\Delta\eta$ | $\eta$ | $+\Delta\eta$ | $-\Delta\eta$ |
| -8.05±5. | .893 | .006 | -.006 | .613 | .027 | -.027 | .832 | .022 | -.024 |
| -70.5 | .926 | .008 | -.009 | .771 | .031 | -.034 | .883 | .018 | -.020 |
| -60.5 | .908 | .012 | -.014 | .771 | .036 | -.041 | .872 | .019 | -.021 |
| -50.5 | .848 | .022 | -.024 | .863 | .031 | -.039 | .839 | .021 | -.024 |
| -40.5 | .877 | .024 | -.027 | .849 | .037 | -.047 | .908 | .018 | -.022 |
| -30.5 | .884 | .029 | -.033 | .873 | .036 | -.048 | .860 | .024 | -.029 |
| -20.5 | .810 | .031 | -.035 | .794 | .060 | -.077 | .891 | .021 | -.025 |
| -10.5 | .789 | .039 | -.043 | .698 | .065 | -.074 | .854 | .025 | -.029 |
| - .5 | .850 | .041 | -.046 | .660 | .065 | -.072 | .884 | .024 | -.029 |
| 9.5 | .780 | .046 | -.049 | .889 | .047 | -.075 | .885 | .024 | -.029 |
| 19.5 | .870 | .039 | -.044 | .914 | .037 | -.060 | .889 | .024 | -.030 |
| 29.5 | .860 | .043 | -.049 | .875 | .047 | -.070 | .862 | .029 | -.035 |
| 39.5 | .829 | .044 | -.051 | .944 | .034 | -.081 | .903 | .024 | -.032 |
| 49.5 | .856 | .050 | -.056 | .800 | .074 | -.103 | .859 | .034 | -.042 |
| 59.5 | .738 | .063 | -.068 | .786 | .089 | -.127 | .775 | .046 | -.053 |

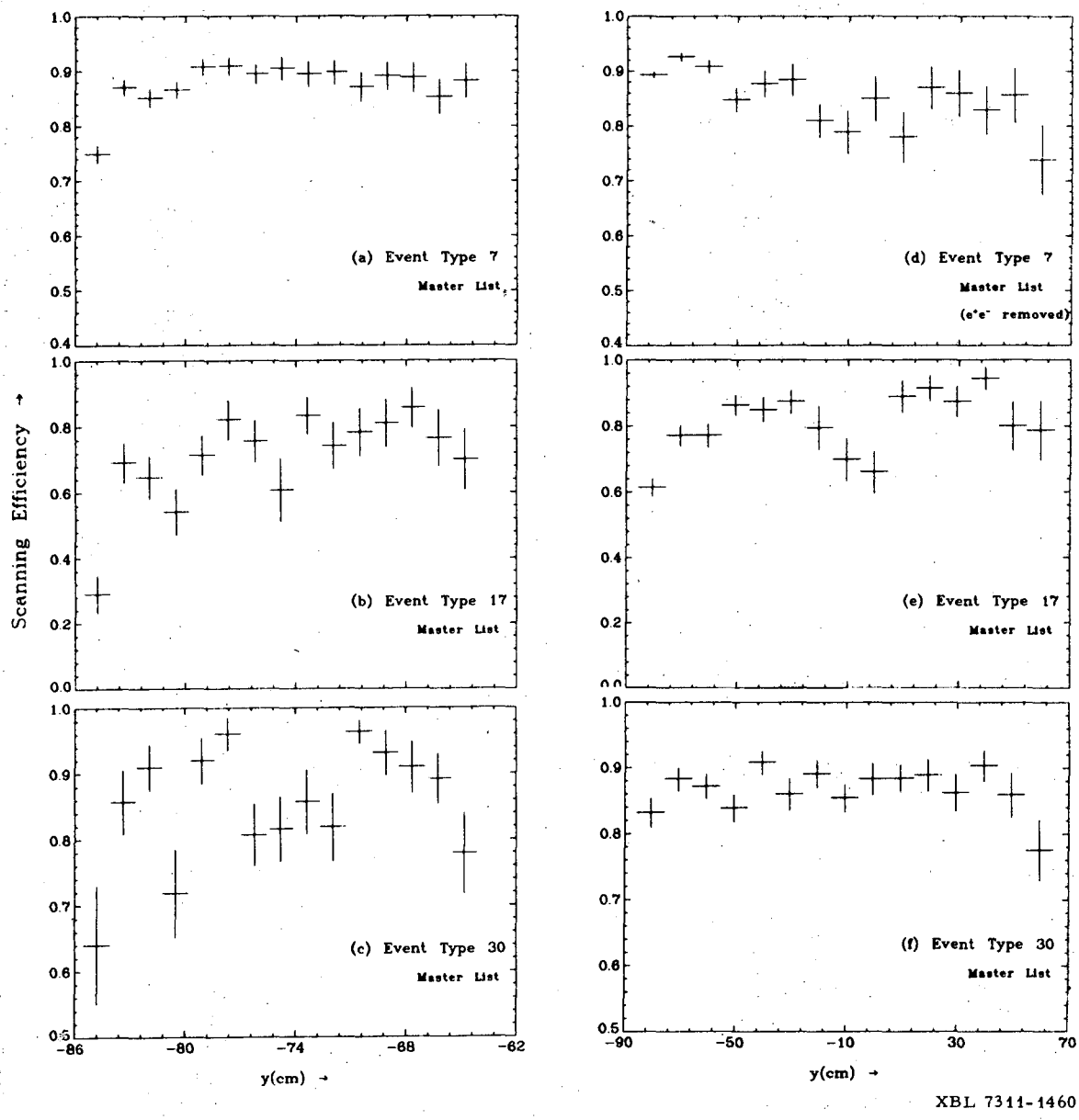


FIGURE II.1 Scanning efficiencies as a function of longitudinal position in the bubble chamber, for event types 7, 17, and 30. Figures (a)-(c) are in the forward part of the chamber, near the plate, $-85.5 \leq y(cm) \leq -62.0$; figures (d)-(f) are for the whole fiducial volume, $-85.5 \leq y(cm) \leq +70.0$.

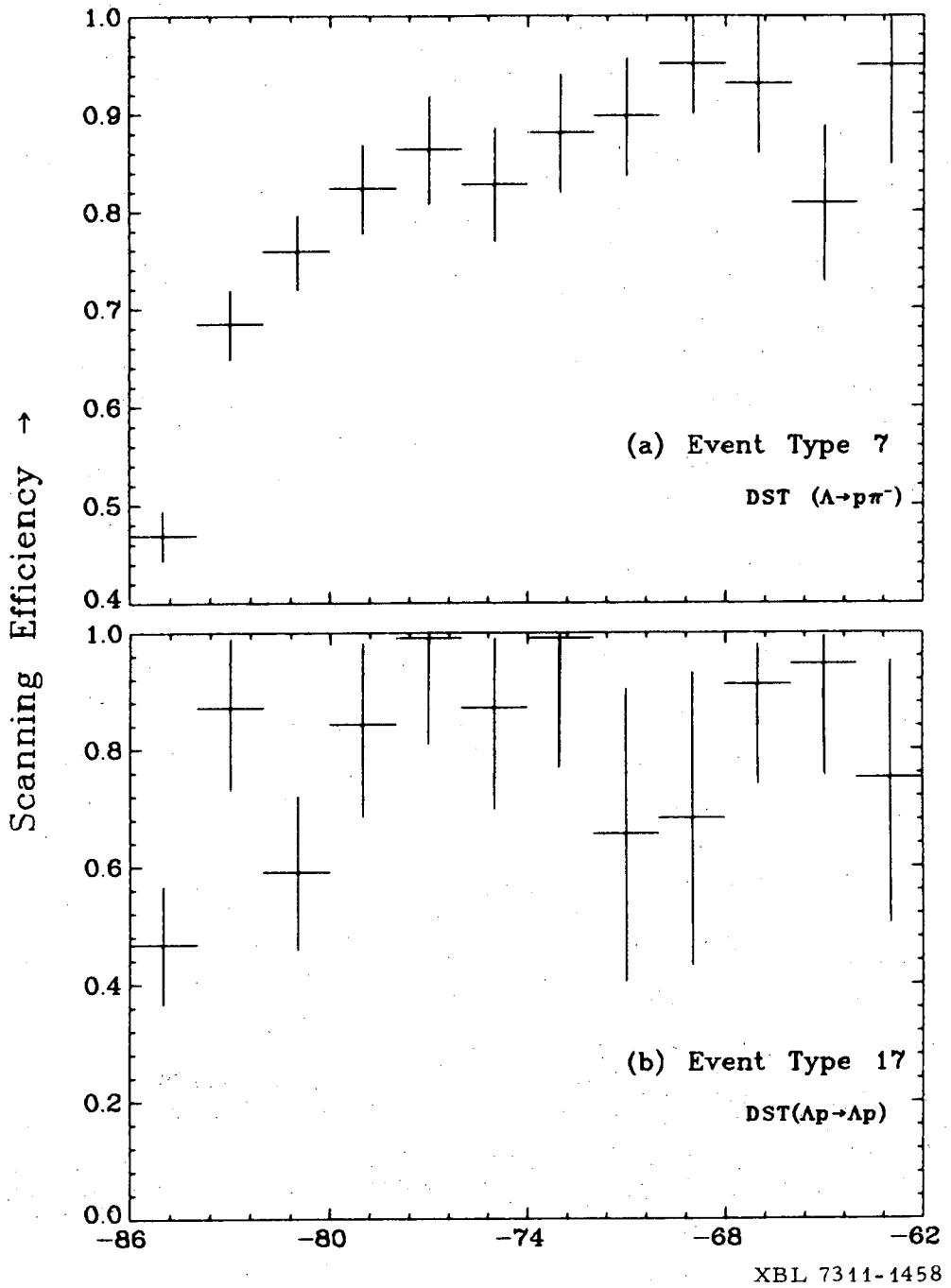


FIGURE II.2 Scanning efficiencies calculated from the Data Summary Tape for the ensemble of free $\Lambda \rightarrow p\pi^-$ decays (a), and for the ensemble of elastic scatters, $\Lambda p \rightarrow \Lambda p$, (b).

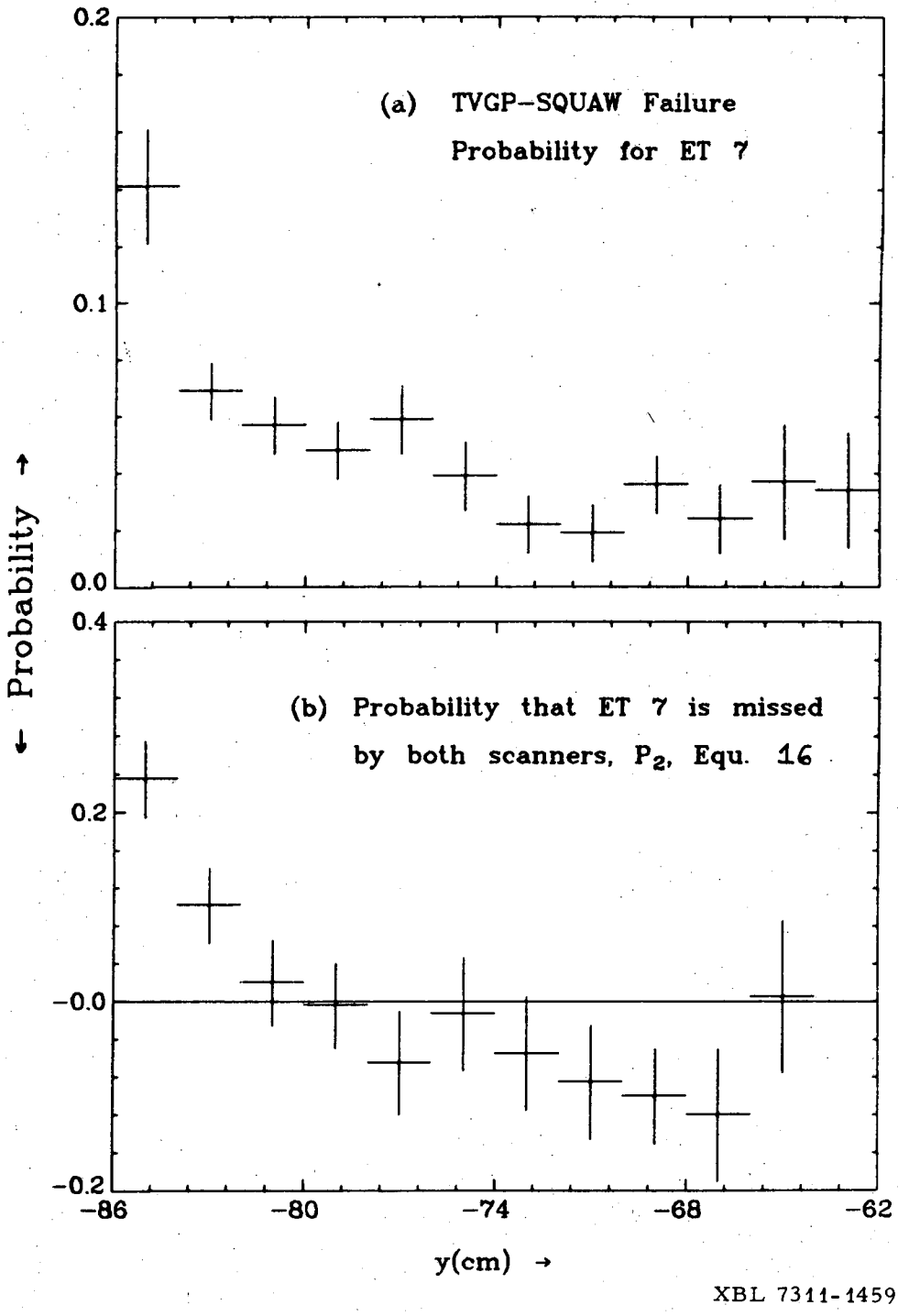


FIGURE II.3 (a) TVGP-SQUAW failure probability for event type 7 as a function of longitudinal position near the plate. (b) Probability that an event type 7 is missed by both scanners, as a function of position. Calculated from equation 16 of this appendix.

APPENDIX III. Neutral Origin Reconstruction.

Contents: A. Algorithm for Finding Track Intersections.

B. Track Fitting.

C. Vertex Reconstruction.

D. TVGP Results.

Appendix III.A Fiducial Referencing.

In the lower energy $\Lambda^o p$ experiment,[1] up to a $\Lambda^o$ momentum of 1200 MeV/c, it was found that the 1-constraint elastic reaction $\Lambda^o p \rightarrow \Lambda^o p$ was nearly completely kinematically unambiguous with competing topologies. At higher energies, $\Lambda^o$ momenta from 1 to 8 GeV/c, this is not at all guaranteed to be the case.[2] Knowledge of the origin of the incident neutral inducing the reaction adds two more constraints to the kinematic solution. This note explains how we have done that.

A. Algorithm for finding track intersections.

The program proceeds as below: In parentheses after each step is noted the subroutine which performs the task. The main control routine is SCORPIO.

(a) Calculate trajectories of all COBWEB measured tracks through the platinum, together with multiple scattering errors, every 5. mm along the trajectory; that is, every 5.mm, store a triplet (x,y,e), where e is normal to the trajectory. (TRACK).

(b) For each beam track, find all outgoing tracks which are within a distance of 400$\mu$ (on film plane) of any point on the beam track. These tracks are the candidates for an intersection. (NOMINAT)

[1] Kadyk, et al., NP B27, 13 (1971).

[2] Bassano, et al., PR 160, 12 39 (1967)

(c) For each point on the beam track, calculate the $\chi^2$ for a point intersection of all outgoing tracks and the beam track. Calculate the (x,y) location of the $\chi^2$ minimum. If there is a clear $\chi^2$ minimum below our $\chi^2$ tolerance, 1. per degree of freedom, go to step (f). If there is a minimum above this $\chi^2$ tolerance, go to (d). If there are multiple minima, or no clear minimum, go to step (e). (COARSE)

(d) Remove from consideration the greatest contributor to the $\chi^2$, then go to step (c), (TROUBLE)

(e) Subdivide the plate into nine (9) sub-plates, and solve the above problem individually for each sub-plate employing the existing machinery of step (c).

(f) Assume the $\chi^2$ distribution is parabolic near its minimum, do a least squares fit to a parabola, and calculate a standard deviation in distance along the beam track such that the $\chi^2$ increases by 1. Store the x,y location and errors for output onto PANAL tape. (VERTEX, ERRORS)

After the problem in each view has been solved, we know which outgoing tracks fit to which beam tracks, and can make a second pass over the plate in which, for each beam track, we do not nominate as a candidate any tracks which have successfully fit to any other beam track. This is a positive definite improvement in the vertex finding efficiency.

B. Track fitting.

In a coordinate system, such as the one below, and for tracks with momentum predominantly along the y-axis, we can suitably parameterize the dependence of x upon y as a linear function with some quadratic deviation,

$$x = ay + by^2$$

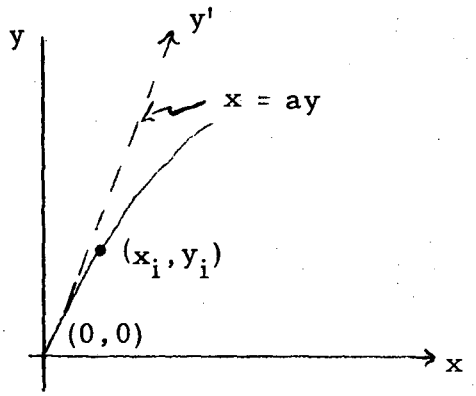


FIGURE III.1

where the origin of the coordinate system is translated to the first measured point of the track. Then for N measured points hypothesized to lie on such a curve, we construct a $\chi^2$ for these points and their errors $(\chi_i, y_i, E_i)$ which is a function of a, b:

$$\chi^2(a,b) = \sum_{i=1}^{N} \left[ \frac{x_i - ay_i - by_i^2}{\epsilon_i} \right]^2 \tag{3.1}$$

In a least squares sense, the minimum in $\chi^2(a,b)$ yields the best estimates of a and b, and is obtained for a, b satisfying

$$\frac{\partial \chi^2}{2a} = \sum_{i=1}^{N} \frac{(x_i - ay_i - by_i^2)y_i}{\epsilon_i^2} = 0 \tag{3.2a}$$

$$\frac{\partial \chi^2}{2b} = \sum_{i=1}^{N} \frac{(x_i - ay_i - by_i^2)y_i}{\epsilon_i^2} = 0 \tag{3.2b}$$

or

$$\begin{aligned} a\, s_1 + b\, s_2 &= s_3 \\ a\, t_1 + b\, t_2 &= t_3 \end{aligned} \tag{3.3}$$

where

$$s_1 = \Sigma \left(\frac{y_i}{\epsilon_i}\right)^2 \qquad t_1 = s_2$$

$$s_2 = \Sigma \frac{y_i^3}{\epsilon_i^2} \qquad t_2 = \Sigma \left(\frac{y_i^2}{\epsilon_i}\right)^2 \tag{3.4}$$

$$s_3 = \Sigma \frac{x_i y_i}{\epsilon_i^2} \qquad t_3 = \Sigma \frac{y_i^2 x_i}{\epsilon_i^2} .$$

Then

$$a = (s_3 t_2 - s_2 t_3)/D$$
$$b = (s_1 t_3 - s_3 t_i)/D \tag{3.5}$$

with

$$D = s_1 t_2 - s_2^2 . \tag{3.6}$$

The momentum at the center of the track is given by

$$P \propto \frac{1}{R} = \frac{[1 + (a + 2b\bar{y})^2]^{3/2}}{2|b|}$$

where $\bar{y}$ is some mean y-value on the track.

Each track so parameterized is given absolute reference to the measured fiducials in each view,[3] and its trajectory extrapolated through the plate with a triplet (x,y,e) stored for 20 points i, such that the third point is just at the downstream edge of the plate, and the eighteenth point is just at the upstream edge. The 8. cm length of the plate in the beam direction spaces the points inside the platinum by approximately 5. mm.

[3] See Appendix III.A for details and constants used.

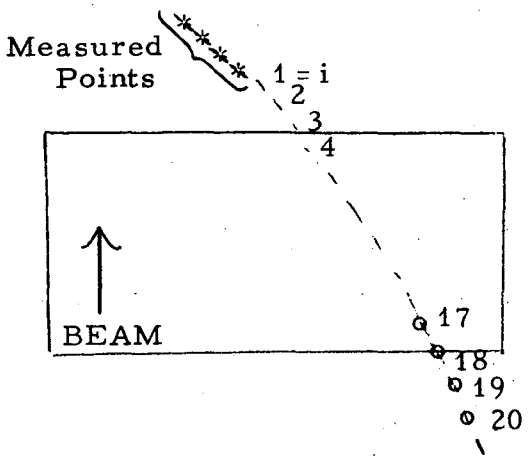


FIGURE III.2

The root-mean-square multiple scattering error perpendicular to the track a distance L into the platinum is taken to be

$$\Delta_{RMS} = \frac{0.015}{P(GeV/c)\beta} \quad \frac{L^{3/2}}{\sqrt{3\, L_{RAD}}}, \text{ with } L_{RAD} = 0.31 \text{ cm.} \tag{3.7}$$

Typically, a $\pi$-meson with momentum 1.GeV/c and traversing half the plate has

$$\Delta_{RMS} \cong 0.1 \text{ cm.}$$

C. Vertex reconstruction.

A vertex point is arrived at by a simple iteration near the chi-squared minimum for the point intersection of the beam track and all candidate outgoing tracks.

The chi-squared distribution along the beam track is searched for a minimum, and three-point Lagrange interpolation is employed to locate the minimum to within typically 0.01 in chi-squared. For these calculated chi-squared points, $\chi^2_{-1}$, $\chi^2_0$, $\chi^2_{+1}$, where $\chi^2_0$ is the least, and for h the abscissa separation between the three points, the chi-squared distribution can be approximated[4] by the function f(y),

$$f(y_0 + ph) \cong \frac{p(p-1)}{2} \chi^2_{-1} + (1-p^2)\chi^2_0 + \frac{p(p+1)}{2}\chi^2_{+1} \tag{3.8}$$

The location of the chi-squared minimum is found by differentiating and solving for p, so that

$$p = \frac{1}{2} \frac{\chi^2_{-1} - \chi^2_{+1}}{(\chi^2_{-1} - 2\chi^2_0 + \chi^2_{+1})}, \tag{3.9}$$

whence the minimum is near $(y_0 + ph)$, where $y_0$ was where $X^2_0$ were evaluated.

If the minimum is greater than CHILIM ( = 1.0) per degree of freedom,[5] the greatest contributor to the chi-squared is eliminated from consideration, and the search repeated.

If there are multiple minima in chi-squared along the beam track, the routine calls SUBURB which subdivide the beam track into approximately 1.0 cm. intervals, and solves the whole problem individually for each interval using existing routines for each task. We can end up with more than one vertex per beam track.

The monte carlo has indicated that whenever the wrong vertex is found, it is always upstream of the correct vertex location. This is easily understood when we consider that the multiple scattering errors on a track, extrapolated upstream through the plate a distance L, increases as $L^{3/2}$. It is much easier to be "close" to a track at the upstream end of the plate.

---

[4] Abramowitz and Stegun, Handbook of Mathematical Functions, Dover, pg. 879 (1965).

[5] This constant can be varied externally.

D. TVGP Results

A sample of free $\Lambda^o$ and $K_1^o$ decays were measured with beam tracks and outgoing tracks (event type 97). Vertex points (x,y) with errors ($\delta_x$, $\delta_y$) found by SCORPIO were reconstructed in three dimensions by TVGP, each vertex with a weight matrix.

$$w = \begin{pmatrix} (1/\delta_x)^2 & 0. \\ 0. & (1/\delta_y)^2 \end{pmatrix}$$

in each view. Improper treatment of the x,y,z three dimensional error matrix for these TVGP reconstructed points was detected and corrected[7] in the subroutine LSVERT. Without correction, any attempt to reconstruct neutral particle origins in this manner would have been impossible.

SQUAW attempted 3-constraint fits, for all good 1-constraint $\Lambda^o$, $K_1^o$ decay fits, to these reconstructed origins. A series of distributions of relevant fitted and spatial quantities are in Figs. III.3 through III.8.

Firstly, the fitted $\chi^2$ distributions are (Fig. III.3) the 1C, in which only the mass of the particle in the initial state is known, and all four-vectors in the final state are measured; (Fig. III.4) the 3C, in which only the magnitude of the momentum in the initial state is unknown; and (Fig. III.5) the 2C distribution, defined to be the 3C minus the 1C chi-squared. The most relevant is the 2C chi-squared distribution, which isolates the kinematics of the decay from the 2-dimensional directional constraints provided by knowledge of the origin. The curve superposed is a mathematical chi-squared distribution for 2 constraints. Note that nuclear scattering of the outgoing neutral particle will contribute

[7] Thanks to Dr. Frank Solmitz.

to a long thin tail on the 2C chi-squared distribution which cannot be removed.

Secondly, the 3-constraint pull quantities on the fitted dip and azimuth of the incident decaying neutral (Fig. III.6), the proton or pi-plus (Fig. III.7), and the pi-minus (Fig. III.8) are given in Figs. III.6 to III.8.

Thirdly, there are several distributions relating to the origin points themselves. We begin with some definitions.

Coords in SIOUX coordinate system:

x = transverse to beam,

y = beam direction

Z = depth in chamber; paralax factor ~ 6.

Connecting neutral track (reconstructed to origin point x, y, z, and event interaction point):

$\ell$ = length

$\Delta\phi$ = azimuth error

$\Delta\lambda$ = dip error

Semi-major axes of TVGP three-dimensional error ellipse on point (x, y, z):

$\Delta x \cong \ell \cdot \Delta\phi$

$\Delta y = \Delta\ell$

$\Delta z \cong \ell \cdot \Delta\lambda$ .

In Fig. III.9, the y-error on reconstructed $LH_2$ origins is approximately a bubble-width ( ~ 0.5 mm) and checks that the calculations and constants of Appendix III.A are roughly correct. A $LH_2$ origin is any vertex, or bubble, in the chamber, and is measured as single one-point

track in each view with assigned errors $\Delta x = 15.\mu$, $\Delta y = 30.\mu$ on film plane.

The $\Delta$-error distribution, Figs. III-10 and III.11, for points reconstructed inside the platinum, shows the width $\langle \Delta x \rangle \cong 0.4$ mm expected from the multiple scattering of a 12.0 GeV/c $K^-$ in $\sim$ 25 radiation lengths of platinum (Fig. III.11). One disturbing feature is the presence of events at $\Delta x \cong 0.7$ cm. This persists in the $\Delta y$ and $\Delta z$ distributions, and will be discussed later.

The y-error distribution, Figs. III.12 and III.13 shows that most $\Delta y$ are less than 1 cm. The sharp structure at $\Delta y \cong 2.5$ cm is due to origins points given the half-width of the plate ($\pm$ 4.0 cm) in all three views. The structure at $\Delta y \approx 1.4$ cm is related to the $\Delta x \cong 0.7$ cm structure.

The z-error distribution, Fig. III.14 reflects the 82" chamber paralax factor of $\sim 6$. We expect that, for a given ensemble of origins, $\langle \Delta z \rangle \approx 6 \langle \Delta x \rangle$. This is well-satisfied for the two dominant peaks in Figs. III.11 and III.14 where $\langle \Delta x \rangle = 0.03$ cm and $\langle \Delta z \rangle \cong 0.19$ cm.

Figures III.15, 16, 17 display the x,y, and z distributions of the origin points, with the platinum plate denoted for reference.

The quantized structure in the $\Delta x$, $\Delta y$, and $\Delta z$ distributions is believed to be due to large errors assigned to film plane origin points in 2 of 3 views. For instance, suppose a good intersection is found in view 1, but no origin is found in view 2. Then the center of the plate is chosen as the y-coordinate in view 2 with an error

$$\left.\begin{array}{l} \Delta y = 2640.\mu \text{ on film} \\ \cong 4.0 \text{ cm in space} \end{array}\right\} \quad \begin{array}{l} \text{no origin found} \\ \text{on beam track} \end{array}$$

Routinely, the y-error on any origin in View 3 is set to

View 3 origins

$\Delta y = 2200.\mu$ on film

$\cong 3.3$ cm in space

$\Delta x = 50.\mu$ on film

$\cong 0.75$ cm in space

TVGP combines these three views with differing errors and arrives at a three-dimensional error illipse. Such origins as the above are not very reliable in any case and should probably be ignored, or corrected for, in the analysis.

APPENDIX III A. Referencing reconstructed tracks to fiducials in each view.

In each view (IW) we record the constants in the figure at right:

DFA (IW) XB (IW)

DFB (IW) STEP (IW)

and EM (IW)

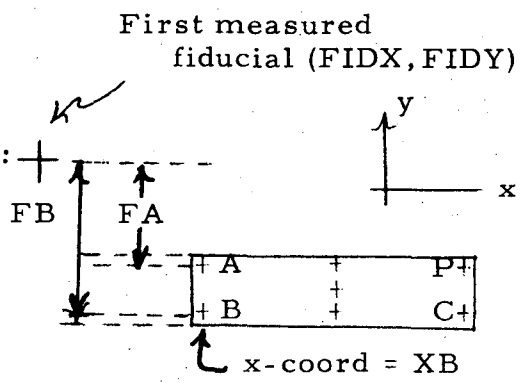


in units of microns on the film plane, where EM is the slope of the plate in the x-y plane to one-half centimeter in space.

| | VIEW 1 | VIEW 2 | VIEW 3 |
|---|---|---|---|
| DFA | 20907 $\mu$ | 20724 $\mu$ | 17982 $\mu$ |
| DFB | 26228 $\mu$ | 26001 $\mu$ | 23382 $\mu$ |
| EM | 0.0299 | 0.0313 | 0.0563 |
| X | 35025 $\mu$ | 38000 $\mu$ | 37833 $\mu$ |
| STEP | 319.59 $\mu/\frac{1}{2}$ cm | 323.83 $\mu/\frac{1}{2}$ cm | 327.42 $\mu/\frac{1}{2}$ cm |

Then for beam tracks, the distance from the dirst COBWEB measured point (XO, YO) to the edge of the platinum in view IW is approximately

YSHIFT = FIDY (1, IW, MM) - DFB (IW) - YO + EM (IW) * (XO - XB(IW))

and for outgoing tracks.

YSHIFT = FIDY (1, IW, MM) - DFA(I, W) - YO + EM(IW) * (XO - XB(IW))

Then the first point of the platinum track bank (PTK (3,20,40)) is translated to be

y = 2.*STEP (IW) - YSHIFT (for outgoing track)

y = YSHIFT - 2.*STEP (IW) (for beam tracks)

This is the same coordinate system to which COBWEB measured tracks are normally referenced. The origin reconstruction in program SCORPIO is performed in this coordinate system, and the vertex points reconstructed in the platinum are subsequently translated back to the original COBWEB corrdinate system for output onto the PANAL tape.

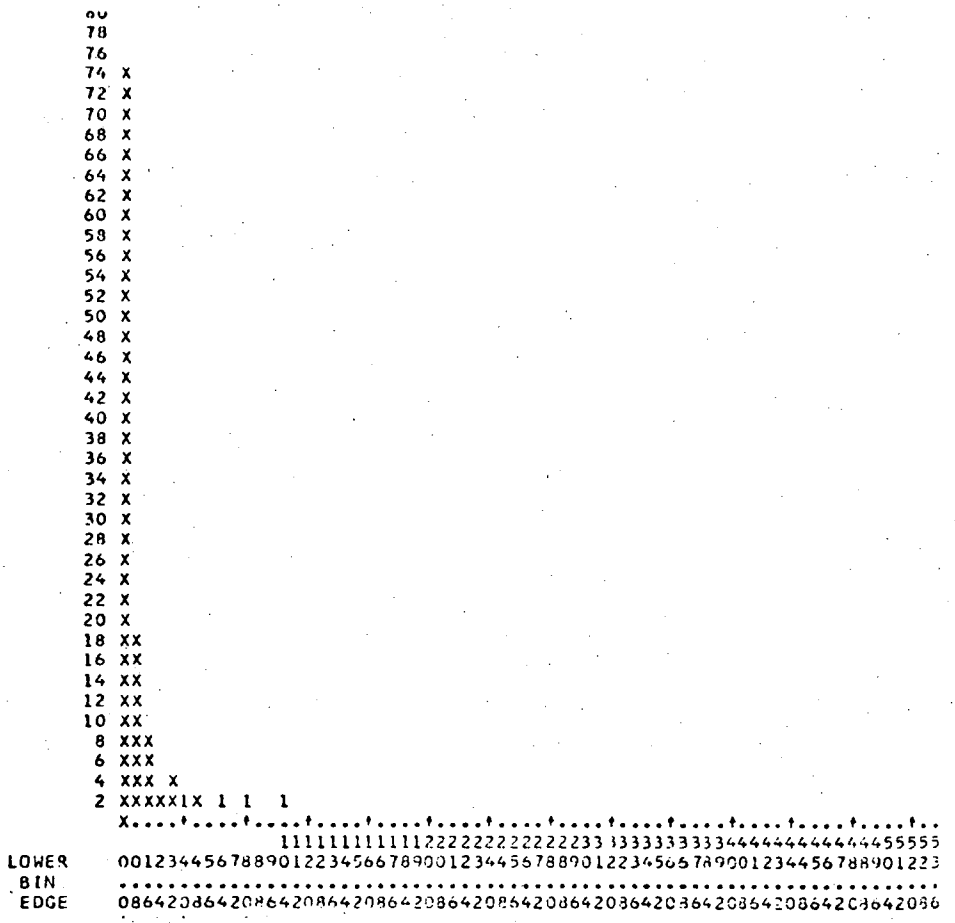


Figure III. 3 One-constraint chi-squared distribution for the sample.

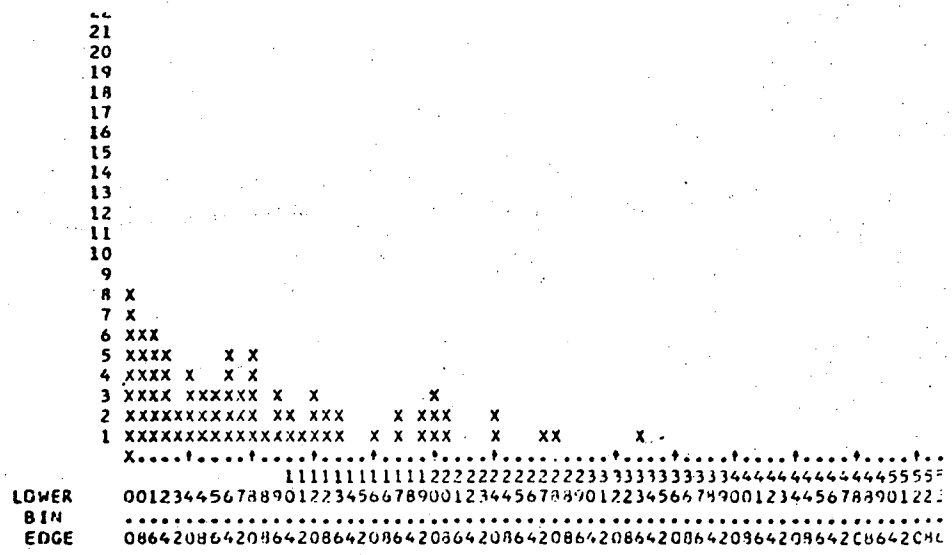


Figure III. 4 Three-constraint chi-squared distribution.

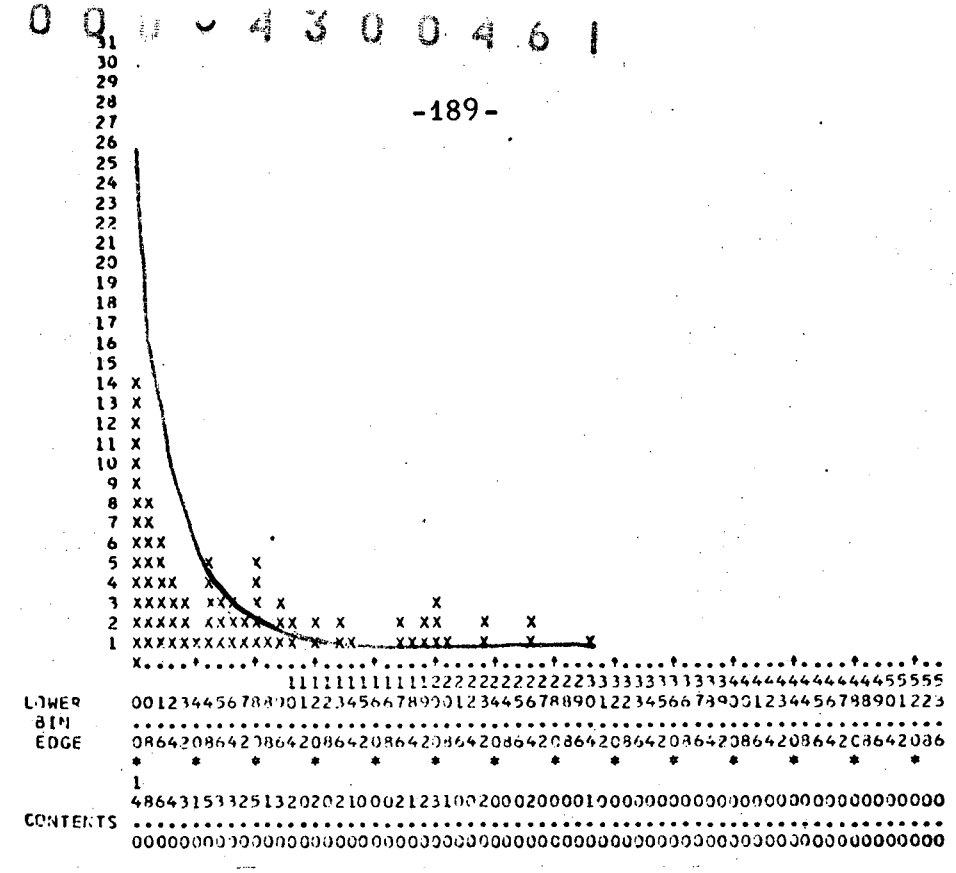


Figure III. 5 Two-constraint chi-squared, precisely equal to the difference of the three- and one-constraint chi-squared, which isolates the constraints imposed by the transverse origin location information.

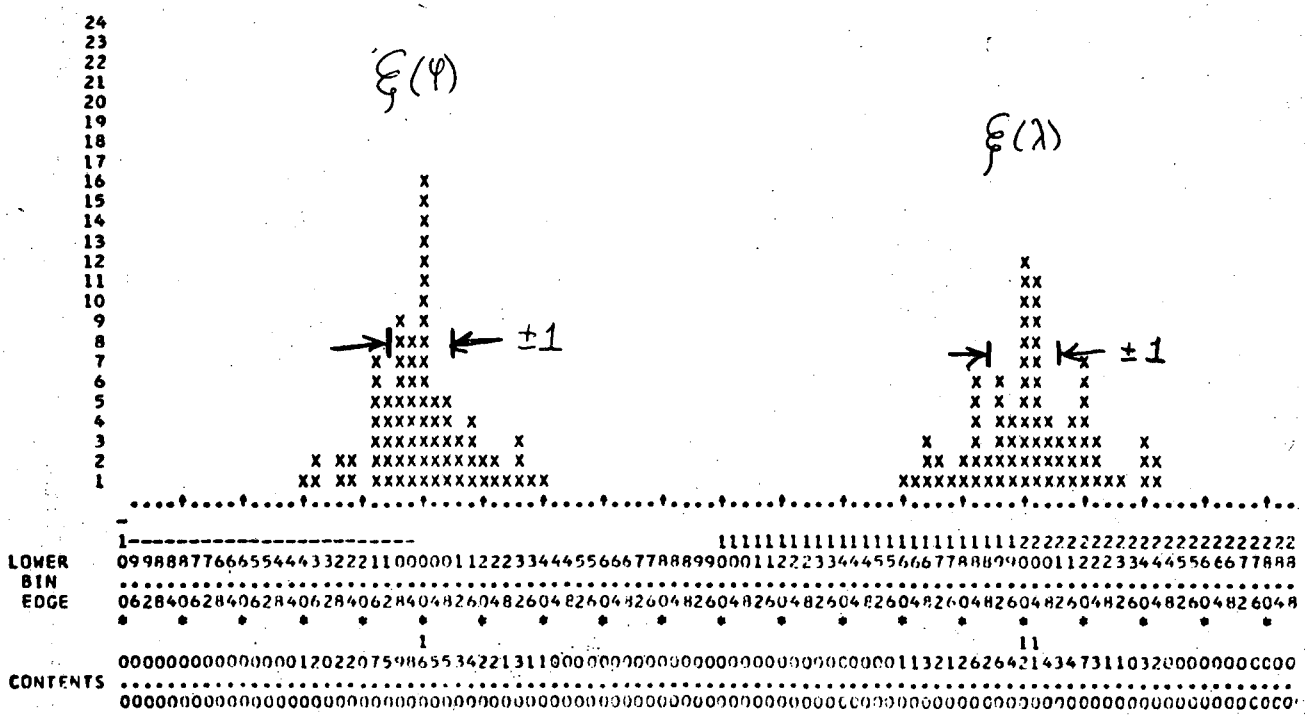


Figure III. 6 Pull quantities, normalized to a Gaussian distribution, for the two angular directional constraints in azimuth and dip angle for an ensemble of $\Lambda \rightarrow p\pi^-$ and $K_1^0 \rightarrow \pi^+\pi^-$

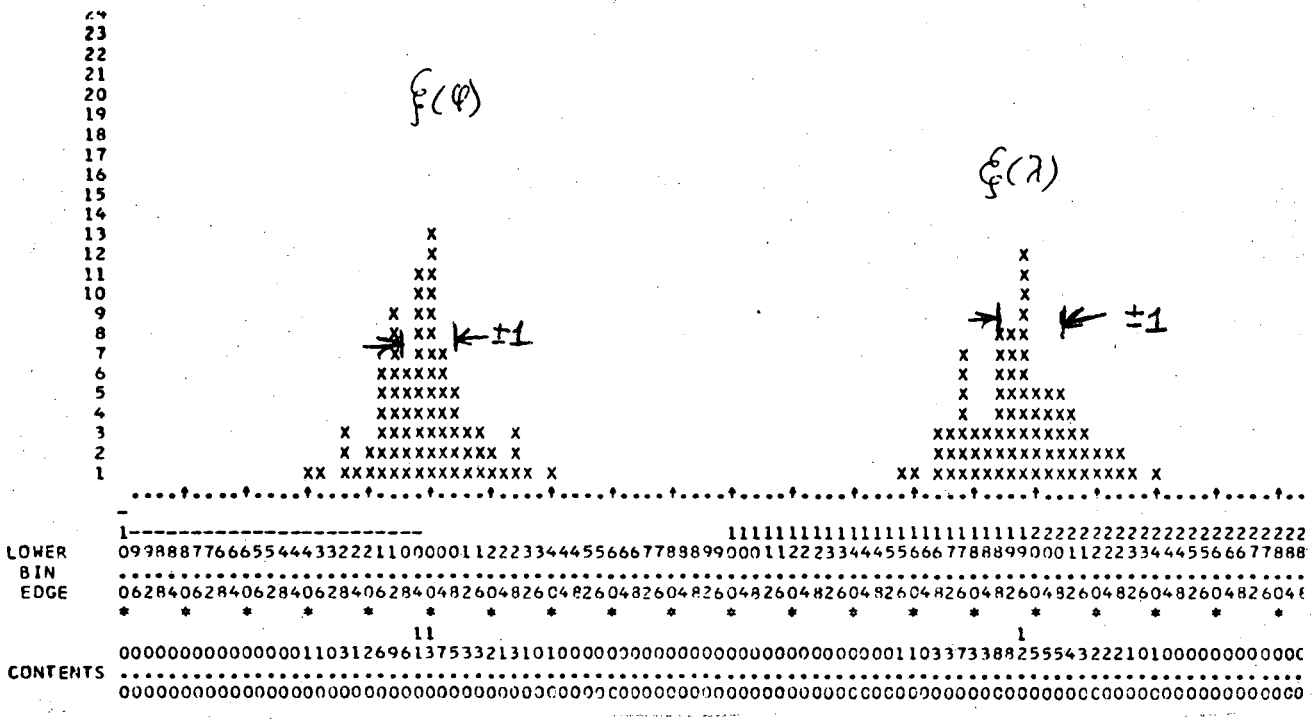


Figure III. 7 Pull quantities for the P or $\pi^+$ in the same decays as in the previous figure.

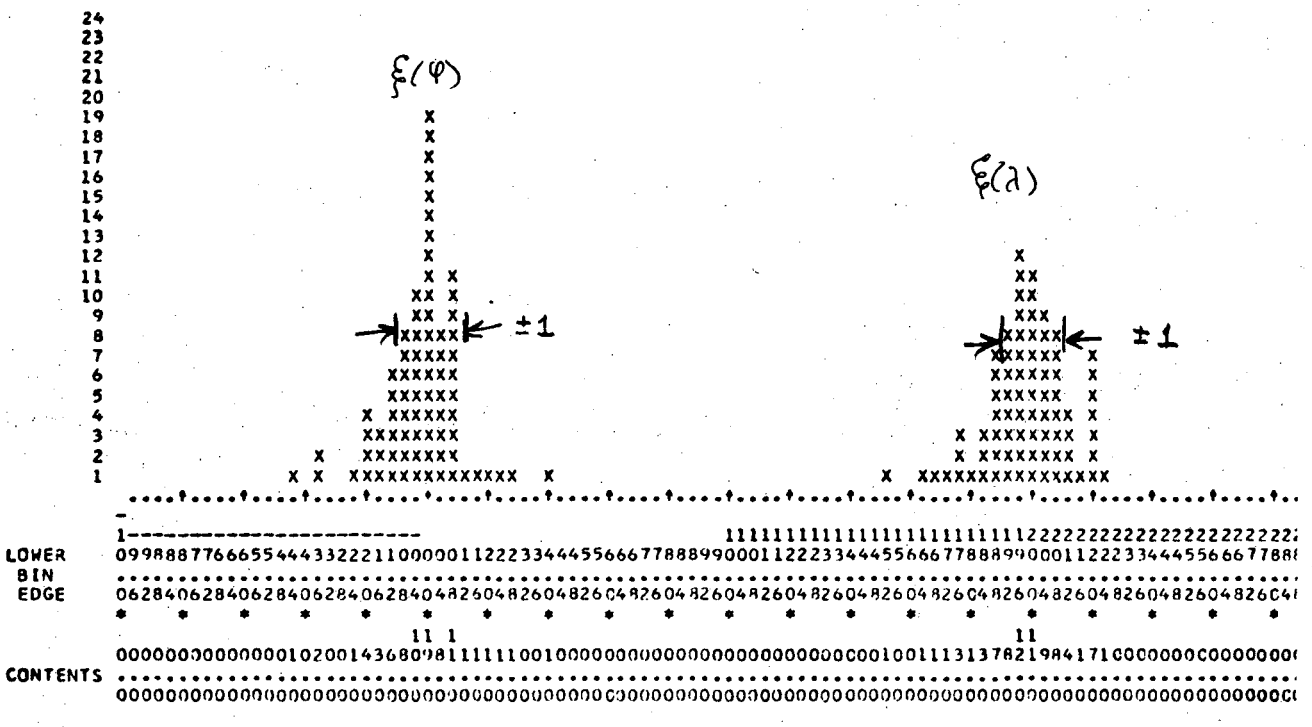


Figure III. 8 Pull quantities on the $\pi^-$ for the same decays as above.

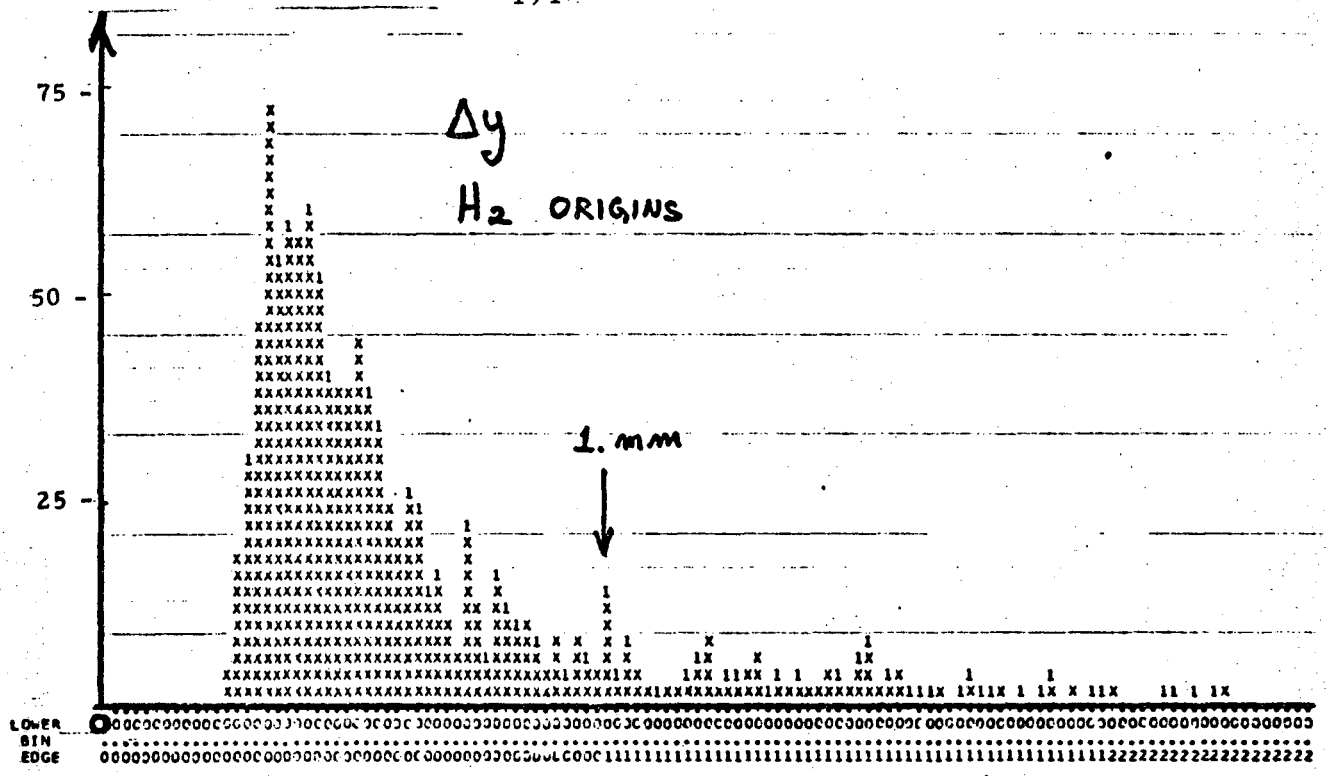


Figure III. 9 Distribution of reconstructed origin errors along the beam direction (y-coordinate) for origins located in the liquid hydrogen.

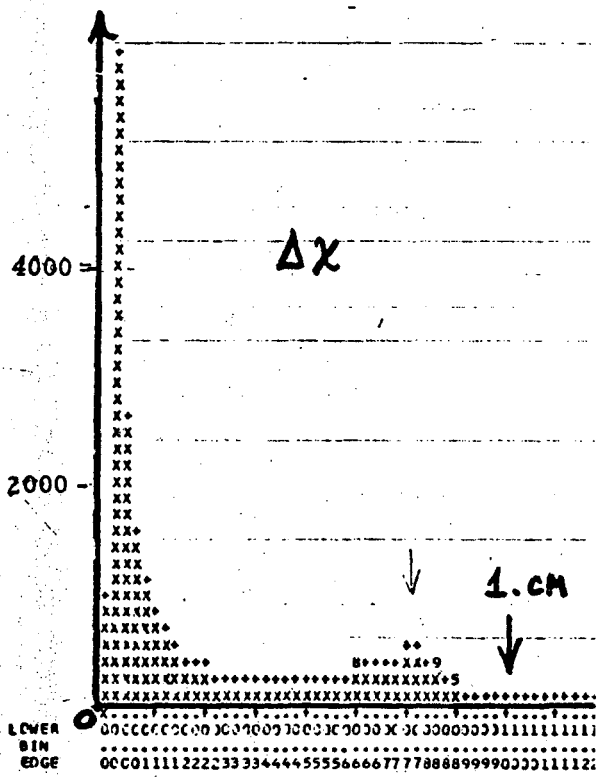


Figure III. 10 Distribution of origin errors transverse to the beam (x-coordinate).

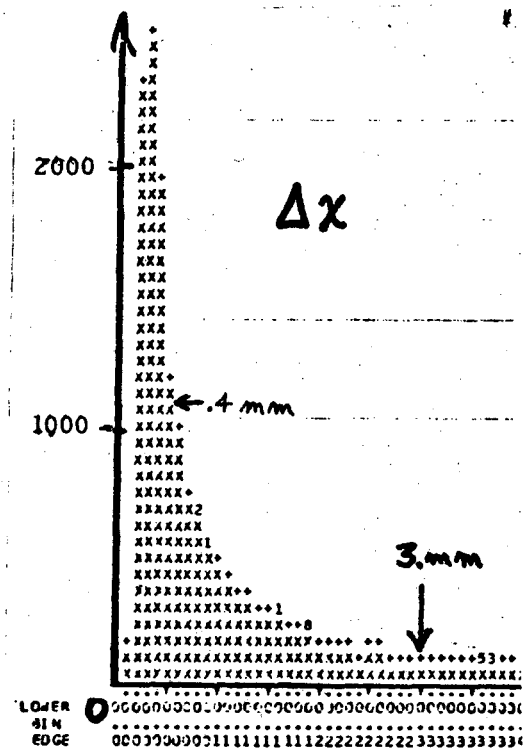


Figure III. 11 Same as III. 10, but with finer scale.

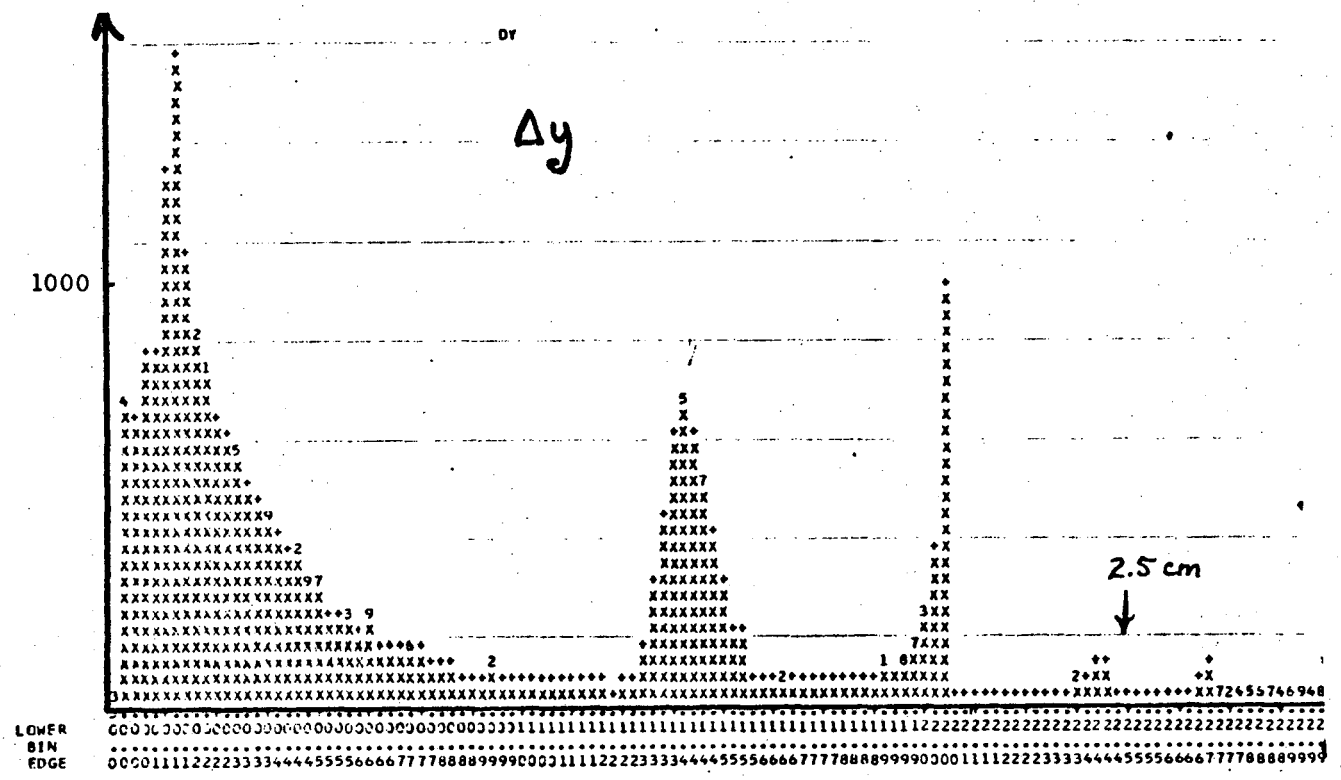


Figure III. 12 Distribution of reconstructed origin errors along the beam direction (y-coordinate) for origins located in the platinum plate and the liquid hydrogen.

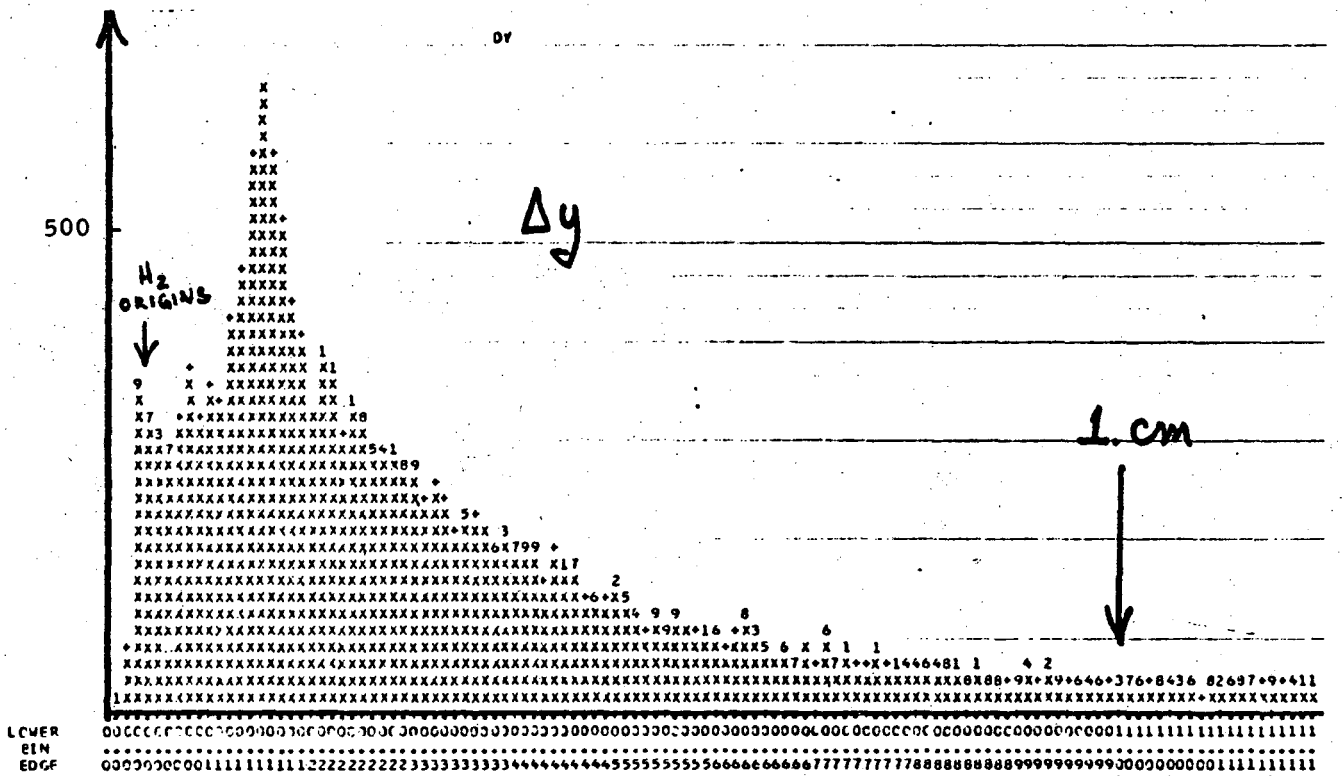


Figure III. 13 Same as III. 12, but for $\Delta y \leq 1.$ cm.

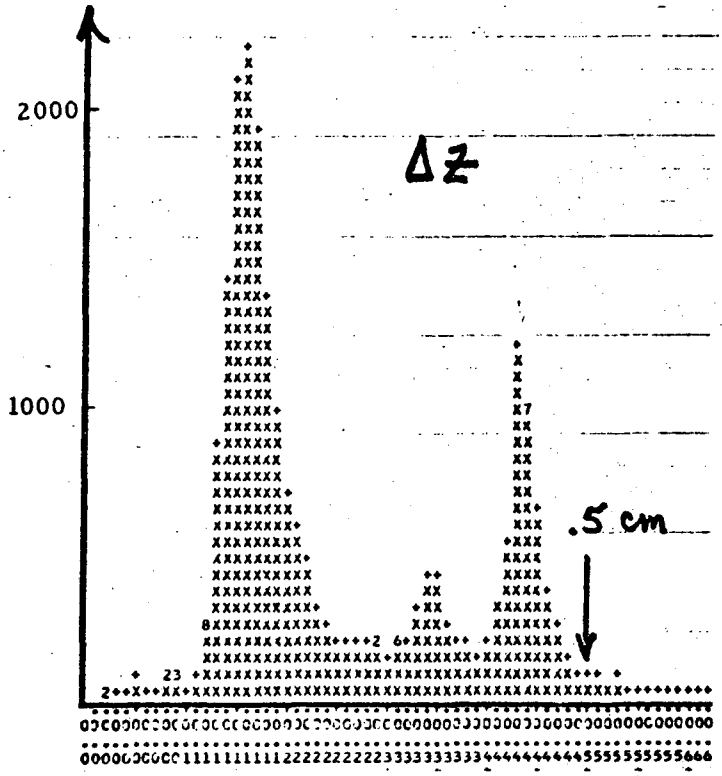


Figure III. 14 Distribution of reconstructed origin errors in chamber depth for origins inside the platinum plate.

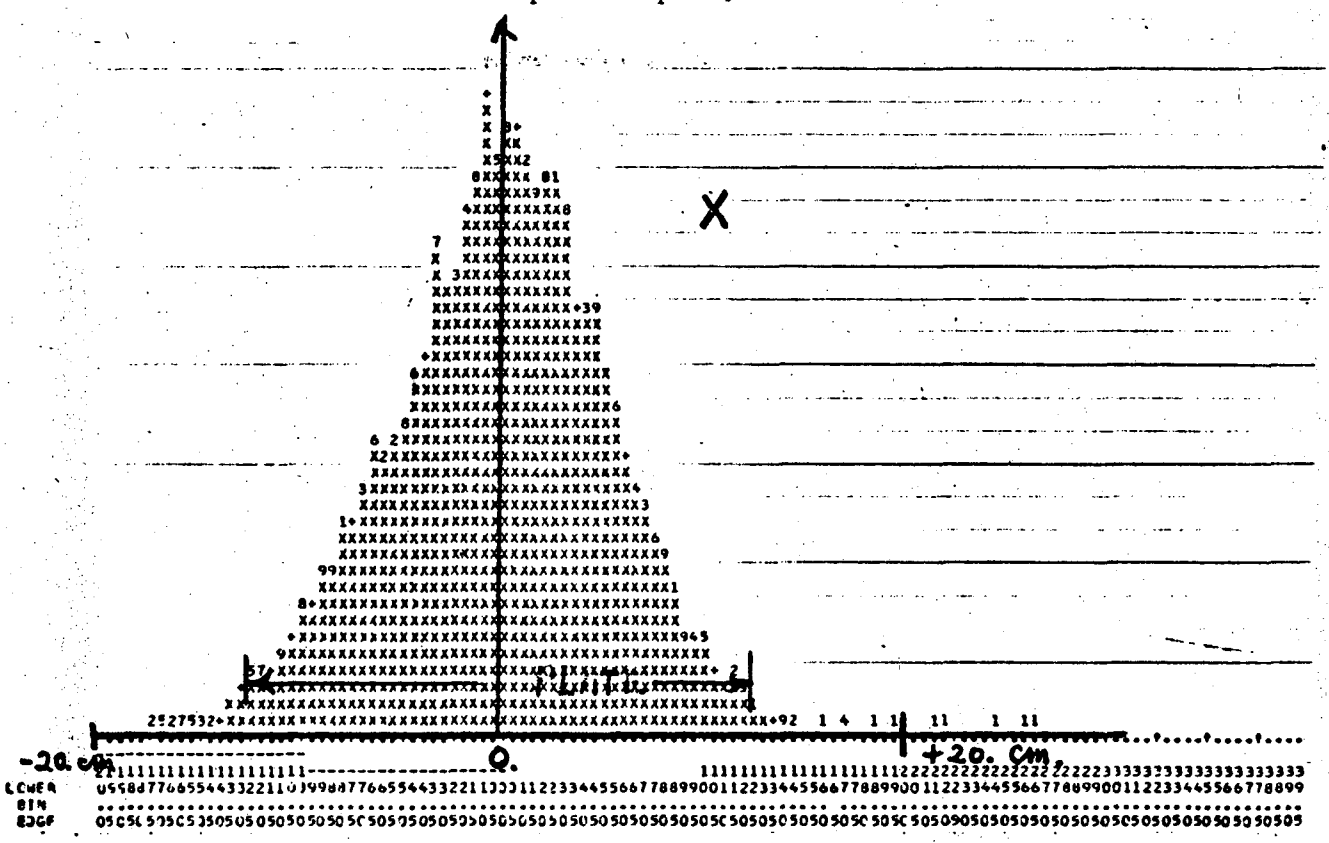


Figure III. 15 Distribution of reconstructed origin coordinates transverse to beam (x-coordinate). The plate location is denoted for reference.

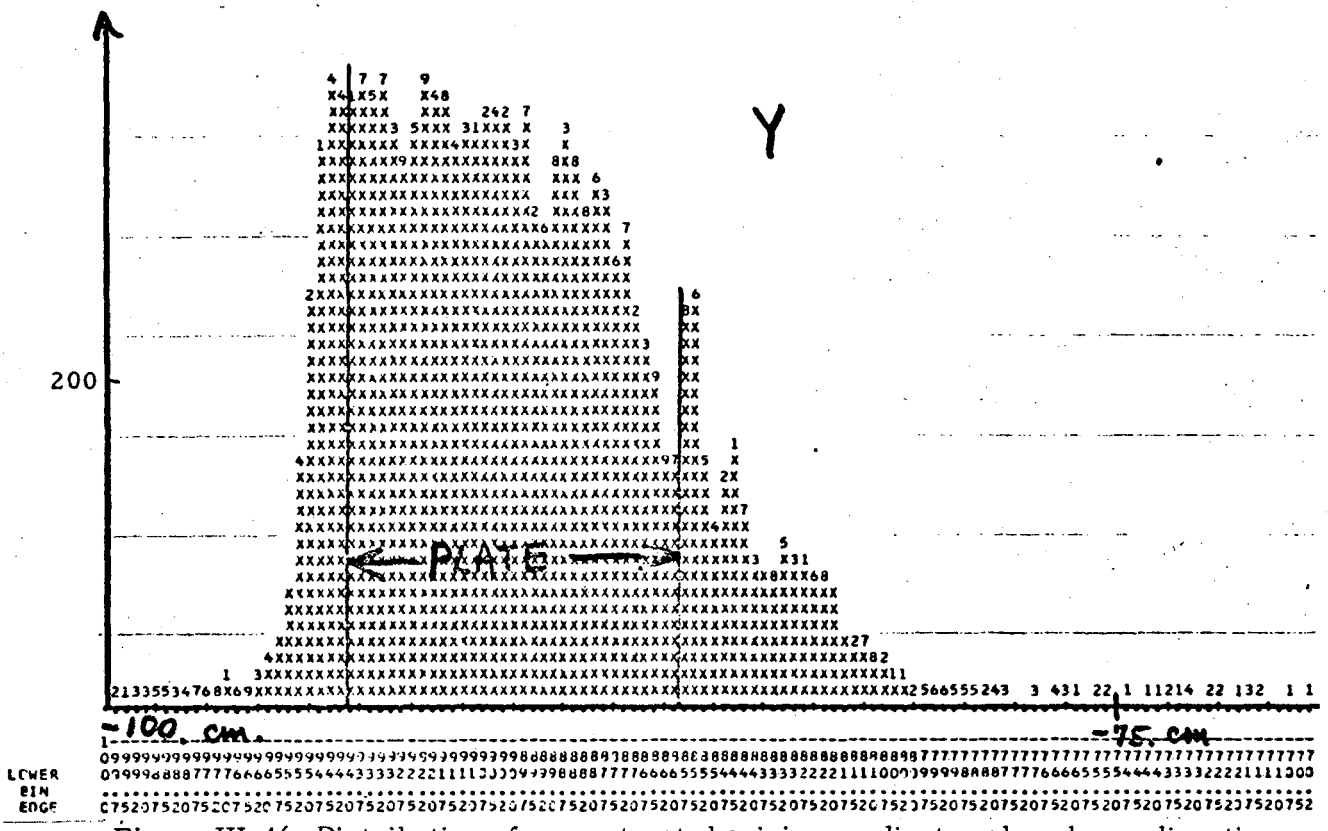


Figure III. 16 Distribution of reconstructed origin coordinates along beam direction.

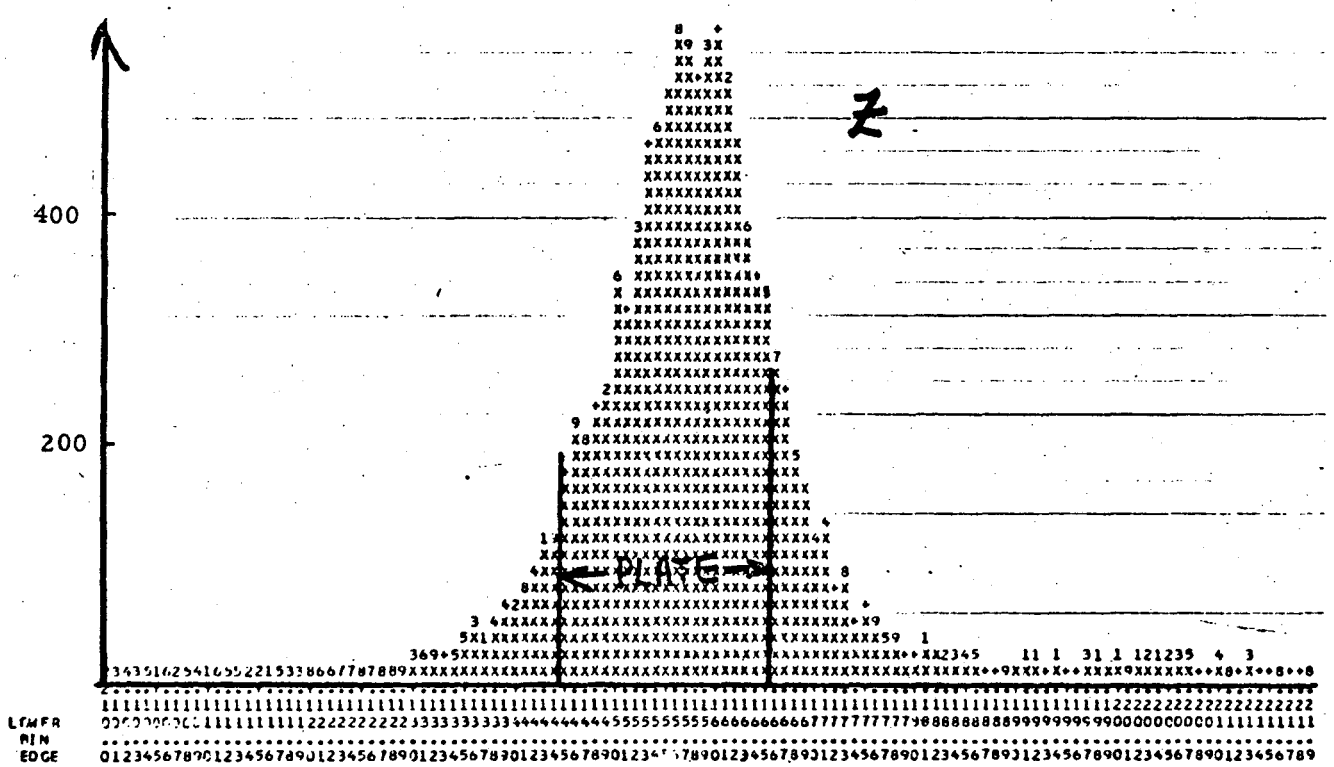


Figure III. 17 Distribution of reconstructed origin coordinates in chamber depth (z-coordinate).

APPENDIX IV. Lorentz Invariant Phase Space.

The two- and three-body phase space distributions in Sec. IV were calculated according to Hagedorn[1], employing the recursion relation stated by him. In Hagedorn's notation, the four-momentum of particles $i = 1 \ldots k$ out of $n$ particles ($k < n$), and the four-momentum of the remaining $(n-k)$ particles, are

$$P_k = \sum_{i=1}^{k} p_i \qquad M_k^2 = P_k^2$$

$$P_{n-k} = \sum_{i=k+1}^{m} p_i \qquad M_{n-k}^2 = P_{n-k}^2 .$$

The probability distribution of the mass $M_k$ is given by

$$P(M)dM^2 = \frac{R_{n-k+1}(P;M, m_{k+1} \cdots m_n)\, R_k(P_k;m_1 \cdots m_k)}{R_n(P;m_1 \cdots m_n)} ,$$

where $R$ is the phase space integral

$$R_n(P;m_1 \cdots m_n) = \int \cdots \int \sum_{i=1}^{n} d^4p_i\, \delta(p_i^2 - m_i^2)\, \delta^4\Big(\sum_{j=1}^{n} p_j - P\Big).$$

These integrals were evaluated using the program written by P. Yager.[2]

---

[1] R. Hagedorn, Relativistic Kinematics, 1963, W.A. Benjamin.

[2] P. Yager, program HNREVIS, Feb. 1965, unpublished technical note, Univ. of Calif. at Davis, Dept. of Physics.

## APPENDIX V. Analysis of Other Hyperon Physics in This Experiment.

In the course of the $\Lambda$ experiment, we have also scanned the film for topologies other than those restricted by $\Lambda p$ interactions. With a view towards studying the following reactions:

$$\Xi^- \rightarrow \Lambda\pi^- \qquad 5.1\ (a) \qquad 5.1$$

$$\Omega^- \rightarrow \Lambda K^- \qquad (b)$$

$$\rightarrow \Xi^-\pi^0 \qquad (c)$$

$$\Sigma^+ p \rightarrow \Sigma^+ p \qquad (d)$$

$$\Sigma^- p \rightarrow \Sigma^- p \qquad (e)$$

$$\Xi^0 p \rightarrow \Lambda\Lambda\pi^+ \qquad (f)$$

$$\rightarrow \Lambda\Lambda\pi^+\pi^+\pi^- \qquad (g)$$

$$\rightarrow \Sigma^+\Lambda \qquad (h)$$

$$\rightarrow \Sigma^+\Lambda\,\pi^+\pi^- \qquad (i)$$

$$\rightarrow \Sigma^+\Lambda\,\pi^+\pi^+ \qquad (j)$$

$$\rightarrow \Sigma^+\Sigma^-\pi^+ \qquad (k)$$

$$\rightarrow \Xi^- p\,\pi^+ \qquad (l)$$

and possibly others, we have systematically scanned for the topologies of Fig. V.1 in addition to those in Fig. 3, Section I.

The momentum distribution of 1898 $\Xi^-\rightarrow\Lambda\pi^-$ decays is displayed in Fig. V.2 and has not been corrected for decay losses inside the platimum plate. The distribution cosine of the decay proton with respect to the decay $\Lambda$ direction for $\Xi^-\rightarrow\Lambda\pi^-$ decays is shown in Fig. V.3. A non-isotropic distribution of this cosine reveals parity violation in the decay, where the distribution is described by

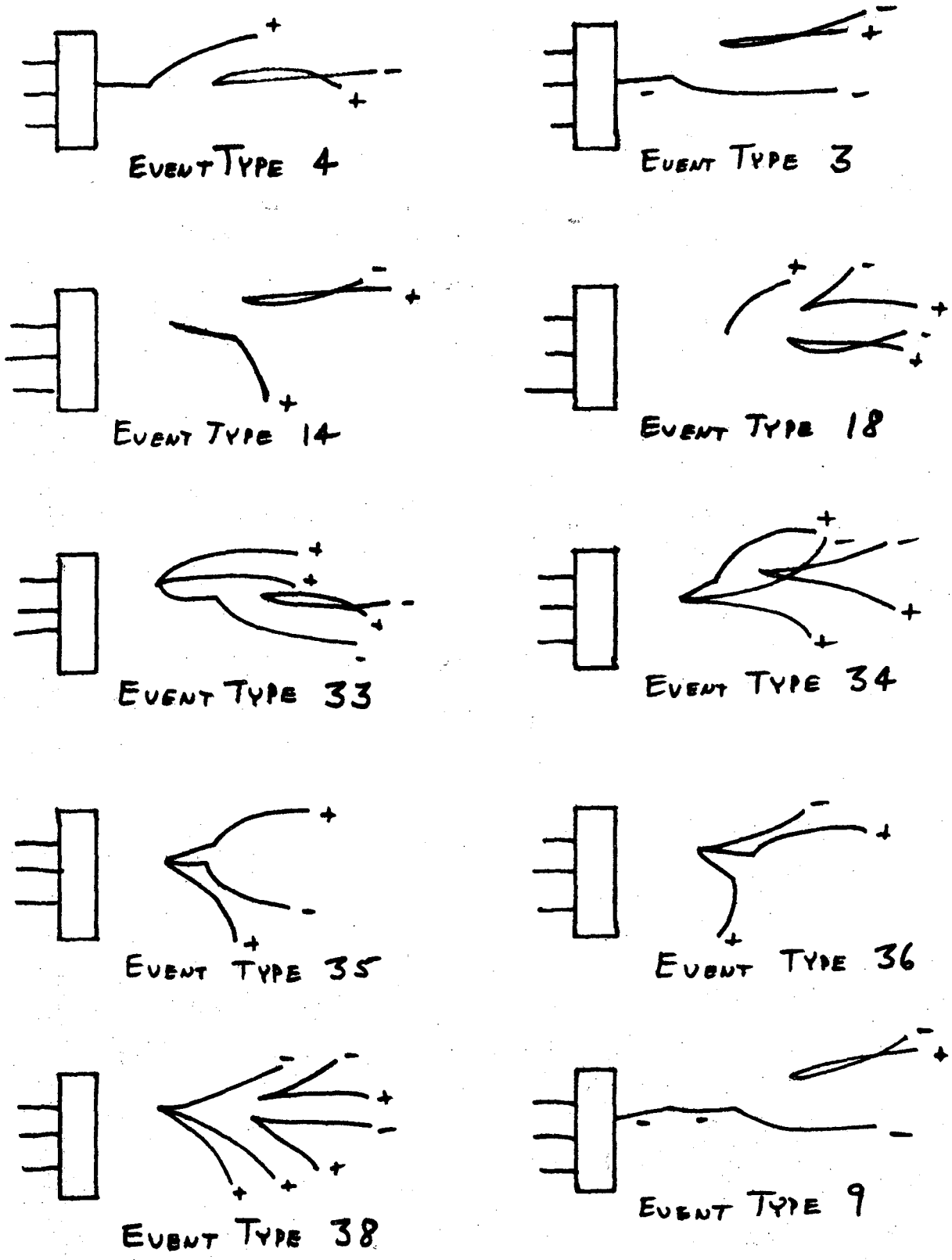


Figure V.1. Event type topologies for multi-strange particle events.

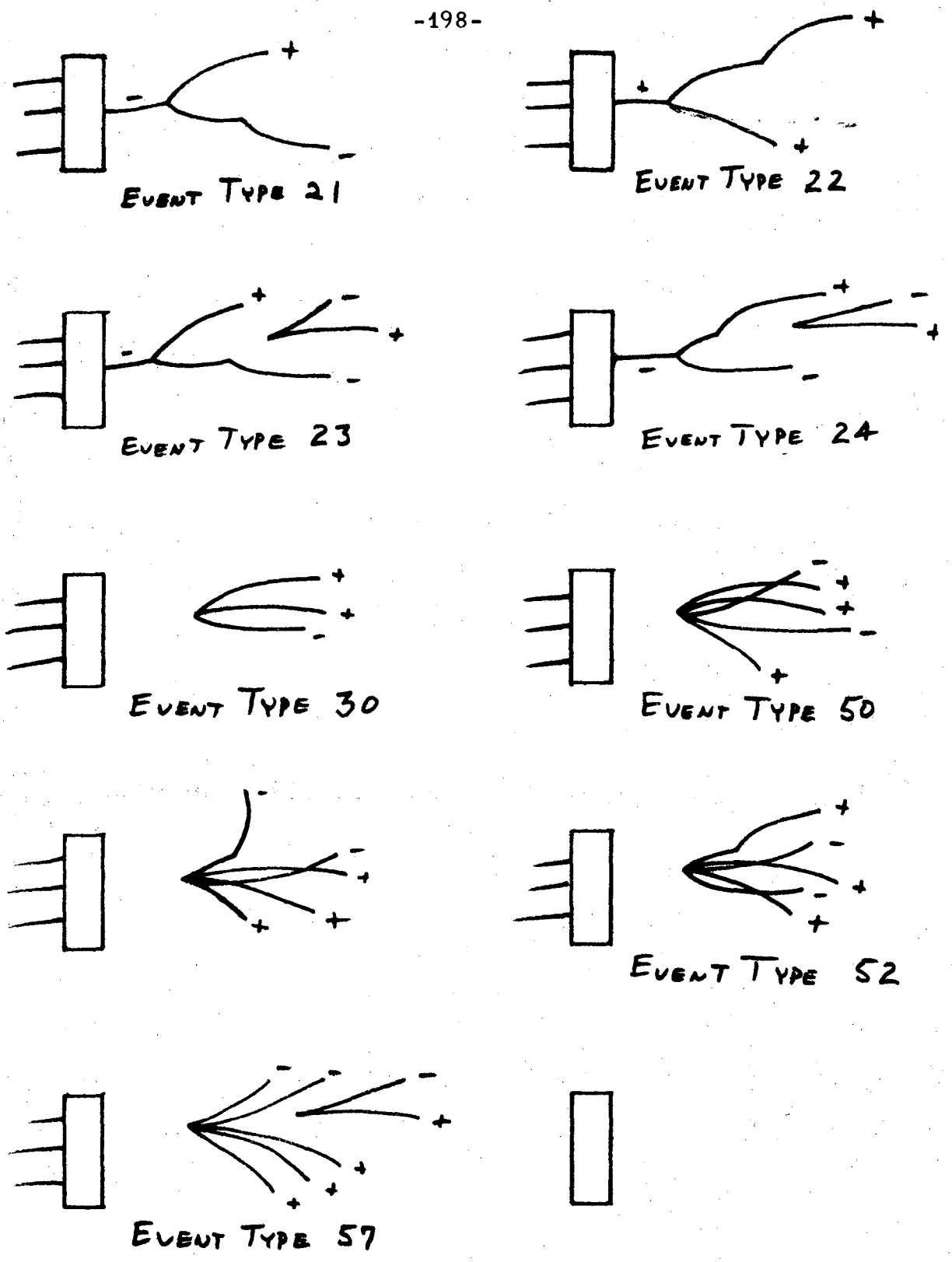


Figure V.1. (continued)

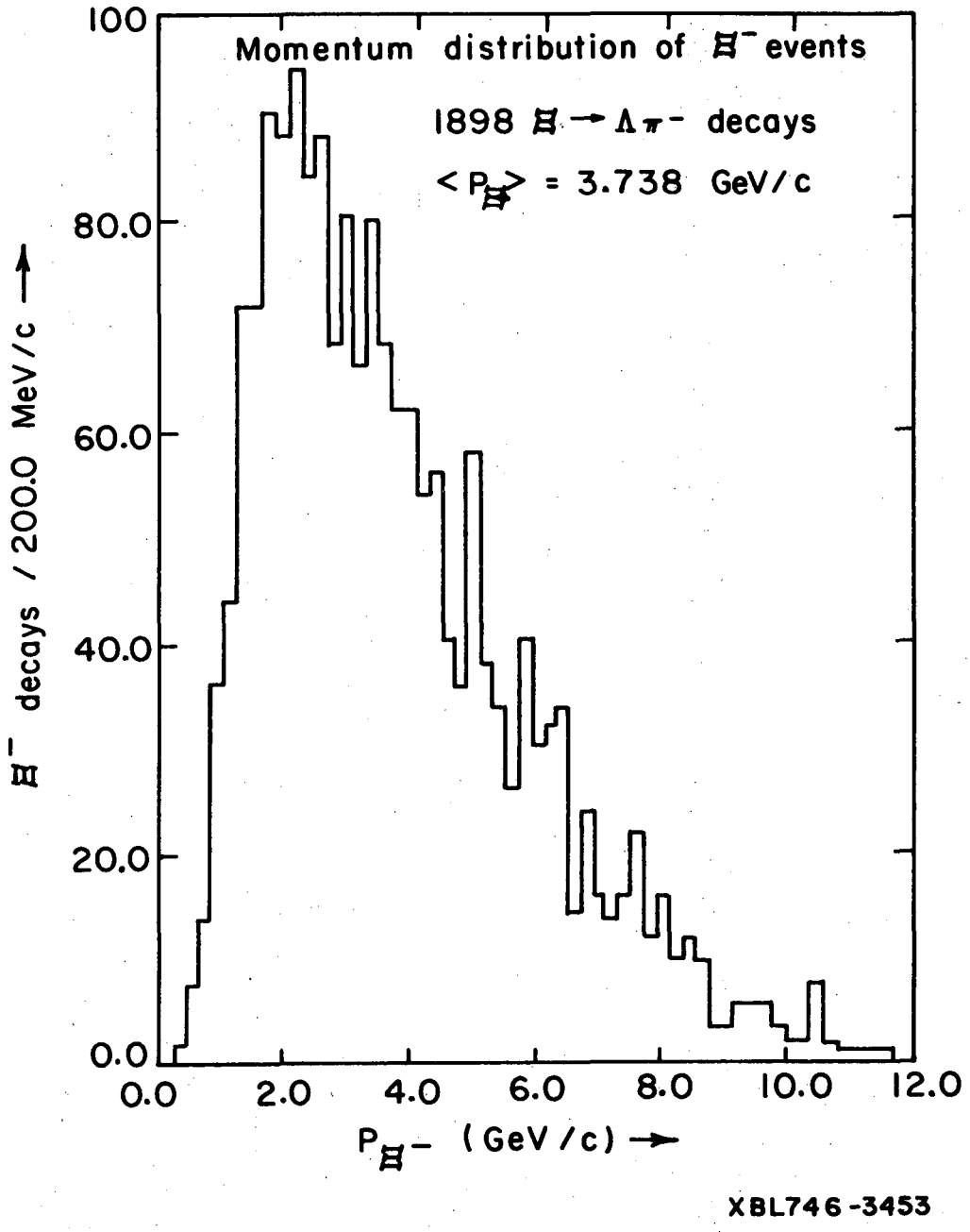


Figure V.2. Laboratory momentum distribution of $\Xi^- \to \Lambda\pi^-$ decays observed on this experiment.

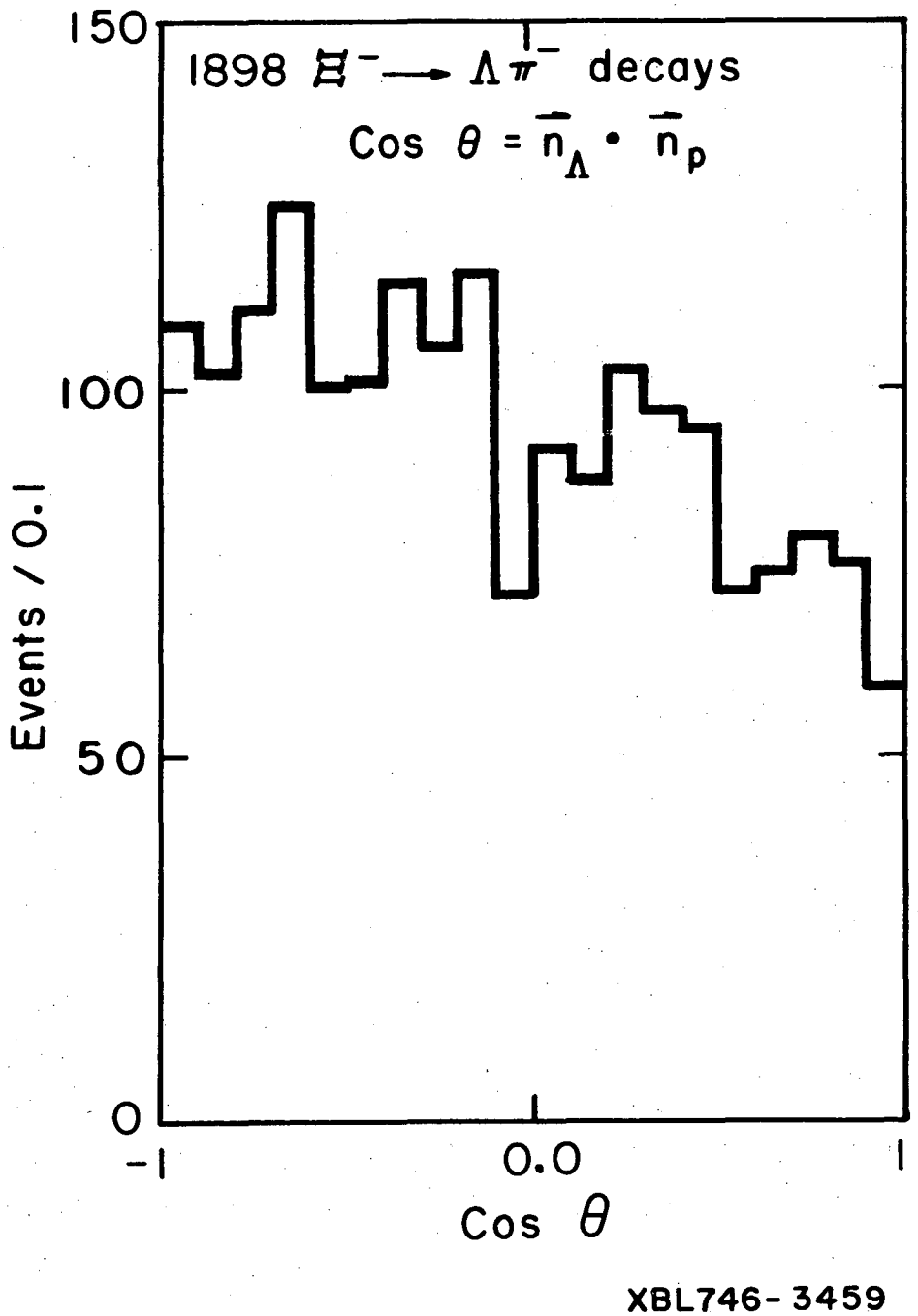


Figure V.3. Distribution of the parity violating cosine in $\Xi^- \rightarrow \Lambda\pi^-$ decay.

$$\frac{dN}{d(\cos\theta)} \propto 1 + \alpha_\Lambda \alpha_{\Xi^-} \cos\theta \qquad 5.2$$

under the assumption that the $\Xi^-$ decays only vis S and P waves. Then

$$\alpha_{\Xi^-} = \frac{2\,\mathrm{Re}\, S^* P}{|S|^2 + |P|^2},$$

and $\alpha_\Lambda$ is the corresponding parameter in $\Lambda \to p\pi^-$ decay, $\alpha_\Lambda = 0.647 \pm 0.013$. Hence a non-zero $\alpha_{\Xi^-}$ measures a non-zero slope in the cosine distribution, and this is equivalent to a non-zero contribution of an S-wave amplitude in the decay. The initial state $\Xi^-$ has positive parity, $P_{\Xi^-} = +1$, and the final state $\Lambda\pi^-$ has parity

$$(P_\Lambda = +1)\,(P_\pi = -1)\,(-1)^\ell = -1 \qquad \text{(S-wave)}$$
$$= +1 \qquad \text{(P-wave)}$$

hence S-wave decay violates parity conservation.

Figure V.4 displays the variation of a likelihood function for the probability distribution 5.2

$$\mathcal{L} = \prod_{i=1}^{N} \{1 + \alpha_\Lambda \alpha_{\Xi^-} \cos\theta_i\}$$

whose maximum value is obtained at

$$\alpha_{\Xi^-} = -0.394 \pm 0.070.$$

No corrections have been applied to the data for this measurement.

The $\Omega^- \to \Lambda K^-$ decay is nearly completely unambiguous with $\Xi^- \to \Lambda\pi^-$ decay, essentially because there is very little kinematic overlapping of the decay kinematics as seen in the laboratory in Fig. V.5.

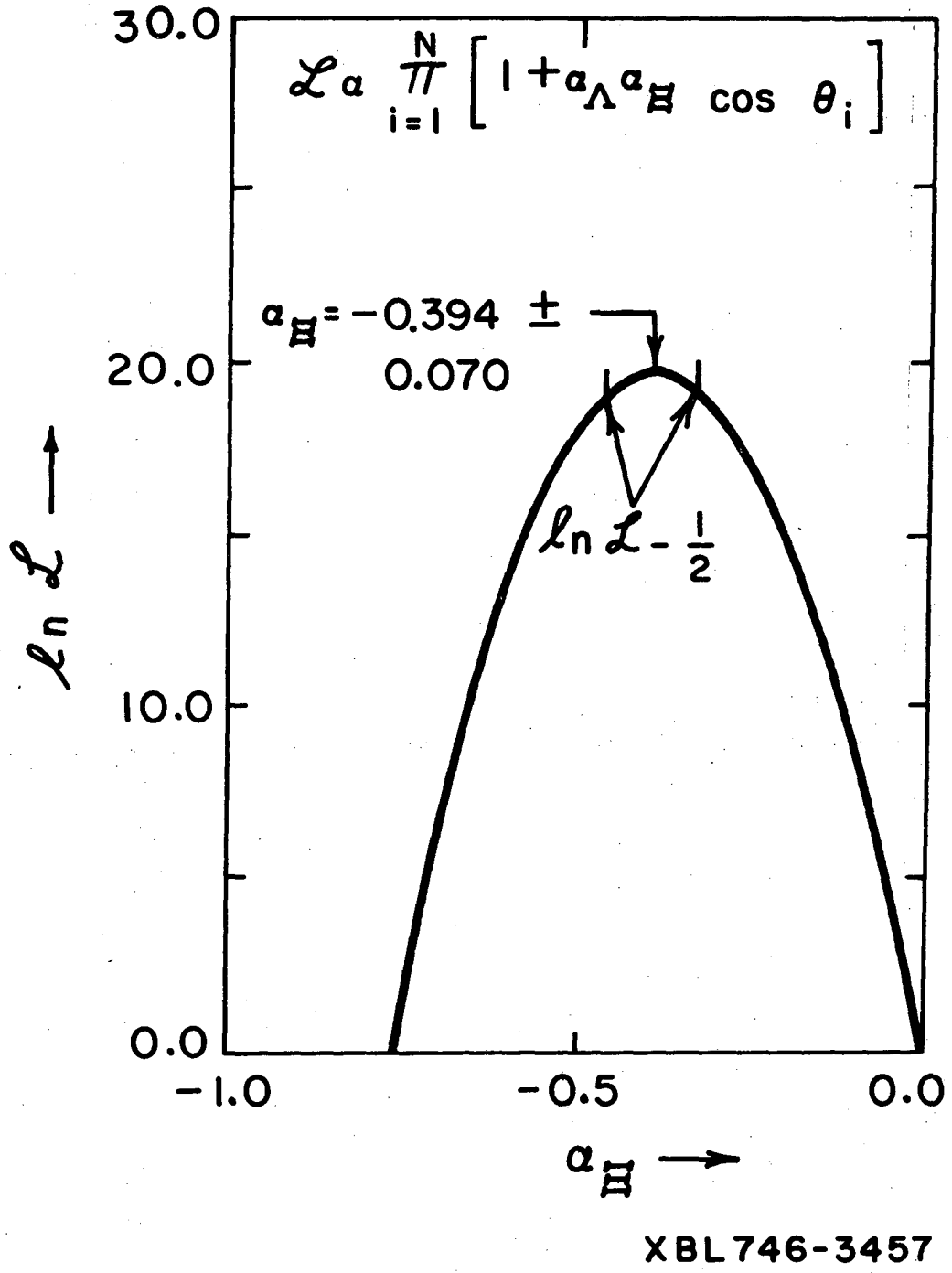


Figure V.4. Variation of the likelihood function as a function of the parity violating parameter $\alpha_\Xi$.

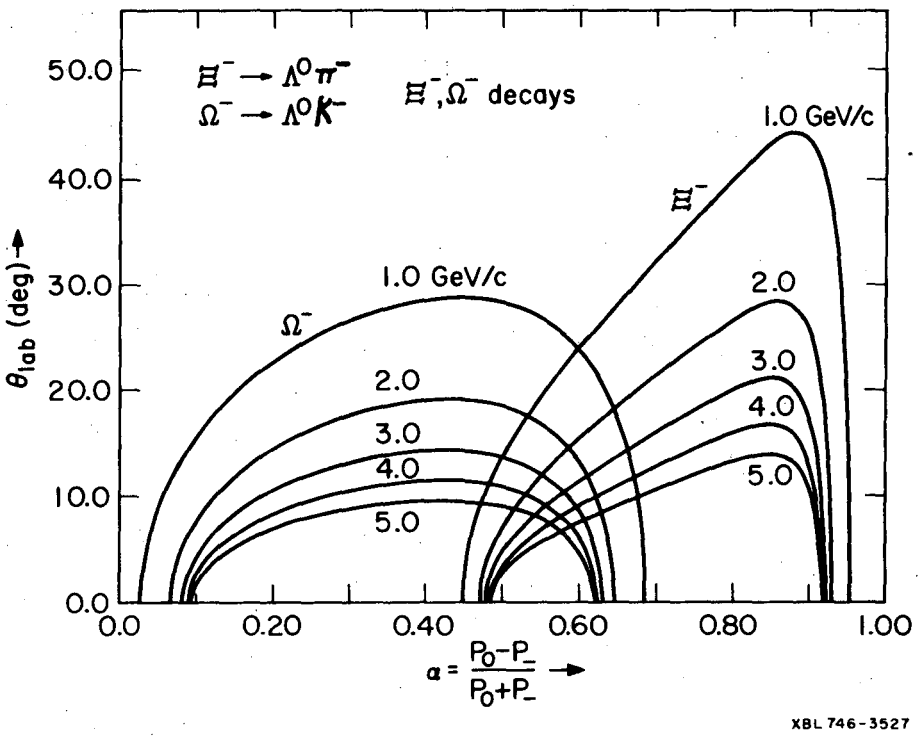


Figure V.5. Dependence of the laboratory opening angle (between the $\Lambda$ and the negative decay track on the momentum balance these two tracks, for $\Xi^-$ and $\Omega^-$ decays from 1 to 5 GeV/c.

The momentum distribution of 20 $\Omega^-$ decays is shown in Fig. V.6.

The mean momenta of hyperons produced in this experiment are given in Table V.1.

Table V.1. Hyperon mean momenta.

| | $\langle P \rangle$ GeV/c |
|---|---|
| $\Lambda$ | 2.2 |
| $\Sigma^{\pm}$ | --- |
| $\Xi^-$ | 3.74 |
| $\Omega^-$ | 4.78 |

Twenty-five (25) unambiguous $\Xi^0$ p interactions have been analyzed, representing an inelastic cross section of 21 ± 4 mb over the $\Xi^0$ momentum range from 1.5 to 12 GeV/c. The above cross section estimate was made assuming that the number of $\Xi^0$ hyperons produced is the same as the number of $\Xi^-$ hyperons in 12 GeV/c $K^-$-Platinum nucleus collisions; the resultant $\Xi^0$ pathlength distribution is shown in Fig. V.7. A rough binning of this distribution is

$$L_{\Xi^0} \text{ (0-1.5 GeV/c)} = 3.3 \times 10^3 \text{ cm}$$

$$L_{\Xi^0} \text{ (1.5-6 GeV/c)} = 46.5 \times 10^3 \text{ cm}$$

$$L_{\Xi^0} \text{ (6-12 GeV/c)} = 21.0 \times 10^3 \text{ cm.}$$

The $\Xi^0$ p interactions observed are given in Table V.2, where the incident $\Xi^0$ momentum is listed for each event; also, the SU(2) corrected numbers of events in each channel and the corresponding

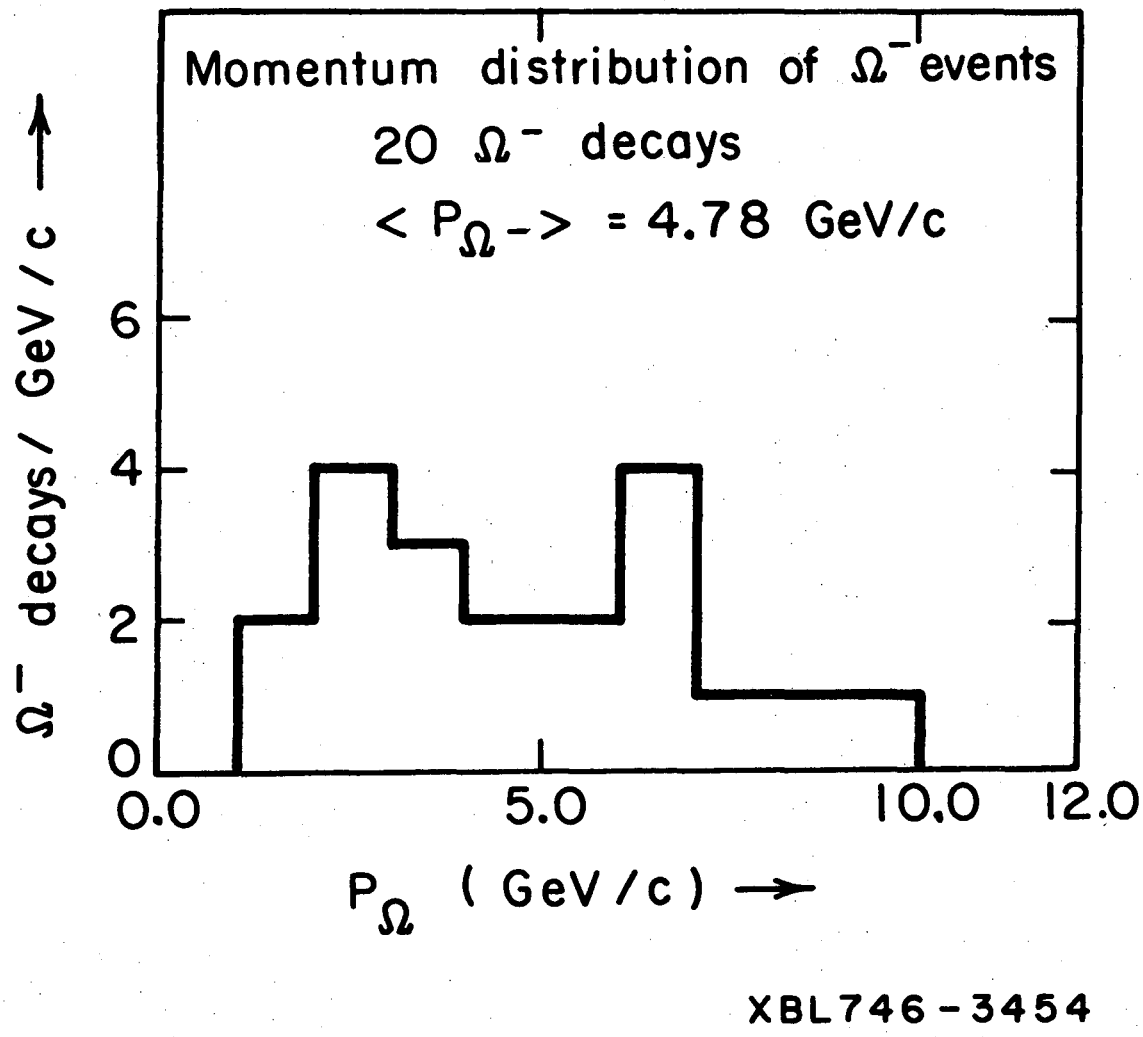


Figure V.6. Momentum distribution of $\Omega^-$ decays observed in this experiment.

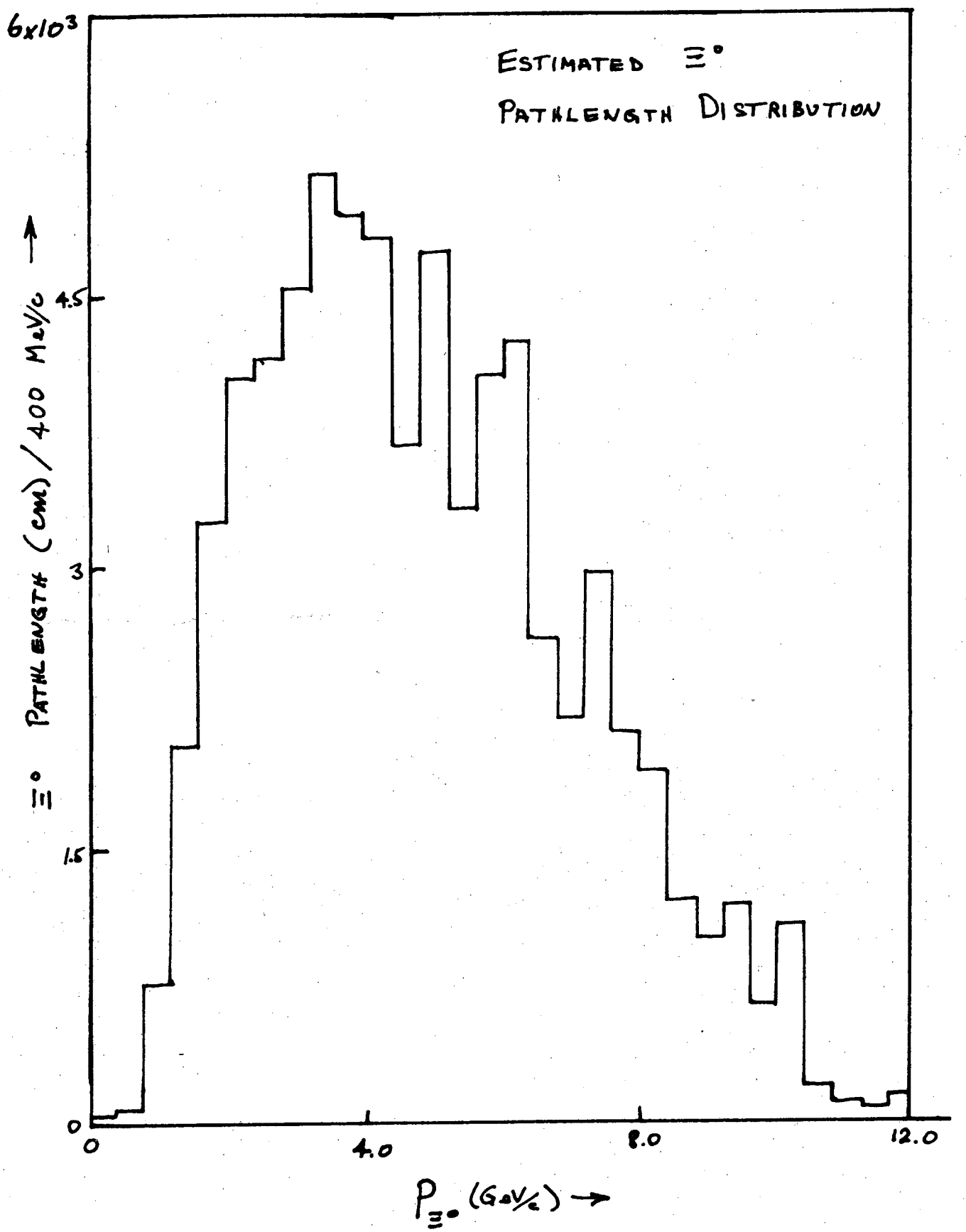


Figure V.7. Estimated $\Xi^0$ pathlength distribution.

Table V.2. $\Xi^0 p$ interactions and cross sections.

| Reaction | Number of events | $P_{\Xi^0}$ values | Number corrected by SU(2) | $\sigma$ (mb) |
|---|---|---|---|---|
| $\Xi^0 p \rightarrow \Xi^- p \pi^+$ | 5 | 2.42, 2.69, 7.22, 3.86, 2.65 | 5.0 | $3.1 \pm 1.4$ |
| $\Xi^0 p \rightarrow \Xi^- p \pi^+ (n\pi^0)$ | 2 | 4.14, 3.36 | 2.0 | $1.2 \pm 0.9$ |
| $\Xi^0 p \rightarrow \Lambda\Lambda \pi^+$ | 2 | 2.66, 2.02 | 3.0 | $1.9 \pm 1.1$ |
| $\Xi^0 p \rightarrow \Lambda\Lambda \pi^+ (n\pi^0)$ | 2 | 6.10, 8.87 | 3.0 | $1.9 \pm 1.1$ |
| $\Xi^0 p \rightarrow \Lambda\Lambda \pi^+ \pi^+ \pi^-$ | 1 | 4.82 | 1.5 | $0.9 \pm 0.9$ |
| $\Xi^0 p \rightarrow \Lambda \Sigma^+$ | 3 | 3.43, 2.22, 8.17 | 4.0 | $2.5 \pm 1.5$ |
| $\Xi^0 p \rightarrow \Lambda \Sigma^+ (n\pi^0)$ | 3 | 5.74, 8.80, 2.17 | 6.0 | $3.7 \pm 2.2$ |
| $\Xi^0 p \rightarrow \Lambda \Sigma^+ \pi^+ \pi^-$ | 3 | 8.99, 3.98, 3.88 | 4.0 | $2.5 \pm 1.5$ |
| $\Xi^0 p \rightarrow \Lambda \Sigma^- \pi^+ \pi^+$ | 3 | 4.71, 3.87, 6.61 | 3.0 | $1.9 \pm 1.1$ |
| $\Xi^0 p \rightarrow \Sigma^- \Sigma^+ \pi^+$ | 1 | 4.49 | 2.0 | $1.2 \pm 0.9$ |
| | 25 | | 33.5 | $21 \pm 4$ mb |

cross section averaged over all momenta are given. The SU(2) corrections are for the visible $\Lambda$ decay probability in both the inital $\Xi^-$ flux observed and final state $\Lambda$ decays, and undetected $\Sigma^+ \rightarrow p\pi^0$ decays.

Distributing the incident $\Xi^0$ momentum values, $P_{\Xi^0}$, and calculating both a high and a low momentum inelastic cross section indicates that this cross section indicates that this cross section is roughly constant in $\Xi^0$ momentum.

An examination of the reactions obtained in Table V.2 indicates that, apart from reactions like

$$\begin{aligned} \Xi^0 p &\rightarrow \Xi^0 p \\ \Xi^0 p &\rightarrow \Xi^0 p\pi^0 \\ &\rightarrow \Xi^0 n\pi^+, \end{aligned}$$

our ensemble represents nearly the whole of the inelastic cross section in the few GeV region. We make this assertion on the basis of our $\Lambda p$ data and nucleon-nucleon data in which the three- and four-pion production cross sections are only 10-15 percent of the one- and two-pion production cross sections. In addition there are many candidates for the reactions

$$\Xi^0 p \rightarrow Y \bar{K} N + \text{pions},$$

but this class is totally ambiguous with the class

$$np \rightarrow Y K N + \text{pions},$$

since the $K, \bar{K}$ decays visibly as a $K_1^0 \rightarrow \pi^+\pi^-$. Indeed, the available phase space for the former is only slightly larger than for the latter, at the same momentum, and so we have assigned these events to the

np class since the n flux is much larger than the $\Xi^0$ flux. Furthermore, in the $\Lambda p$ reactions we have found that the cross section for

$$\Lambda p \rightarrow \bar{K} N N + \text{pions}$$

is negligibly small, and we have taken it so in the total cross section measurement (Sec. III).

We may estimate that the missing channels $\Xi^0 p \rightarrow \Xi^0 p \pi^0$ and $\Xi^0 p \rightarrow \Xi^0 n \pi^+$ (with or without additional pions) have cross sections roughly equal to the first two listed in Table V. 2. Then an estimate of the total inelastic $\Xi^0 p$ cross section is

$$\begin{matrix} \text{total} \\ \Xi^0 p \text{ inelastic} \\ \text{cross section} \end{matrix} = 25 \pm 5 \text{ mb}$$

from 1.5 to 12 GeV/c.

APPENDIX VI. Propagation of the $\overline{K}^0$ amplitude through the Platinum Plate.

The wave functions for $K^0$ and $\overline{K}^0$ states are linear combinations of states of definite lifetime, $K_1^0$ and $K_2^0$,

$$K^0 = \frac{1}{\sqrt{2}} [K_1^0 + i K_2^0]$$

$$\overline{K}^0 = \frac{1}{\sqrt{2}} [K_1^0 - i K_2^0].$$

Suppose the incident wave is represented as a mixture of $K^0$ and $\overline{K}^0$, $\psi = a K^0 + \overline{a}\, \overline{K}^0$. The propagation of this wave through a nuclear medium can be described[1] as an electromagnetic wave propagating through a medium with a complex index of refraction. Thus the coefficients $a, \overline{a}$ obey the differential equation

$$\frac{\partial a}{\partial \chi} = i \left\{ \frac{2\pi N}{R^2} A(0) + 1 \right\} k a \equiv i n k a$$

$$\frac{\partial \overline{a}}{\partial \chi} = i \left\{ \frac{2\pi N}{R^2} \overline{A}(0) + 1 \right\} k a \equiv i n k \overline{a}.$$

Transforming to the basis states $K_1^0$ and $K_2^0$, including the weak interaction decay terms $(a/\tau)$ for the states $K_1^0$ and $K_2^0$, and transforming from space coordinate $\chi$ to laboratory time t, yields

$$\frac{d}{dt} a_1 = i\beta ck \left\{ \left(\frac{n+\overline{n}}{2}\right) a_1 - i \left(\frac{n-\overline{n}}{2}\right) a_2 \right\} - \left(i\omega_1 + \frac{1}{2\gamma\tau_1}\right) a_1$$

Decay Terms

$$\frac{d}{dt} a_2 = i\beta ck \left\{ \left(\frac{n+\overline{n}}{2}\right) a_1 + i \left(\frac{n-\overline{n}}{2}\right) a_1 \right\} - \left(i\omega_2 + \frac{1}{2\gamma\tau_2}\right) a_2$$

where

$\beta c$ = velocity of $K^0$ particle in laboratory

$t$ = laboratory time

$\frac{d}{dt} = \frac{\partial}{\partial t} + \beta c \frac{\partial}{\partial \chi}$ (total time derivative)

$\beta, \gamma$ = Lorentz transformation parameters

$\omega_{1,2}$ = de Broglie frequencies: $(\hbar \omega_{1,2})^2 = (\hbar ck)^2 + (m_{1,2} c^2)^2$

$\tau_{1,2}$ = proper lifetimes of $K_1^0$ and $K_2^0$ states.

Inspection of the differential equation indicates that the cross terms linking $a_1$ and $a_2$ depend on the difference of the forward scattering amplitudes of the $K^0$ and $\bar{K}^0$ states, which is proportional to $(n - \bar{n})$. The solution to the above equation is

$$\begin{bmatrix} a_1(t) \\ a_2(t) \end{bmatrix} = \left( \frac{a_1(0) - R\, a_2(0)}{1 - R^2} \right) e^{-\lambda_1 t} \begin{bmatrix} 1 \\ R \end{bmatrix} + \left( \frac{a_2(0) - R\, a_1(0)}{1 - R^2} \right) e^{-\lambda_2 t} \begin{bmatrix} R \\ 1 \end{bmatrix}.$$

As $R \to 0$, we have the vacuum solutions

$$a_1(t) = a_1(0)\, e^{-\lambda_1 t}$$

$$a_2(t) = a_2(0)\, e^{-\lambda_2 t},$$

hence $R$ essentially measures the amount of matter in the beam path. Changing to the $K^0$, $\bar{K}^0$ basis, we have

$$\begin{bmatrix} a(t) \\ \bar{a}(t) \end{bmatrix} = \frac{1}{\sqrt{2}} \left( \frac{a_1(0) - R\,a_2(0)}{1 - R^2} \right) e^{-\lambda_1 t} \begin{bmatrix} 1 + i\,R \\ 1 - i\,R \end{bmatrix}$$

$$+ \frac{1}{\sqrt{2}} \left( \frac{a_2(0) - R\,a_1(0)}{1 - R^2} \right) e^{-\lambda_2 t} \begin{matrix} R + i \\ R - i \end{matrix} .$$

In this experiment, the initial conditions are

$$K^0 = 0$$

$$\bar{K}^0 = 1$$

subsequent to a $K^-$ collision in the platinum plate. Then

$$a_1(0) = \frac{1}{\sqrt{2}}$$

$$a_2(0) = \frac{i}{\sqrt{2}} ,$$

and the solution for amount of $K^0$ and $\bar{K}^0$ amplitudes as a function of time through the platinum is

$$\begin{bmatrix} a(t) \\ \bar{a}(t) \end{bmatrix} = \frac{1}{2} \left( \frac{1 - iR}{1 - R^2} \right) e^{\lambda_1 t} \begin{bmatrix} 1 + i\,R \\ 1 - i\,R \end{bmatrix}$$

$$+ \frac{1}{2} \left( \frac{i - R}{1 - R^2} \right) e^{-\lambda_1 t} \begin{bmatrix} R + i \\ R - i \end{bmatrix} .$$

The physical quantities in this expression are

$$\lambda_1 = \omega + \Delta$$

$$\lambda_2 = \omega - \Delta$$

$$R = - \left[ \frac{\left( \frac{\omega_2^0 - \omega_1^0}{\gamma} \right) + \frac{1}{2\gamma} \left( \frac{1}{\tau_2} - \frac{1}{\tau_1} \right) + 2\Delta}{\beta c k (n - \bar{n})} \right]$$

with

$$\omega = \frac{1}{2}\left[i(\omega_2 + \omega_1) + \frac{1}{2\gamma}\left(\frac{1}{\tau_2} - \frac{1}{\tau_1}\right) - i\beta c k (n + \bar{n})\right]$$

$$\Delta = \frac{1}{2}\left\{\left[\frac{i(\omega_1^0 - \omega_2^0)}{\gamma} + \frac{1}{2\gamma}\left(\frac{1}{\tau_1} - \frac{1}{\tau_2}\right)\right]^2 + \left[i\beta ck(n - \bar{n})\right]^2\right\}.$$

The units are defined by

$$\hbar = c = 1$$

whence

$$\hbar c = 0.1973 \quad \text{GeV-Fermi} = 0.624 \quad \text{GeV-mb}^{1/2}$$
$$hc = 6.58 \times 10^{-25} \text{ GeV-sec.}$$

Hence the units in this calculation are

$t, \tau_1, \tau_2$ in $\text{GeV}^{-1}$

$\omega, \Delta, \omega_1, \omega_2, k$ in GeV

$R, n, \bar{n}$ in 1.

The numerical solution to these equations is shown in Fig. VI.1 as a function of the amount of Platinum traversed. The forward scattering amplitudes were taken from Bohm, et al., Nucl. Phys. 27B, 594 (1958).

The $K^0$ and $\bar{K}^0$ probabilities are shown inside the platinum plate, Fig. VI. 2 and throughout the liquid hydrogen, Fig. VI. 3. Averaging the distributions of Fig. VI. 2 over the K-interaction spatial distribution inside the platinum ($\approx e^{-y/8.0\text{cm}}$) implies that the regenerated $K^0$ probability is roughly

$$|a(y = 8.0 \text{ cm})|^2 \tilde{=} 0.03,$$

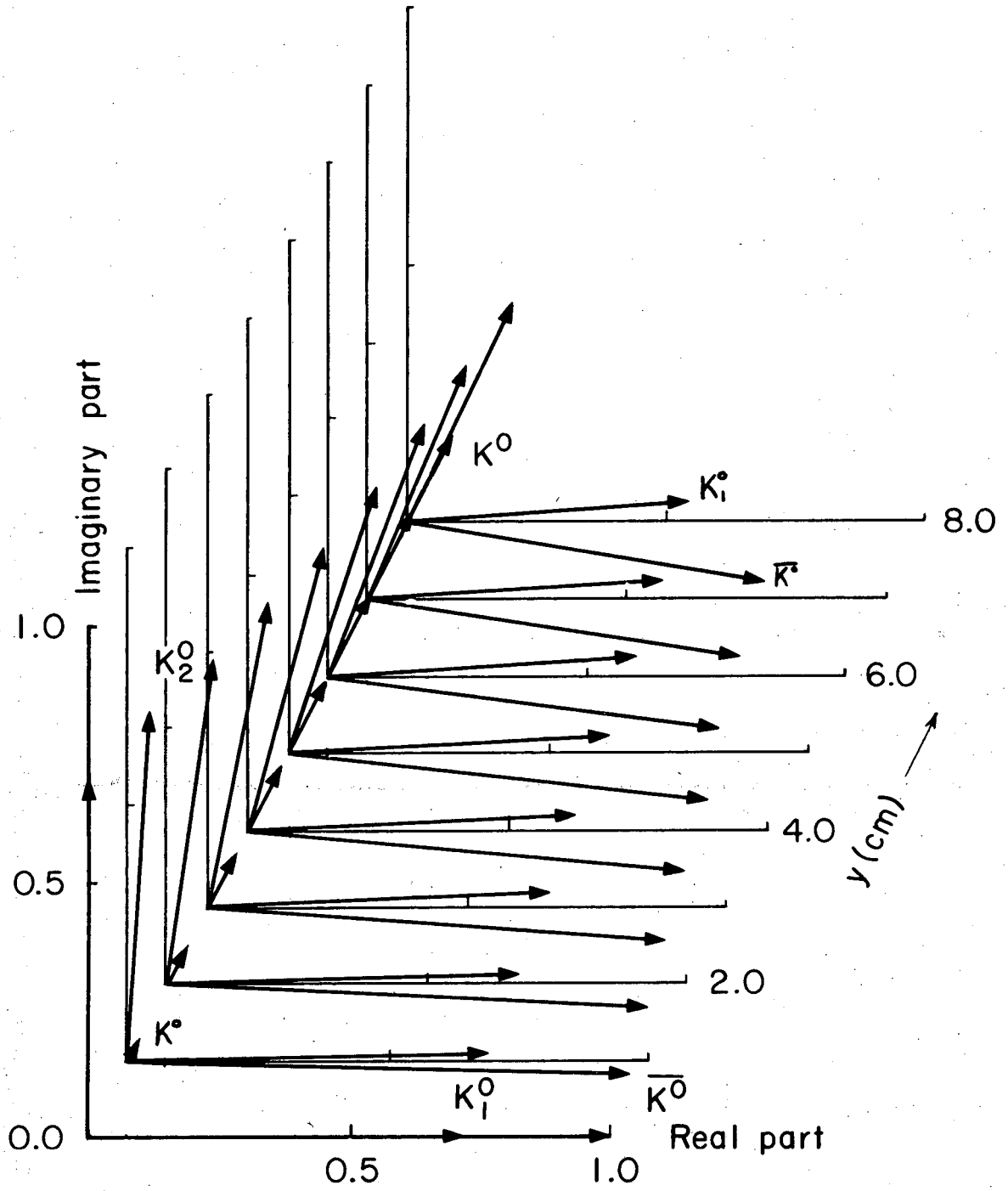


Figure VI.1. Spatial dependence of the complex amplitudes involved in the kaon propagation problem.

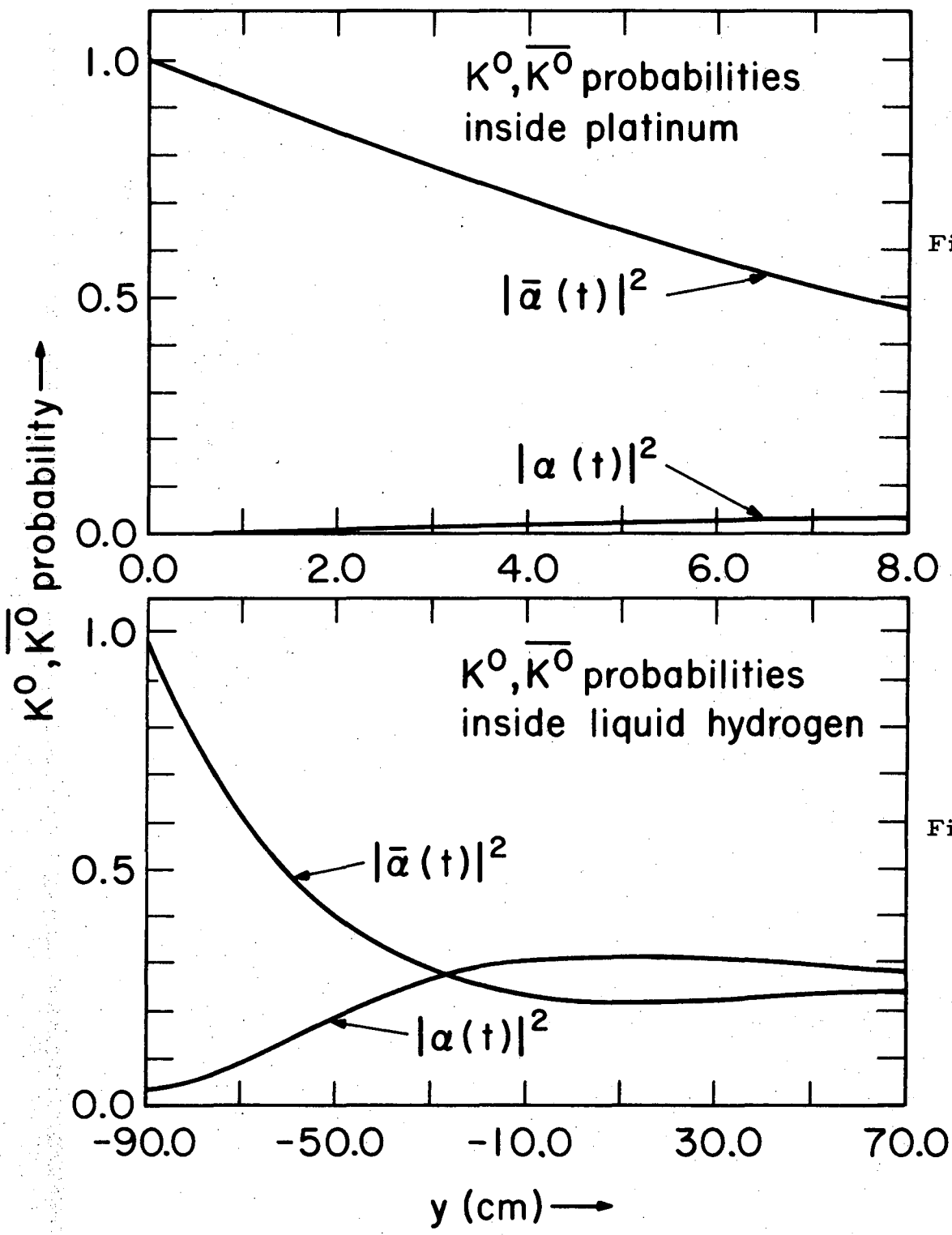


Figure VI.2.

Figure VI.3.

XBL 747-3602

and hence that the probability that a $K_1^0 \rightarrow \pi^+\pi^-$ decay in the liquid hydrogen originating from a nuclear interaction producing a $\overline{K}^0$ is

$$|\overline{a}\ (y \tilde{=} 8.0\ \text{cm})|^2 \tilde{=} 0.97.$$

This number has been used to renormalize the $\overline{K}^0$ amplitude in the calculation of the total cross section in Sec. III.

---

[1] Ken M. Case, Phys. Rev. 103, 1449 (1956).
M. L. Good, Phys. Rev. 106, 591 (1957).

## APPENDIX VII. SU(3) Isoscalar Factors; U-Spin and Quark Model Calculations.

This appendix is included to facilitate the checking of the assertions made in Section VI.

A table of SU(3) isoscalar factors first given by J. J. de Swart in Rev. Mod. Phys. 35, 916 (1963) and printed in Rev. of Mod. Phys. 45, 1 (1973) is reproduced as Fig. VII. 1.

Although all SU(3) relationships can be calculated from the above tables, it is sometimes convenient instead to employ U-spin invariance, which is completely equivalent to unbroken SU(3). The advantage is the relative simplicity of the Clebsch-Gordon coefficients over the SU(3) coefficients. The U-spin multiplets in SU(3) are obtained by a clockwise rotation of the SU(3) weight through 120°. The weight diagram is symmetric under the rotation, and the resultant U-spin structure is such that conservation of U-spin, when treated in the same way as conservation of isotopic spin, is equivalent to unbroken SU(3). The U-spin multiplets for the $J^P = 1/2^+$ baryon, $0^-$ meson, $1^-$ meson octets, and the $3/2^+$ baryon decuplet, are given in Fig. VII. 2. A table of Clebsch-Gordon coefficients is given in Fig. VII. 3.

The analogy with I-spin can be made more clear by noting that the rotation which interchanges $p \rightarrow n$ is on I-spin rotation; that which interchanges $n \leftarrow \lambda$ is U-spin; and that which interchanges $p \leftarrow \lambda$ is V-spin.

# SU(3) ISOSCALAR FACTORS

$$[8] \otimes [8] = [27] \oplus [10] \oplus [10^*] \oplus [8]_1 \oplus [8]_2 \oplus [1].$$

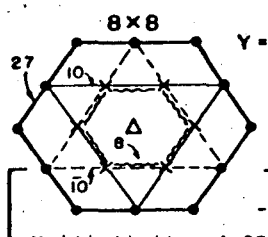


Multiplicity of 27:

●=1, ×=2, Δ=3

* Five single-coefficient tables are omitted. The one involving a $\{10^*\}$ has a negative coefficient, i.e. $(NK|10^*) = -1$. The others, involving $\{27\}$ and $\{10\}$, are all +1.

$Y = 1$ $I = 1/2$ N

| $\xi_1 \rightarrow$ | $\underset{+}{27}$ | $\underset{D}{8}$ | $\underset{F}{8}$ | $\underline{10^*}$ |
|---|---|---|---|---|
| Nπ | $\sqrt{5}/10$ | $3\sqrt{5}/10$ | 1/2 | -1/2 |
| ΣK | $-\sqrt{5}/10$ | $-3\sqrt{5}/10$ | 1/2 | -1/2 |
| Nη | $3\sqrt{5}/10$ | $-\sqrt{5}/10$ | 1/2 | 1/2 |
| ΛK | $3\sqrt{5}/10$ | $-\sqrt{5}/10$ | -1/2 | -1/2 |

$Y = 1$ $I = 3/2$ Δ

| $\xi_1 \rightarrow$ | $\underset{+}{27}$ | $\underline{10}$ |
|---|---|---|
| Nπ | $\sqrt{2}/2$ | $-\sqrt{2}/2$ |
| ΣK | $\sqrt{2}/2$ | $\sqrt{2}/2$ |

$Y = 0$ $I = 0$ Λ

| $\xi_1 \rightarrow$ | $\underset{+}{27}$ | $\underset{D}{8}$ | $\underset{+}{1}$ | $\underset{F}{8}$ |
|---|---|---|---|---|
| NK̄ | $\sqrt{15}/10$ | $\sqrt{10}/10$ | 1/2 | $\sqrt{2}/2$ |
| ΞK | $-\sqrt{15}/10$ | $-\sqrt{10}/10$ | -1/2 | $\sqrt{2}/2$ |
| Σπ | $-\sqrt{10}/20$ | $-\sqrt{15}/5$ | $\sqrt{6}/4$ | 0 |
| Λη | $3\sqrt{30}/20$ | $-\sqrt{5}/5$ | $-\sqrt{2}/4$ | 0 |

$Y = 0$ $I = 1$ Σ

| $\xi_1 \rightarrow$ | $\underset{+}{27}$ | $\underset{D}{8}$ | $\underset{F}{8}$ | $\underline{10}$ | $\underline{10^*}$ |
|---|---|---|---|---|---|
| NK̄ | $\sqrt{5}/5$ | $-\sqrt{30}/10$ | $\sqrt{6}/6$ | $-\sqrt{6}/6$ | $\sqrt{6}/6$ |
| ΞK | $\sqrt{5}/5$ | $-\sqrt{30}/10$ | $-\sqrt{6}/6$ | $\sqrt{6}/6$ | $-\sqrt{6}/6$ |
| Σπ | 0 | 0 | $\sqrt{6}/3$ | $\sqrt{6}/6$ | $-\sqrt{6}/6$ |
| Ση | $\sqrt{30}/10$ | $\sqrt{5}/5$ | 0 | 1/2 | 1/2 |
| Λπ | $\sqrt{30}/10$ | $\sqrt{5}/5$ | 0 | -1/2 | -1/2 |

$Y = -1$ $I = 1/2$ Ξ

| $\xi_1 \rightarrow$ | $\underset{+}{27}$ | $\underset{D}{8}$ | $\underset{F}{8}$ | $\underline{10}$ |
|---|---|---|---|---|
| Ξπ | $-\sqrt{3}/10$ | $-3\sqrt{5}/10$ | 1/2 | 1/2 |
| ΣK̄ | $\sqrt{5}/10$ | $3\sqrt{5}/10$ | 1/2 | 1/2 |
| Ξη | $3\sqrt{5}/10$ | $-\sqrt{5}/10$ | -1/2 | 1/2 |
| ΛK̄ | $3\sqrt{5}/10$ | $-\sqrt{5}/10$ | 1/2 | -1/2 |

$Y = -1$ $I = 3/2$

| $\xi_1 \rightarrow$ | $\underset{+}{27}$ | $\underline{10^*}$ |
|---|---|---|
| Ξπ | $\sqrt{2}/2$ | $-\sqrt{2}/2$ |
| ΣK̄ | $\sqrt{2}/2$ | $\sqrt{2}/2$ |

The phase factor $\xi_1 = \pm 1$, from de Swart's Table I, enters in his symmetry formula (14.3):

$$\langle \mu_1 \mu_2 | \mu \rangle = \xi_1 (-1)^{I_1+I_2-I} \langle \mu_2 \mu_1 | \mu \rangle .$$

This factor is irrelevant if you are doing your own self-consistent calculations; it enters when you try to check someone else who chose $\mu_2 \otimes \mu_1$ instead of $\mu_1 \otimes \mu_2$.

$$[10] \otimes [8] = [35] \oplus [27] \oplus [10] \oplus [8].$$

* Four single coefficient tables are omitted; only the $\{27\}$ is -1; the three with $\{35\}$ are +1.

$Y = 1$ $I = 1/2$ N

| $\xi_1 \rightarrow$ | $\underline{27}$ | $\underset{+}{8}$ |
|---|---|---|
| Δπ | $-\sqrt{5}/5$ | $-2\sqrt{5}/5$ |
| ΣK | $-2\sqrt{5}/5$ | $\sqrt{5}/5$ |

$Y = 1$ $I = 3/2$ Δ

| $\xi_1 \rightarrow$ | $\underset{+}{35}$ | $\underline{27}$ | $\underline{10}$ |
|---|---|---|---|
| Δπ | 1/4 | $-\sqrt{5}/4$ | $\sqrt{10}/4$ |
| Δη | $\sqrt{5}/4$ | 3/4 | $\sqrt{2}/4$ |
| ΣK | $\sqrt{10}/4$ | $-\sqrt{2}/4$ | -1/2 |

$Y = 0$ $I = 0$ Λ

| $\xi_1 \rightarrow$ | $\underline{27}$ | $\underset{+}{8}$ |
|---|---|---|
| Σπ | $-\sqrt{10}/5$ | $-\sqrt{15}/5$ |
| ΞK | $-\sqrt{15}/5$ | $\sqrt{10}/5$ |

$Y = 0$ $I = 1$ Σ

| $\xi_1 \rightarrow$ | $\underset{+}{35}$ | $\underline{27}$ | $\underline{10}$ | $\underset{+}{8}$ |
|---|---|---|---|---|
| Σπ | $\sqrt{3}/6$ | $-3\sqrt{5}/10$ | $\sqrt{3}/3$ | $-\sqrt{30}/15$ |
| Ση | $\sqrt{2}/2$ | $\sqrt{30}/10$ | 0 | $-\sqrt{5}/5$ |
| ΞK | $\sqrt{3}/3$ | $-\sqrt{5}/5$ | $-\sqrt{3}/3$ | $\sqrt{30}/15$ |
| ΔK̄ | $\sqrt{3}/6$ | $\sqrt{5}/10$ | $\sqrt{3}/3$ | $2\sqrt{30}/15$ |

$Y = 0$ $I = 2$

| $\xi_1 \rightarrow$ | $\underset{+}{35}$ | $\underline{27}$ |
|---|---|---|
| Σπ | $\sqrt{3}/2$ | -1/2 |
| ΔK̄ | 1/2 | $\sqrt{3}/2$ |

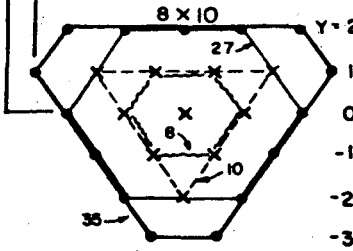


Multiplicity of 35:

●=1, ×=2

$Y = -1$ $I = 1/2$ Ξ

| $\xi_1 \rightarrow$ | $\underset{+}{35}$ | $\underline{27}$ | $\underline{10}$ | $\underset{+}{8}$ |
|---|---|---|---|---|
| Ξπ | 1/4 | $-7\sqrt{5}/20$ | $\sqrt{2}/4$ | $-\sqrt{5}/5$ |
| Ξη | 3/4 | $3\sqrt{5}/20$ | $-\sqrt{2}/4$ | $-\sqrt{5}/5$ |
| ΩK | $\sqrt{2}/4$ | $-3\sqrt{10}/20$ | -1/2 | $\sqrt{10}/5$ |
| ΣK̄ | 1/2 | $\sqrt{5}/10$ | $\sqrt{2}/2$ | $\sqrt{5}/5$ |

$Y = -1$ $I = 3/2$

| $\xi_1 \rightarrow$ | $\underset{+}{35}$ | $\underline{27}$ |
|---|---|---|
| Ξπ | $\sqrt{2}/2$ | $-\sqrt{2}/2$ |
| ΣK̄ | $\sqrt{2}/2$ | $\sqrt{2}/2$ |

$Y = -2$ $I = 0$ $\Omega^-$

| $\xi_1 \rightarrow$ | $\underset{+}{35}$ | $\underline{10}$ |
|---|---|---|
| Ωη | $\sqrt{2}/2$ | $-\sqrt{2}/2$ |
| ΞK̄ | $\sqrt{2}/2$ | $\sqrt{2}/2$ |

$Y = -2$ $I = 1$

| $\xi_1 \rightarrow$ | $\underset{+}{35}$ | $\underline{27}$ |
|---|---|---|
| Ωπ | 1/2 | $-\sqrt{3}/2$ |
| ΞK̄ | $\sqrt{3}/2$ | 1/2 |

Figure VII.1.

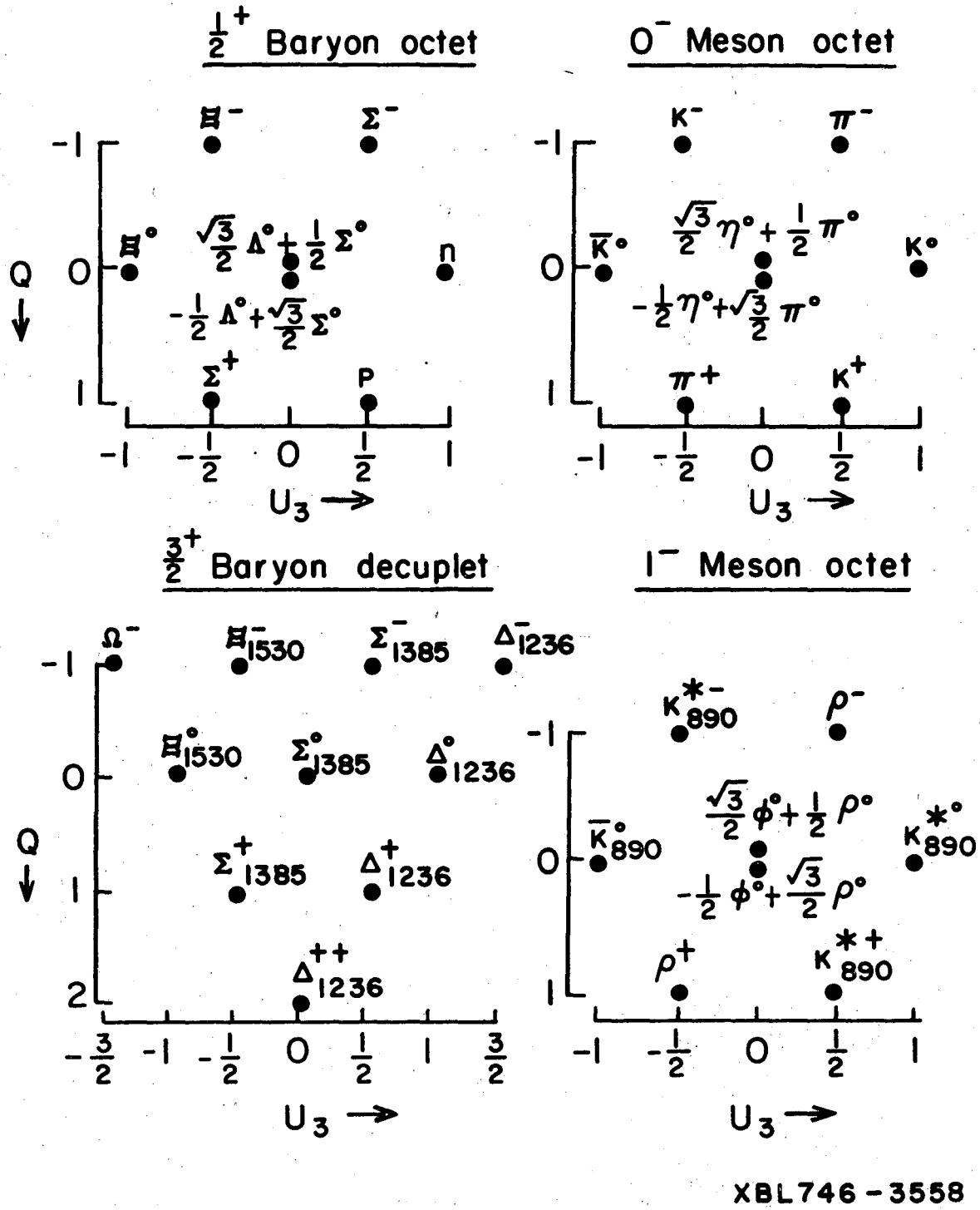


Figure VII.2.

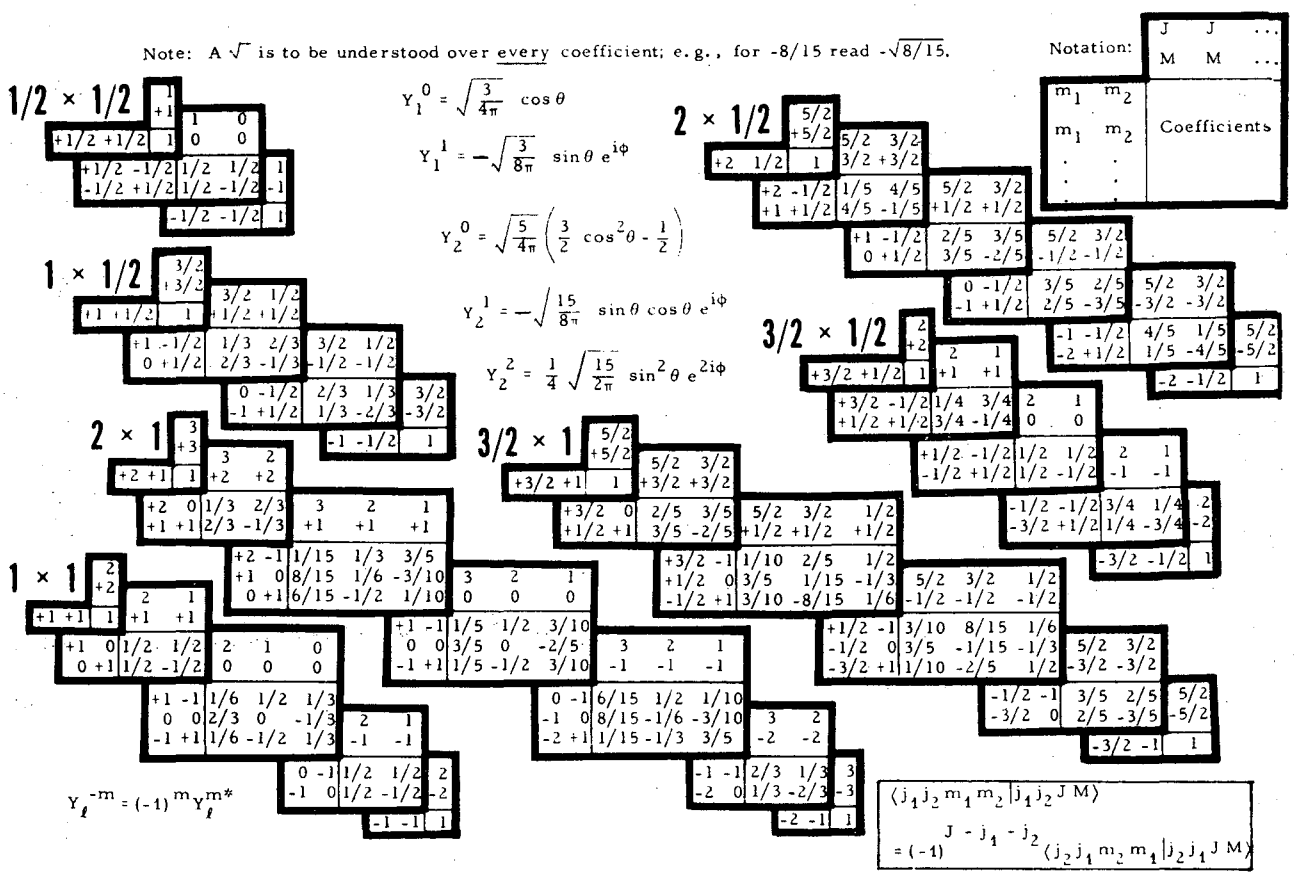
CLEBSCH-GORDAN COEFFICIENTS AND SPHERICAL HARMONICS
Note: A √ is to be understood over every coefficient; e.g., for -8/15 read -√8/15.
Notation:
Coefficients
1/2 × 1/2
1 × 1/2
2 × 1/2
1 × 1
2 × 1
3/2 × 1/2
3/2 × 1
$Y_1^0 = \sqrt{\frac{3}{4\pi}}\cos\theta$
$Y_1^1 = -\sqrt{\frac{3}{8\pi}}\sin\theta\, e^{i\phi}$
$Y_2^0 = \sqrt{\frac{5}{4\pi}}\left(\frac{3}{2}\cos^2\theta - \frac{1}{2}\right)$
$Y_2^1 = -\sqrt{\frac{15}{8\pi}}\sin\theta\cos\theta\, e^{i\phi}$
$Y_2^2 = \frac{1}{4}\sqrt{\frac{15}{2\pi}}\sin^2\theta\, e^{2i\phi}$
$Y_\ell^{-m} = (-1)^m Y_\ell^{m*}$
$\langle j_1 j_2 m_1 m_2 | j_1 j_2 J M\rangle = (-1)^{J - j_1 - j_2}\langle j_2 j_1 m_2 m_1 | j_2 j_1 J M\rangle$

Figure VII.3.

We use the "baryon first" convention; hence

$$|K^- p\rangle = \frac{1}{\sqrt{2}} |1\ 0\rangle + \frac{1}{\sqrt{2}} |0\ 0\rangle$$

and not

$$= \frac{1}{\sqrt{2}} |1\ 0\rangle - \frac{1}{\sqrt{2}} |0\ 0\rangle .$$

Various state vectors of interest in U-spin space are listed below. The notation is $|U\ U_3\rangle$.

Lambda-nucleon initial state:

$$|\Lambda p\rangle = \frac{1}{\sqrt{2}} |\tfrac{3}{2}\ \tfrac{1}{2}\rangle - |\tfrac{1}{2}\ \tfrac{1}{2}\rangle . \qquad \text{VII.1}$$

Lambda-nucleon final states:

$J^P\ \langle \frac{1}{2}^+\ \frac{1}{2}^+ |$ states:

$$\langle \Sigma^0 p| = \frac{1}{\sqrt{6}} \langle \tfrac{3}{2}\ \tfrac{1}{2}| + \frac{1}{\sqrt{3}} \langle \tfrac{1}{2}\ \tfrac{1}{2}| \qquad \text{VII.2a}$$

$$\langle \Sigma^+ n| = \frac{1}{\sqrt{3}} \langle \tfrac{3}{2}\ \tfrac{1}{2}| + \sqrt{\frac{2}{3}} \langle \tfrac{1}{2}\ \tfrac{1}{2}| \qquad 2b$$

$\langle \frac{3}{2}^+\ \frac{1}{2}^+ |$ states:

$$\langle \Sigma^0_{1385}\, p| = \sqrt{\frac{2}{3}} \langle \tfrac{3}{2}\ \tfrac{1}{2}| - \sqrt{\frac{1}{3}} \langle \tfrac{1}{2}\ \tfrac{1}{2}| \qquad \text{VII.3a}$$

$$\langle \Sigma^+_{1385}\, n| = \sqrt{\frac{1}{3}} \langle \tfrac{3}{2}\ \tfrac{1}{2}| + \sqrt{\frac{2}{3}} \langle \tfrac{1}{2}\ \tfrac{1}{2}| \qquad 3b$$

$$\langle \Lambda \Delta^+| = \sqrt{\frac{1}{2}} \langle \tfrac{3}{2}\ \tfrac{1}{2}| - \langle \tfrac{1}{2}\ \tfrac{1}{2}| \qquad 3c$$

$$\langle \Sigma^- \Delta^{++}| = \langle \tfrac{1}{2}\ \tfrac{1}{2}| \qquad 3d$$

$$\langle \Sigma^+ \Delta^0| = \sqrt{\frac{1}{3}} \langle \tfrac{3}{2}\ \tfrac{1}{2}| + \sqrt{\frac{2}{3}} \langle \tfrac{1}{2}\ \tfrac{1}{2}| \qquad 3e$$

$\langle \frac{3}{2}^+ \frac{3}{2}^+ |$ states:

$$\langle \Sigma^+_{1385} \Delta^0 | = \sqrt{\frac{1}{3}} \langle \tfrac{3}{2} \tfrac{1}{2} | + \sqrt{\frac{2}{3}} \langle \tfrac{1}{2} \tfrac{1}{2} | \qquad \text{VII.4a}$$

$$\langle \Sigma^-_{1385} \Delta^{++} | = \langle \tfrac{3}{2} \tfrac{1}{2} | \qquad 4b$$

$$\langle \Sigma^0_{1385} \Delta^+ | = \sqrt{\frac{2}{3}} \langle \tfrac{3}{2} \tfrac{1}{2} | - \sqrt{\frac{1}{3}} \langle \tfrac{1}{2} \tfrac{1}{2} |. \qquad 4c$$

Nucleon-nucleon initial state:

$$|n\ p\rangle = |\tfrac{3}{2} \tfrac{1}{2}\rangle \qquad \text{VII.5a}$$

$$|p\ p\rangle = |1\ 1\rangle \qquad 5b$$

Nucleon-nucleon final states:

$\langle \frac{3}{2}^+ \frac{3}{2}^+ |$ states:

$$\langle \Delta^0 \Delta^+ | = \langle \tfrac{3}{2} \tfrac{3}{2} | \qquad \text{VII.6a}$$

$$\langle \Delta^- \Delta^{++} | = \langle \tfrac{3}{2} \tfrac{3}{2} | \qquad 6b$$

$\langle \frac{3}{2}^+ \frac{1}{2}^+ |$ states

$$\langle n\ \Delta^+ | = \langle \tfrac{3}{2} \tfrac{3}{2} | \qquad \text{VII.7a}$$

$$\langle p\ \Delta^0 | = \langle \tfrac{3}{2} \tfrac{3}{2} | \qquad 7b$$

$$\langle n\ \Delta^{++} | = \langle 1\ 1 | \qquad \text{VII.8a}$$

$$\langle p\ \Delta^+ | = \langle 1\ 1 | \qquad 8b$$

Let $a_{3/2}$, $a_{1/2}$, and $a_1$ denote the U-spin matrix elements:

$$a_{3/2} = \langle \tfrac{3}{2}\, u_3 \,|\tfrac{3}{2}\, u_3 \rangle \qquad \text{VII.9a}$$

$$a_{1/2} = \langle \tfrac{1}{2}\, u_3 \,|\tfrac{1}{2}\, u_3 \rangle \qquad 9b$$

$$a_1 = \langle 1\, u_3 \,|1\, u_3 \rangle . \qquad 9c$$

Then amplitudes of interest are

$J^P$ $\langle \frac{1}{2}^+ \; \frac{1}{2}^+ \,|$ states:

$$\langle \Lambda p|\Lambda p \rangle = \tfrac{1}{2} a_{3/2} + a_{1/2} \qquad \text{VII.10a}$$

$$\langle \Sigma^0 p \,|\Lambda p\rangle = \frac{1}{\sqrt{12}} a_{3/2} - \frac{1}{\sqrt{3}} a_{1/2} = \sqrt{\tfrac{1}{2}}\langle \Sigma^+ n \,|\Lambda p\rangle \qquad 10b$$

$\langle \frac{3}{2}^+ \; \frac{1}{2}^+ \,|$ states:

$$\langle \Sigma^0_{1385} p \,|\Lambda p\rangle = \sqrt{\tfrac{1}{3}}\, a_{3/2} + \sqrt{\tfrac{1}{3}}\, a_{1/2} \qquad 10c$$

$$\langle \Sigma^+_{1385} n \,|\Lambda p\rangle = \sqrt{\tfrac{1}{6}}\, a_{3/2} - \sqrt{\tfrac{2}{3}}\, a_{1/2} \qquad 10d$$

$$\langle \Lambda \Delta^+ |\Lambda p\rangle = \tfrac{1}{2}\, a_{3/2} + a_{1/2} \qquad 10e$$

$$\langle \Sigma^- \Delta^{++} |\Lambda p\rangle = - a_{1/2} \qquad 10f$$

$$\langle \Sigma^+ \Sigma^0 \,|\Lambda p\rangle = \sqrt{\tfrac{1}{6}}\, a_{3/2} - \sqrt{\tfrac{2}{3}}\, a_{1/2} \qquad 10g$$

$\langle \frac{3}{2}^+ \; \frac{3}{2}^+ \,|$ states:

$$\langle \Sigma^+_{1385} \Delta^0 \,|\Lambda p\rangle = \sqrt{\tfrac{1}{6}}\, a_{3/2} - \sqrt{\tfrac{2}{3}}\, a_{1/2} \qquad 10h$$

$$\langle \Sigma^-_{1385} \Delta^{++} |\Lambda p\rangle = \sqrt{\tfrac{1}{2}}\, a_{3/2} . \qquad 10i$$

The amplitudes involving the neutron are simpler since the neutron is a pure U-spin state. Some are

$\langle \frac{1}{2}^+ \frac{1}{2}^+ |$ states:

$$\langle np|np\rangle = a_{3/2} \qquad \text{VII.11a}$$

$$\langle pp|pp\rangle = a_1 \qquad 11b$$

$\langle \frac{3}{2}^+ \frac{1}{2}^+ |$ states:

$$\langle \Delta^+ n|np\rangle = a_{3/2} \qquad 11c$$

$\langle \frac{3}{2}^+ \frac{3}{2}^+ |$ states:

$$\langle \Delta^0 \Delta^+ | np\rangle = a_{3/2} \qquad 11d$$

$$\langle \Delta^- \Delta^{++}|np\rangle = a_{3/2}\,. \qquad 11e$$

The relationships presented by Kaiser (our equations 69 a-d) can be obtained from VII. 10a-h and VII. 11a-e.

The quark model relationship

$$\sigma_T(\Lambda p) = \sigma_T(pp) + \sigma_T(K^- n) - \sigma_T(\pi^+ p) \qquad \text{VII. 12}$$

may be obtained in the following manner. Let the quarks be labelled p, n, $\lambda$; let, for example, "pn" denote the amplitude for scattering of a "p" and an "n" quark. Then the additive quark model[61] simply asserts that the amplitude for the scattering of two physical particles is the

sum of all quark-quark amplitudes obtained by combination. Thus the physical states are

$$\text{Proton} = \begin{pmatrix} p \\ p \\ n \end{pmatrix} \qquad \pi^+ = \begin{pmatrix} p \\ \bar{n} \end{pmatrix}$$

$$\text{Neutron} = \begin{pmatrix} p \\ n \end{pmatrix} \qquad K^- = \begin{pmatrix} \lambda \\ \bar{p} \end{pmatrix} \qquad \text{VII.14}$$

$$\text{Lambda} = \begin{pmatrix} p \\ n \\ \lambda \end{pmatrix}$$

and the particle-particle amplitudes are

$$A(pp) = \{4\,pp + 4n\,p + nn\} \qquad \text{VII.15a}$$

$$= \{5\,pp + 4n\,p\}, \qquad \text{by charge symmetry}$$

$$A(\pi^+ p) = \{2\,pp + 2\bar{n}\,p + pn + \bar{n}n\} \qquad 15b$$

$$A(K^- n) = \{2\lambda n + \lambda p + \bar{p}p + 2\bar{p}n\} \qquad 15c$$

$$= \{3\lambda p + \bar{n}n + 2\bar{n}p\}, \qquad \text{by charge symmetry}$$

and

$$A(\Lambda p) = \{2\,pp + 3pn + 2\lambda p + nn + \lambda n\} \qquad 15d$$

$$= \{3\,pp + 3pn + 3\lambda p\}, \qquad \text{by charge symmetry}$$

hence

$$A(pp) + A(K^- n) - A(\pi^+ p) = \{3pp + 3np + 3\lambda p\} \qquad \text{VII.16}$$

$$= A(\Lambda p).$$

The optical theorem states that the imaginary part of the above relationship evaluated at zero scattering angle is proportional to the total cross section (at the same center of mass momentum), and so VII.13 is obtained. Another relationship, and a possibly more useful one, is obtained by making a rotation in isospin space; then

$$A(np) + A(K^- p) - A(\pi^+ n) = \{3\,pp + 3\,np + 3\lambda\, p\} \qquad \text{VII.17a}$$
$$= A(\Lambda\, p)$$

and hence by the optical theorem

$$\sigma_T(\Lambda p) = \sigma_T(np) + \sigma_T(K^- p) - \sigma_T(\pi^+ n).$$

APPENDIX VIII. Details of the Total Cross Section Calculation.

1. $\Lambda$ and $K_1^0$ Decay Distributions.

The scanning efficiency calculated from the master list scan data[39] alone is shown in Figs. II.1(a, b) of APPENDIX II over two regions in the chamber, from -86.0 to -66.0 cm in 1.4-cm bins and from -86.0 to +70.0 cm in 10.-cm bins, respectively. The calculation assumes that events are randomly missed on either scan. This efficiency fails to describe the observed decay distributions of either $\Lambda \to p\pi^-$ or $K_1^0 \to \pi^+\pi^-$ decays. However, from the known $\Lambda^0$ and $K_1^0$ mean lifetimes, one can also calculate a scanning efficiency from the data summary tape (DST) as follows: in Fig. VIII.1, define a fiducial volume[40] (FID3) sufficiently far from the plate such that scanning losses due to visual obscuration are small. Then for all decays inside FID3 with decay lengths $\lambda_i$, assuming they came from the plate, form the sum

$$dN^{calc}_{(y)} = \sum_i \frac{e^{-y/\lambda_i}}{\left[e^{-y_1/\lambda_i} - e^{-y_2/\lambda_i}\right]} \frac{dy}{\lambda_i}$$

where the y coordinate is along the line-of-flight of the $V^0$. The ratio of the experimental decay distribution to this calculated distribution is a measure of the scanning efficiency,

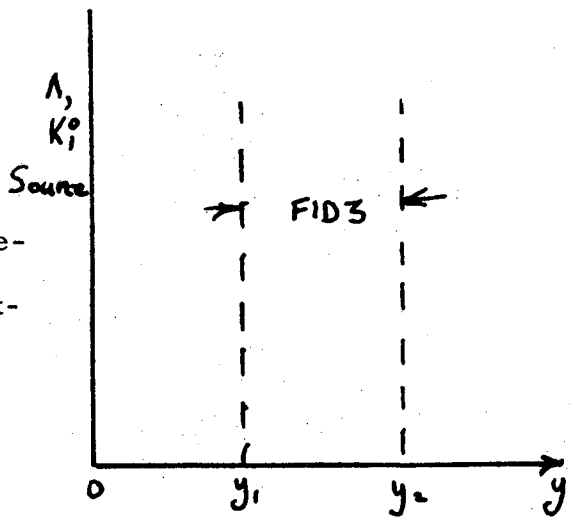


Fig. VIII.1

$$\eta_{DST}(y) = \frac{dN^{expt'l}(y)/dy}{dN^{calc}(y)/dy},$$

shown in Fig. II. 2(a). This efficiency is guaranteed to make the experimental and calculated distributions agree. Two corrections to this efficiency must be applied; $\Lambda$ from the decay $\Xi^0 \to \Lambda\pi^0$ and $\Lambda$, $K_1^0$ produced in the $LH_2$ are sources of non-plate produced $V^0$ particles invalidating to a small degree one assumption of the above calculation. The number of $\Xi^- \to \Lambda\pi^-$ decays ($N_o$), and the $\Lambda$ decay distribution is characterized by a spatial distribution of the form

$$\frac{dN}{dy}(\Lambda \text{ decays/cm}) = N_o \frac{e^{-y/\lambda_\Lambda}}{\lambda_\Xi - \lambda_\Lambda}\left\{e^{-y\left[\frac{\lambda_\Xi - \lambda_\Lambda}{\lambda_\Xi \lambda_\Lambda}\right]} - 1\right\}$$

$$\simeq \frac{N_o}{\lambda_K}\,\sigma_\Lambda \eta_o \left\{1 - e^{-y/\lambda_\Lambda}\right\}, \text{ for } (\lambda_K >> \lambda_\Lambda),$$

where $\lambda_\Xi$ and $\lambda_\Lambda$ are typical mean decay lengths of measured $\Xi^-$ particles and their $\Lambda$ from subsequent decay.

$\Lambda$ and $K_1^0$ decays believed by the scanner to have been produced in the $LH_2$ are identified as such, and the spatial distribution of these decays, Figs. 17(a, b), shows the expected dependence for $\Lambda$ decays of

$$\frac{dN}{dy}(\Lambda \text{ decays/cm}) = \frac{N_K \sigma_\Lambda \eta_o}{\lambda_K + \lambda_\Lambda}\left\{1 - e^{-y\left[\frac{\lambda_K + \lambda_\Lambda}{\lambda_K \lambda_\Lambda}\right]}\right\}$$

where $\lambda_K$ and $\lambda_\Lambda$ are the mean $K^-$ and produced -$\Lambda$ mean decay lengths, $N_K$ the number of $K^-$ beam particles exiting from the plate, $\sigma_\Lambda$ the $\Lambda$-production cross section in $K^-p$ collisions, and $\eta_o$ the $LH_2$ target density.

The subtraction of the $LH_2$-produced and $\Xi^0$-produced $\Lambda$ in FID3 affects the calculated efficiency, which in turn modifies the decay population inside FID3. Consequently, an iterative procedure was used to arrive at the final ET 7 scanning efficiency. The result of these iterations are given in Table VIII.1.

The difference of the experimental and the above calculated decay distributions for $\Lambda \rightarrow p\pi^-$ and $K_1^0 \rightarrow \pi^+\pi^-$ are shown in Fig. 18(a, b) throughout the entire fiducial volume. There is not an exact cancellation near the plate since Table VIII.1 was determined from an earlier, smaller sample of data.

Table VIII.1. Iterative calculation of the $\Lambda^0$ ET 7 scanning efficiency.

| y bin | 0th | 1s | 2nd Iteration |
|---|---|---|---|
| -86. to -84. | .448 | .467 | .469 |
| -84. -82. | .677 | .682 | .684 |
| -82. -80 | .741 | .756 | .758 |
| -80. -78. | .831 | .821 | .823 |
| -78. -76. | .853 | .862 | .863 |
| -76. -74. | .860 | .827 | .827 |
| -74. -72. | .918 | .880 | .880 |
| -72. -70. | .940 | .898 | .897 |
| -70. -68. | 1.142 | 1.113 | 1.112 |
| -68. -66. | .792 | 773 | .772 |
| -66. -64. | .925 | .809 | .808 |
| -64. -62. | .925 | .951 | .949 |

2. Flux Calculations.

The selection criteria used for both the $\Lambda$ and the $\overline{K}^0$ flux are

(i) Decay fiducial volume; $\Lambda \rightarrow p\pi^-$ and $K_1^0 \rightarrow \pi^+\pi^-$ decay points must be inside FID1, defined to be:

FID1: $-20.0 \leq (\text{cm}) \leq +20$

$-86.0 \leq (\text{cm}) \leq +70$

$+ 3.0 \leq (\text{cm}) \leq +34$

(ii) Lambda identify if mark 1 (1c $\Lambda \rightarrow p\pi^-$ fit) is successful, ($\chi^2 < 12$, confidence level $> 0.001$).

(iii) $K_1^0$ identity if mark 2 (1-constraint $K_1^0 \rightarrow \pi^+\pi^-$ fit) is successful, and mark 1 not successful.

(iv) Well-defined pathlength sample. $\Lambda$, $K_1^0$ decay used only if measured on a pathlength roll, i.e.,

Roll numbers ending in 0 for $101 \leq \text{Roll} \leq 301$

Roll numbers ending in 8 for $2001 \leq \text{Roll} \leq 2637$.

The number of measured $\Lambda$, $K_1^0$ on these rolls is a known fraction of the total in the film, $f_M = 0.0667$.

3. Hyperon Event Counts.

A hyperon event is defined to be an event type 17, 31, 32, or 37, lying inside the fiducial volume FID1, with a final state $V^0$ or charged decay accepted by the post scanner[32] as

ET 17, 37 / Mark 10 (3-constraint $\Lambda \rightarrow p\pi^-$ decay)

ET 31, 32 / Any mark with a $\Sigma^\pm$ decay.

Each such hyperon is weighted by the inverse of the following detection probabilities; scanning efficiency, hyperon escape probability from the fiducial volume FID1, SU(2) branching fractions to undetected final states, and a prong efficiency to account for unanalyzed multiprong neutral interactions. In detail these are:

(i) scanning efficiency: the spatial dependence of the scanning efficiency for event types 17 and 30 are shown in Figs. II.1(b-c) and II.1(e-f) in Appendix II. The event type 37 efficiency is taken to be the probability of observing an event type 30 and an event type 7 one mean decay length ($\lambda$) downstream. The ET 31, 32 efficiencies are separated into two parts: the three-prong efficiency which we measure accurately from the numerous three-prong type 30 events and the charged decay prong efficiencies which we measure from the center-of-mass decay angular and proper lifetime distributions of $\Sigma^{\pm}$ decays. The latter efficiencies are 0.94 and 0.95 for $\Sigma^{+}$ and $\Sigma^{-}$; respectively.

(ii) prong efficiencies: we have measured only one-prong and three-prong recoil neutral interactions; of course, all other odd-prongs allowed by energy conservation are possible in $\Lambda p$ and $\bar{K}^0 p$ collisions. To correct for these unmeasured events, we have calculated from the pre-scanned events on the master list (ML. 91) the ratio of five-prong to three-prong populations for positive, negative, and $V^0$ decay topologies,

$$\frac{N(ET\ 51)}{N(ET\ 31)} = 0.180 \equiv r_{51}$$

$$\frac{N(ET\ 52)}{N(ET\ 32)} = 0.151 \equiv r_{52}$$

$$\frac{N(ET\ 57)}{N(ET\ 37)} = 0.118 \equiv r_{57},$$

and have then weighted each three-prong event by the inverse of the appropriate prong efficiency,

$$P_{51} = \frac{1}{1+r_{51}} = 0.848$$

$$P_{52} = \frac{1}{1+r_{52}} = 0.868$$

$$P_{57} = \frac{1}{1+r_{57}} = 0.895.$$

We have neglected seven-prong events, which contributed less than 1% of the data.

(iii) Hyperon escape probability from FID1. For a hyperon of mean life $\tau$, momentum p, and having a potential flight path from its production to the edge of the fiducial volume, $\ell$, the probability that the hyperon will decay inside the fiducial volume before exiting is

$$P = 1 - e^{-\ell/\lambda}, \quad \lambda = \frac{p}{m} c\tau.$$

Each hyperon is weighted by $P^{-1}$.

(iv) SU(2) branching ratios to undetected final states.

a) $\Lambda \to n\pi^0$ decays. We weight each $\Lambda \to p\pi^-$ decay by $BR(\Lambda \to p\pi^-)^{-1} = (.642)^{-1}$.

b) $\Sigma^+ \to p\pi^0$ decays. We weight each unambiguous $\Sigma^+ \to p\pi^0$ decay by 0, each unambiguous $\Sigma^+ \to n\pi^+$ decay by $BR(\Sigma^+ \to n\pi^+)^{-1} = (.484)^{-1}$, and each ambiguous $\Sigma^+ \to p\pi^0 / n\pi^+$ decay by 1.

c) $\Lambda p \to \Sigma^+ n$. We weight each unambiguous $\Lambda p \to \Sigma^0 p$ event by

$$\frac{\sigma(\Lambda p \to \Sigma^+ n) + \sigma(\Lambda p \to \Sigma^0 p)}{\sigma(\Lambda p \to \Sigma^0 p)} = \frac{\left|\langle \frac{1}{2}\frac{1}{2}| 11 \frac{1}{2} -\frac{1}{2}\rangle\right|^2 + \left|\langle \frac{1}{2}\frac{1}{2}|10\frac{1}{2}\frac{1}{2}\rangle\right|^2}{\left|\langle \frac{1}{2}\frac{1}{2}|10\frac{1}{2}\frac{1}{2}\rangle\right|^2}$$

$$= 3.$$

d) $\Lambda p \to \Sigma^+ n\pi^0$. We weight each unambiguous reaction $\Lambda p \to \Sigma^+ p\pi^-$ by the factor 2 somewhat arbitrarily to account for undetected $\Sigma^+ n\pi^0$ final states.

4. Calculation of the Error $\sigma(y_i)$ on the Hyperon Discrepancy Distribution.

The error $dE_i$ in each bin $y_i$ has a statistical contribution from the event counts in that bin and a systematic error from the scanning efficiency, which are independent. Approximating the number of hyperons as a weight times the number of observed hyperons

$$E_i = w_i N_i,$$

where $w_i$ is some mean weight for all events in the bin $y_i$. Then

$$dE_i^2 = (w_i\, dN_i)^2 + (dw_i\, N_i)^2$$

$$= E_i^2 \left[\frac{1}{N_i} + \left(\frac{dw_i}{w_i}\right)^2\right],$$

where $w_i$ is essentially the inverse mean scanning efficiency for event types 17, 31, 32, and 37.

The error on the calculated number of hyperons, $C_i$, has three parts:

(i) error from $\Lambda$ flux;

(ii) error from $\bar{K}^0$ flux produced in the $LH_2$; and

(iii) error from the $\bar{K}^0$ flux produced in the platinum plate.

In turn, these are

(i) The number of hyperons produced by $\Lambda p$ interactions can be approximated by some mean weight times the number of $\Lambda$ decays,

$$N_Y = wN_{dec}.$$

The weight w involves the density of $LH_2$, the branching ratio $BR(\Lambda \rightarrow p\pi^-)$, escape correction weights, and the inverse scanning efficiency for $\Lambda$ decays. The error in the weight is dominated by the uncertainty in the scanning efficiency, and taking w to be the inverse scanning efficiency,

$$dN_Y^2 = N_Y^2 \left[\frac{1}{N_{dec}} + \left(\frac{dw}{w}\right)^2\right].$$

(ii) The error on the number of hyperons produced in $\bar{K}^0 p$ interactions, where the $\bar{K}^0$ was produced in the $LH_2$, can be treated in the same way as above, subject to the assumption the $K_1^0$ decay distribution is the same as the $\bar{K}^0 p$ interaction distribution in the $LH_2$. Then

$$dN_Y^2 = N_Y^2 \left[\frac{1}{N_{K_1\,dec}} + \left(\frac{dw}{w}\right)^2\right],$$

where the weight w is the inverse scanning efficiency for $K_1^0$ decays.

(iii) The error on the number of hyperons produced by $\bar{K}^0$ from the platinum plate may again be obtained by taking

$$N_{calc} = \bar{w}\ N_{exp},$$

but the weight $\bar{w}$ must be taken to be the same as the weight for $\Lambda p$ interactions in (i) above. Then

$$dN_{calc}^2 = N_{calc}^2 \left[\frac{\bar{w}}{N_{calc}} + \left(\frac{d\bar{w}}{\bar{w}}\right)^2\right].$$

The total error on the calculated number of hyperons is the sum in quadrature of the errors in (i)-(iii) above.

APPENDIX IX. Tables of cross sections.

(a). The elastic cross section, $\Lambda p \rightarrow \Lambda p$.

In 100 MeV/c bins from 300 MeV/c to 2500 MeV/c.

| $P_\Lambda$ (GeV/c) | $\sigma$ (mb) |
|---|---|
| 0.3 - 0.4 | 17.2 ± 8.6 |
| 0.4 - 0.5 | 26.9 7.8 |
| 0.5 - 0.6 | 7.0 4.0 |
| 0.6 - 0.7 | 9.0 4.0 |
| 0.7 - 0.8 | 13.6 4.5 |
| 0.8 - 0.9 | 11.3 3.6 |
| 0.9 - 1.0 | 11.3 3.8 |
| 1.0 - 1.1 | 21.1 4.8 |
| 1.1 - 1.2 | 14.0 3.4 |
| 1.2 - 1.3 | 9.6 2.9 |
| 1.3 - 1.4 | 13.5 3.4 |
| 1.4 - 1.5 | 26.0 4.8 |
| 1.5 - 1.6 | 16.4 3.7 |
| 1.6 - 1.7 | 15.9 4.1 |
| 1.7 - 1.8 | 23.5 5.0 |
| 1.8 - 1.9 | 23.3 6.0 |
| 1.9 - 2.0 | 19.8 4.4 |
| 2.0 - 2.1 | 20.1 5.6 |
| 2.1 - 2.2 | 16.3 4.5 |
| 2.2 - 2.3 | 17.6 5.1 |
| 2.3 - 2.4 | 18.0 4.8 |
| 2.4 - 2.5 | 9.6 3.4 |

In bins of equal incident $\Lambda$ path-length from 0.4 to 10 GeV/c.

| $P_\Lambda$ (GeV/c) | $\sigma$ (mb) |
|---|---|
| 0.4 - 1.2 | 14.8 ± 1.6 |
| 1.2 - 1.8 | 17.5 1.7 |
| 1.8 - 2.6 | 17.1 1.7 |
| 2.6 - 3.6 | 15.3 1.5 |
| 3.6 - 4.9 | 11.4 1.3 |
| 4.9 - 6.7 | 8.6 1.2 |
| 6.7 -10. | 6.5 1.2 |

The differential elastic cross section as a function of Λ momentum, $\frac{d\sigma}{dt}(mb/GeV^2)$.

| $P_\Lambda$(GeV/c) \ $-t(GeV/c)^2$ | 0.01-0.11 | 0.11-0.21 | 0.21-0.31 | 0.31-0.41 | 0.41-0.51 |
|---|---|---|---|---|---|
| 1.0 - 1.5 | 32.9 ±6.0 | 30.2 ±5.7 | 19.4 4.6 | 13.4 3.8 | 15.7 4.1 |
| 1.5 - 2.0 | 51.6 ±7.8 | 54.5 8.0 | 23.3 5.2 | 24.7 5.4 | 7.1 2.9 |
| 2.0 - 3.0 | 43.4 ±5.8 | 32.4 5.0 | 20.4 4.0 | 8.4 2.6 | 16.0 3.5 |
| 3.0 - 5.0 | 45.4 ±5.0 | 26.3 3.8 | 22.6 3.5 | 8.6 2.2 | 4.9 1.6 |
| 5.0 -10.0 | 29.6 ±4.0 | 14.5 2.0 | 16.4 3.0 | 4.12 1.5 | 3.5 1.4 |

| $P_\Lambda$(GeV/c) \ $-t(GeV/c)^2$ | 0.51-0.61 | 0.61-0.71 | 0.71-0.81 | 0.81-0.91 | 0.91-1.0 |
|---|---|---|---|---|---|
| 1.0 - 1.5 | 6.6 ±2.6 | 9.8 ±3.2 | 8.6 3.0 | 6.6 2.1 | 4.4 2.1 |
| 1.5 - 2.0 | 4.1 ±2.2 | 0. 0. | 7.1 2.9 | 1.4 1.3 | 1.5 1.3 |
| 2.0 - 3.0 | 8.4 ±2.6 | 1.4 1.1 | 5.6 2.1 | 0. 0. | 1.1 .9 |
| 3.0 - 5.0 | 1.4 ± .9 | 2.7 1.2 | 0.7 .6 | 0. 0. | 0.7 .6 |
| 5.0 -10.0 | 0. ±0. | 0. 0. | 1.0 .7 | 0. 0. | 0. 0. |

(b). The double pion production reaction, $\Lambda p \rightarrow \Lambda p \pi^+ \pi^-$, averaged over bins of equal incident $\Lambda$ pathlength from threshold to 10 GeV/c.

| $P_\Lambda$ (GeV/c) | $\sigma$ (mb) |
|---|---|
| 1.37 - 2.1 | 0.21 ± 0.15 |
| 2.1 - 3.1 | 3.0 ± 0.5 |
| 3.1 - 4.5 | 4.8 ± 0.7 |
| 4.5 - 6.3 | 5.2 ± 0.7 |
| 6.3 - 10.0 | 2.9 ± 0.6 |

(c). The single pion production reactions, $\Lambda p \rightarrow \Sigma p \pi$, averaged over bins of equal incident $\Lambda$ pathlength, from threshold to 10 GeV/c.

| $\Lambda p \rightarrow \Sigma^- p \pi^+$ | | $\Lambda p \rightarrow \Sigma^+ p \pi^-$ | |
|---|---|---|---|
| $P_\Lambda$ (GeV/c) | $\sigma$ (mb) | $P_\Lambda$ (GeV/c) | $\sigma$ (mb) |
| 1.18 - 1.9 | 0.94 ± 0.25 | 1.16 - 1.9 | 0.69 ± 0.29 |
| 1.9 - 2.9 | 2.7 ± 0.4 | 1.9 - 2.9 | 2.6 ± 0.6 |
| 2.9 - 4.3 | 3.0 ± 0.4 | 2.9 - 4.3 | 1.5 ± 0.4 |
| 4.3 - 6.0 | 1.6 ± 0.4 | 4.3 - 6.1 | 1.1 ± 0.3 |
| 6.0 -10.0 | 0.74 ± 0.24 | 6.1 -10.0 | 0.50 ± 0.28 |

(d). The total cross section.

| $P_\Lambda$ (GeV/c) | $\sigma$ (mb) |
|---|---|
| 1.0 - 1.5 | 23.6 ± 6.8 |
| 1.5 - 2.0 | 24.5 ± 6.8 |
| 2.0 - 3.0 | 29.2 ± 6.6 |
| 3.0 - 5.0 | 32.1 ± 8.0 |
| 5.0 -10.0 | 36.1 ± 8.0 |

(e). Resonance production cross sections.

| | $P_\Lambda$(GeV/c) | (mb) |
|---|---|---|
| $\Lambda p \rightarrow \Sigma^- \Delta^{++}$ | 4 ± 1 | 1.25 ± 0.5 |
| $\Lambda p \rightarrow \Sigma^+ \Delta^0$ | 4 ± 1 | 0.0 ± 0.23 |
| $\Lambda p \rightarrow \Sigma^-_{1385} \Delta^{++}$ | 4 ± 1 | 0.75 ± 0.3 |
| $\Lambda p \rightarrow \Sigma^+_{1385} \Delta^0$ | 4 ± 1 | 0.12 ± 0.3 |

(f). $\Xi^0 p$ reaction cross sections, averaged from 1.5 to 12.0 GeV/c. (Appendix V, Table V.2).

*TECHNICAL INFORMATION DIVISION*
*LAWRENCE BERKELEY LABORATORY*
*UNIVERSITY OF CALIFORNIA*
*BERKELEY, CALIFORNIA 94720*